INITIATION AND DEVELOPMENT OF SAND DUNES IN RIVER CHANNELS

by

Jeremy George Venditti

B.Sc. University of Guelph, 1995

M.Sc. University of Southern California, 1997

A THESIS SUBMITTED IN PARTIAL FULFILLMENT OF

THE REQUIREMENTS FOR THE DEGREE OF

DOCTOR OF PHILOSOPHY

in

THE FACULTY OF GRADUATE STUDIES

(Department of Geography)

We accept this thesis as conforming

to the required standard

……

……

……

……

……

……

THE UNIVERSITY OF BRITISH COLUMBIA

July 2003

ABSTRACT

This study investigated the initiation of bedforms from a flat sand bed and the transition between two-dimensional (2D) and three-dimensional (3D) bedforms in stream channels. Experiments were undertaken in which a narrowly graded, 0.5 mm sand was subjected to a 0.155 m deep, non-varying mean flow ranging from 0.30-0.55 m s^{-1} in a 1 m wide flume.

The initial flow conditions over the flat beds, prior to bedform development, were examined using laser Doppler anemometry to ensure that the flow agrees with standard models of flow and turbulence over hydraulically rough flat beds. Two types of bedform initiation were observed. The first occurs at lower flow strengths and is characterised by the propagation of defects via flow separation processes and local sediment transport to develop bedform fields. The second type of bedform initiation begins with the imprinting of a cross-hatch pattern on the flat sediment bed under general sediment transport which leads to chevron shaped forms that migrate independently of the initial structure. The chevron shapes are organised by a simple fluid instability that occurs at the sediment transport layer-water interface. Predictions from a Kelvin-Helmholtz instability model are nearly equivalent to the observations of bedform lengths in the experiments.

The 2D bedforms initiated by the Kelvin-Helmholtz instability developed into dune features that grew exponentially towards equilibrium dimensions. Dune heights and lengths increased with flow strength while their migration rate decreased. There was no obvious transition from small ripples at the beginning of the runs to dunes when the sandwaves are larger. Morphological estimates of sediment transport associated with the dunes and estimates associated with 'sand sheets,' which are superimposed bedforms on the dunes, were identical, indicating that the material moved over the dunes is controlled by the sheets.

Bedform phase diagrams suggest that 2D dunes should be formed under the hydraulic and sedimentary conditions observed in the experiments, but the bedforms became distinctly 3D. Overhead video revealed that, once 2D dunes are established, minor, transient excesses or deficiencies of sand are passed from one crestline to another. The bedform field appears capable of

‘swallowing’ a small number of such defects but, as the number grows with time, the resulting morphological perturbations produce a transition in bed-state to 3D forms that continue to evolve, but remain pattern-stable.

A second set of experiments was conducted to determine if the 2D-3D bedform transition could be linked to drag reduction processes. Laboratory measurements of turbulent fluctuations in clear water over fixed 2D and 3D dune beds with identical lengths and heights were obtained in a 17 m long, 0.515 m wide flume. The measurements reveal that some 3D bedforms, particularly random arrangements, reduce form drag over dunes. This reduces the applied boundary shear stress and should also reduce or stabilise the sediment transport rate, imparting greater stability to the bed.

TABLE OF CONTENTS

LIST OF TABLES

LIST OF FIGURES

LIST OF SYMBOLS

a , b , c	line fitting coefficients
A	bedform cross-sectional area
A_b	planimetric bedform area
b_0 , b_1	intercept and slope of a least-squares regression
C_D , C_{Di} , $\overline{C}_{De}$	drag coefficient, its initial value and its mean equilibrium value
C_{D*}	drag coefficient based on the form drag component of shear separated using the Smith and McLean model
C_{DR}	drag coefficient based on the form drag component of shear estimated from Reynolds stress profile
C_{DS}	drag coefficient based on the form drag component of shear estimated from depth slope product
C_{ku} , C_{kw}	line fitting coefficients
CV	coefficient of variation
d , d_{st} , d_e	flow depth, its initial value, its mean and its equilibrium value
$\overline{d}$, d_{max} , d_{min}	mean, maximum and minimum flow depth
d_{tl}	depth of the transport layer
D , D_{50}	grain size and its median
D_*	dimensionless grain size parameter
D_u , D_w	line fitting coefficients
f_{min}	frequency of sand sheet passage
f_p	pump frequency
ff , ff_S , $ff_{0.2}$, ff_R , ff_B	friction factor, an estimate based on the depth slope product, an estimate based on the law of the wall, an estimate based on Reynolds stress profile and an estimate based on a measured Reynolds stress near the bed
F_D , F_{Di} , $\overline{F}_{De}$	drag force, its initial value and its mean equilibrium value
F_{D*}	drag force based on the form drag component of shear separated using the Smith and McLean model
F_{DR}	drag force based on the form drag component of shear estimated from Reynolds stress profile
F_{DS}	drag force based on the form drag component of shear estimated from depth slope product
Fr	Froude number
F_{tot} , F_{form} , F_{sf}	Total drag force and its form component and skin component
g	gravitational acceleration
I_u , I_w	streamwise and vertical turbulence intensity
h	generic bedform height
H , H_i , H_e	dune height, its initial value and its equilibrium value
H_{min} , $\overline{H}_{min}$	sand sheet height and its mean value over a dune
k	time step in autocorrelation

k_s, $k_{s0.2}$, k_{sR}, k_{sB}	equivalent sand roughness, an estimate based on the law of the wall, an estimate based on Reynolds stress profile and an estimate based on a measured Reynolds stress near the bed
K	bedload discharge coefficient
ℓ	characteristic length of a body
l	generic bedform length
L, L_i, L_e	dune length, its initial value and its equilibrium value
L_a	areal bedform length
L_c	distance along bedform crest
L_E	Eulerian integral length scale
$\overline{L}_i$	mean initial dune length
L_{K-H}	Kelvin-Helmholtz instability wavelength
L_{min}, $\overline{L}_{min}$	sand sheet length and its mean value over a dune
L_{xy}	oblique striation separation
M_s, M_w	mass of sediment, mass of water
n	number of observations
P	porosity of sand
Q	discharge
Q_s, Q_{si}, Q_{se}	bedload transport rate, its initial value and its equilibrium value
Q_{s-HS}	Bedload transport measured using a Helley-Smith sampler
Q_{s-d}, Q_{s-ss}	bedload transport estimated from morphology of dunes and sand sheets
r	Spearman rank order correlation coefficient
r_{ADV}	ADV correlation coefficient
R, R_e	dune migration rate and its equilibrium value
Re, Re_g	Reynolds number and grain Reynolds number
R_b	generic bedform migration rate
Ri	Richardson number
R_{min}	sand sheet migration rate
R_{uw}	boundary layer correlation coefficient
$R(t)$	autocorrelation function
S, S_i, S_e	water surface slope, its initial value and its equilibrium value
t	time or experimental time
t_{2D}	time to the development of 2D bedforms
t_{3D}	time to the development of 3D bedforms
t_c	time to when bedforms extend across the channel
t_i	time of first bedform observation or time to develop first bedform
t_{lag}	time between arrival of bedform SFB at to echo-sounder 1 and 2
t_{max}	time to a local maximum in Λ_{NDS-im}
t_{pass}	time required for a bedform to pass one echo-sounder
t_{tot}	duration sand sheets are passing one echo-sounder over a dune
T	dimensionless shear stress parameter
T_B	burst period

T_E	Eulerian integral time scale
TKE	turbulent kinetic energy
u , u_i , u' , U	streamwise velocity, its instantaneous value, its fluctuation about the mean and its at-a-point time-averaged mean
u_* , u_{*S} , $u_{*0.2}$, u_{*R} , u_{*B}	shear velocity, an estimate based on the depth slope product, an estimate based on the law of the wall, an estimate based on Reynolds stress profile and an estimate based on a measured Reynolds stress near the bed
u_{*cr}	critical shear velocity for particle entrainment
u_1 , u_2	velocity of upper fluid and velocity of lower fluid in Kelvin-Helmholtz instability
$\overline{U}$, $\overline{U}_e$	mean flow velocity and its equilibrium value
$U_{0.5}$	velocity at z = 5 mm
U_b	velocity of a body
U_{max}	maximum streamwise velocity
U_p , U_{pd}	particle velocity and its depth averaged value
U_{rms} , W_{rms}	streamwise and vertical at-a-point root-mean-square velocity
U_z	velocity at z
v , v_i , v' , V	cross-stream velocity, its instantaneous value, its fluctuation about the mean and its at-a-point time-averaged mean
V_{tl} , V_s , V_w	volume of transport layer, volume of sediment, volume of water
w , w_i , W , w'	vertical velocity, its instantaneous value, its time-averaged mean and its fluctuation about the mean
x	distance along the flume
x_{front}	distance from first sand sheet crestline to the downstream dune crestline
x_{rear}	distance from upstream crestline to the first sand sheet crestline
x_R	reattachment length
x_{wl}	separation of water level sensors
y	distance across the flume
y_b	distance that bedform extended across flume
y_w	flume width
z , z_{min} , z_{max}	height about datum, its maximum value and its minimum value
z_{bed}	change in the mean bed elevation
z_C , z_{Tr}	height of the bedform crest and trough
z_o , $z_{o0.2}$, z_{oR} , z_{oB}	roughness height, an estimate based on the law of the wall, an estimate based on Reynolds stress profile and an estimate based on a measured Reynolds stress near the bed
z_{WS} , z_{WSe}	water surface level and its equilibrium value
z_{WS-max} , z_{WS-min}	maximum and minimum water surface level
β	bedform shape factor
δ	thickness of velocity interface
ε	eddy viscosity
φ , ϕ , γ	rotation angles
κ	von Karman constant

λ_s	streak spacing
λ_x	streamwise distance lobes of three-dimensional bedforms extend downstream
λ_y	cross-stream distance between lobes of three-dimensional bedforms
$\Lambda_{Allen-a}$, $\Lambda_{Allen-b}$	measures of bedform three-dimensionality
Λ_{NDS}, Λ_{NDS-im}	non-dimensional span and its image average
ν	kinematic viscosity
θ , θ_{cr}	dimensionless shear stress and its critical value for particle entrainment
ρ	density
ρ_1, ρ_2	density of upper fluid and density of lower fluid in Kelvin-Helmholtz instability
ρ_s	density of quartz sand
ρ_{tl}	density of the transport layer
ρ_w	density of water
τ , τ_S , $\tau_{0.2}$, τ_R , τ_B	shear stress, an estimate based on the depth slope product, an estimate based on the law of the wall, an estimate based on Reynolds stress profile and an estimate based on a measured Reynolds stress near the bed.
τ_*	shear stresses separated using Smith and McLean [1977] model
τ_{cr}	critical shear stress for particle entrainment
τ_{Si} , $\overline{\tau}_{Se}$	initial and equilibrium shear stress based on the depth-slope product
τ_{tot} , τ_{sf} , τ_{form}	total spatially averaged shear stress, its skin component and its form component
τ_{uw}	time-averaged at a point Reynolds stress
ξ	average departure of z about its mean

DEDICATION

For Sammie

ACKNOWLEDGEMENTS

This work would not have been possible without the intellectual and financial support of Michael Church. His boundless enthusiasm and encouragement were integral. Sean Bennett of the National Sedimentation Laboratory, United States Department of Agriculture (NSL-USDA) in Oxford Mississippi also contributed substantially by facilitating the research. Their combined guidance and patience were invaluable and greatly appreciated. I would also like to thank the other members of my committee (O. Slaymaker and M.Quick) for careful and insightful reviews of the material presented herein.

M. Römkens (Director of NSL-USDA) and C. Alonso (Research Leader-Watershed and Channel Processes Unit) kindly provided access to NSL-USDA facilities. R. Millar, G. Lawrence and M. Quick kindly provided access to the Engineering Hydraulics Laboratory (EHL) at UBC.

Technical support was provided by J. Cox, J. Milam, and D. Wren at NSL-USDA and by I. Liu and V. Kujala at UBC. The image analysis could not have been accomplished without the help of several undergraduate assistants, primarily N. Manklow, with some help from C. Christie. Several other tasks including the data collection at EHL-UBC were done with help from N. Manklow, C. Christie, and J. Rempel. A. Vigna helped prepare many of the diagrams and David Printing Services Ltd. provided complimentary printing services.

Financial support was provided through a University Graduate Fellowship, a Natural Science and Engineering Research Council of Canada (NSERC) Post-Graduate Scholarship, and a Research Assistantship provided through a NSERC operating grant to M. Church. Funds for the experiments were provided by S. Bennett and the Watershed and Channel Processes Unit (NSL-USDA experiments) and a NSERC operating grant to M. Church (NSL-USDA and EHL-UBC experiments). The video image frame grabber was purchased using a Ph.D. Research Grant from the American Association of Geographers – Geomorphology Specialty Group.

Chapter 1: Introduction

1.1 Introduction

Alluvial river channels are the manifestation of a suite of hydraulic and sedimentary processes acting within the channel and watershed. These processes act to modify and adjust the channel system at spatial and temporal scales ranging from those of individual particle movements to ones of meander-bend migration and floodplain evolution. Our ability to understand and predict fluvial processes across this range of scales remains rudimentary because of the complex nature of the interaction of fluids and sediments under the constraint of varying boundary conditions [*McLean et al*., 1996]. In sand-bedded alluvial channels, the bottom boundary consists of a labile bed comprising bedforms of many different scales and geometries. A deeper knowledge of how sandy fluvial bedforms interact with the flow field is crucial to understanding sediment transport processes in sand-bedded rivers and, ultimately, to the evolution of alluvial systems.

This study seeks to address the processes responsible for the initiation and subsequent growth of bedforms in alluvial channels. The physics of these features have fascinated researchers from many disciplines. However, in spite of nearly a century of effort, no comprehensive theory capable of describing the spectrum of observed shapes and sizes exists [*Raudkivi*, 1999]. Given this lack of a complete theory, the research proposed here seeks to determine why a flat sand bed becomes unstable and how this instability leads to bedform development. Before detailing the specific objectives and methodology for this research, a brief background is presented which discusses problems associated with current theory of bedform development.

1.2 Background

1.2.1 Classical Conception of a Continuum of Bedforms

Observations in rivers and flumes within the past 50 years have revealed that in flows over sand beds a typical sequence of bedforms evolves as the velocity increases (Figure 1.1) [*e.g., Simons et al.,*

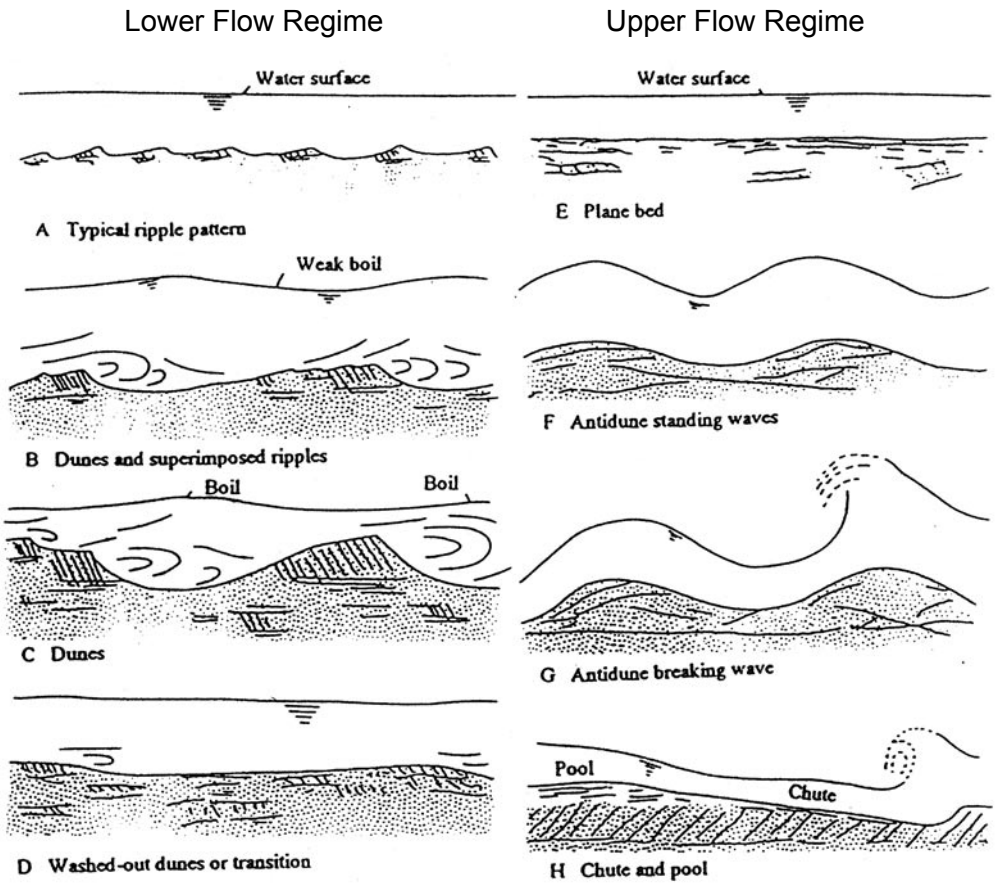

Figure 1.1: Typical sequence of bedforms in alluvial channels. Bed morphologies A-E occur with increasing flow strength [from *Simons and Richardson*, 1965].

1961; *Guy et al.*, 1966; *Simons and Richardson*, 1966]. This continuum of bedforms is conceived as occurring under a graduated set of flow regimes. All features up to and including dunes (Figure 1.1) are generally termed *lower flow regime* bedforms and typically are characterised by small bed-material transport rates. The lower regime flow sequence is plane bed - ripples - dunes, with increasing resistance to flow. The *upper flow regime* begins with restoration of a plane bed on which the lower regime bedforms are 'washed away'. Relatively large bed-material discharges and small flow resistance characterise the upper regime. Following plane bed, antidunes begin to form with upstream breaking waves over the dune crest. This type of bed is typically followed by the formation of a pool-and-chute morphology [*Simons and Richardson*, 1966].

1.2.2 Bedform Morphology and Terminology

A confusing variety of terms are used to describe lower regime bedforms (e.g., ripples, dunes, sandwaves, and megaripples) [*Ashley*, 1990]. Bedforms may be only a few centimetres or several metres in height, up to 1000 m in length, and display an unmistakable regularity, although the characteristics of any one bedform field can only be quantified statistically [*Ashley*, 1990; *Raudkivi*, 1999]. These topographic features are often highly asymmetrical with an upstream (stoss) slope averaging 2^o to 6^o and a lee slope near the angle of repose (~30^o) [*McLean,* 1990]. A simple empirical relation, proposed by *Flemming* [1988] on the basis of several thousand measurements, relates bedform height, H, and length, L, as

$$H = 0.0677 L^{0.81} . \qquad 1.1$$

Extensive data compilations by *Allen* [1968] and *Flemming* [1988] demonstrate that there is a break in the continuum of observed bedforms defining two sub-populations of bedforms, which have become almost universally known as 'ripples' and 'dunes'. Ripples are conventionally thought to be restricted to sediments in which $D \leq 0.7$ mm [*Bridge*, 2003]. It is widely acknowledged that equilibrium ripple dimensions scale with the grain size, D, or a grain Reynolds number,

$Re_g = U_* D / n$ (u_* is the shear velocity and n is the kinematic viscosity). In contrast, dunes, the focus of the work presented here, typically scale with the flow depth [*Bridge*, 2003]. Despite the efforts of some authors to generate a process based separation of ripples and dunes [*e.g. Bennett and Best*, 1996], there is no consensus on how the terms ripple and dune should be applied.

Techniques to divide ripples from dunes vary amongst sources and some authors choose to make no distinction at all. Early work by *Allen* [1968] indicated that bedforms developed in sand have an aspect ratio, H / L, varying between 0.01 and 0.20, although exceptions can occur, and suggested for ripples $0.05 < H / L < 0.20$ while for dunes $0.01 < H / L < 0.10$. *Bridge* [2003] concurred, suggesting H / L is typically <0.06 for dunes and <0.10 for ripples, but noted that H / L is dependent on a measure of the shear stress.

From an empirical standpoint, ripples appear to have larger aspect ratios in general, although the data of *Guy et al.* [1966] indicate that there is significant overlap in H / L values for ripples and dunes. Ripples have aspect ratios between 0.03 and 0.10 at Re_g = 7, 0.04 - 0.10 at Re_g = 10 and 0.08 - 0.10 at Re_g = 15. At the same Re_g values, dunes have $H / L << 0.10$. Based on *Guy et al.* [1966], ripples have a lower limit of 0.05 whereas for dunes, H / L can be much less but only slightly greater. Thus, a separation between ripples and dunes based on the aspect ratio may still be valid. Nonetheless, based on a consensus amongst many researchers, *Ashley* [1990] suggested dunes are all features with $L > 0.60$ m while ripples are simply smaller bedforms.

In cross-section, bedforms tend to take on one of three morphologies: symmetric, asymmetric, or humpback (Figure 1.2a). Symmetric bedforms are approximately sinusoidal and are thought to lack flow separation [e.g. *Kostaschuk and Villard*, 1996; *Best and Kostaschuk*, 2002]. Asymmetric bedforms are roughly wedge-shaped, with the lee side angle at repose, and exhibit strong separation cells. Humpback dunes have a steep lee side slope but sediment accumulates on their stoss slope whereas asymmetric bedforms usually plane out [*Saunderson and Lockett*, 1983].

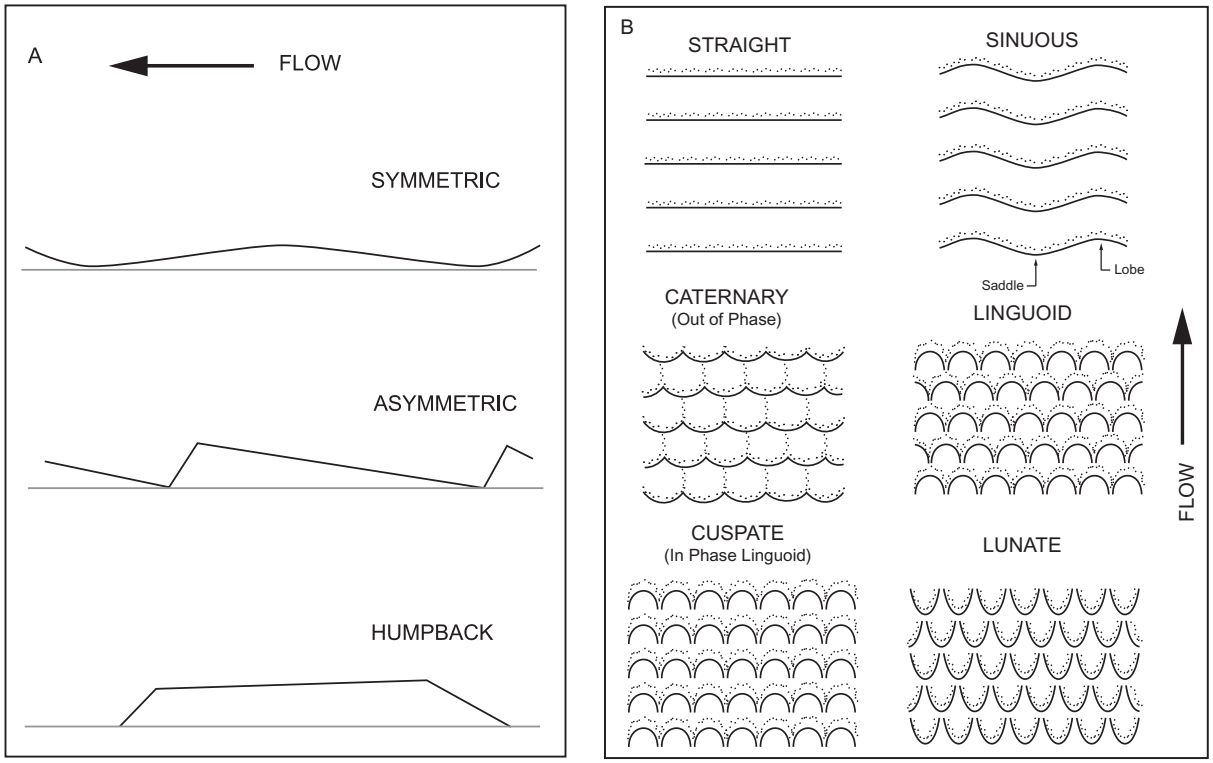

Figure 1.2: Types of (a) cross-sectional and (b) planimetric dune morphologies. Panel a is adapted from *Bridge* [2003] and panel b is adapted from *Allen* [1968].

The planimetric morphology of fully developed bedforms is divided into two subclasses: two-dimensional (2D) and three-dimensional (3D). Two-dimensional ripples and dunes have fairly regular spacing, heights and lengths. Their crestlines tend to be straight or slightly sinuous and are oriented perpendicular to the mean flow lines. In contrast, 3D features have irregular spacing, heights and lengths with highly sinuous or discontinuous crestlines [*Ashley*, 1990].

A great number of secondary descriptors have been proposed for the planimetric morphology of bedforms, but *Allen's* [1968] is the most comprehensive (Figure 1.2b). Two-dimensional morphologies are straight or slightly sinuous. Sinuous crests may be aligned, where the lobes and saddles line up, or out of phase, where lobes line up with saddles. Three-dimensional morphologies are highly sinuous, catenary, linguoid, or lunate. Catenary features have crestlines that open downstream (barchanoid saddles) and have continuous crestlines, while lunate features are the same with discontinuous crestlines. Linguoid features have crestlines that form lobes with discontinuous crests. Highly sinuous, catenary and linguoid morphologies can be aligned or out of phase. *Allen* [1968] suggested the term 'cuspate' for aligned linguoid features and indicated that aligned lunate features are not common.

1.3 Theories of the Organisation and Development of Two-Dimensional Bedforms

1.3.1 Initiation of Particle Motion

Most contemporary ideas on dune development envision the generation of bedforms from a plane bed. At sufficiently small flow velocities, sand particles on a planar bed will resist the fluid forces acting on them and will remain in position. As the flow velocity increases, a threshold is reached where the lift and drag forces due to the flow exceed the submerged weight of the grain and other resisting forces on the bed. The critical stage of initiation of transport is difficult to determine and several methods have been proposed. Early work suggested that the initiation of sediment transport could be described in terms of the ratio of critical bed shear stress and the submerged weight of a single layer of bed materials [*e.g., Shields*, 1936]. More recent work has reasoned that the

entrainment of sediment can be understood as a statistical interaction process between the distribution of instantaneous bed shear stresses caused by near-bed turbulence and the critical bed shear stresses for individual particles. The overlap of the distributions define the entrainment level [Grass, 1970]. The seminal work of *Kline et al.* [1967] and *Kim et al.* [1971] defined random (or quasi-random) streaks, ejections, and sweeps in the boundary layer generated by bursting processes that are ubiquitous in turbulent flows over smooth boundaries. Sedimentologists drew an analogy between these microturbulent features and the macroturbulent features observed in river channels to provide the instantaneous lift and drag forces necessary to locally entrain sediment from the bed [*Best*, 1992]. The way in which sediment, once mobilised, is organised into unmistakably regular sandwaves has been the subject of considerable controversy in the literature. Over the last 50 years, most work on bedform development has focused on one of two theories.

1.3.2 Perturbation Analysis

The most pervasive theory for the generation of bedforms has been perturbation analysis (also referred to as linear stability analysis). Initially proposed by *Exner* in the 1920s [as described by *Leliavsky*, 1955], and later developed by *Anderson* [1953], perturbation analysis involves the linearisation of the equations of motion of both fluid and sediment over an infinitesimally small bed perturbation or defect. Subsequently the response of the perturbation to flow is used to predict suppression or growth of the perturbation [*McLean*, 1990]. This approach ascribes the initial instability that generates bedforms to a phase difference between the maximum bedload transport rate and the bed topography. Simply stated, the maximum fluid stress occurs upstream of the perturbation crest and, assuming sediment transport is some function of the local stress, deposition occurs at the perturbation crest, producing bedform growth. This stress maximum is thought to be the result of topographic accelerations over the bedform. In all cases, the shift in transport is upstream of the shear stress maximum. If the lag did not exist, incipient bedforms would become unstable and erosion would ultimately clear the defect from the bed.

Reasons proposed for this lag include: 1) phase differences between surface and bed waves [*Kennedy*, 1963]; 2) convective acceleration of the fluid over the stoss slope [*Smith*, 1970; see also *McLean*, 1990; *Wiberg and Smith*, 1985]; 3) increased sediment suspension by turbulence at the stress maximum, increasing the transport length for grains [*Engelund*, 1970]; and 4) the effect of gravity on sediment transported up the dune slope enhancing sediment flux on downward sloping boundaries (near the dune crest) and reducing flux on upward sloping boundaries (near the dune slip-face) [*Fredsoe*, 1974]. Unfortunately, *McLean* [1990] notes that none of these assumptions can be justified in light of the spatial and temporal variations in turbulence over bedforms.

1.3.3 Flow over 2D Dunes

Fluid flows over 2D laboratory bedforms and negative steps have been studied extensively, and several major components are commonly recognised in the flow field (Figure 1.3). Typically, there is an outer region that is not directly influenced by the detailed geometry of the bedforms insofar as the flow here responds largely to the spatially averaged resistance effect communicated to it from below. The outer region is connected to the mobile sediment bottom via several intervening zones whose dynamics differ from classic turbulent boundary layer flows over flat beds. In particular, the presence of a dune leads to significant form drag due to asymmetries in the flow field on the upstream (stoss) and downstream (lee) sections of the dune. As the flow moves up the gently sloping stoss side of the dune, the streamlines converge and the fluid is accelerated toward a maximum depth-averaged velocity near the crest. At the slip-face crest, the streamlines detach from the surface and flow separation occurs in the lee of the dune. Provided that the lee side slope is sufficiently steep, a distinct separation cell or recirculation 'bubble' occupies the near-bottom region immediately downstream of the dune crest. Flow in the separation cell can be quite variable, but in a time-averaged sense, there exists a counter-rotating eddy with upstream velocity along the bottom. At the downstream margin of the cell, the separated flow reattaches to the bottom at a downstream distance that is, on average, 3.5 - 5 H [*Engel*, 1981; *Bennett and Best*, 1995*; Venditti and Bennett*, 2000]. The

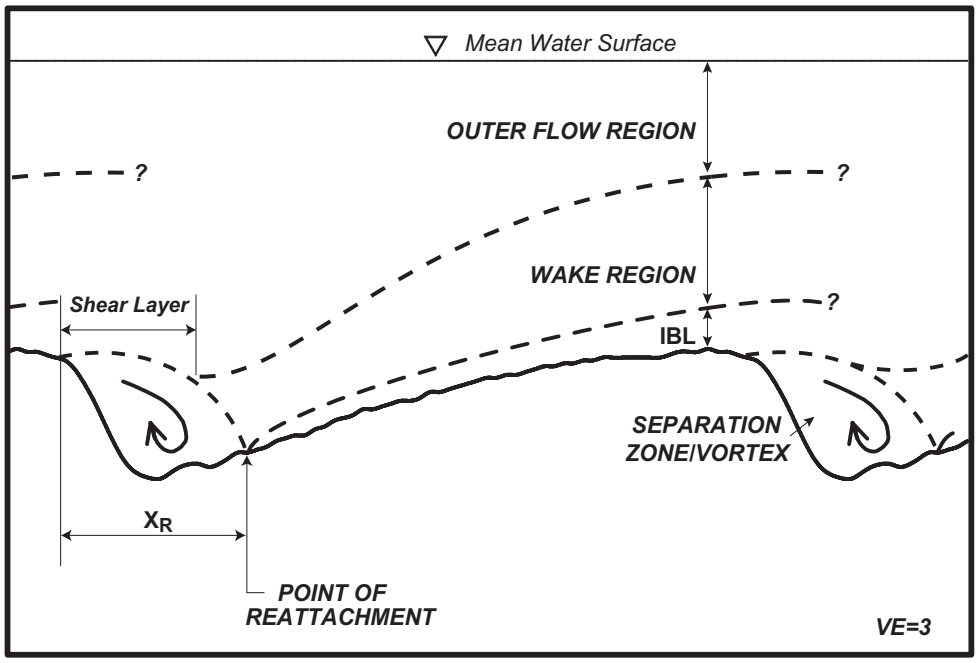

Figure 3: Schematic of the boundary layer structure over a dune [based on *McLean*, 1990]. X_R is the horizontal distance from the crest to the reattachment point and IBL is an abbreviation for the internal boundary layer [from *Venditti and Bauer*, in review].

reattached flow accelerates up the stoss side of the dune, and an accompanying internal boundary layer (IBL) grows in thickness from the point of reattachment toward the dune crest. The character of the IBL is related to skin friction imparted by grain roughness, although disturbance by eddies from the wake region can be frequent (*Nelson et al.*, 1993).

The near-bottom flow region (i.e., the separation cell and IBL) is linked to the outer flow region through the intervening wake region and shear layer. The dynamics of these latter two flow features are relatively poorly understood, although they have generated considerable interest because of ramifications for sediment transport, the stability of bedforms, and the existence of quasi-coherent flow structures [*McLean*, 1990; *Nelson et al.*, 1993; *McLean et al*., 1994; *Bennett and Best*, 1995; *Venditti and Bennett*, 2000]. For example, the origin of kolks and boils in large fluvial systems [e.g., *Matthes*, 1947], which are typically heavily sediment-laden, has been variously ascribed to the boundary layer bursting process [*Jackson*, 1976; *Yalin*, 1992], Kelvin-Helmholtz instabilities on the shear layer [*Kostaschuk and Church*, 1993; *Bennett and Best*, 1995; *Venditti and Bennett*, 2000], shear-layer destabilisation coupled with ejection of slow-moving fluid from the recirculation bubble [*Nezu and Nakagawa*, 1993] and vortex shedding and amalgamation [*Müller and Gyr*, 1986]. Most authors now acknowledge some interplay amongst the latter three processes [see discussion in *Nezu and Nakagawa*, 1993]. These periodic motions can cause orders of magnitude variations in sediment transport rates at-a-point and are thought to be responsible for much of the vertical mixing in rivers [*Lapointe*, 1992, 1996; *Kostaschuk and Church*, 1993]. Acknowledgement of the complexity of the turbulent boundary layer structure over bedforms has led several investigators to examine the generation of bedforms from a flow structure approach.

1.3.4 Empirical Flow Structure Approach

This approach to bedform development can be properly attributed to *Raudkivi* [1963; 1966] who proposed, from a series of experiments, that the process of flow separation over a bed defect and the characteristics of the separated flow control dune generation. Technological advances in recent years

have allowed researchers to detail the characteristics of the flow field depicted in Figure 1.3. This has resulted in a 'rediscovery' of *Raudkivi*'s ideas in the wake of the failure of perturbation analysis approaches to bedform development.

Over a flat bed, coherent flow structures thought to be analogous to microturbulent sweeps, ubiquitously observed over smooth surfaces, are envisioned to create flow parallel ridges which flare at their downstream ends creating small accumulations of sediment or 'defects' [*Best*, 1992]. Reattachment of the flow over the defects is said to enhance the turbulence intensity, erosion, and sediment transport processes in the lee of the defect. Movement of grains is maintained by the turbulent agitation from eddies in the wake. As the wake diffuses, the shear is not sufficient to maintain transport and material settles into a new bed defect. Once an incipient train of bedforms is established on the boundary, erosion in the lee of the defects and deposition at the peaks build the bedforms. As this process continues, the defects are streamlined to generate ripple forms [*Raudkivi*, 1963; 1966].

The development of bedforms from the turbulent flow field described above is only hypothetical; the process has not been interpreted mathematically. Measurement programs have not been initiated to provide experimental evidence that the flow processes described above occur over smaller bedforms and bed defects, although these processes can be observed in the patterns of sediment movement [*Best*, 1992]. Also complicating this conceptual model is the fact that flow separation is not always observed over developed bedforms. *McLean and Smith* [1979] and *Kostaschuk and Villard* [1996] noted that there was no evidence for flow separation over asymmetrical dunes in the Columbia and Fraser Rivers. Without flow separation, the flow and sediment transport processes described above could not operate. However, it should be acknowledged that initial generation and propagation of defects is a smaller scale phenomenon than observations in the Columbia and Fraser Rivers.

A more substantial problem is that there is a large temporal scale transition between the processes of fluid flow and bedform adjustment that has not been addressed. Turbulent flow fields are highly

dynamic and sensitive to small changes in the bulk hydraulics. Similarly, the turbulent flow field is highly disorganised and characterised by the generation of eddy structures by non-periodic and, possibly, non-linear processes [*Venditti and Bennett*, 2000; *Venditti and Bauer, in review*]. In contrast, changes in the highly organised bed structure are typically slow, since significant volumes of sediment must be moved. It is not clear how the highly structured, slowly evolving bedforms can result from random turbulent structures unless the turbulence becomes phase locked. *Best* [1992] noted that burst events were concentrated over fixed, flow parallel ridges in experiments. Yet the development of the flow parallel ridges on a sand bed is still dependent on the random turbulent structures.

1.3.5 An Alternative Theory

Interestingly, discussions of bedform development have largely ignored the possibility that at the earliest stage of development, bedforms may be simply a manifestation of pre-existing, wave-like variations in the bed shear stress. However, the literature is not devoid of reference to this possibility. *Gilbert* [1914] was first to suggest that bedform initiation is related to 'rhythms in the flow of water and turbulence'; a view widely held by scientists from the former Soviet Union [*Allen*, 1968]. Based on Helmholtz's principle of 'least work', *Bucher* [1919] held that bedforms are formed to afford a surface of least friction. Helmholtz's concept was later refined to explain the periodic disruption of a stratified fluid interface, now known as a Kelvin-Helmholtz wave structure. Unfortunately, *Bucher's* [1919] ideas have been deemed incorrect because the larger-scale bedforms were envisioned to be in-phase with surface waves, a phenomenon now understood to be associated with the upper flow regime and antidunes [*Allen*, 1968].

Later work by *Liu* [1957] resurrected the idea of bedforms generated by a pre-existing fluid flow condition by applying theory for an instability generated at the interface of a density stratified fluid. The instability was envisioned to occur at the interface of the sediment laden wall region and the viscous sub-layer region of a turbulent flow resulting in a shear layer characterised by periodic

streamwise variations in velocity along the bed. Unfortunately, difficulties in measuring the velocities and densities of each layer impeded acquisition of a mathematical solution by *Liu* [1957]. So, the concept was extended to develop a criterion for the first appearance of bedforms based on flow variables (streamwise velocity, kinematic viscosity) and sediment characteristics (mean grain-size, fall velocity). The work is largely discounted because the analysis predicts symmetric bedforms [*Allen*, 1968]. However, there is no reason to assume that an instability that gives rise to well-organised variations in sediment transport must continue to dominate the flow once a bedwave is established. This line of thought deserves revisitation. Nonetheless, moving to this type of explanation still does not address the fundamental question of how 3D bedforms, now understood to be equilibrium forms [*Baas et al.*, 1993; *Baas* 1994; *Baas*, 1999], are developed.

1.4 Three-Dimensional Bedform Development

The mechanisms responsible for the development of 3D bedforms have not been previously addressed in the literature. Several authors have suggested that 2D bedforms form under 2D flow conditions while 3D bedforms occur when the flow is 3D [e.g., *Allen*, 1968; *Costello and Southard,* 1981; *Ashley*, 1990; *Southard and Boguchwal*, 1990; *Southard*, 1992]. Explicit assumptions are made that 2D bedforms are in equilibrium with the flow over them and that there is some change in the flow structure at higher velocities triggering change in bedforms. Recent observations have suggested that neither assumption is fulfilled. The flow field over 2D bedforms appears two-dimensional when the time-averaged flow statistics are examined. However, the mean flow structure, characterised in Figure 1.3, is the manifestation of eddy structures that have been observed to have a strong cross-stream component [*Venditti and Bennett*, 2000; *Venditti and Bauer, in review*]. A partial explanation for why both bedform morphologies exist when the flow is 3D may be that 2D bedforms are not the equilibrium bedform for a given set of flow conditions.

The assumption that 2D bedforms are in equilibrium arises from classical conceptions of bedform stability and the nature of the experiments that have defined this stability. Classical concepts of a

continuum of bedforms assume that transitions amongst lower regime plane beds, ripples, dunes, and upper regime plane beds, are sharp. In many cases, transitions occur within an increase of a few centimetres per second in flow velocity. The transition between 2D and 3D bedforms is envisioned to occur in much the same way, despite the fact that the transition is not sharp [*Costello and Southard,* 1981].

Most research on small-scale bedforms suggests that, under low flow conditions, bedforms exhibiting a 2D straight-crested morphology are common and, at higher flow velocities, 3D forms are established exhibiting linguoid shapes [*Southard and Boguchwal*, 1990; *Southard*, 1992]. The time required to form each morphology is relatively short in both circumstances (tens of minutes to hours) [*Southard*, 1992]. The experiments of *Baas et al.* [1993] suggested that this is not strictly true because although 2D ripples appear to be in equilibrium, given enough time they will develop into 3D linguoid ripples. The time required for this transition to occur may be several days in some cases. Given the short time periods commonly used in laboratory experiments, it is easy to understand why the transition had not previously been examined in depth. Furthermore, the frequent changes in mean hydraulics of rivers and tidal environments may prevent bedforms from reaching equilibrium form. The reason why 3D bedforms are observed to exist in the upper part of the stability fields may simply be that it takes less time for a turbulent flow field to move the sediment required for the transition.

Further support for this hypothesis can be found in recent experimental fluid mechanics work suggesting that 2D surfaces offer considerably higher resistance to flow than 3D surfaces. Experiments by *Sirovich and Karlsson* [1997] have convincingly shown that hydraulic drag can be reduced by up to 20 percent by changing patterns of perturbations from a strictly 2D alignment to an out-of-phase (three-dimensional) alignment. This effectively modulates the burst sweep cycle, reducing boundary shear stress. It can be hypothesised that the 2-3D transition reduces the applied stress by disrupting the turbulence structure over a bedform.

It is well known that sediment transport rates are dependent on the applied shear stress. A mechanism that reduces (or stabilises) the shear stress should also reduce (or stabilise) the sediment

transport rate. Thus, passive drag reduction processes such as those proposed by *Sirovich and Karlsson* [1997], may protect the bed from erosion by reducing the applied shear stress. This can contribute to the stability of the bed and the channel by reducing susceptibility to degradation.

The physical processes involved in the initiation and development of equilibrium bedforms are not well understood. Whether the ideas of *Liu* [1957] and the numerous investigators interested in the turbulence structure over bedforms can be integrated into a coherent explanation of bedform initiation has not yet been determined. The mechanics associated with the 2-3D bedform transition have not been elucidated. The contribution of drag reduction processes to sand bed stability has not been addressed. Therefore, experiments designed to readdress the issue of bedform initiation and to document the transition between 2D and 3D forms are timely.

1.5 Problem Statement and Objectives

Following the questions raised in the foregoing review, this research project employed a phenomenological approach to examine the physical processes that transform a flat sand bed into 2D bedforms and then into a 3D state. The specific objectives of the research were as follows:

(1) to obtain a detailed set of observations in a controlled laboratory experiment of the process that leads to the development of 2D bedforms on an initially flat bed;

(2) to determine whether the development of small-scale 2D bedforms can be described accurately as a simple near-bed shear layer instability;

(3) to obtain a detailed set of observations in a controlled laboratory experiment of the process that leads to the transition between 2D and 3D bedforms;

(4) to determine what effects the different bedform morphologies (2D and 3D) have on flow resistance and to determine if drag reduction plays a role in the 2-3D bedform transition.

The bedforms studied in these experiments are conventionally classified as dunes based on the combination of grain size and flow conditions selected.

1.6 Dissertation Layout

In order to achieve the research objectives, two sets of experiments were conducted. The first examined the development of 2D bedforms on a flat sand bed and the later transition to 3D bedforms at three different flow strengths. These experiments provide the data for Chapters 2, 3 and 4. The second set of experiments examined turbulence and flow resistance over fixed 2D and 3D dunes and provides the data for Chapter 5.

The runs conducted in the first set of experiments were continuous from the initiation of bedforms through 2D and then 3D morphologies. As such, it is useful to discuss the type of waveforms that developed, their scaling and their associated role in sediment transport before addressing the specific research objectives. With this in mind, the next chapter examines the growth of dunes during the experiment and their longitudinal morphology. Included is an examination of the morphology and dynamics of 'sand sheets,' which are small-scale bedforms superimposed on the dunes. Sand sheets are responsible for sediment flux over the dunes.

Chapter 3 addresses research objectives 1 and 2 by discussing the initiation of bedforms on a flat sand bed. An extensive analysis of the initial mean and turbulent flow conditions is presented in order to establish that the bedforms were initiated in flow that does not deviate significantly from conventional models of uniform flow over flat beds. A series of micro-scale grain movements and bed deformations are documented which lead to incipient dune crestlines. An attempt is made to link these bed deformations to some observable flow condition. A simple Kelvin-Helmholtz model of fluid-solid interface instability is applied in order to predict incipient dune lengths.

Chapter 4 addresses research objectives 3 and, to a certain extent, 4 by examining the transition between 2D and 3D dunes. First, a definition of 3D bedform morphology is presented that does not rely on secondary descriptors. A series of small-scale grain movements and bed deformations leading to the 2-3D dune transition are documented. An attempt is made to link the transition and the level of three-dimensionality to drag reduction processes.

Final conclusions concerning drag reduction over 2D and 3D morphologies are left to the final new research chapter. Chapter 5 examines turbulent flow over fixed bedforms that had the same length and height, but varying crestline shapes. This provides the best test of how shifts to 3D morphologies affect resistance to flow.

All the chapters containing new research are sufficiently focused so that separate measurements and analysis techniques were used in each chapter. Therefore, each new research chapter has a section called Experimental Procedures in which measurement and analysis techniques are presented.

Chapter 2: Waveforms Developed from a Flat Bed in Medium Sand

2.1 Introduction

The purpose of this chapter is to discuss the types of waveforms observed in the experiments, including their morphology, scaling, and role in sediment transport in the channel. Two types of waveforms were identified: dunes and smaller bedforms superimposed on the dunes. The latter features cannot be classified as ripples, dunes or bedload sheets, but have characteristics shared with all these features. Thus, the features are termed 'sand sheets' in recognition of their geometric similarity to bedload sheets that develop in coarse, heterogeneous sediments. These types of superimposed waveforms are known to control the hydraulic surface drag and sediment transport rates [*Whiting et al.*, 1988; *Bennett and Bridge*, 1995], with important implications for evolution of the dunes. Low relief bedforms (sand sheets) that are in equilibrium with the bedforms upon which they are superimposed have not been examined extensively. Therefore, considerable attention is given to accurately describing sand sheet features and discussing their implications for sediment transport.

2.2 Experimental Procedures

The experiments were conducted at the National Sedimentation Laboratory, United States Department of Agriculture, in Oxford Mississippi using a tilting, recirculating flume 15.2 m long, 1 m wide, and 0.30 m deep. The flume recirculates both sediment and water. The flume was filled with ~2250 kg (5000 lbs.) of washed and sieved white quartz sand from the Ottawa Sand Company with a median grain size diameter, D_{50} = 0.500 mm. Figure 2.1 shows the grain size distribution of the bulk sand mixture.

The size of the flume permits scale issues to be ignored in the experiment. The experimental conditions (velocity, flow depth, and grain-size) for these experiments were reasonable for small sand-bedded channels. It is therefore assumed that the observations in this flume have a 1:1 scaling

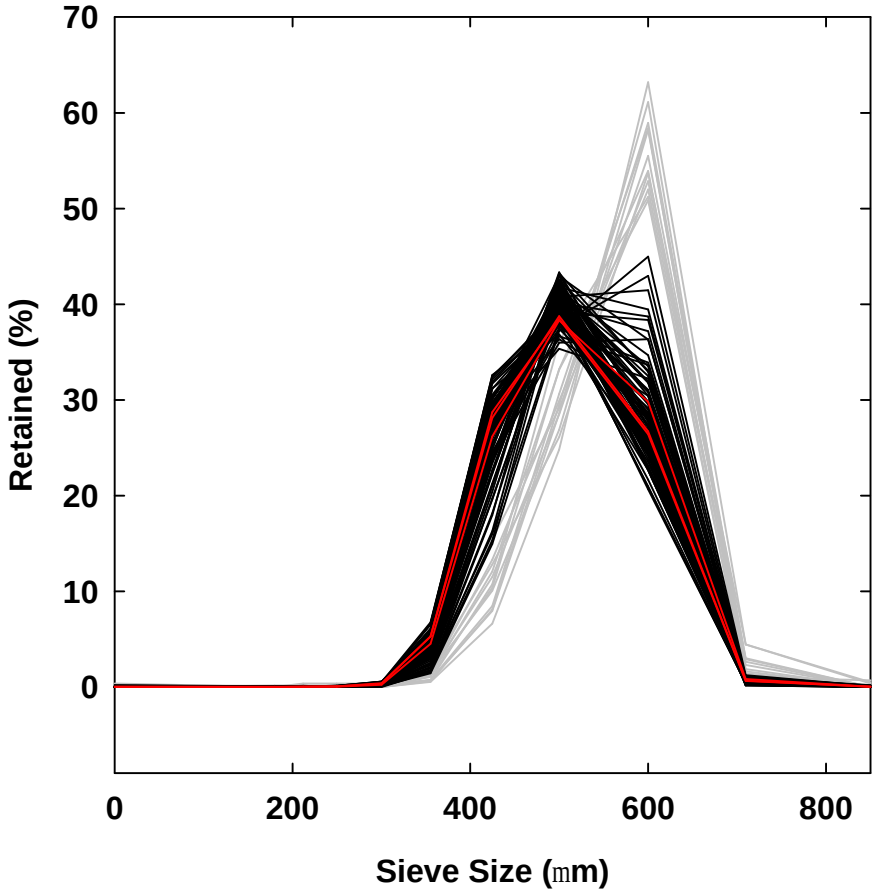

Figure 2.1: Grain size distributions of sand used in the experiments. Displayed are the bulk distributions (red) and 109 Helly-Smith bed load samples (black). Bedload size distributions that peak at 0.600 mm (gray) were all from extremely small samples. Most of the catch was likely caused by the introduction of the sampler to the bed and are therefore regarded as error.

with ‘real’ river channels. However, discretion will need to be exercised before experimental results are applied to natural channels since many of the bedform scaling relations may exhibit fractal characteristics. Further, particular effects of using extremely well sorted sand, not common in natural channels, are not well understood.

2.2.1 Flow Conditions

Bedform development was observed over five separate flow stages with the pump controller set at frequencies, f_p = 23.5, 22.5, 21.5, 19.0 and 17.0 Hz which corresponded to mean discharges, Q , of 0.0759, 0.0723, 0.0696, 0.0611, and 0.0546 $m^3 s^{-1}$. Runs were ~12 hours long. Discharge during run 30 was increased from 0.0546 $m^3 s^{-1}$ to 0.0759 $m^3 s^{-1}$ after 12 hours to observe the effect of a flow change. Run 30 was ~24 hours in length. These five flow stages were selected to provide a test of similarity amongst the observations over a significant range of hydraulic conditions. Further, the hydraulic conditions were selected to cover the two-dimensional (2D) dune portion of conventional stability diagrams in order to determine whether three-dimensional (3D) dunes would develop, given enough time in a wide flume. *Southard and Boguchwal* [1990] provide the most extensive bedform phase diagrams and plotting methodology in the literature to date. Figure 2.2 plots the bedform phase boundaries and shows that the hydraulic conditions used here all plot in the 2D dune field.

Several runs were conducted at each f_p where different processes were monitored. Labels are assigned to each flow strength to streamline the text and provide a link to other runs discussed in subsequent chapters. Flow strength A refers to all runs conducted at f_p = 23.5 Hz, B all runs at f_p = 22.5 Hz, C all runs at f_p = 21.5 Hz, D all runs at f_p = 19.0 Hz and E all runs at f_p = 17.0 Hz. The label E_A is used to denote the high flow portions of runs where the flow strength was increased from f_p = 17.0 Hz to f_p = 23.5 Hz. Flow strength E_A is equivalent to flow strength A. However, the initial condition for flows A and E_A are different. There are no bedforms at the start of flow A, but

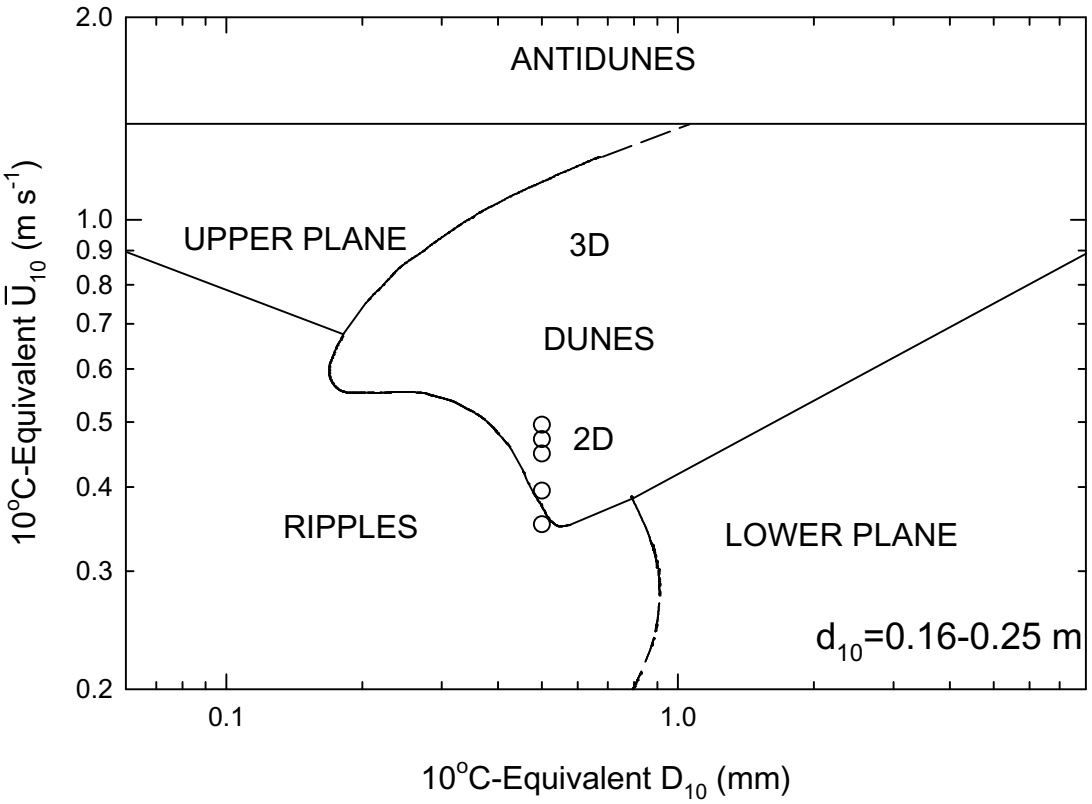

Figure 2.2: Bedform phase diagram digitised after *Southard and Boguchwal* [1990]. The mean velocity U_{10}, flow depth, d_{10}, and grain size, D_{10}, have been adjusted to their 10^o C equivalent using the methods in *Southard and Boguchwal* [1990]. Open circles are the runs discussed here.

bedforms are already present when the flow was increased from E to E_A and this affects the results. Therefore, it is useful to use different labels.

At the beginning of each experimental run, the sediment bed was artificially flattened using a 1 ½ inch piece of aluminium angle mounted across the flume, at bed level, on a cart that travelled the length of the flume. Flattening was done in several cm of water with the flume pump off. The flume was then carefully filled to 0.152 m. Flow in the flume modified this flow depth, d, and established the water surface slope, S, which were monitored using two ultrasonic water level probes along 2.25 - 2.27 m of the flume. The probes were located at 8.66 m and 10.91-10.93 m from the head box (Figure 2.3).

Prior to the onset of bedforms, the mean flow velocities ($\overline{U} = Q / y_w d$ where y_w is the flume width) were ~0.30, 0.34, 0.38, 0.41, and 0.44 m s^{-1} and the Froude numbers ($Fr = \overline{U} / \sqrt{gd}$) were 0.29, 0.33, 0.37, 0.39, and 0.41. Table 2.1 further summarises the initial hydraulic conditions for the experiment. The bulk shear stress ($t_S = r_w gdS$, where r_w is the fluid density, and g is gravitational acceleration) for the experiments ranged between 0.8260 and 1.7811 Pa, shear velocity ($u_* = \sqrt{t_S / r_w}$) ranged between 0.0288 and 0.0422 m s^{-1}, and Reynolds numbers ($Re = \overline{U} d / n$, where n is the kinematic viscosity of the fluid) were in the fully turbulent range at ~10^5. Many of the flow parameters listed in Table 2.1 changed as bedforms were initiated and grew.

Although it will be discussed in great detail in the next chapter, it is important to note that bedforms seemed to be initiated instantaneously over the entire bed surface (from the head box to tail box) at the flow strengths A, B and C. At the smaller discharges, sediment was transported but bedforms were not initiated. Bed defects (divots or mounds) needed to be manually generated that could propagate downstream to form the ripple field. During Runs 29 (flow D) and 30 (flow E) the defects were lines in the sand that ran across the flume at ~9 m (30 ft) from the head box. The defects crossed the central 50 cm of the flume width, were 10 mm deep, and ~20 mm wide.

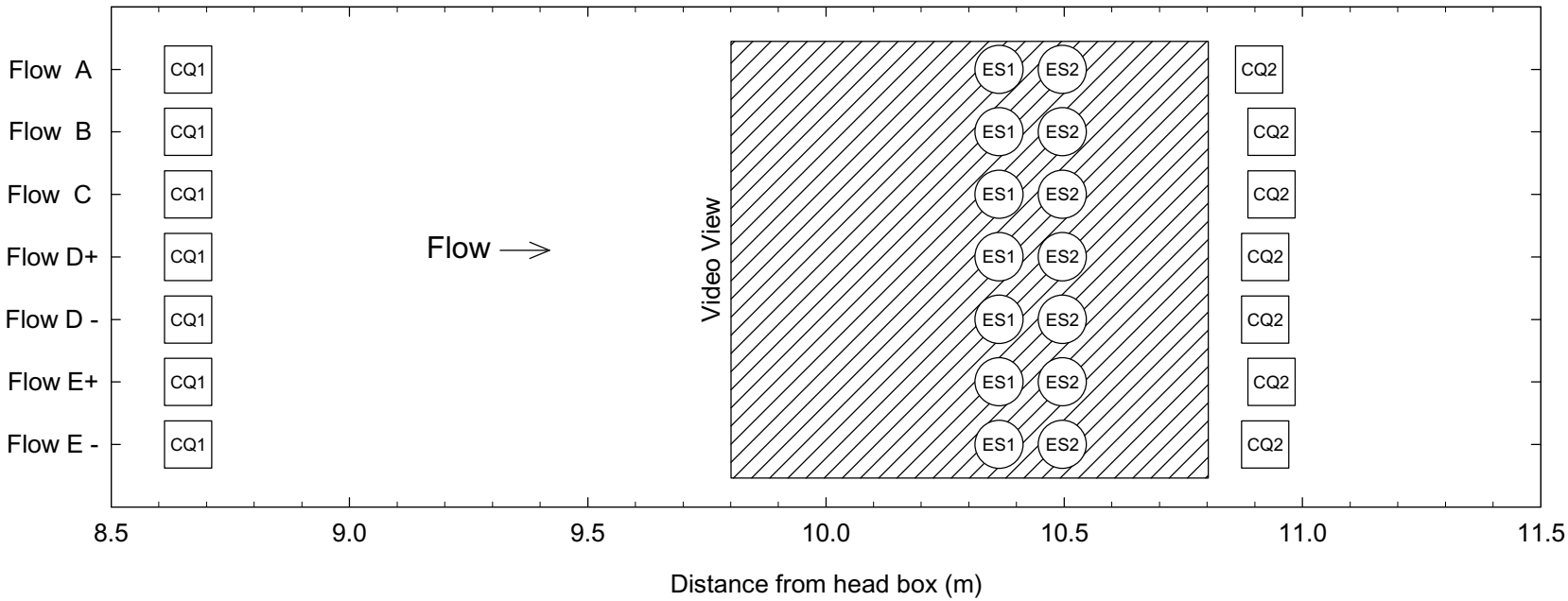

Figure 2.3: Instrument positions along flume. CQ = Contaq ultra-sonic water level sensors; ES=echo-sounders; 1 and 2 refer to upstream and downstream probes. Flows A-E refer to flow strengths. A plus sign indicates bedforms were developed from a positive defect and a minus sign indicates the bedforms were developed from a negative defect.

Table 2.1: Summary of initial flow parameters.

Flow Parameter	Flow A	Flow B	Flow C	Flow D	Flow E
f_p, Hz	23.5	22.5	21.5	19.0	17.0
d, m	0.1516	0.1517	0.1533	0.1530*	0.1534*
$\overline{U}$, m s^{-1}	0.5009	0.4768	0.4538	0.3993	0.3558
U_{max}	0.5929	0.5588	0.5370	0.4556	0.4014
Fr	0.4107	0.3908	0.3700	0.3259	0.2900
Re	75936	72331	69568	61093	54580
Q, m^3 s^{-1}	0.0759	0.0723	0.0696	0.0611	0.0546
$S \times 10^{-4}$	12	11	7	5.5	5.5
	Determinations based on depth slope product				
u_{*S}, m s^{-1}	0.0422	0.0405	0.0324	0.0287	0.0288
t_S, Pa	1.7811	1.6337	1.0506	0.8239	0.8260
ff_S	0.0569	0.0576	0.0409	0.0414	0.0523

*Based on average of two runs. $Fr = \overline{U}/(gd)^{0.5}$, $Re = r_w d\overline{U}/m$, $ff = 8t_o / r_w \overline{U}^2$, $u_* = (t_S / r_w)^{0.5}$.

2.2.2 Bedload Samples

Bedload transport measurements were taken throughout the experiments at each flow strength using a miniaturised Helley-Smith sampler with a 50×50 mm mouth. The body of the sampler was scaled to the mouth. Bedload samples were collected during runs 53 (A), 54 (B) 57 (C), 55 / 56 (D) and 58/59 (E).

At the beginning of the experiments, samples of flat bed transport were taken. As bedforms developed, samples were taken as single sandwaves travelled into the sampler mouth. Later in the experiments, when the bedforms became too large to sample entirely, samples were taken over the crest, stoss slope and trough of the bedforms. Most samples over the crest and stoss regions consisted of minor bedforms that travelled into the sampler mouth as they moved over larger primary bedforms. The sampler destroyed most of the bedforms on which it was situated, and so the next sample that could be taken was over the next bedform. Thus, samples were infrequent in some sections of the records.

Figure 2.1 shows that the grain size distributions of 109 bedload samples taken during the flume runs are identical to the bulk grain size distributions. All sediment sizes in the flume were in motion at all times. Bedload size distributions that peak at 0.600 mm were all extremely small samples. Most of the catch was likely caused by the introduction of the sampler to the bed and is therefore regarded as erroneous.

2.2.3 Echo-Sounders

Changes in the bed topography were monitored using two acoustic echo-sounders built by the National Center for Physical Acoustics (NCPA) at the University of Mississippi. The minimum operating depth is about 0.04 m and the reported resolution is about 0.05 mm [personal communication with NCPA]. The sensors were mounted in the centre of the channel with a streamwise separation of 0.133 m at ~10.36 and ~10.50 m from the head box (Figure 2.3). Instrument

signals were sampled 60 000 times at 4 Hz. This provided 3-4 hour time series of changes in bed topography. Echo-soundings were collected during runs 26 (A), 27 (B) 28 (C), 29 (D) and 30 (E).

There was some minor signal contamination in the echo-sounder records that appears to have been caused by poor quality cables connecting the computer hardware and the probe heads. To overcome this problem a computer algorithm was developed to first remove any singular spikes or drop-outs in the data. Then whenever the signal variance (calculated over five points) exceeds a set limit, the points are replaced. The algorithm repeats in this fashion until all variances are below the limit. Trial and error indicated that a variance limit of 5×10^{-7} m^2 removed the signal contamination but retained the bed morphology. Nevertheless, some of the signal was noticeably altered and deemed unsuitable for analysis.

2.2.4 Video

In addition to the echo-sounders, bedform shape, size, and migration rates were recorded using a Super-VHS video camera mounted above the flume and centred at ~10.30 m from the head box. Super-VHS video captures video at 60 frames/sec with a resolution of 600 horizontal lines/frame, both much higher than normal video. The video was focused to capture an area of the bed 0.8×0.9 m. The video was illuminated with four 100 W floodlights mounted to the flume sidewalls and oriented to intersect at the camera focal point. The side lighting produced a glare-free image with light shadows that highlighted millimetre-scale changes in the bed structure. The video records were sub-sampled from the tapes using a frame grabber at intervals that ranged between 1 and 10 sec. This produced series of images that were then subjected to further analysis.

All lengths and areas measured from these images were made with reference to a grid with 0.1 m squares, installed at the height of the flume walls in the video view. Since the video camera was focused at the bed, features observed on the bed were actually larger than they appeared relative to the overhung grid. A 0.1 m square was placed at several locations at the bed height to determine the

magnitude of the distortion between the height of the flume walls and the bed in the video view. Maps in Figure 2.4a show there is ± 5.0 % (± 5 mm) spatial variation in the squares that are formed by the grid (i.e. not all the squares are exactly 0.1×0.1 m). Maps in Figure 2.4b and 2.4c show there is ± 2.5 % (± 2.5 mm) spatial variation in the lines that make up the grid. This variation does not affect any of the measurements because measured areal features are digitised in a GIS software package that registers x and y positions on the image based on the corners of the grid.

Figure 2.4d shows that feature areas are 28 % larger on the bed than at the height of the grid and that feature areas in the centre of the image will appear to be 4 % larger than at the edges of the images. Lines on the bed were found to be 15% larger as compared to the installed grid although lines in the centre of the video view area are ~2.5 % larger than on the outer edge (Figure 2.4e). Lines should be the square root of the distortion in the area (i.e. $\sqrt{1.28}$ =1.13 or 13 %). The difference between the observed and expected distortion is caused by the spatial variation in the areas and sides of the squares that make up the grid. The measured distortion is used for corrections.

In order to correct for areas measured with reference to the grid, areas measured from the images are multiplied by 1.28 and all lengths are multiplied by 1.15. The radial distortion in lengths and areas from the centre of the image is accepted as error in the data set. Only a small portion of the video data (Run 54 at f_p =22.5 Hz) is presented in this chapter. Chapters 3 and 4 contain a more complete discussion of this data set.

2.3 Waveforms

Examination of the echo-sounding records revealed three basic waveforms present in the flume experiments: long sediment pulses (Figure 2.5a), dunes (Figure 2.5b) and sand sheets (Figure 2.5c). The long sediment pulses were observed to have a period of 2-3 hours (although shorter periods are observed) and vertical relief of 0.08-0.10 m. These waveforms move through the system slowly and are likely bar forms. They are more prevalent in the runs with a larger flow (flows A and B) and are

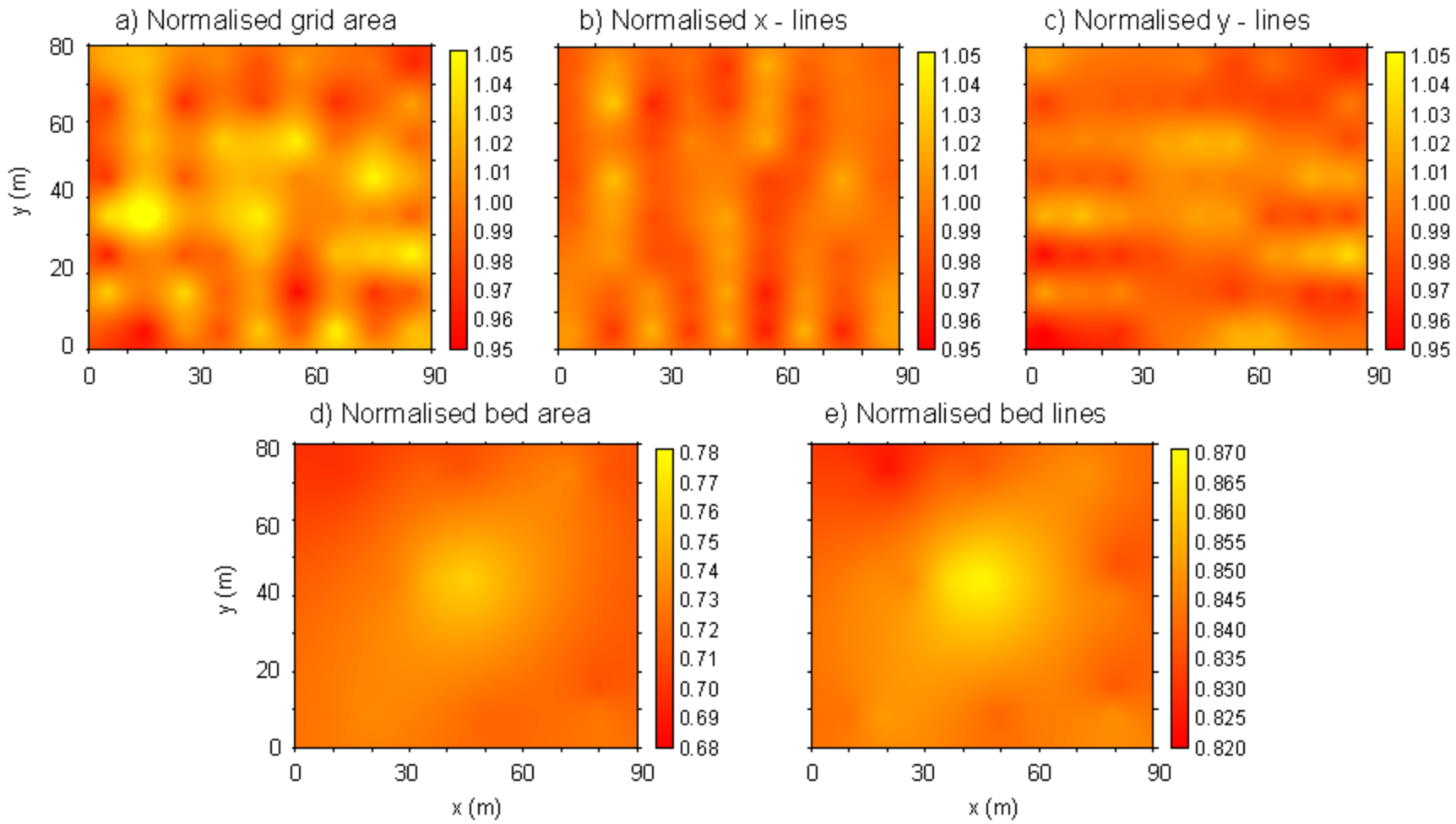

Figure 2.4: Normalised maps of the spatial variation in: (a) the squares that are formed by the grid normalised by the area of a 0.1 × 0.1 m square (0.01 m²), (b, c) in 0.10 m line sections that make up the grid normalised by 0.10 m, (d) 0.1 × 0.1 m squares placed at the bed height normalised by 0.01 m² and (e) in 0.10 m line sections squares placed at the bed height normalised by 0.1 m. Distance along the flume is *x* and distance across the flume is *y*.

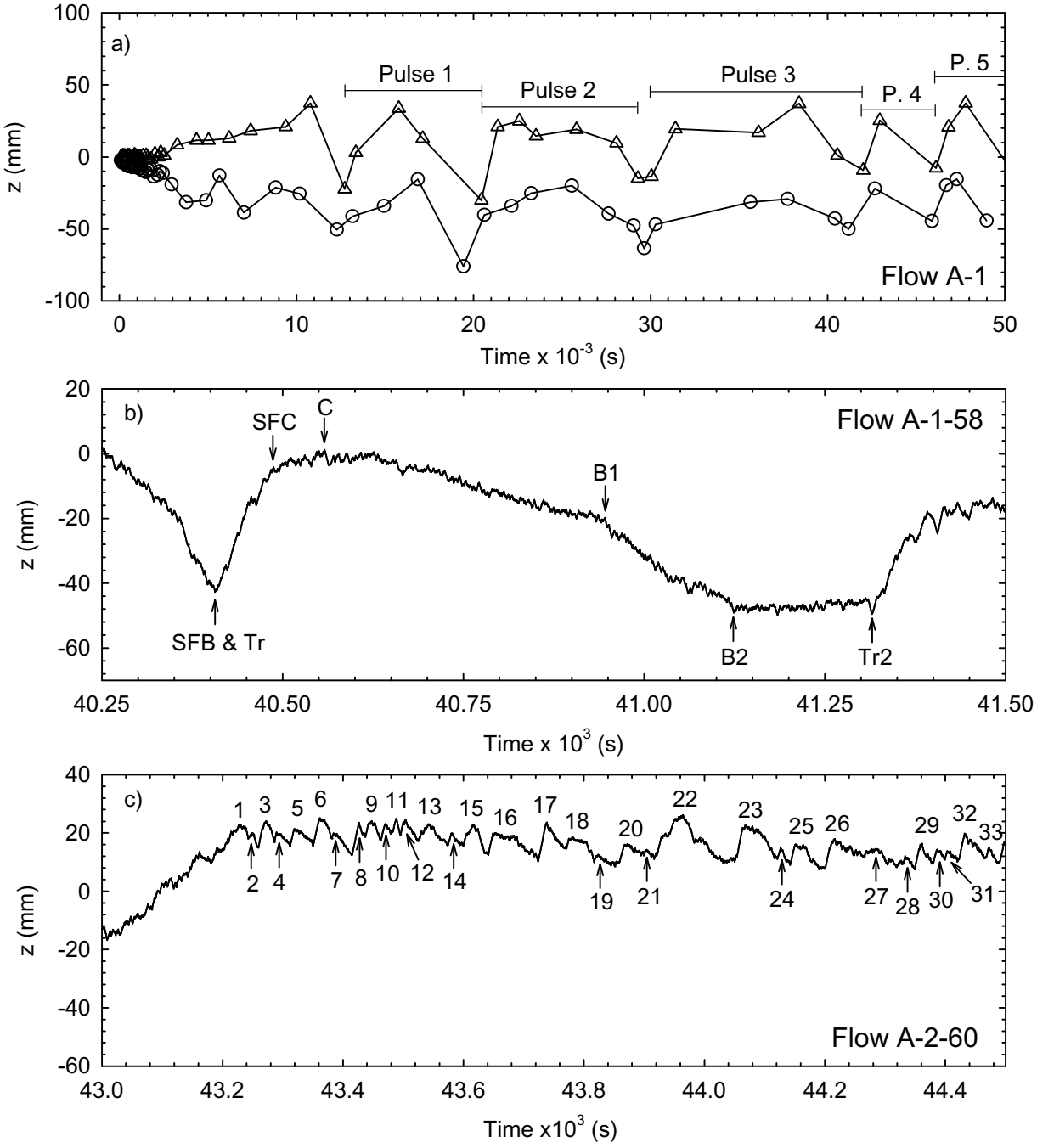

Figure 2.5: Examples of the waveforms observed in the experiments including (a) long sediment pulses (Flow A-1), (b) dunes (Flow A-1-58) and (c) sand sheets (Flow A-2-60). The number in the corners identify the flow strength (A), followed by the echo-sounder (1 or 2, see Figure 2.3) and bedform number (58 or 60). Circles are the trough heights and triangles are the crest heights. *Tr* is the dune trough, *SFB* and *SFC* are the slip face base and crest, *C* is the dune crest, *B1* and *B2* are slope breaks and *Tr2* is the upstream dune crest. Flow over these forms would be right to left.

nearly absent in lower flow runs (flows C, D and E), appearing only after several hours. The forms reappeared when the flow strength was increased from E to E_A. Unfortunately, there are only a few observations of these waveforms per run preventing a more detailed discussion of their characteristics. Records revealing these waveforms can be found Appendix A.

Data are more readily available on the characteristics of the meso-scale dunes and the micro-scale sand sheets superimposed upon them. It is worth noting that spectral analysis was not employed in this investigation to identify bedform H and L [see *Kennedy and Willis*, 1977 for methodology). Most spectral techniques are based on sine waves, assume time series stationarity and require the pattern be stable for many cycles. The bedforms observed are not sinuous and dune forms in this investigation grow from a flat bed by gradually increasing both H and L. Bedform dimensions reach a statistical stability only later in the experimental runs. Even after equilibrium is attained, the time series are still characterised by varying H and L, which cause statistically insignificant and erroneous spectral peaks.

In order to examine the dune bedforms, the bed height time series were plotted to highlight each bedform as in Figure 2.5b. The time series were decomposed by identifying several bedform features and acquiring a time, t, and bed height, z, for each point. The features included: (1) bedform trough, *Tr*, the point with the minimum height, z_{min}, in the lee of the bedform; (2) slipface base, *SFB*, and slipface crest, *SFC*, which are the lowest and highest points bounding the bedform slipface; (3) bedform crest, *C*, the local maximum height, z_{max}, on the bedform; (4) a first stoss surface slope break, *B1*, that commonly defined the downstream extent of the upstream dune trough, and (5) a second stoss surface slope break, *B2*, that commonly occurred between the first slope break and the z_{min} of the upstream bedform. Points were often combined on bedforms (i.e. *SFB* often co-occurred with *Tr* and *SFC* often co-occurred with *C*). Stoss surface slope breaks were observed on many bedforms but were absent on others.

The sand sheets migrated over the stoss surface of the primary dune forms at rates much larger than the dune migration rate. The bed height time series were plotted to highlight the dune stoss slope and hence groups of sand sheets as in Figure 2.5c. The time series were then decomposed to identify t and z of the sand sheet trough and crest. These smaller bedforms were far too small and numerous to identify other points (*SFB*, *SFC*, *B1* and *B2*), although many larger sheets display these features. The morphologic characteristics and sediment transport rate associated with these forms and the dune forms are discussed in more detail below.

2.4 Dune Morphology and Scaling

2.4.1 Dune Heights, Lengths and Migration Rates

The development of dune L and H at flow strengths A-D is shown in Figure 2.6 and flow strength E is displayed in Figure 2.7. Dune height was calculated as $H = z_{max} - z_{min}$ for each echo-sounder time series, providing two separate H values. Dune wavelength was calculated by: (1) determining a time lag, t_{lag}, between the arrival of the dune *SFB* at echo-sounders 1 and 2 (see Figure 2.2), (2) determining the time it took for a bedform to pass one of the echo-sounders, t_{pass}, (3) computing a dune migration rate $R = 0.133 \text{ m}/t_{lag}$, and (4) computing the wavelength $L = R \cdot t_{pass}$. Since each echo-sounder provided a t_{pass} value, a common R value produced two estimates of L for each bedform.

Initial dune heights observed in the time series, H_i, varied between 1.0 and 4.6 mm depending on the run. Initial dune length observed in the time series, L_i, varied between 0.034 and 0.105 m (Table 2.2). There appears to be no relation between H_i and run $\overline{U}$. However, L_i does seem to increase with $\overline{U}$ with the exception of flow C. There are greater discrepancies between H measured by echo-sounders 1 and 2 at the lower flow velocities (Table 2.2). Presumably this is because R

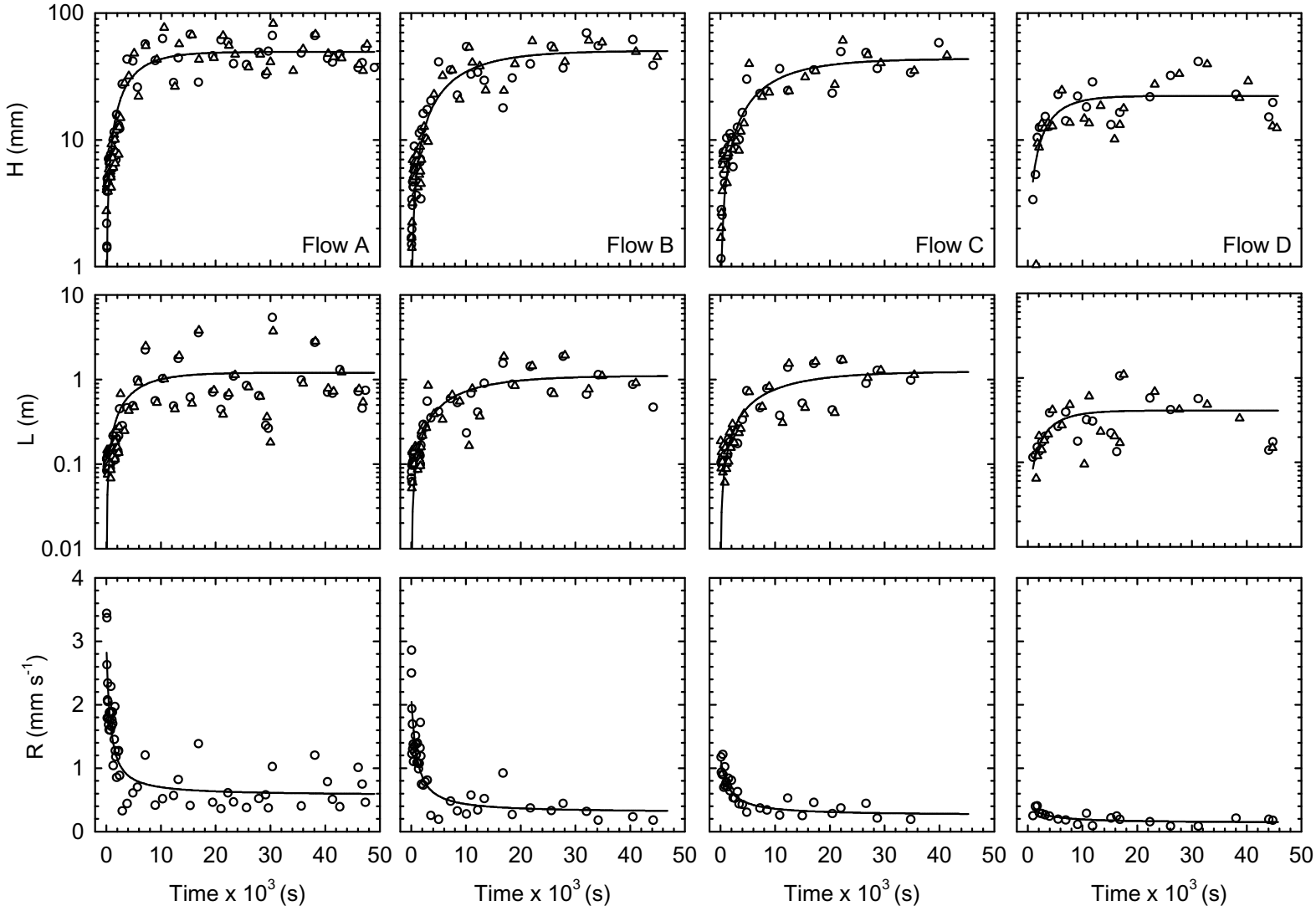

Figure 2.6: Dune growth curves for height, H , length, L , and migration rate, R for flows A-D. Line fitting parameters are in Table 2.3. Circles are measurements from echo-sounder 1 and triangles are measurements from echo-sounder 2 (see Figure 2.3).

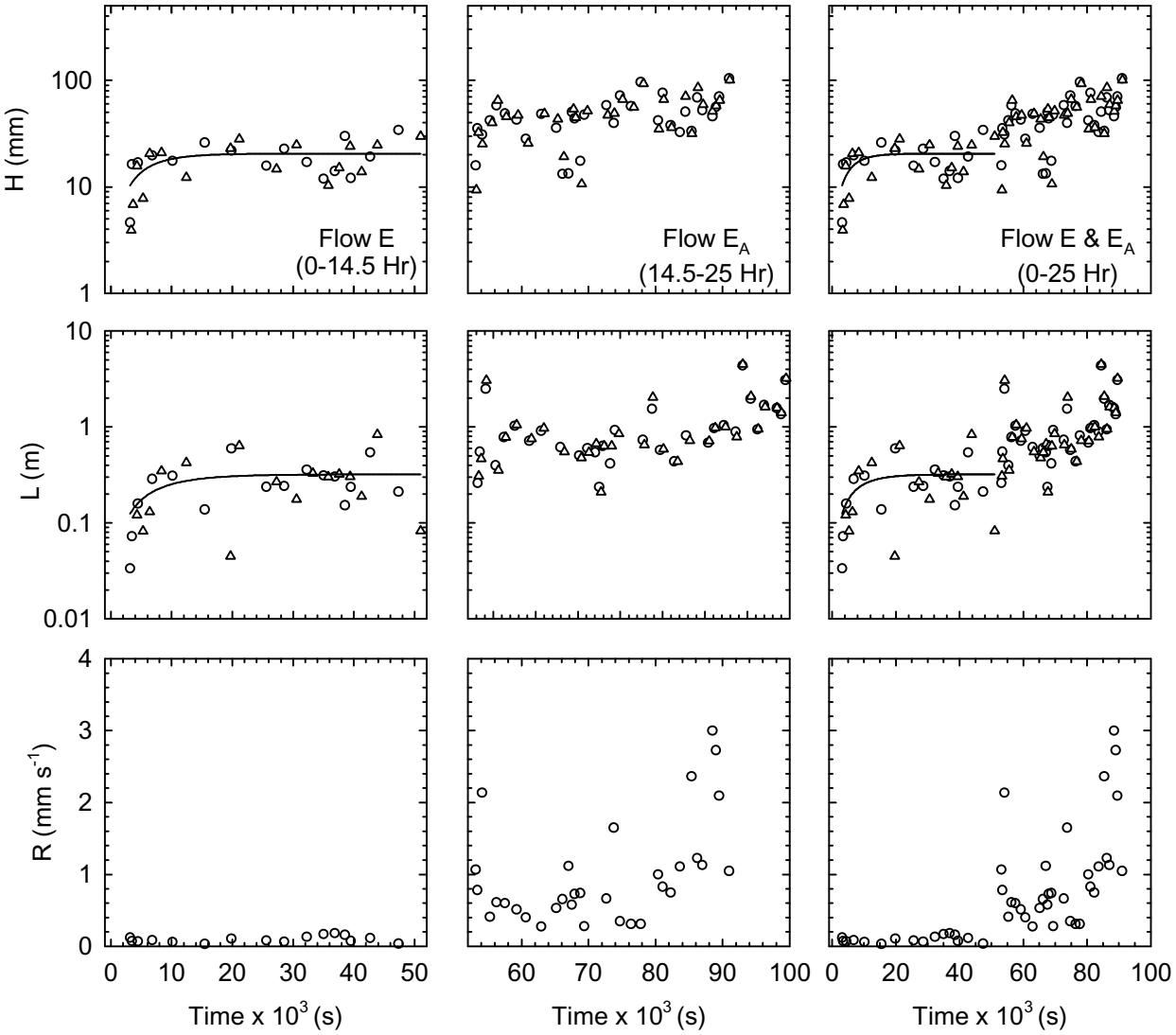

Figure 2.7: Dune growth curves for height, H , length, L , and migration rate, R for Flows E and E_A. Line fitting parameters are in Table 2.3. Circles are measurements from echo-sounder 1 and triangles are measurements from echo-sounder 2 (see figure 2.3).

Table 2.2: Bedform dimensions.

Flow	Run	H_i mm	L_i m	t_i s	$\overline{H}_e$ mm	CV_{He}	$\overline{L}_e$ m	CV_{Le}	$\overline{R}_e$ 10^{-2} m s^{-1}	CV_{Re}
A	26	A=2.19 B=2.74	0.0946†	Instant	47.70	0.277	1.172	0.929	0.0650	0.449
B	27	A=1.69 B=1.70	0.0842†	Instant	41.61	0.323	0.860	0.567	0.0371	0.501
C	28	A=1.15 B=2.66	0.1046	Instant	35.88	0.319	0.954	0.502	0.0334	0.311
D	29	A=3.66 B=1.03	0.0646	963.41	21.52	0.397	0.383	0.678	0.0172	0.349
E	30a	A=4.63 B=3.91	0.0336	3149.42	19.67	0.340	0.300	0.593	0.0097	0.485
E_A	30b	n/a	n/a	n/a	n/a	n/a	n/a	n/a	n/a	n/a

† Based on all bedforms observed during first 3 min.

decreases with flow velocity (Figures 2.6 and 2.7) and there is more time for the bedform to evolve between locations 1 and 2.

At flow strengths D and E, H_i and L_i are somewhat erroneous statistics as the initial bedforms were developed at 9.14 m from the head box and migrated 1.22 m downstream to where the probes were located over some time period, t_i. At flow D t_i = 963 s and at flow E t_i = 3149 s. Therefore, H_i and L_i are related to this time lag between development and observation. In contrast, at flow strengths A and B, the bedforms developed instantaneously and thus H_i and L_i should be a fair representation of initial bedform values. Flow C also developed bedforms over the entire bed shortly after the desired flow strength was reached, but the first bedform observation occurred several minutes into the run, which presumably bolstered L_i. The issue of initial bedform properties is discussed in greater detail in Chapter 3.

Once established, the dune bedforms grow in H and L while R decreases toward equilibrium values. In these experiments, the dunes undergo continuous growth in H and L rather than growth caused by capturing smaller bedforms to form larger bedforms as has been suggested by some authors [e.g. *Costello and Southard*, 1971; *Leeder*, 1980; *Raudkivi and Witte*, 1990; *Coleman and Melville*, 1992]. The growth of the dune bedforms is approximately exponential and can be expressed by the following

$$H = a_H \left(1 - e^{-b_H \cdot t}\right) \qquad 2.1$$

$$L = a_L \left(1 - e^{-b_L \cdot t}\right) \qquad 2.2$$

where a_H, a_L, b_H and b_L are coefficients derived from least-squares regression (Figure 2.6 and Figure 2.7). Bedform migration rates decrease exponentially with time and can be expressed using

$$R = a_R \, e^{\left(\frac{b_R}{x + c_R}\right)} \qquad 2.3$$

where a_R, b_R, and c_R are coefficients derived from least-squares regression (Figure 2.6 and Figure 2.7). Values for a, b, and c are given in Table 2.3. All model fits are significant at the 95 %

Table 2.3: Model fitting results

Flow	Run	a_H mm	b_H 10^{-4}	r_H^2 %	p_H	a_L m	b_L 10^{-4}	r_L^2 %	p_L	a_R m s^{-1}	b_R	c_R	r_R^2 %	p_R
A	26	50.36	1.147	0.84	<0.0001	1.208	1.798	0.31	<0.0001	0.0566	2416	1422	0.80	<0.0001
B	27	49.36	2.113	0.82	<0.0001	1.017	1.068	0.67	<0.0001	0.0297	4699	2384	0.78	<0.0001
C	28	43.54	1.120	0.84	<0.0001	1.244	0.959	0.69	<0.0001	0.0253	4593	3032	0.84	<0.0001
D	29	22.20	2.455	0.40	<0.0001	0.411	2.386	0.21	0.0026	0.0135	5118	4411	0.52	0.0014
E	30a	20.5	2.211	0.29	0.0013	0.320	1.563	0.18	0.0160	n/a	n/a	n/a	n/a	n/a
E_A	30b	n/a	n/a	n/a	n/a	n/a	n/a	n/a	n/a	n/a	n/a	n/a	n/a	n/a

confidence interval, but more bedforms are observed in the runs with larger flow strengths and consequently the model fit is better (see r^2 values). Equations 2.1 - 2.3 could not be successfully applied to flow E_A. When the bed started developing from a flat bed (flow A), equilibrium was established after only 1.5 - 2 hours. However, 12 hours was not sufficient time for the bed to reach equilibrium when the flow started from a bed that already had bedforms (flow E_A).

Regardless of $\overline{U}$, H_e, L_e and R_e (subscript e indicates equilibrium values) are reached after ~1.5 hours, but all are strongly dependent on $\overline{U}$, increasing with flow strength. Coefficients of variation, CV, defined as the ratio of the standard deviation to the mean, are large for H_e, L_e and R_e.

2.4.2 Variability and Measurement Error in Dune Properties

There are two sources of variation in the dune data set. The first is natural variation of the phenomenon. The second is error associated with the measurements. Neither R nor L were measured quantities but depended on lag and passage times and their calculation from these times imply certain assumptions, primarily that the dune movement is consistent and dune morphology does not vary while being measured. Instrument related measurement error, which normally is an additional source of variance, is minimal because the sampling frequency was large and the vertical instrument resolution (± 0.05 mm) is small compared with the phenomena being observed. However, the practical vertical resolution of the measurements system is equivalent to D.

Nearly all the variation in H is natural and $CV_{He} \approx 0.28$ - 0.40 with a mean for all flow strengths during the equilibrium phase of ~0.33 (Table 2.2). Error associated with the vertical resolution of the measurement system accounts for 3.7 - 7.5 % ($D / s\,H$) of the total variation. *Villard and Church* [2003] observed similar variation during dune field surveys in the Fraser River where most CV_H values were between 0.3 and 0.5. A large degree of this variation derives from the 3D nature of the bed (discussed in greater detail in Chapter 4).

Villard and Church [2003] observed CV_R values between 0.4 and 0.7, but some larger values occur when the flow conditions had recently changed. Most CV_{Re} values are within this range, varying between 0.31 and 0.50 with a mean for all flows of ~0.42 (Table 4.2). It is difficult to determine how much of the variation in R is natural and how much is related to the way the measurements were taken. Some of the variability in R is related to its calculation from t_{lag}. Potential inaccuracies in t_{lag} could derive from the bedform stalling in its downstream progression, the crestline locally accelerating or decelerating between the echo-sounders, or changes in the bedform morphology before being recognised at the downstream echo-sounder. Variability in the crest movement along its length was most pronounced later in the experimental runs when the bedforms were large. Examination of the time series suggests that changes in the local migration rate were rare over the 0.133 m echo-sounder separation. *SFB* was selected to define the arrival of the dune at a sensor because this location experienced the least change between the two echo-sounders. Quantification of the error resulting from potential inaccuracies in t_{lag} cannot reasonably be accomplished.

The dune length also varied naturally but was subject to the greatest potential error as variability in R is combined with error associated with the calculation of L. As such CV_{Le} is greater than CV_{He} and CV_{Re}, ranging between 0.42 and 0.68 with a mean for all flows of ~0.55 (Table 4.2). This measure of variability in L is not strictly comparable to values obtained by *Villard and Church* [2003], as they measured dune length directly. Aside from the error inherited from R, variance is derived from the determination of t_{pass}. Bedforms stalled and were subject to acceleration and deceleration frequently. This is somewhat mitigated by the fact that stalls are likely balanced by greater than average progression. However, the bed was tremendously dynamic as bedforms continuously modified their morphology. Quantification of the error compounded from the error in determining R and the potential inaccuracies in t_{pass} cannot reasonably be accomplished.

2.4.3 Controls on Dune Growth

Figure 2.8 plots all observations of H and L at all flows and demonstrates that there is a non-linear relation between these bedform dimensions. Observed H varied between 1.0 and 96.1 mm and L varied between 0.03 and ~2 m, although there are a few observations of $L > 2$ m. At most flow strengths, bedforms were observed across the entire range of H and L values displayed. At flow strength E, observations were restricted to the lower portion of the range while at flow E_A, observations were restricted to the upper portion. This is not surprising because bedforms at flow E were generally the smallest equilibrium forms observed and there was no period of rapid bedform growth from a flat bed at flow E_A.

For $H < 40$ mm and $L < 0.8$ m, H and L are coupled as the relation appears linear. Most of these observations are of bedforms developing from the flat bed towards the equilibrium. When the bedforms dimensions exceed $H \approx 40$ mm and $L \approx 0.8$ m, the linkage between dune H and L is not as well-defined. This suggests that when the dunes are in the equilibrium phase, H and L vary independently within some boundaries. It is not clear what controls equilibrium height and length of bedforms.

There is no consensus on the reasons for bedform growth and what the ultimate equilibrium size of a bedform should be for a given flow, although considerable progress has been made through empirical studies conducted over the last 50 years and through the construction of bedform phase diagrams. As mentioned in Chapter 1, perturbation analysis has been applied extensively to the problem of bedform growth. Unfortunately, the predictions produced by this approach are largely controlled by the conditions imposed upon the equations and thus there is not much physical insight into bedform growth.

Recent work by *Raudkivi and Witte* [1990] and *Coleman and Melville* [1992] has suggested that bedforms actually grow in length and height by the coalescence of smaller bedforms, because smaller bedforms have larger migration rates, R, and can overtake the larger features on a bed. An artificial

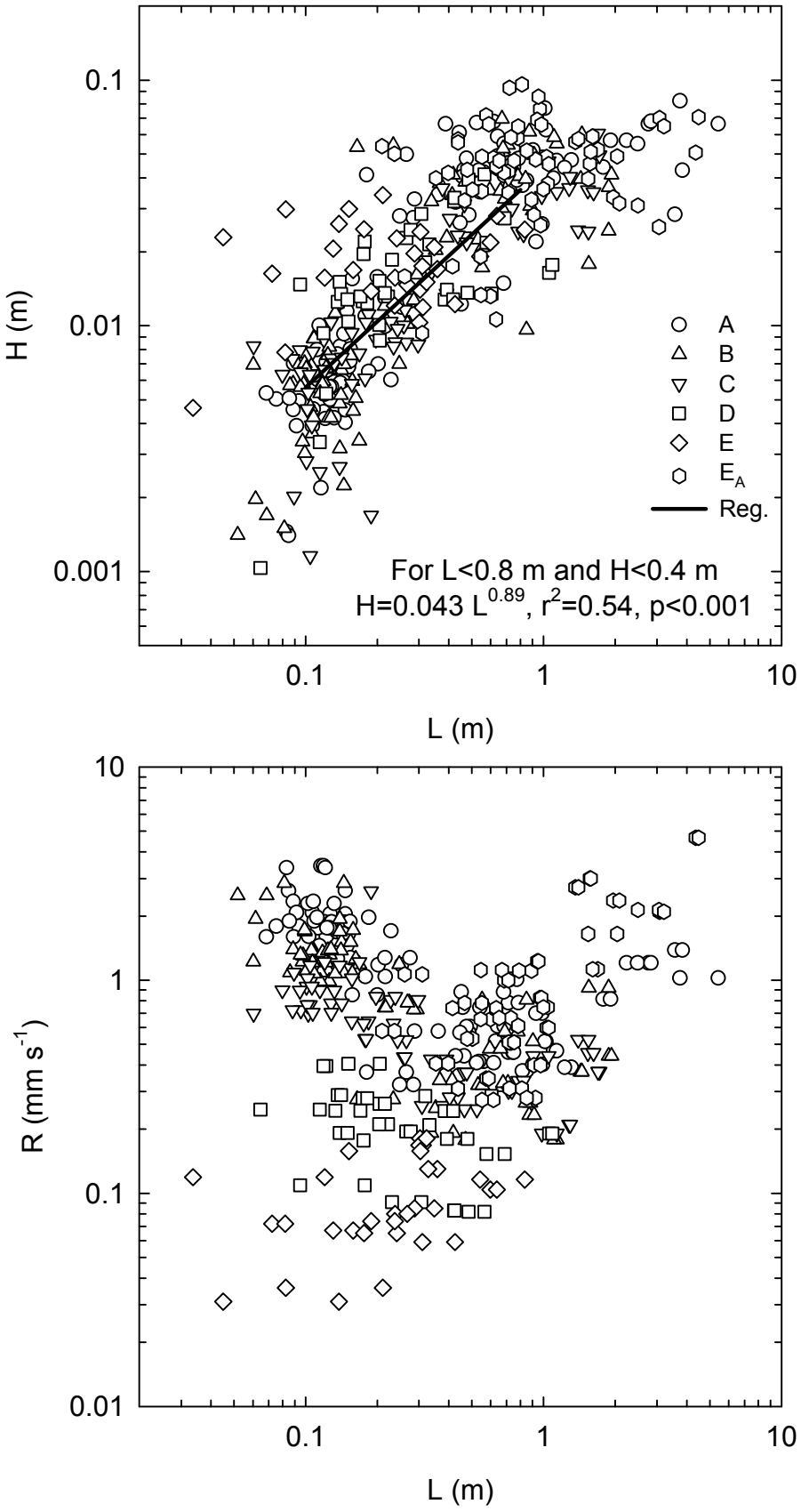

Figure 2.8: Bedform height, H , and migration rate, R , plotted as a function of bedform length, L .

limit to dune height is imposed to produce equilibrium bedforms. This idea has been referred to as a 'bedform unification model'. *Ditchfield and Best* [1990] argued against this idea, indicating there is no relation between bedform size and migration rate, R. They also suggested that bedforms may both grow or attenuate without interaction with other bedforms, or they may coalesce as they migrate. Figure 2.8 also plots R against L for all flow stages. For flows A, B and C, the there is a general decrease in R with L while at flows D and E, R with L values are clustered in one region of the plot. At flow E_A there appears to be a positive relation. Thus, the relation is not as simple as suggested in unification models. A further problem with applying this theory to the observations here is that, although bedform coalescence was observed during the experiments, it was limited to the sand sheets combining with the dune crestline. This was an equilibrium process that maintained transport over the dune and did not cause dune growth. Widespread bedform coalescence did not occur within the dune population; rather, crest realignment by the growth of scour induced crest lobes dominated (this observation is described and discussed in greater detail in Chapter 4).

Many others have ignored the actual dune growth process and sought out an explanation for the limiting height or length of bedforms. *Yalin* [1992] has suggested that dune height is generally 0.2 - 0.25 d and most of the observations here loosely confirm this scaling. However, $\overline{H}_e$ varied over a wider range (0.13 - 0.32 d) with only flow strengths B and C being within *Yalin's* [1992] range. *Yalin* [1992] attempted to explain the limiting height of dunes by examining the limiting length and assuming the bedform will maintain a near constant aspect ratio. He attempted to link dune length to a burst period, T_B, which is the time between large depth-scale turbulent events. Assuming $\overline{U}\,T_B/d$ is a constant ≈5, $\overline{U}\,T_B \approx 5\,d$ which is similar to observed dune lengths (i.e. 5 - 6 d). Unfortunately, this scaling breaks down when the bedforms become large [see *Raudkivi and Witte*, 1990].

Others have argued that dune size is limited by a balance between shear stress, sediment transport rate, dune migration rate and form drag. The limiting condition under this balance is flow depth over the crest when no further deposition can occur in the crest region as it begins to act as an upper stage

plane when in equilibrium [*Bennett and Best*, 1996]. This explanation does not address the problem of why the dunes grow in the first place. Thus, the limiting condition for bedform growth is open to debate.

2.4.4 Dune Classification and Scaling

It is necessary to justify the use of the term dune to describe the large scale features in the experiments; whether these bedforms are classified as ripples or dunes is dependent upon the classification scheme used.

Using *Ashley's* [1990] classification, bedforms where L exceeds 0.6 m are dunes. This artificially divides a data set that does not have individual groupings of L or H into ripples and dunes. Using a data set like that of *Guy et al.* [1966] does not provide a satisfactory classification either. Using u_* values determined from velocity profiles rather than values from the depth slope product, the grain Reynolds numbers, $Re_g = u_* D / n$ for the experiments are 15 (A), 13 (B), 11 (C), 8.5 (D) and 8 (E). Estimates of u_* values determined from velocity profiles are ~0.45-0.75 u_{*S}. The data of *Guy et al.* [1966] indicate that ripples have aspect ratios, H / L between 0.08 and 0.10 at Re_g = 15, 0.04 - 0.10 at Re_g = 10 and 0.03 - 0.10 at Re_g = 7.

Figure 2.9 plots H / L for all the runs as a function of the bedform number (1 was the first observed). Interestingly, there is no systematic change in H / L with time (bedform number). There is considerable scatter in the data but the average $H / L \approx 0.05$ for flows A, B and C and ~0.06 for flows D and E. There was no change in H / L when the flow was increased. There is clear overlap between the ranges from the data of *Guy et al.* [1966] and the data in Figure 2.8. However, there is no justification for choosing one term over another.

In light of this confusion, the bedforms are classified based on their aspect ratio using the ranges provided by *Allen* [1968]. *Allen* [1968] indicated that H / L varies between 0.20 and 0.01 for bedforms developed in sand, although exceptions can occur. For ripples $0.05 < H / L < 0.20$ while for

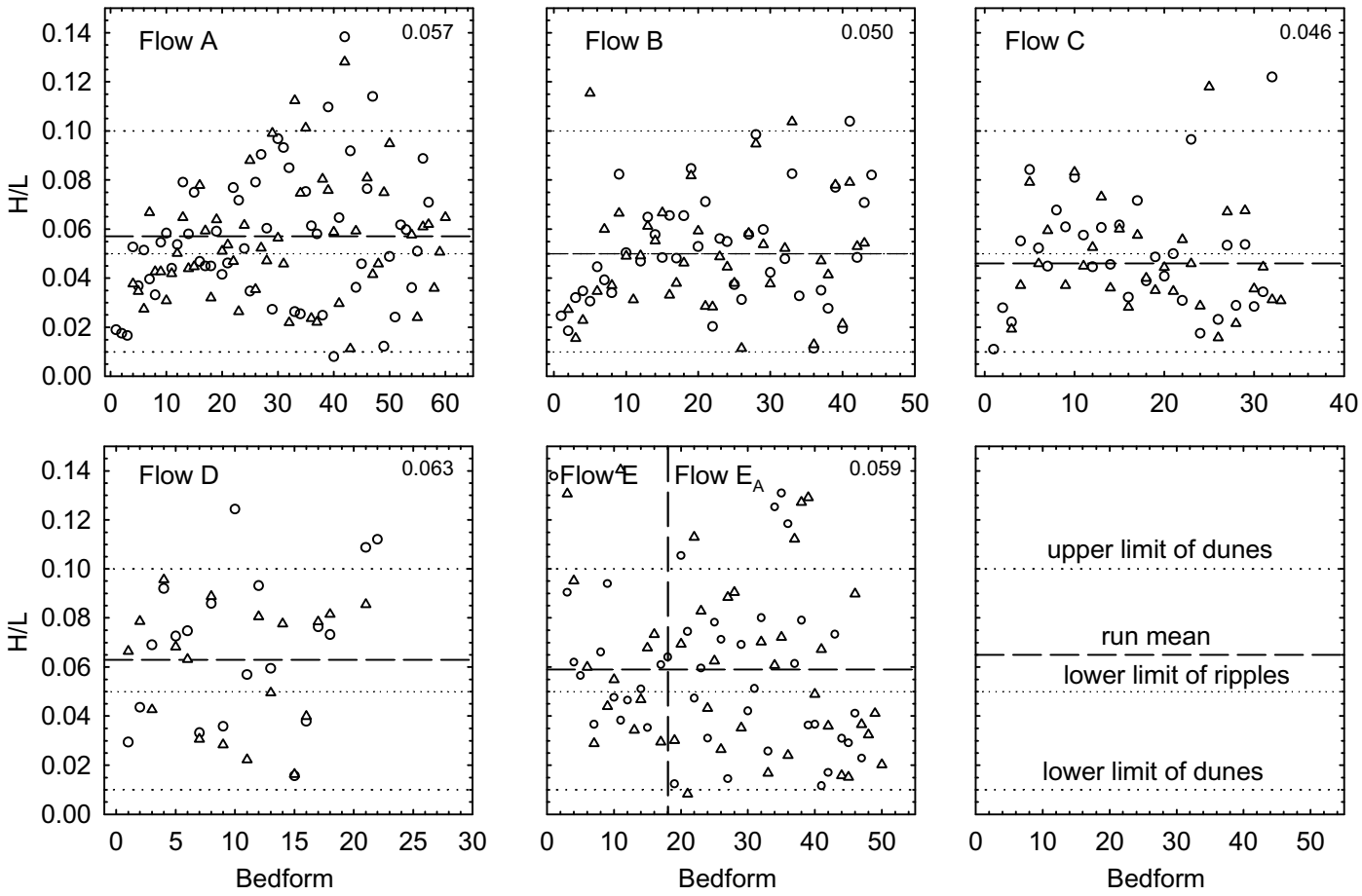

Figure 2.9: Dune aspect ratio, H / L, plotted as a function of bedform observed (H is dune height and L is dune length). The dashed vertical line indicates when the flow strength was changed from flow E (f_p =17.0 Hz) to flow E_A (f_p =23.5 Hz). Circles are measurements from echo-sounder 1 and triangles are measurements from echo-sounder 2 (See figure 2.3). Upper and lower limits for dunes and lower limit for ripples are based on *Allen* [1968].

dunes $0.01 < H / L < 0.10$. Based on this classification, most of the bedforms are clearly dunes and, since there is no clear grouping of dune shapes, it is reasonable to conclude that they are all dunes. Reinforcing this classification, the bedforms appear to scale with depth, not grain size, and the bedform phase diagram from *Boguchwal and Southard* [1990] (Figure 2.2) indicates that the flow strength is too great to develop ripples.

That there is no observable change in the bedform steepness with time is significant because it suggests that the bedforms that first develop are not ripples that transform into dunes when they become large. This is emphasised by examining Figure 2.10 which plots the normalised bedform shape where the distance along the bedform, x, is normalised by each dune L and z is normalised by H. The bedforms all have approximately the same shape, regardless of bedform size, although there is substantial variation on the stoss slope.

2.4.5 Dune Morphology

Examination of the time series revealed different types of dune crest and different stoss slope types. Bedforms are represented in the literature as having a variety of streamwise shapes including the typical asymmetric shape that is particularly common in narrow flumes. Even sinusoidal shapes have been used for modelling purposes [e.g. *Kennedy*, 1963]. However, naturally occurring bedforms tend to have a wider variety of shapes. Figure 2.11a shows the different crest shapes observed in the experiments. Type C1 displays z_{min} some distance upstream of SFB and z_{max} some distance downstream of SFC. Type C2 is similar but SFC and C coexist. Type C4 is a relatively smooth rise from Tr / SFB to SFC / C. Figure 2.12a demonstrates C1 is the most common crest type (i.e., the slipface is generally separated from z_{min} and z_{max}). Types C3 and C4 are also commonly observed, although the percentage of C4 crests declines with flow velocity. In comparison, type C2 is rarely observed (i.e., if SFB is not z_{min}, z_{max} and SFC are unlikely to coexist).

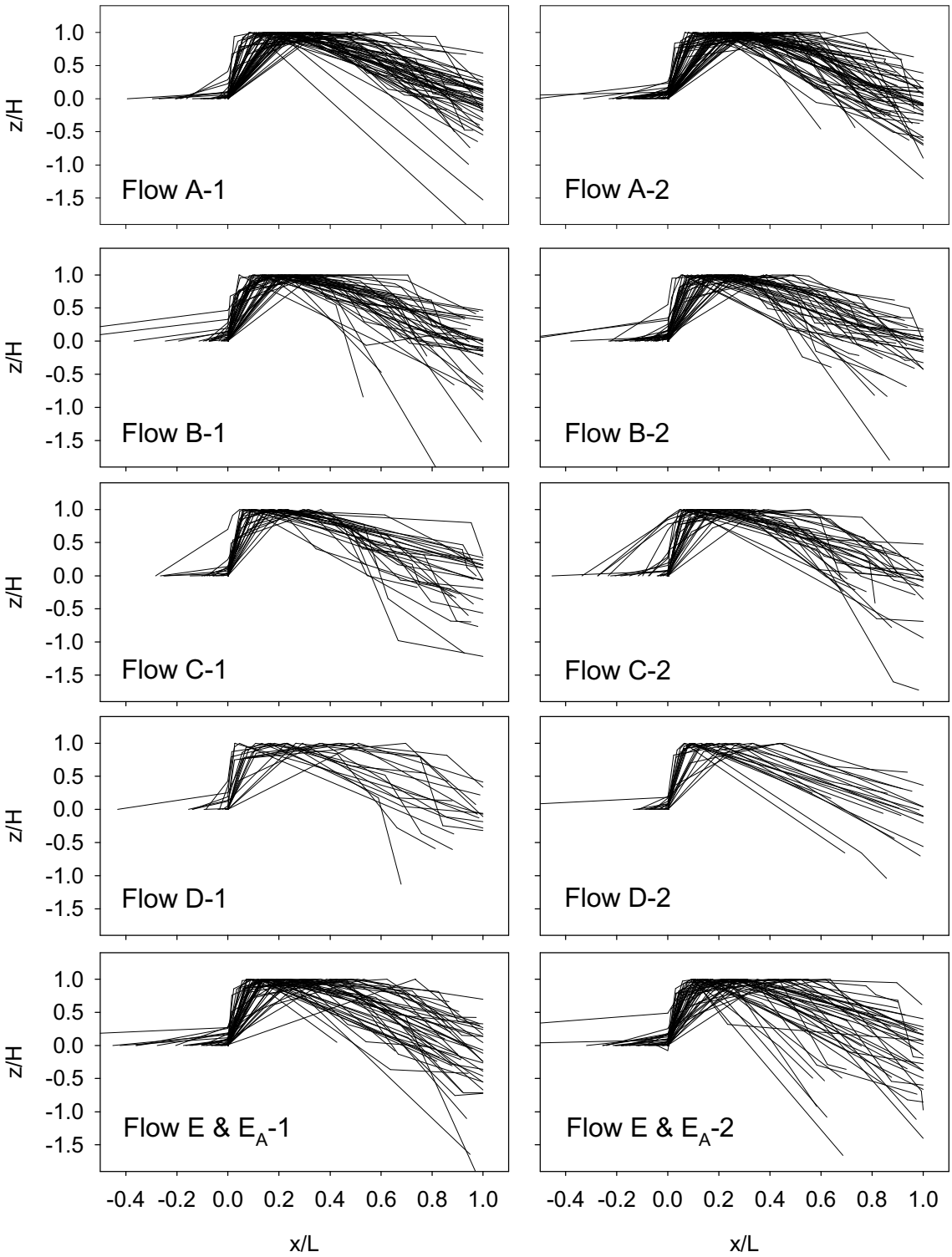

Figure 2.10: Normalised dune shape diagrams where bed height, z, is normalised by dune height, H and distance along the dune, x, is normalised by the dune length, L. x/L=0 occurs at the slipface base while z/H=0 occurs at the dune trough. The numbers 1 or 2 indicate the echo-sounder (see Figure 2.3).

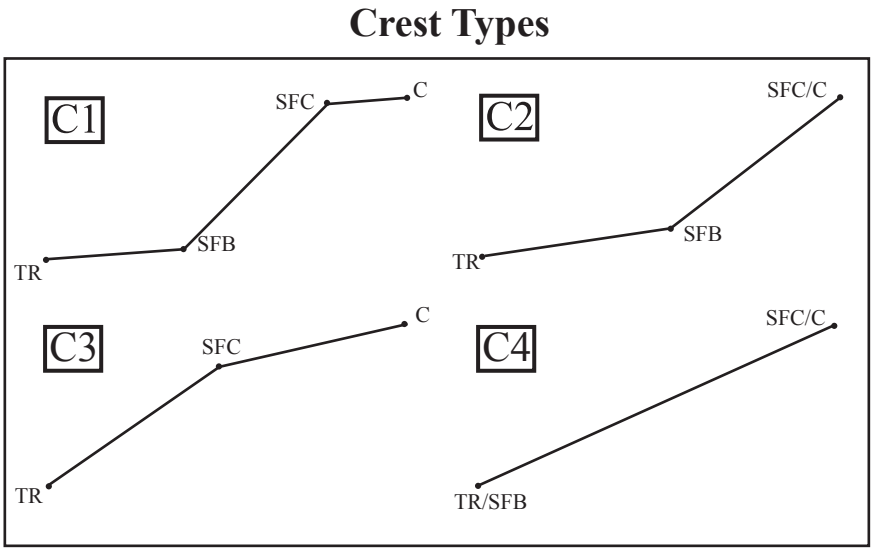

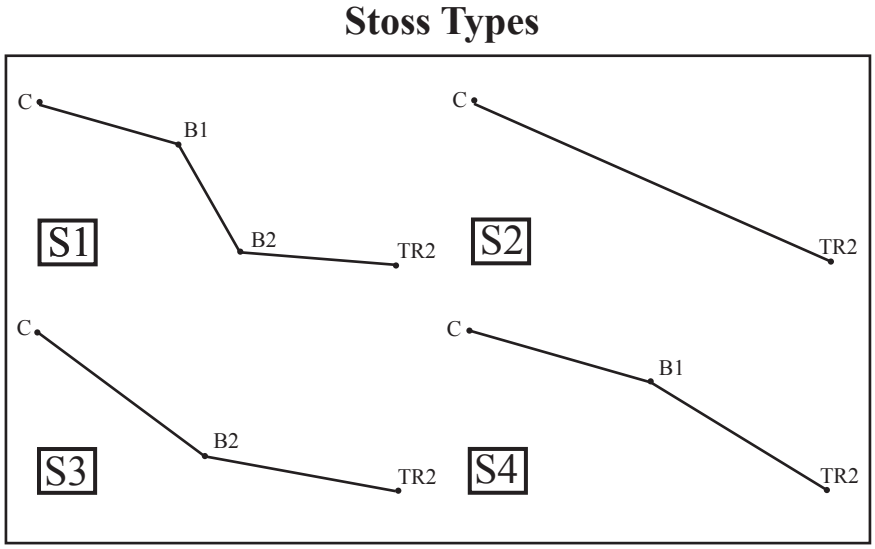

Figure 2.11: Simplified dune crest and stoss types.

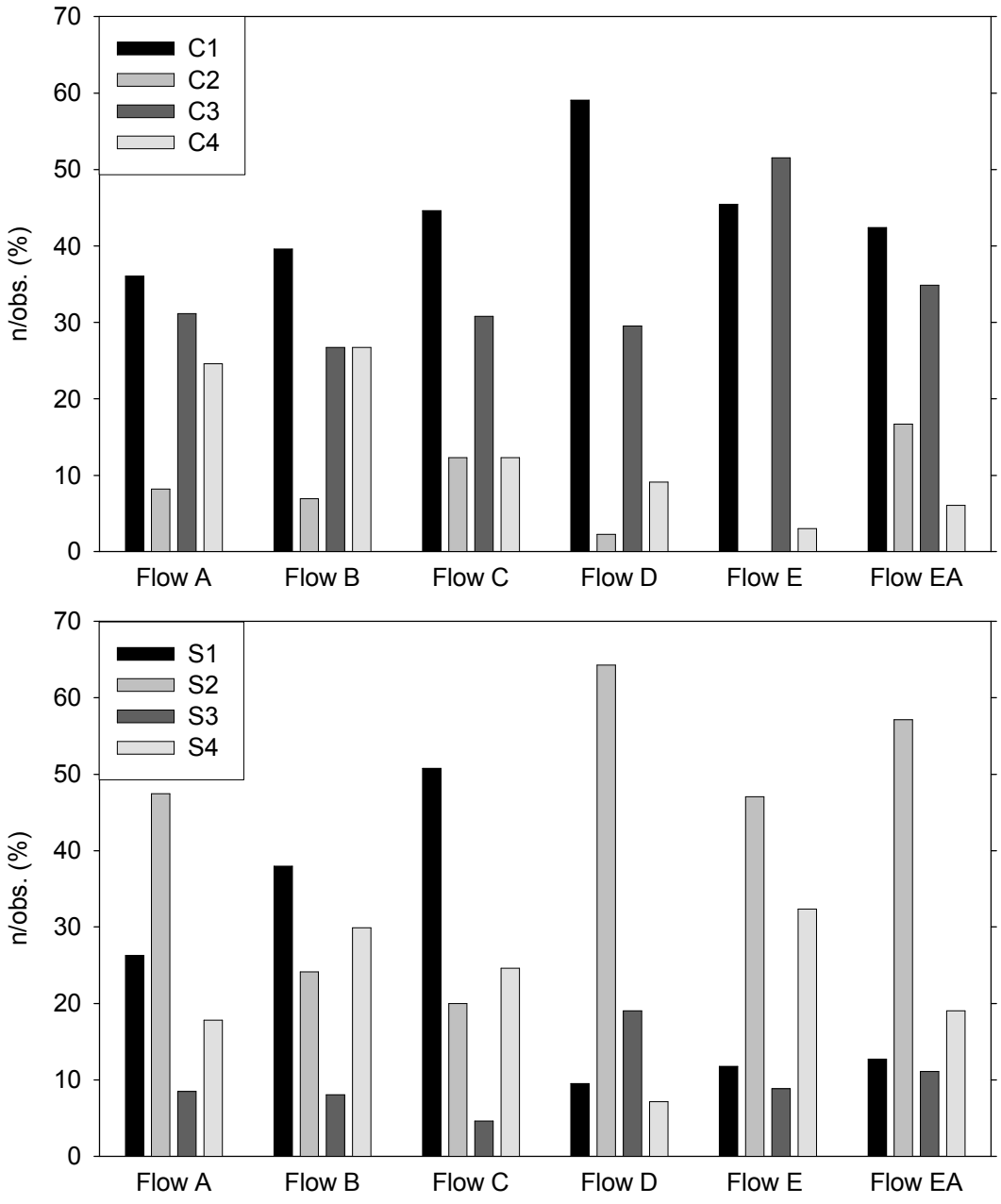

Figure 2.12: Distribution of crest and stoss types observed in each run.

Stoss types observed in the experiments are shown in Figure 2.11b. Type S1 displays a break in slope some distance upstream of the dune crest and another some distance downstream of the upstream z_{min} ($Tr2$). Type S2 shows a gradual decline from the dune crest to the upstream z_{min}. Type S3 shows a slope break that gives the stoss slope a concave shape and S4 has a shape that gives the stoss slope a convex shape. The occurrence of each stoss slope is somewhat more random than the crest type occurrence. Figure 2.12b indicates type S1 occurs most often for Runs 27 and 28 while stoss type S4 is the next most common. For all other runs S2 occurs most often, followed by either S1 or S4. Concave (S3) stoss shapes are the least commonly observed.

There appears to be a relation between the location of the lower slope break (*B2*) and the expected location of the separation cell. Table 2.4 presents the distance between the upstream bedform trough (*Tr2*) and both slope breaks (*B1* and *B2*) normalised by H. The average distance *B2* - *Tr2* ranged between 2.5 and 5.1 H. Given that the average measured slipface angles were all ~30^o the distance *SFC* - *Tr2* is ~1.75 H. Combined, these distances are equivalent to or somewhat longer than x_R (3.5 - 5 H), suggesting the reattachment length controls the location of *B2*. *B1* typically occurs a short distance downstream of x_R and is formed by accumulating sediment from the dune trough.

The distance between *B1* and the crest forms a bedform 'crown' and the distance between the upstream trough and *B2* form a bedform 'pan' in the trough. This morphology is somewhat different from the typical asymmetric shape displayed in Figure 1.2, but is common in laboratory settings [cf. *van Rijn,* 1993] and real rivers [see work by Church, Kostaschuk and collaborators on the Fraser River, personal communication]. Pronounced sand sheets occur over the bedform crowns.

2.5 Sand Sheet Morphology and Scaling

The sand sheets migrating over the dune backs were examined using both portions of the video records and the decomposed echo-sounder time series. The echo-sounder time series were employed

Table 2.4: Mean distance from the upstream trough to the slope breaks on the stoss side of dunes. Adjusted values have had extraordinarily large or small values removed from the mean (i.e. $1 < (B1 \text{ to } Tr2) / H > 15$ and $1 < (B2 \text{ to } Tr2) / H > 10$ were removed from the mean).

Flow	ES	Unadjusted				Adjusted			
		n	*(B1 to-Tr2)/H*	n	*(B2 to Tr2)/H*	n	*(B1 to Tr2)/H*	n	*(B2 to Tr2)/H*
A	1	21	6.6	14	4.0	21	6.6	11	3.8
	2	30	6.9	26	3.2	27	6.4	25	3.6
B	1	29	8.8	17	6.1	27	7.8	15	5.1
	2	24	11.6	21	5.9	18	8.0	17	5.1
C	1	24	8.0	18	5.8	21	6.6	17	5.4
	2	23	8.4	15	4.7	20	6.5	14	3.9
D	1	6	3.5	8	2.5	6	3.5	8	2.5
	2	0	n/a	3	3.5	0	n/a	2	5.0
E & E_A	1	18	5.7	13	5.7	17	6.0	11	3.7
	2	17	12.3	9	3.1	13	4.6	4	3.7

ES = Echo-sounder.

to determine the sand sheet height, H_{min} and frequency, f_{min}. Unfortunately, the method applied to determine R and L could not be applied to determine the sand sheet migration rate, R_{min}, and length, L_{min}. The small bedforms were simply moving too quickly to be identified in one echo-sounder time series and then identified in the downstream echo-sounder time series (i.e., more than one sheet could pass echo-sounder 1 before being sensed by echo-sounder 2).

To overcome this problem, the video records taken at flow strength B were used to determine sheet R_{min} and L_{min}. Additional measurements included the distance from the rear dune crest to the first sand sheet crest, x_{rear}, and the distance from the first sand sheet crest to the downstream dune crest, x_{front}. Nine sections of video taken during flow B were chosen for detailed analysis of the sand sheets over five separate dunes at experimental times of ~2, 3.5, 5.2, 8 and 11.7 hours. Four sections of video were chosen over one dune to determine the consistency of measurements of sand sheets on an individual dune, as it evolved. Once sections of video were chosen, five successive images were drawn from the video, each separated from the next by 10 s. The dune crests and sheet crests were digitised from each image using ArcView. Figure 2.13 defines the measurements taken from the images. Horizontal lines separated by 0.05 m vertically were overlaid on the image and horizontal distances were measured including L_{min}, x_{rear} and x_{front}. By overlaying the sheet crests from successive images, the horizontal distance travelled by the sheet crests could be measured (Figure 2.13). Dividing by the separation time between the images, the migration rate R_{min} could be assessed. Dune length was determined by measuring the areal extent of the dune and dividing by the cross stream extent of the dune (i.e. flume width for these dunes).

2.5.1 Sand Sheet Features from Video

Sand sheet lengths measured from the video were all approximately the same (Figure 2.13), meaning there was no change in L_{min} with distance from the upstream or downstream dune crests.

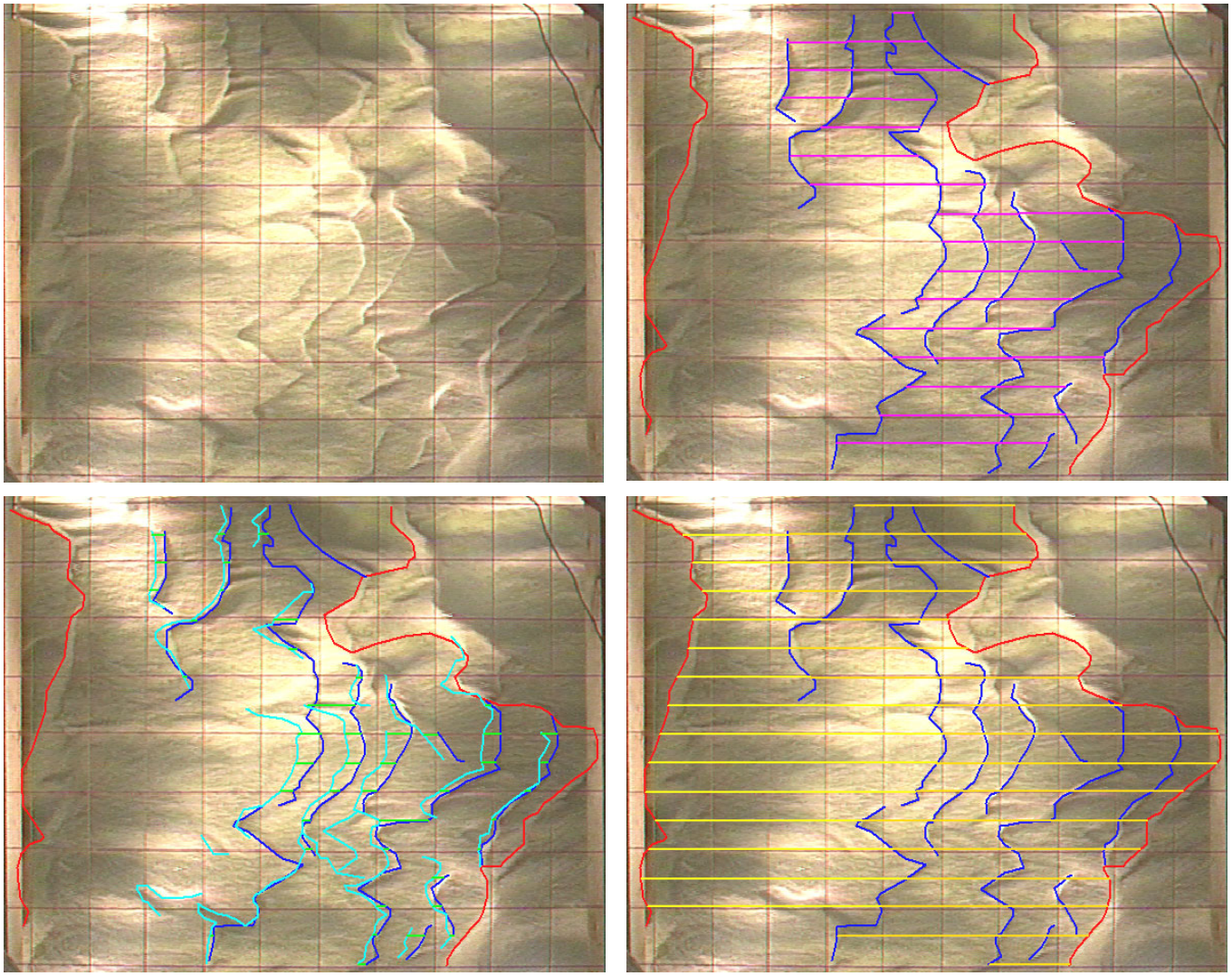

Figure 2.13: Example of the video images grabbed from the overhead video camera. Images taken at t=42260 s into Run 54 at flow strength B (Image number 546-0461). Lines indicate the features digitised from the image including: dune crest lines (red), sandwave sheet crest lines from the current image (purple), sandwave sheet crest lines from the image taken 10 s prior (blue), sandwave sheet lengths (pink), migration distances over the 10 s image separation (green), distance from the upstream dune crest line to the first sandwave sheet crestline (yellow) and the distance from the first sandwave sheet crestline to the downstream dune crest line (orange). Flow is left to right.

Further, L_{min}, averaged for individual measurement sets, did not display any relation to L. Mean L_{min} is unchanged across a range of R values (Figure 2.14). (For the present purposes, L is the best index of bedform size available from the video. Since there is a obvious relation between H and L, L should be a satisfactory scale.) It is safe to conclude that L_{min} is invariant with the dune size. Based on the similarity in the sheet lengths, the measurements can be aggregated (Figure 2.15). Lengths varied between 0.02 and 0.28 m and had a mode of 0.10 - 0.12 m.

The sand sheet migration rate does not appear to increase with distance from the upstream or downstream crests (Figure 2.13), suggesting that the sheets are not accelerating up the stoss slope of dunes. However, in contrast to L_{min}, R_{min} does vary with dune size, roughly decreasing with L. In accordance with visual observations, R_{min} roughly increases with R (Figure 2.14). A strong linear relation is found by regressing a line through seven of the nine points. The two points not used in this regression were somewhat anomalous compared to the others. For seven of the nine measurement sets, R_{min} / R = 8 - 10 while for these anomalous points this ratio was only 6. It appears the reason for this is that the reference dune crestline was accelerating compared to the others surrounding it. Aggregated R_{min} ranged between 0.2 and 5 mm s^{-1} (Figure 2.15). The distribution is far broader than that of L_{min} with significant numbers of observations at the extreme ends of the distribution. The mode lies at ~2 mm s^{-1}.

2.5.2 Sand Sheet Height, Length and Migration Rates from Echo-Sounders

Sand sheet heights, plotted relative to position along the bedform, are displayed in Figure 2.16 and mean heights, averaged over each dune, are displayed in Figure 2.17. The majority of sand sheet heights varied between 1 and 20 mm (i.e. 2 - 4 D), although some H_{min} values were outside this range over the largest dunes. There certainly is a propensity to find larger sheets near the dune crest (Figure 2.16). However, this does not translate into H_{min} consistently increasing towards the dune

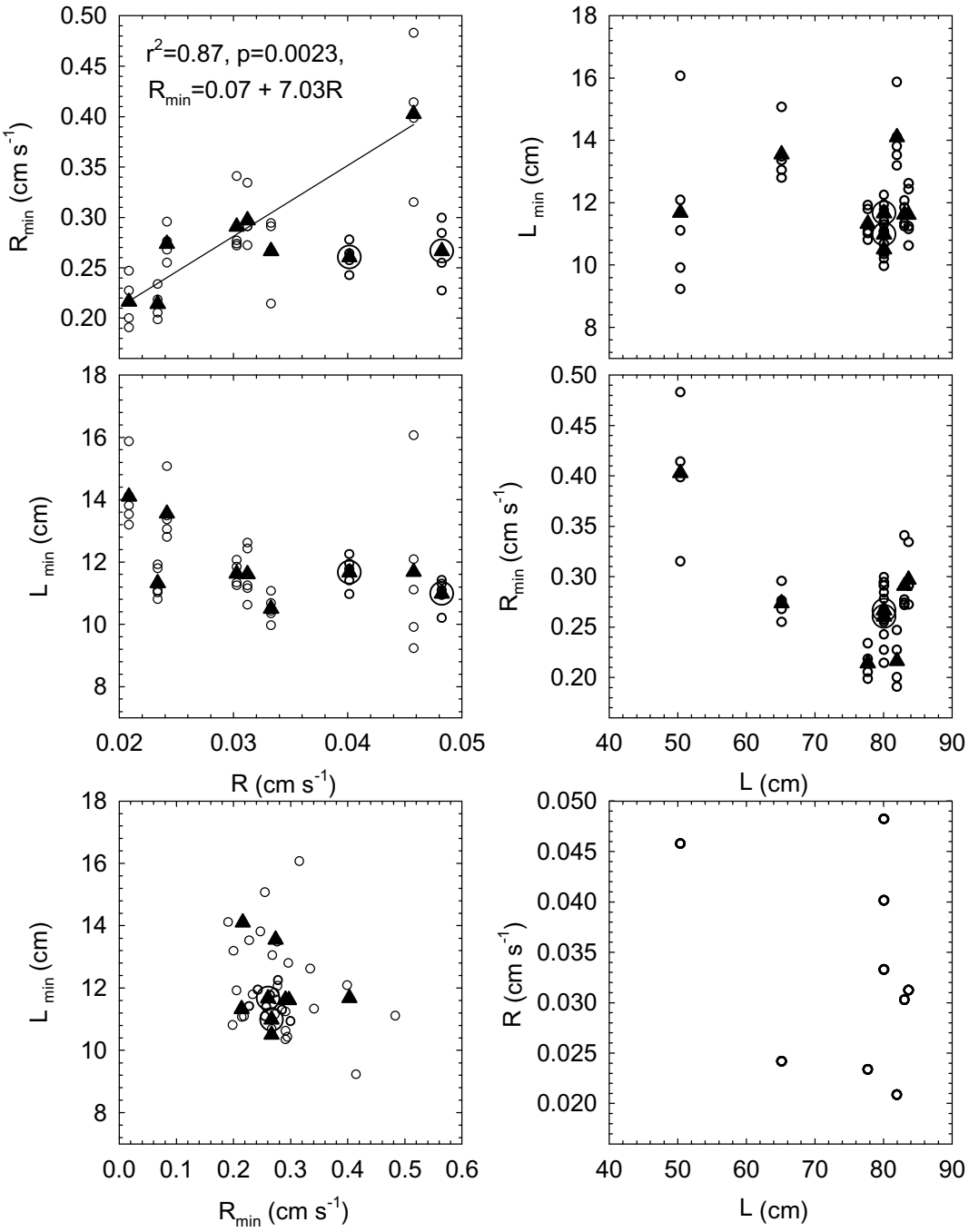

Figure 2.14: Sandwave sheet lengths, L_{min}, and migration rates, R_{min}, plotted against dune lengths, L, and migration rates, R as measured from the video. Plots of L_{min} vs. R_{min} and L vs. R are shown for reference purposes. The image averages (open circles) and averages for each dune (solid triangles) are shown. The circled triangles were removed from the regression between R_{min} and R.

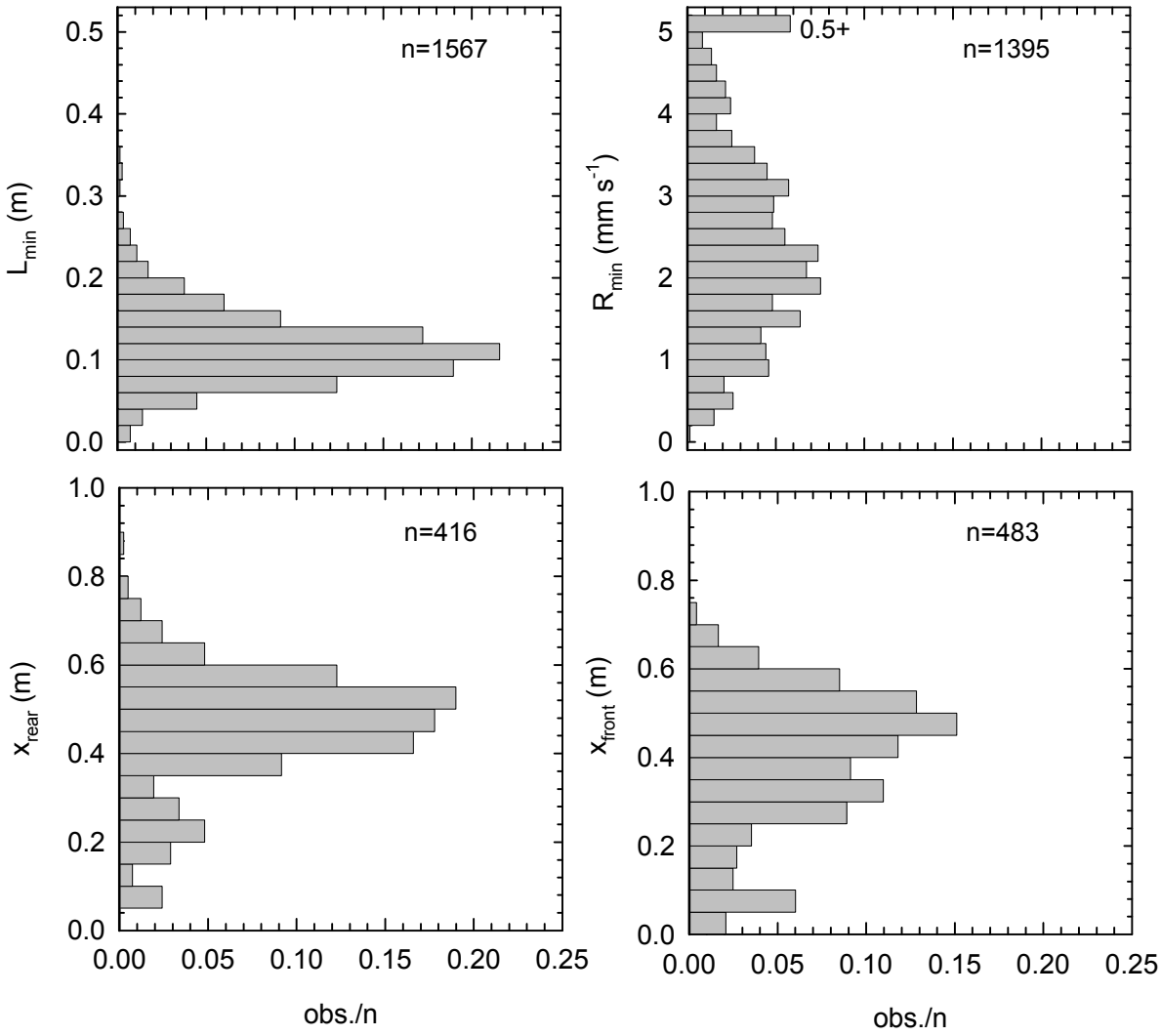

Figure 2.15: Aggregate sandwave sheet properties measured from the video, including lengths, L_{min}, migration rates, R_{min}, the distance from the rear bedform crest to the first sandwave crest, x_{rear}, and the first sandwave crest to the major bedform crest, x_{front}.

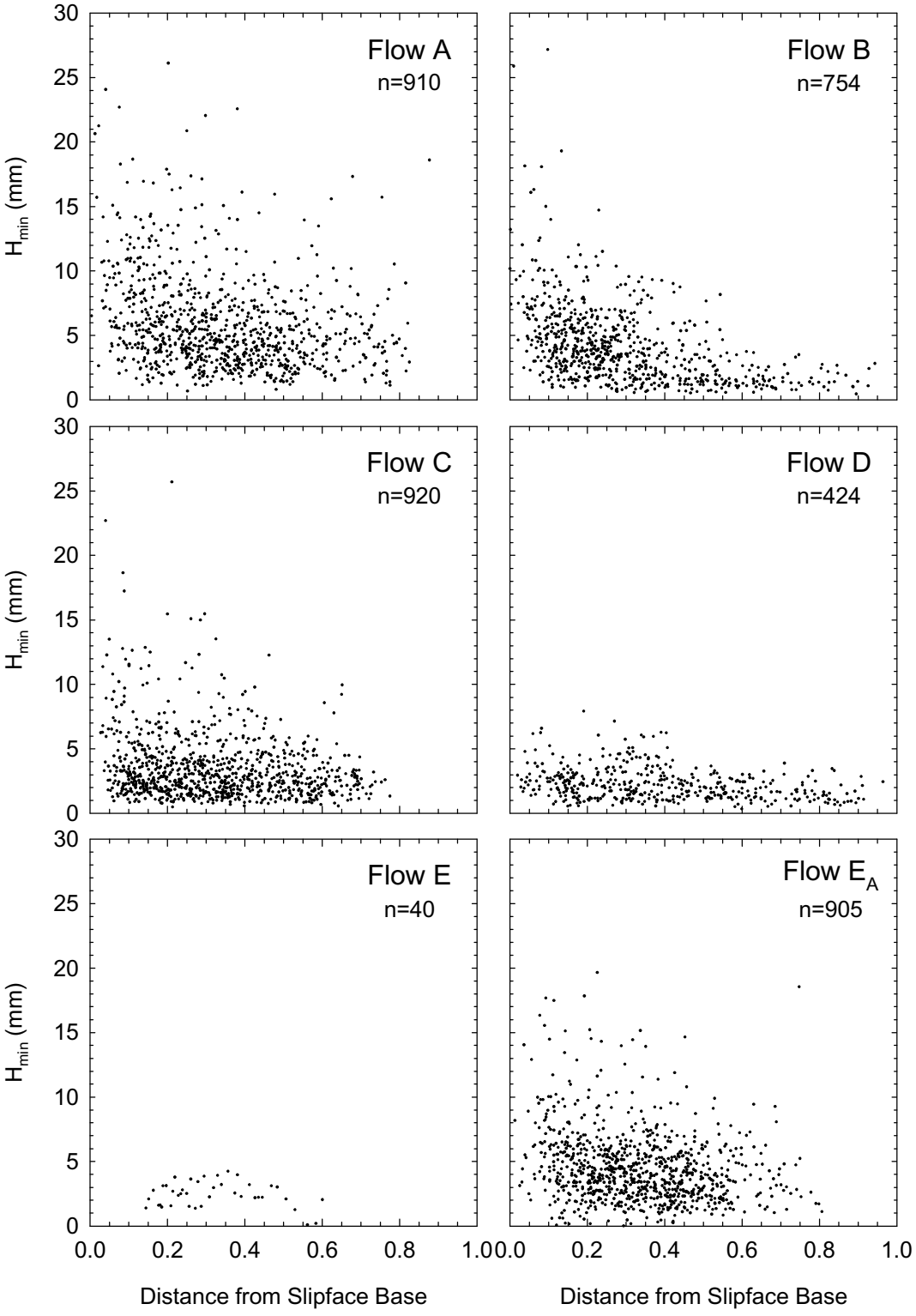

Figure 2.16: Sandwave sheet height, H_{min}, plotted against the distance from the downstream *SFB* normalised by the dune length.

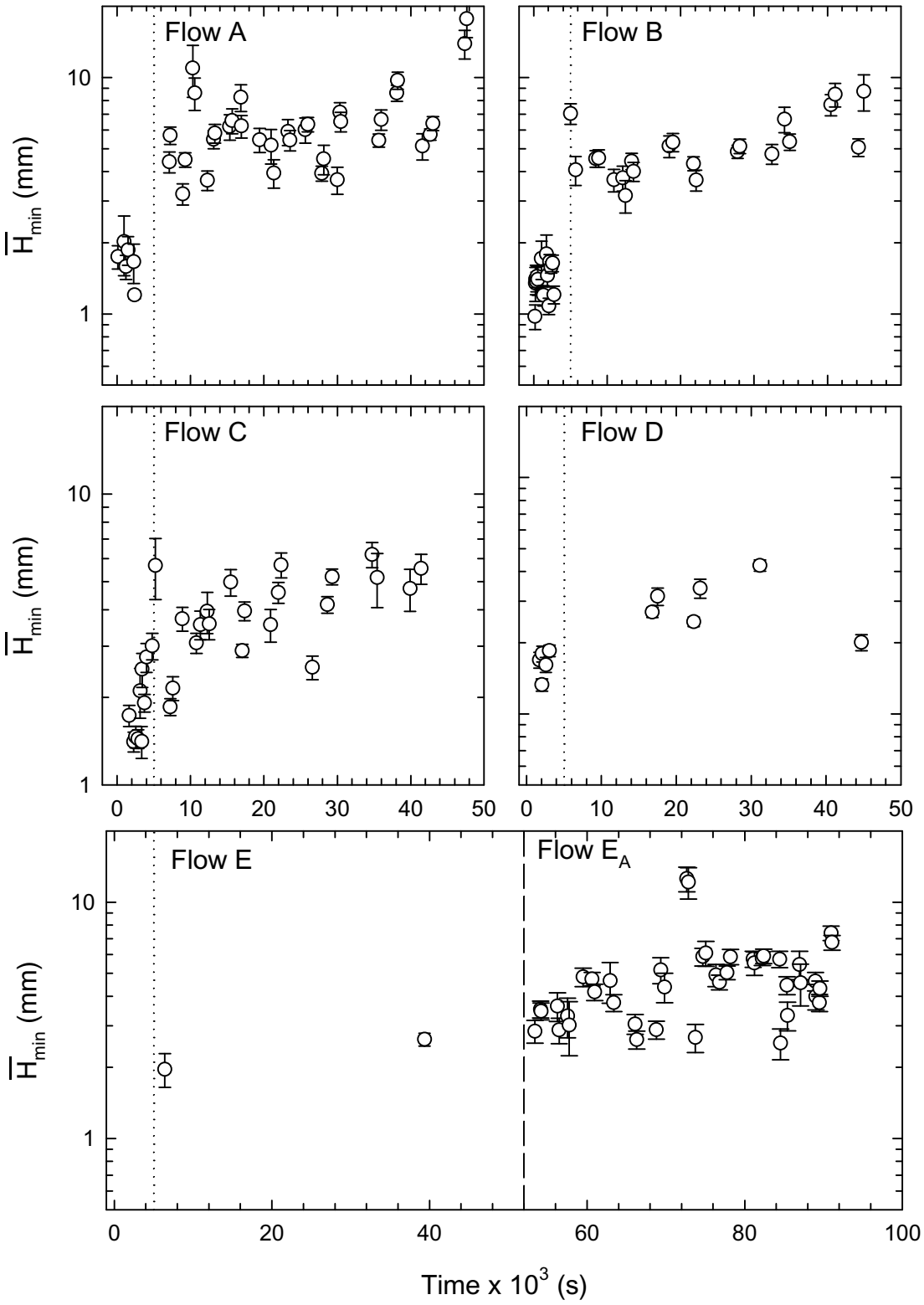

Figure 2.17: Mean sandwave sheet height, H_{min}, plotted against run time. Averages are for individual dunes. Equilibrium dune size occurs at ~5000 s during each run (dotted vertical line). The dashed vertical line indicates when the flow strength was changed from flow E (f_p =17.0 Hz) to flow E_A (f_p =23.5 Hz).

crests. Although sand sheet sequences could be identified where H_{min} increased towards the crest (e.g. Figure 2.18a), many sequences showed rather random sequences of H_{min} (no pattern) towards the dune crest (e.g. Figure 2.18b), and many others displayed nearly constant values of H_{min} (e.g. Figure 2.18c).

Mean sheet height, $\overline{H}_{min}$, increased during the flume run in the same fashion as H and L, increasing dramatically until an equilibrium was established (Figure 2.17). Thus, unlike sheet length, $\overline{H}_{min}$ increased with bedform size. In fact, the normalised sand sheet height, H_{min}/H, is centred at or near 0.1 for all flow strengths with the exception of flow E (Figure 2.19). Since only 2 bedforms were observed to have sheets during flow E, the distribution is undefined. Normalised sheet height generally varied between 0.02 and 0.30, although distributions are skewed towards lower values.

The frequency of sand sheet passage over the back of a dune is the number of crests observed, n, divided by the period of time that sheets are passing the probe, t_{tot} expressed as

$$f_{min} = \frac{n}{t_{tot}}. \qquad 2.4$$

Sand sheet frequencies range between 0.01 and 0.15 Hz, but, with the exception of sheets at flows E and E_A, appear to fall into two groups (Figure 2.20). Over the incipient dunes at the beginning of the runs, many f_{min} values are rather large with more than 8 sheets advecting past the echo-sounders per 100 s. The averages varied between ~12 and 16 sheets/100 s. In contrast, over the larger dunes later in the runs, generally fewer than 8 sheets/100 s are observed and, on average, ~3-4 sheets/100 s are observed. The larger values of f_{min} all occur over rapidly growing and somewhat diminutive dunes.

At flow strength E the higher grouping is not apparent; nearly all f_{min} values are below 8 sheets/100 s. These dunes had comparatively little sediment moving over the stoss slope and there may have been insufficient amounts of sand to produce sheets. When the flow is increased to flow strength E_A the bed already had well developed dunes, and thus differs from other runs in which the

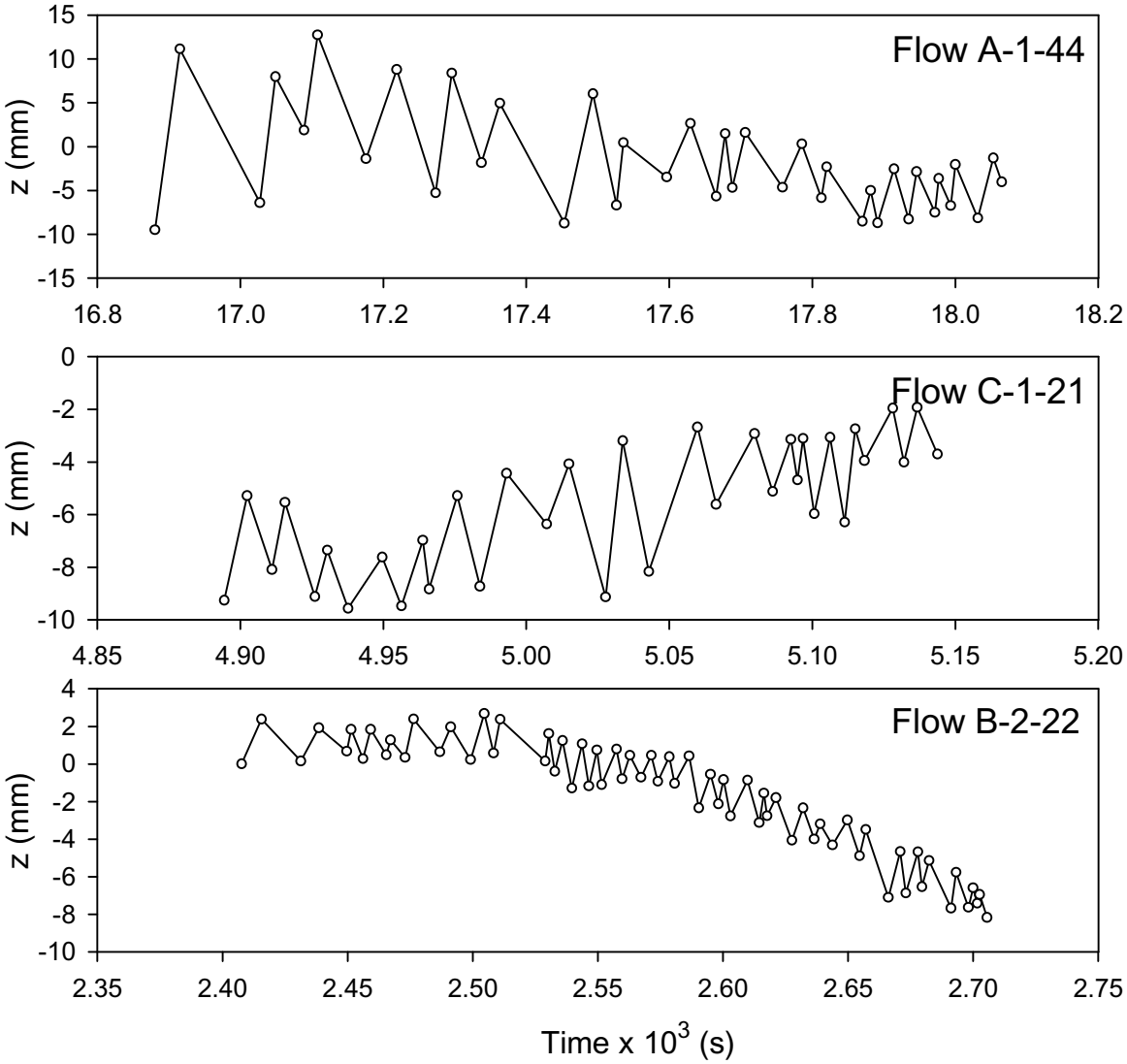

Figure 2.18: Examples of sandwave sheet sequences including sequences where sandwave sheet height, H_{min}, is increasing (Flow A-1-44), where H_{min} seems to randomly occur (Flow C-1-21) and where H_{min} is nearly constant (Flow B-2-22). The number in the top right corner identifies the flow (A-E), followed by the echo-sounder (1 or 2) and the dune number (e.g. 44). The crest of the dune is to the left and passes the sensor first. The overall trend is caused by dune passage. The points are successive z_{max} and z_{min} of sand sheets (i.e. the regular oscillation is exploited by the plotting convention).

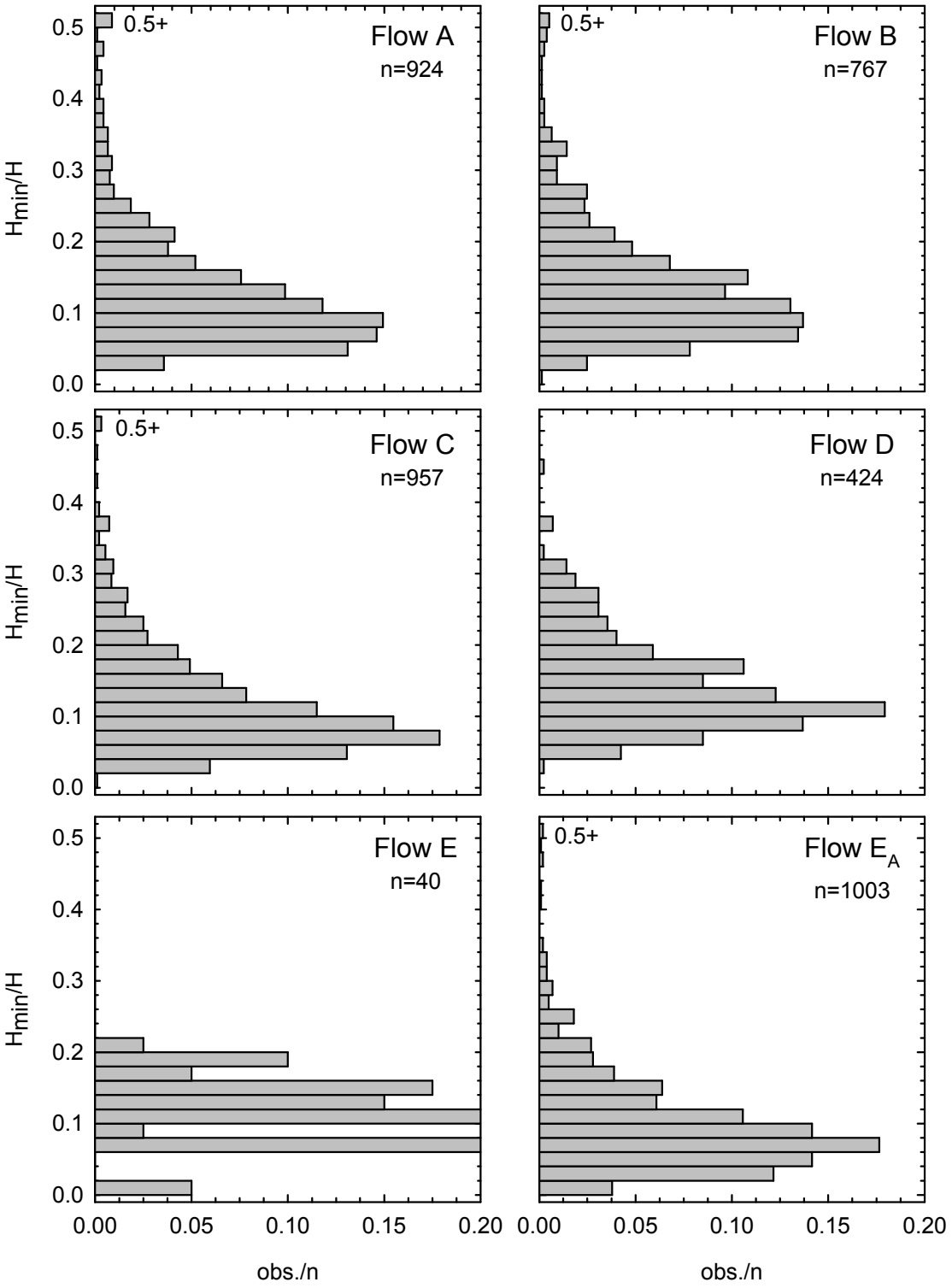

Figure 2.19: Histograms of sandwave sheet height, H_{min}, normalised by dune height, H.

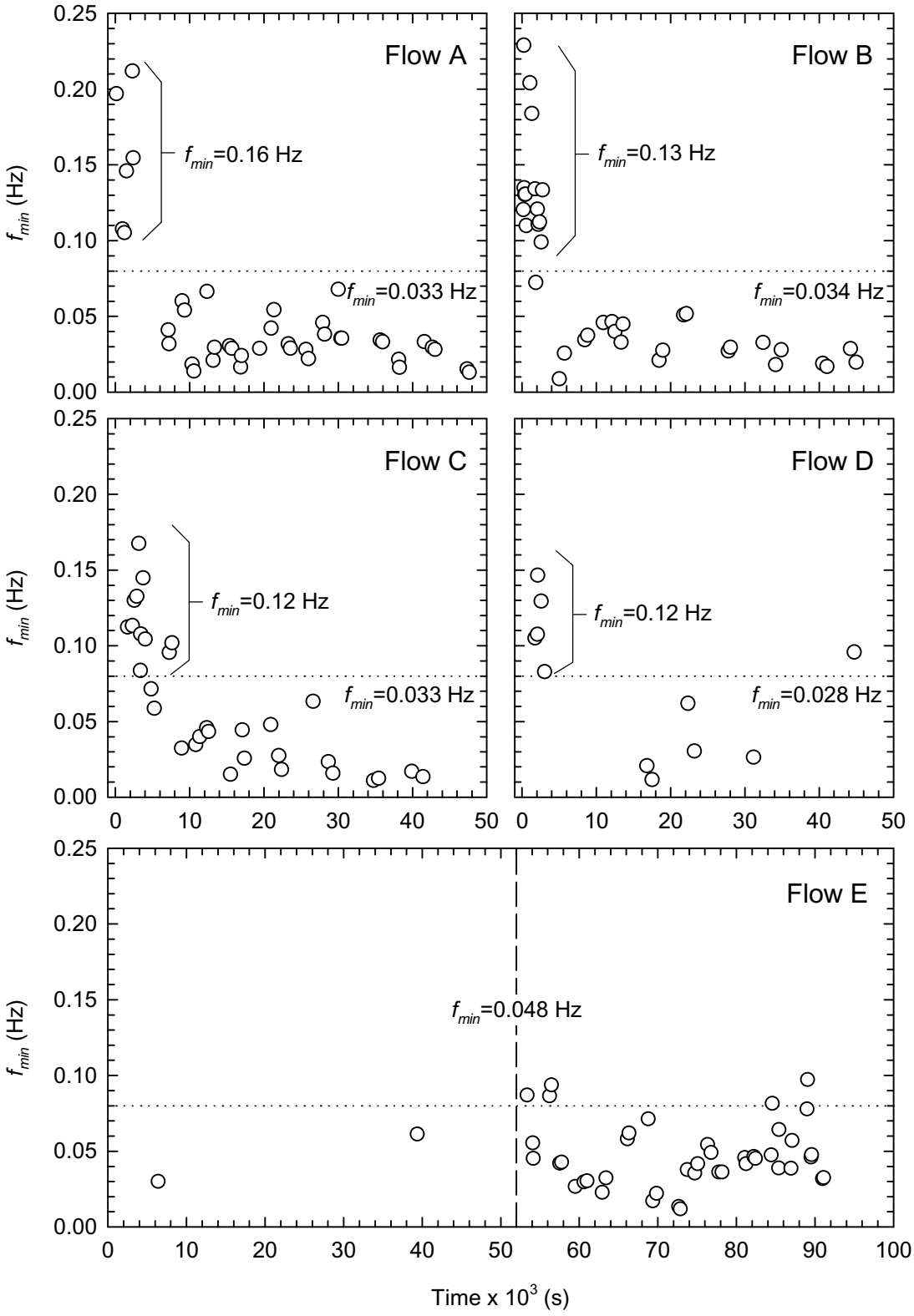

Figure 2.20: Mean sandwave sheet frequency, f_{min}, plotted against run time.

dunes with large f_{min} values are still quite small in size. It is interesting that when the dunes are most unstable (i.e. at the flow change) f_{min} exceeds 8 sheets/100 s.

Using the results obtained from analysis of the video, the sand sheet lengths were estimated by: (1) determining an approximate value of R_{min} for each dune from the regression between R_{min} and R (Figure 2.14) and (2) finding the time that each sheet required to pass the sensor (t_{pass}). Sand sheet length was calculated as

$$L_{min} = R_{min} \times t_{pass} \qquad 2.5$$

Sand sheet lengths, plotted relative to position along the bedform, are displayed in Figure 2.21 and mean lengths, averaged over each dune, are displayed in Figure 2.22. Sheet lengths generally varied between a few millimetres and 0.5 m with a few observations in which L_{min} exceeded that value. There was a propensity to observe large sheet lengths near the crest, but, like patterns observed for H_{min}, there were no consistent patterns in L_{min} over a dune.

In accordance with observations from the video, sheet length did not vary with dune size. The initial increase in $\overline{H}_{min}$ is not observed for sheet length. Mean sheet length, $\overline{L}_{min}$, varied between 0.05 and 0.40 m at the larger flow strengths (A, B and E_A) while at the lower flow strengths (C, D and E), $\overline{L}_{min}$ varied between 0.02 and 0.2 m (Figure 2.22).

Histograms of L_{min} (Figure 2.23) indicate that the bulk of sheet lengths were in the range 0.0 - 0.3 m. The distributions tend to be strongly skewed towards smaller lengths with modes that range between 0.02 and 0.08 m. This differed considerably from the lengths observed from the video. Sheets in the video were observed throughout the record and could be seen over the small initial features by eye. However, the sand sheets observed in the video needed to be at least a few mm high before they could be properly identified. This only occurred later in the record, when f_{min} exceeded 8 sheets/100 s. Further, extremely long waves (i.e. > 0.5 m) were generally ignored.

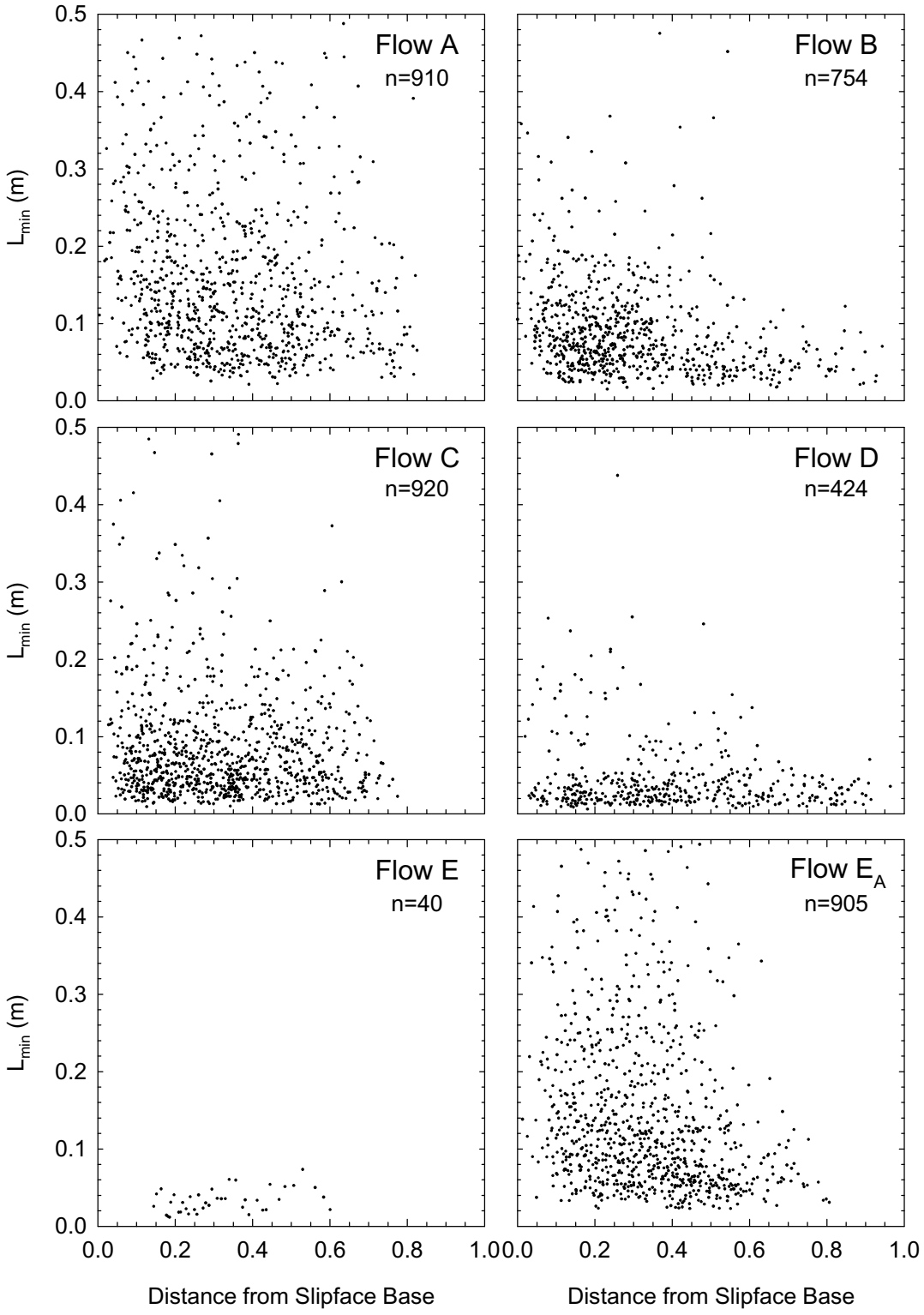

Figure 2.21: Sandwave sheet length, L_{min}, plotted against the distance from the downstream *SFB* normalised by the dune length.

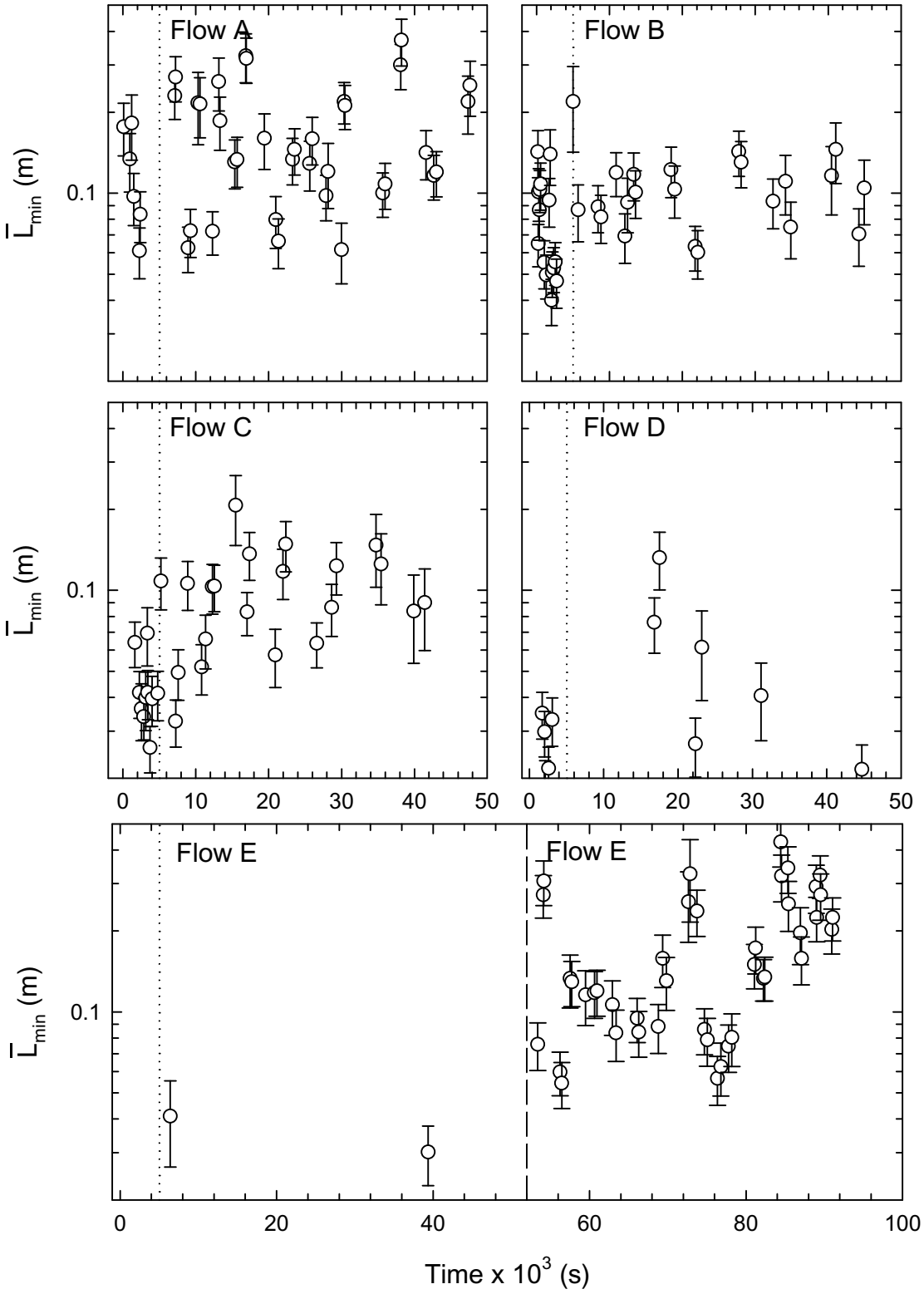

Figure 2.22: Mean sandwave sheet length, L_{min}, plotted against run time. Averages are for individual dunes. Equilibrium dune size occurs at ~5000 s during each run (dotted vertical line). The dashed vertical line indicates when the flow strength was changed from flow E (f_p =17.0 Hz) to flow E_A (f_p =23.5 Hz).

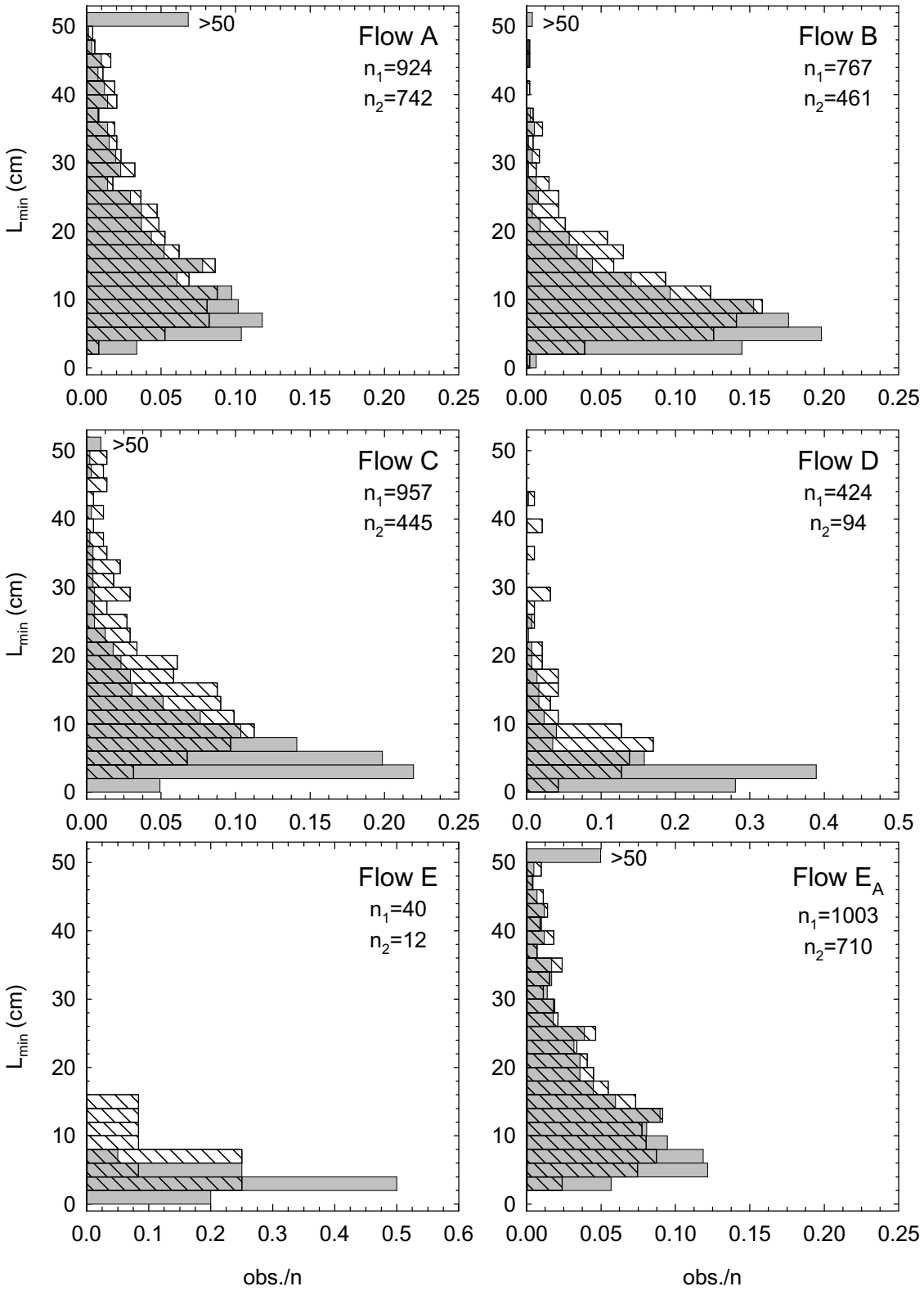

Figure 2.23: Histograms of sand sheet length, L_{min}, calculated using the relation between R_{min} and R. The solid bars are for all lengths. The hatched bars are for data that have been selected to remove lengths where: 1) L_{min} > 0.50 m, 2) corresponding H_{min} < 3 mm and 3) sheet frequencies, f_{min} 0.08 Hz. The number of observations for the unfiltered data (n_1) and filtered data (n_2) are indicated.

In light of this, the data were filtered to remove sand sheet lengths when: (1) L_{min} > 0.05 m, (2) corresponding H_{min} < 3 mm, and (3) f_{min} > 0.08 Hz. If a sand sheet was removed from the analysis because H_{min} < 3 mm, its length was added to the upstream sheet. Histograms of the sand sheet lengths remaining after this filtering are also shown in Figure 2.23. The histogram for sand sheets measured from the video at flow strength B shows a distribution similar to the one in Figure 2.15. Lengths varied between 0.02 and 0.20 m with a mode of 0.08-0.10 m, only slightly smaller than the mode from the video. This suggests that differences between the L_{min} distribution observed from the video and the distribution from the echo-sounders is related to the resolution of the techniques. While the echo-sounders can resolve sand sheets in which H_{min} > 0.5 mm, the video can only practically resolve the larger sheets (> 3 mm). This does not suggest that the L_{min} distribution produced from the echo-sounders is in error.

2.5.3 Variability and Measurement Error in Sand Sheet Properties from Echo-Sounders

There are three substantial sources of variation in the data set: (1) natural variation of the phenomenon, (2) error associated with type of measurements taken and (3) the practical vertical resolution of the measurements system. Estimating how each source of error is represented in the individual measurements of sand sheet properties is difficult. However, variability about the mean values provides some estimate of the total variability, including the measurement error.

The error associated with the type of measurements taken is likely small for H_{min} as height is measured directly. However, the error associated with the vertical resolution of the measurement system is quite substantial. For the dunes, D was only 3.7 - 7.5 % of s_H. For the sand sheets, D can be many times larger than $s_{H_{min}}$. On average, the resolution of the echo-sounder measurements accounts for 25.1 - 61.6 % of the total variation. CV_{Hmin} varied between 0.065 and greater than 1 for

the sand sheets over individual dunes with a mean, calculated for each flow strength, that varied between 0.41 and 0.51.

A substantial portion of the variability in L_{min} is related to how the lengths were calculated. Error associated with the measurement of t_{pass} and the regression used to estimate R_{min} are compounded. $CV_{L\,min}$ varied between 0.11 to greater than 1 for sand sheets over individual dunes with a mean, calculated for each flow strength, that varied between 0.43 and 0.58. This variability is equivalent to the variation in t_{pass} due to how L_{min} is calculated. Potential inaccuracies in sand sheet t_{pass} are caused by the same processes as for the dunes; sheets stalling in their downstream progression or accelerating and decelerating during the measurement period. Sand sheets moved far more consistently and changed little as they migrated over the dunes. Thus, most of the variability observed in t_{pass} is natural.

The error associated with the regression between R and R_{min} is in addition to the variability in L_{min}. The standard error associated with the regression between R and R_{min} is ~16 - 20 % of R_{min} for all flow strengths except E, in which the standard error is ~28 % (recall that there are only two dunes with sheets observed on them at flow strength E). Using rules for combining errors from multiple measured quantities [*Beers*, 1957], the standard error associated with $\overline{L}_{min}$ varied between 17.6 and 36.6 % of $\overline{L}_{min}$ for individual bedforms. Mean values, calculated for each flow strength, are ~22 % of $\overline{L}_{min}$ for all flow strengths but E, for which the standard error is ~30 % of $\overline{L}_{min}$.

2.5.4 Sand Sheet Classification and Scaling

Superimposed bedforms are common and have been reported extensively in the literature [see review in *Allen* 1968 or *Ashley*, 1990]. The sand sheets described here do not appear to be fundamentally different from previous descriptions of superimposed bedforms where both scales are in equilibrium at the same time [e.g. *Pretious and Blench*, 1951; *Jackson*, 1976]. Superimposed

bedforms are often observed where only one scale is in equilibrium [see *Allen and Collinson*, 1974]. Those features may be fundamentally different from the sand sheets observed here.

Despite their similarity to features previously observed, sand sheets cannot be classified as ripples or dunes, but have characteristics shared with both features. Their relatively small lengths and heights are reasonable for ripples. That the features do not grow as they migrate downstream suggests that they are not growing to scale with a boundary layer depth (i.e. the depth of the internal boundary layer). Thus, their length and height when they appear on the stoss slope appear to be their equilibrium dimensions, which is typical of ripple features that scale with grain size. However, the sand sheets tend to have an aspect ratio far smaller than that observed for ripples.

Figure 2.24 shows histograms of the sand sheet aspect ratio (H_{min}/L_{min}) at each flow. Based on the separation between ripples and dunes given by *Allen* [1968], some of the sand sheets could be ripple forms. However, most sheet aspect ratios are less than the upper limit for dunes of 0.1 proposed by *Allen* [1968]. Further, at flow strengths A, B, C and E_A, more than 55 % of the sheets have aspect ratios less than the lower limit for ripples (0.05) suggested by *Allen* [1968] and data from *Guy et al.* [1966]. Even at flow strength D, 36 % of the sheets have aspect ratios smaller than 0.05. Only at flow strength E are most sheet aspect ratios greater than 0.05 (Recall that H_{min} and L_{min} distributions are not well defined at flow E). Modal aspect ratios are between 0.02 and 0.05, depending on the run.

These aspect ratios suggest sand sheets are not ripples but low relief dunes. In this respect, the sand sheets are similar to bedload sheets, first described by *Whiting et al*. [1988], which represent an additional scale of sediment transport organisation in poorly sorted sediments. They have been observed over flat gravel beds and superimposed on dunes. Bedload sheets are typically several coarse grain-sizes high, lack a well-defined slipface and have aspect ratios between 0.003 and 0.040 which classify them as low relief dunes [*Bennett and Bridge*, 1995]. It is generally agreed that

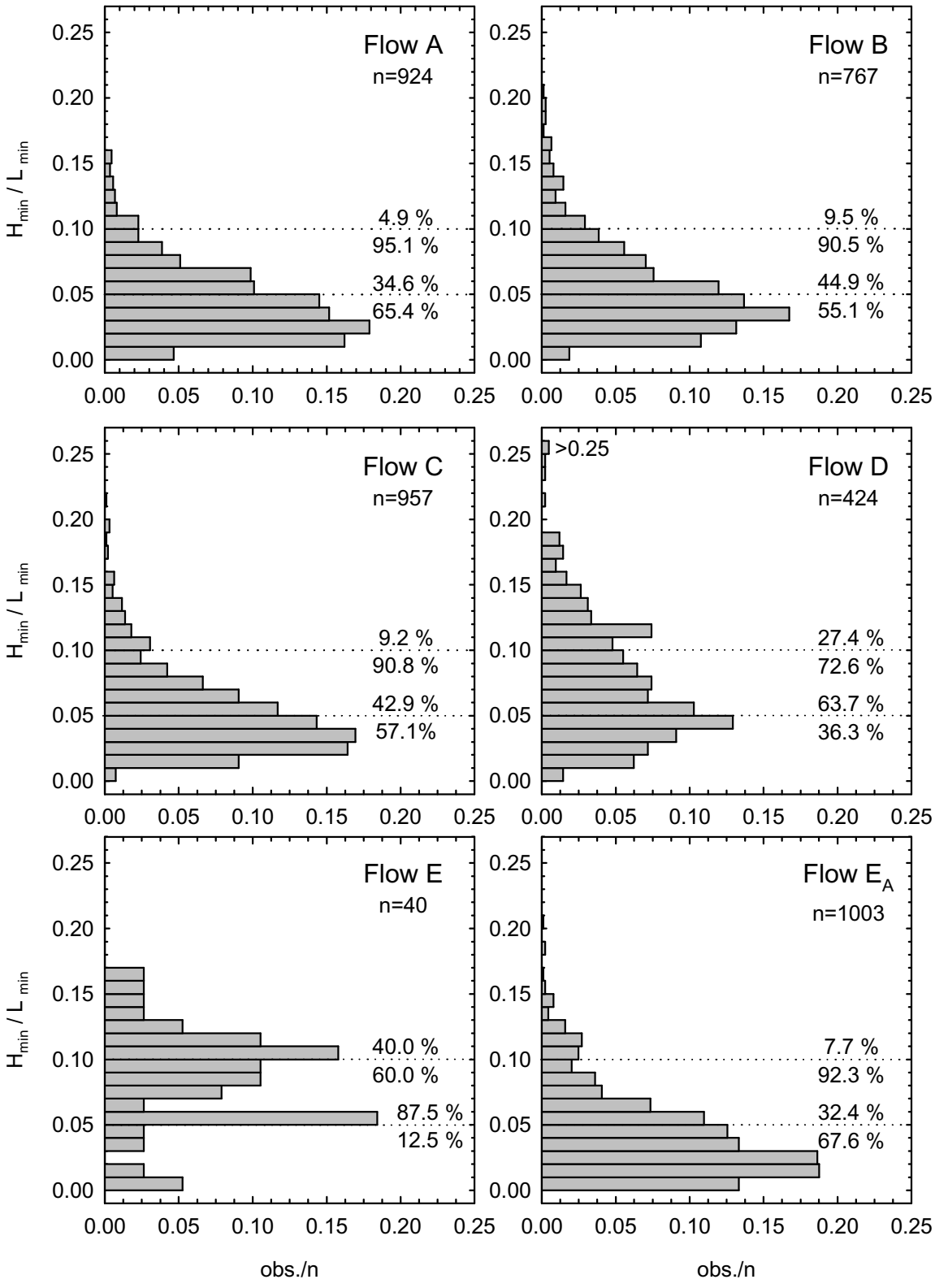

Figure 2.24: Histograms of sand sheet aspect ratio (H_{min} is and sheets height and L_{min} is sand sheet length). The dotted line at 0.1 indicates the typical upper limit of dunes and the dotted line at 0.05 indicates the usual lower limit of ripples.

bedload sheets are caused by selective entrainment and transport in heterogeneous sediment [*Whiting et al*., 1988; *Bennett and Best* 1995].

Interestingly, since the identification of bedload sheets by *Whiting et al.* [1988], descriptions of them have fallen into two categories, those developed on otherwise flat beds [*Wilcock,* 1992; *Bennett and Bridge*, 1995] and those developed on the stoss slope of bedforms [*Livesey et al.,* 1998]. It is not possible to divide these studies based on sheet aspect ratio. While some bedload sheets over dunes appear to be flatter than dunes, many of the features could be classified as ripples based on aspect ratio. *Livesey et al.* [1998] describe bedload sheets with an aspect ratio that would classify them as ripples.

Describing the sand sheets over the dunes as bedload sheets seems inappropriate because the origins of the forms cannot be attributed to selective entrainment and transport. No sediment sorting can occur along the streamwise axes of sand sheets because the sand is homogeneous. The height of the sand sheets is not limited to a few grains. However, the sand sheets do share several morphological characteristics with bedload sheets. At 0.1 H , H_{min} is similar to bedload sheet heights previously observed over dunes as are sand sheet lengths [e.g. *Whiting et al.*, 1988; *Livesey et al.,* 1998]. Most sand sheets did not have a defined slipface and are classified as low relief or incipient dunes based on their aspect ratios.

2.5.4 The Origin of Sand sheets

Development of the sand sheets seems to be related to a minimum 'fetch' length beyond the bedform crest. This is revealed in measurements from the video of the distance from the rear dune crest to the first sand sheet crest (x_{rear}) and the distance from the first sand sheet crest to the downstream dune crest (x_{front}). Most x_{rear} values are between 0.4 and 0.6 m and while most x_{front} values are between 0.2 and 0.6 m. While x_{rear} did not vary with L , x_{front} did (Figure 2.13). Thus, proximity to the dune crest does not appear to be an important factor. However, a minimum x_{rear}

value of ~0.5 m is necessary for the sheets to form. This appearance is further substantiated by the fact that no sheets appeared in the video until the bedforms reached a wavelength of ~0.5 m.

Interestingly, x_R does not appear to control x_{rear}. For the first measurement set from the video, H is ~0.025 m and near $\overline{H}_e$ for the other measurements from the video. Assuming $x_R \approx 5H$, x_R = 0.125 m for the first measurement set and ~0.20 m for other measurements sets. $x_{rear} \approx 3\,x_R$ for the first measurement set and ~2 x_R for the other measurements. The reattachment length must play some role in where the sand sheets begin to form on the dune; echo-soundings indicate sand sheets generally do not form upstream of x/L = 0.8 (see Figure 2.16 and 2.21). The separation bubble would sit at approximately $0.8 < x/L < 1.0$ over most of the bedforms.

Given that the length over which the sand sheets develop is somewhat limited, it seems likely that sheets could further develop into either full sized ripples or dunes. These features are similar to those developed at the beginning of the experimental runs over the flat bed. Therefore it is possible that the same processes that control sandwave initiation and development over a flat bed, discussed in the next chapter, may be operating here.

2.6 Sediment Transport Rates

Probably the most compelling reason to study bedforms is to gain a better understanding of their implications for sediment transport processes. It is therefore logical to end the discussion of the dunes and sand sheets with estimates of the transport rates that are associated with each. Although bedload transport measurements were made during the experiments, they were too infrequent to provide a complete picture of the sand transport associated with the waveforms. Nearly all the bed material was transported as bedload. Sand suspension and sand bypassing bedforms as it travelled downstream were observed to be negligible. Thus, more complete quantification of the transport can be accomplished by using morphological estimates based on the characteristics of the waveforms themselves.

2.6.1 Morphological Estimates of Transport Rates

Assuming all bed material moves as bedload, estimates of the sediment transport rate can be determined from the morphology of the dunes and sand sheets separately. *Simons et al.* [1965] indicate the volumetric dry sediment transport rate of bedforms moving at a migration rate, R_b, per unit time and unit width is

$$Q_s = b\,(1-P)\,R_b\,h \qquad 2.6$$

where P is the sediment porosity, h is the bedform height and b is the bedform shape factor. Values of b can be calculated as

$$b = \frac{A}{h\,l} \qquad 2.7$$

where A is the cross-sectional area of the bedform and l is the bedform length. If the bedforms are triangular, b =0.5. Bedforms in natural channels rarely have a perfectly triangular shape and so a variety of b values has been suggested in the literature [c.f. *ten Brinke et al.*, 1999; *van den Berg*, 1987]. However, most authors have suggested b =0.55-0.60.

Engel and Lau [1981] suggested an alternative approach based on the idea that there is a zero net transport point at the flow reattachment point (Figure 2.25a). Upstream of the reattachment point sediment flux is negative and downstream the flux is positive. Therefore only that portion of the dune above the zero net transport rate is included in sediment flux (Figure 2.25a). The dune is assumed to be perfectly triangular. In this formulation b is replaced by K, a coefficient dependent on x_R, H/L, the lee slope angle, and the bedform shape, and H is replaced by x, the average departure of z about $\bar{z}$. For a triangular shape $x = H/4$ and, using H/L =0.05 (the approximate mean of the bedforms under examination here), K is 1.44 or $2.88b$. For a triangular shape, $Q_s(b,H)$ will produce estimates that are 72 % of $Q_s(K,x)$.

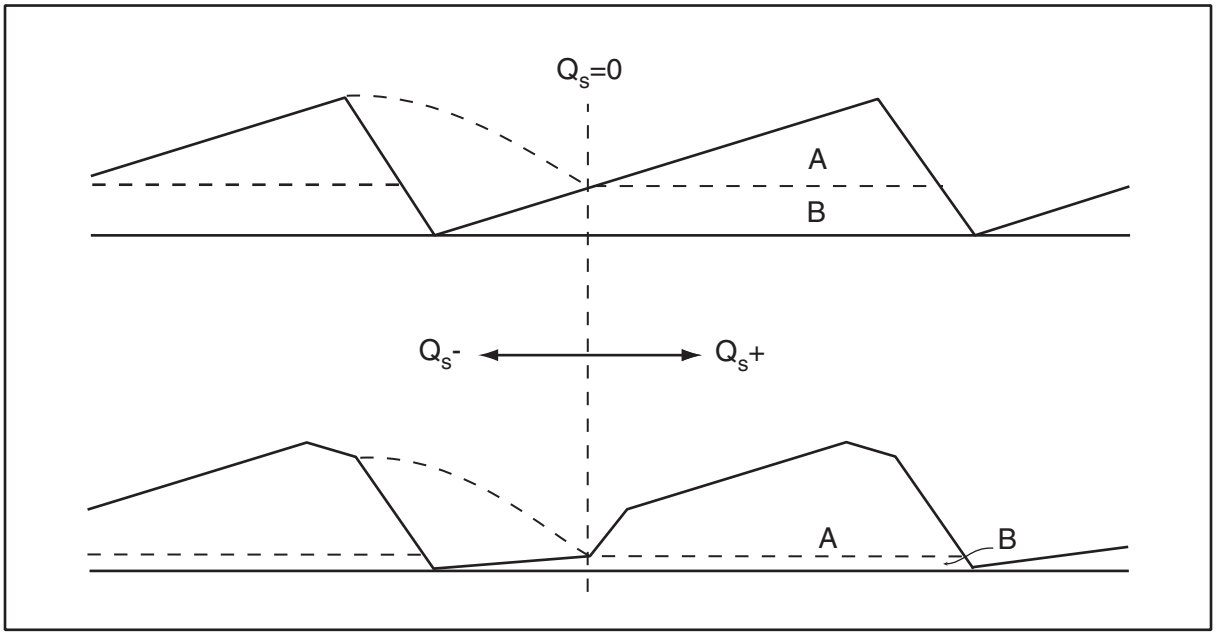

Figure 2.25: Definition diagram for Engel and Lau's [1986] supposition that only that portion of the dune above the reattachment point contributes to the transport rate. The dune shape used in their formulation (a) and the shape observed in these experiments (b) are displayed.

There are several problems with the *Engel and Lau* [1981] approach. For example, this approach would seem to give a positively biased estimate of the transport rate, because logically, the negative sediment flux should be subtracted from the positive flux. Another problem is that the observed dunes differ significantly from the simplified form depicted in Figure 2.25a. Most dunes had a well-defined pan that encapsulated the separation cell and so the reattachment point occurred near the base level of the dunes (Figure 2.25b). Thus, the volume of sediment below the reattachment point on the dune back is much smaller than envisioned by the *Engel and Lau* [1981].

2.6.2 Dune and Sand sheet Related Transport Rates

Figure 2.26 plots the sediment transport rates for (1) dunes, Q_{s-d}, (2) sand sheets, Q_{s-ss}, and (3) Helley-Smith bedload samples, Q_{s-HS}. To estimate the dune related transport rate, $h = H$ and $R_b = R$ in Equation 2.6. Values of H and R are those presented in Figures 2.6 and 2.7. The porosity of 0.5 mm sand is ~0.4 [*van Rijn*, 1993]. Rather than using an estimated and fixed value of b, the echo-sounder time series were used to calculate b directly from Equation 2.7 with $h = H$ and $l = L$. In order to determine A, each bedform was plotted using only the features shown in Figure 2.11 (i.e. *Tr*, *SFB*, *SFC*, *C*, *B1* and *B2*). Cross-sectional area is only the portion above a datum line running between Tr and the upstream Tr. Figure 2.27 plots b against the bedform number. b ranged between 0.3 and 0.8 with greater variance later in the runs. Mean b varied amongst the runs but is ~0.56.

To estimate the sand sheet related transport, $h = \overline{H}_{min}$ and $R_b = R_{min}$ in Equation 2.6. Thus, sheet heights and migration rates are averaged over a dune. Since the sand sheets have approximately the same morphological scaling as the dunes, a b value of 0.56 is used for all sheets.

Both Q_{s-d} and Q_{s-HS} increased in the same fashion as dune L and H, initially rising quickly and settling into an equilibrium value. Q_{s-ss} was generally larger than Q_{s-d} and Q_{s-HS} when the

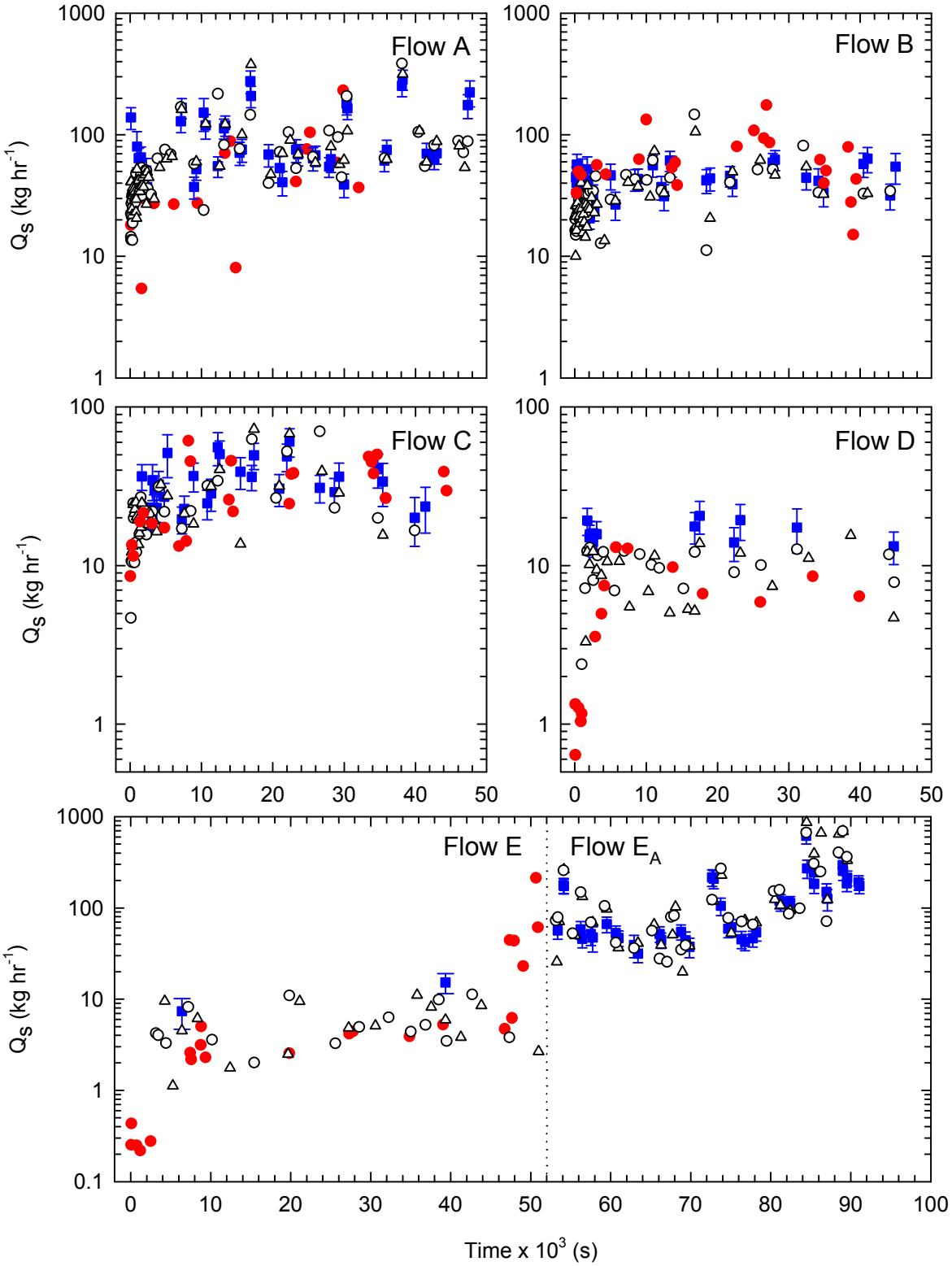

Figure 2.26: Sediment transport rates, Q_s, determined from the morphologic characteristics of the dunes (open circles for echo-sounder 1 and open triangles for echo-sounder 2), the morphologic characteristics of the sandwave sheets (closed squares), and Helly-Smith bedload samples (closed circles). Sand sheet error bars are the standard error of the estimate.

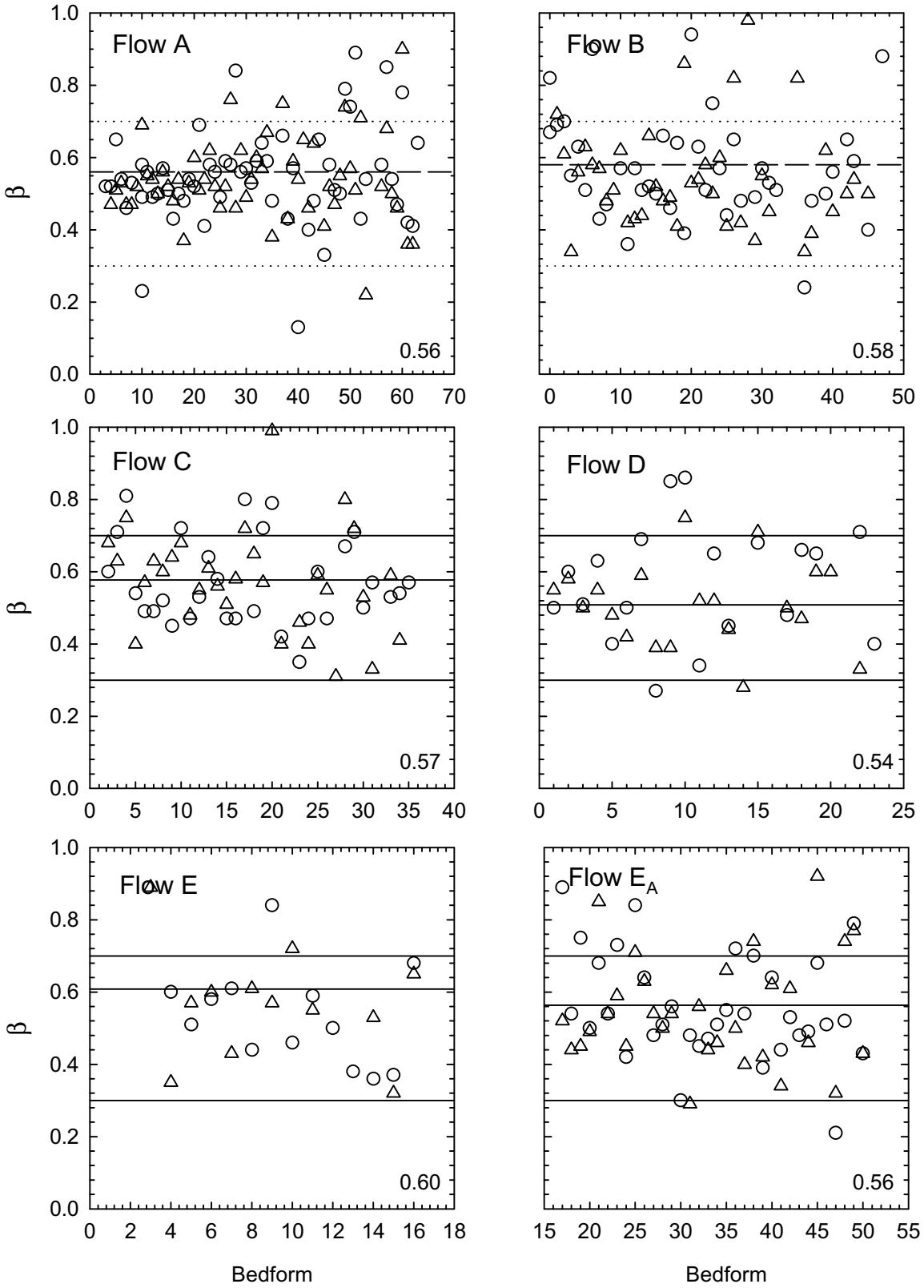

Figure 2.27: Bedform shape factor, β . Circles are measurements from echo-sounder 1 and triangles are measurements from echo-sounder 2 (See figure 2.3).

transport rate was increasing towards an equilibrium at flow strengths A, B, C and D. These estimates of Q_{s-ss} are from sand sheets with a frequency greater than 8 sheets/100 s. It appears that these sheets were moving more sand than the incipient dune forms and may be a fundamentally different sheet than those observed later in the experiments. This makes sense because in order for the dune to grow, sand sheets must appropriate more sand from the dune back than moves past the dune crest.

Table 2.5 provides the initial mean transport rates, $\overline{Q}_{si}$, and the average equilibrium transport rates, $\overline{Q}_{se}$. Transport rate increases with flow strength, which is expected for homogeneous sand. Interestingly, $\overline{Q}_{se-d}$ at flow strength E_A is larger than at flow strength A by ~70 %, suggesting that the time required for a run to reach equilibrium when bedforms are already present may be significantly longer than when they are not present. Transport rates differ amongst the different methods used to obtain Q_s. Sources of variability and error need to be considered before a comparison of Q_s from the different methods can be accomplished.

2.6.3 Variability and Measurement Error in Transport Rates

Ideally the error associated with each transport measurement or estimate could be determined and error bars given in Figure 2.26. Unfortunately, the error associated with Q_{s-d} is derived from the error associated with H and R. As noted above, it is not possible to accurately assess the error associated with calculated R values making it impossible to report a total error associated with Q_{s-d}. Similarly, the error associated with Q_{s-HS} cannot be assessed accurately because there is no standard against which to test the samples. However, several authors have reported the efficiency of a full-sized Helley-Smith sampler. Both *Sterling and Church* [2002] and *Emmett* [1980] indicated that the Helley-Smith sampler has an efficiency of ~100 % for 0.5 mm sand. However, these studies

Table 2.5: Mean sediment transport rates with the standard error as upper and lower boundaries. Subscript i indicates the initial values and e the equilibrium values (mean of estimates/measurements taken after 5000 s). Helley-Smith samples in the dune trough are removed from the averages. No Helley-Smith samples were taken at flow E_A. The initial Helley-Smith transport values are for a flat bed. For flows A-E, Q_{si} is the mean of values in the first 10 min of the experiment. Because the dunes at flows D and E were generated well upstream of the echo-sounders, no initial dune related transport could be detected.

Flow	Helley-Smith Samples				Dunes				Sand sheets	
	n_i	$\overline{Q}_{si}$ (kg hr^{-1})	$\overline{Q}_{se}$ (kg hr^{-1})	CV_{Qse}	n_i	$\overline{Q}_{si}$ (kg hr^{-1})	$\overline{Q}_{se}$ (kg hr^{-1})	CV_{Qse}	$\overline{Q}_{se}$ (kg hr^{-1})	CV_{Qse}
A	1	18.12	70.17 ± 18.47	0.85	21	27.69 ± 1.84	102.44 ± 7.66	0.75	111.71 ± 12.28	0.64
B	1	33.28	71.23 ± 9.76	0.58	17	20.74 ± 1.27	47.91 ± 4.83	0.55	46.47 ± 2.33	0.24
C	2	11.04 ± 2.46	35.64 ± 3.23	0.33	5	15.76 ± 1.49	34.16 ± 3.85	0.54	36.67 ± 2.66	0.33
D	6	1.50 ± 0.42	9.01 ± 1.13	0.33	0	n/a	9.45 ± 0.62	0.33	17.05 ± 1.19	0.17
E	5	0.29 ± 0.04	13.67 ± 8.22	0.32	0	n/a	5.66 ± 0.58	0.53	11.32 ± 3.93	0.49
E_A	n/a	n/a	n/a	n/a	0	n/a	173.47 ± 25.45	1.16	126.01 ± 16.84	0.87

examined trapping efficiencies of coarse heterogeneous sediments. It is not clear if the results apply to homogeneous sand.

In contrast to Q_{s-d} and Q_{s-HS}, the error associated with Q_{s-ss} can be accurately assessed as the standard error of the mean ($s/\sqrt{n}$) can be calculated for H_{min} and combined with the error associated with the regression used to estimate R_{min} using rules for combining errors found in *Beers* [1957]. Thus, the error associated with Q_{s-ss} is presented as error bars in Figure 2.26 and generally ranged between 17 and 37 % of the Q_{s-ss} estimate with a mean of ~21 % for each run.

Variability in the transport estimates or measurements can also be examined through estimates of the mean equilibrium transport rates. Sources of this variability vary amongst the different methods for estimating Q_{se}. In general, CV_{Qse} varied between 1.16 and 0.17 (Table 2.5). The largest variability was observed at flow strengths E_A (CV_{Qse} = 0.87 - 1.16) and A (CV_{Qse} = 0.64 - 0.85). Variability in Q_{se} is largest for Q_{se-HS}, intermediate for Q_{se-d} and least for Q_{se-ss} (Table 2.5).

The variability in the Helley-Smith bedload samples increases with the flow strength and has several sources. First there is natural variability in the amount of sediment moving over the bedform, which is related to bedform size and three-dimensional morphology. Another source of variability in Q_{s-HS} is where the sample was taken (i.e. over the dune crest, stoss slope or trough). In general bedload samples taken over the crest and stoss slopes were equivalent in size. Samples over the dune troughs tended to be small or even negligible in size. Error was also incurred when the sampler's position on the bed caused sediment movement into the mouth simply by its presence. A final and substantial source of error in Q_{s-HS} occurred when the sampler base could not be placed flush with the bed slope along the streamwise or cross-stream directions. Notes taken during the experiments were used to remove those samples with obvious error. However, it should be noted that no bedload sample was completely free of these measurement errors.

There does not appear to be a consistent pattern in the variability associated with Q_{se-d} and Q_{se-ss} aside from CV_{Qse} being largest at flows A and E_A. The sources of variability in Q_{se-d} and Q_{se-ss} are directly related to variability in the bedform heights and migration rates whose variability is discussed above. The variability in Q_{se-d} is larger than for Q_{se-ss} because the variability in the heights and migration rates is greater for the dunes than the sand sheets.

2.6.4 Transport Rate Estimate Agreement

Agreement between the morphological estimates of sand transport and $\overline{Q}_{s-HS}$ is highly variable. The ratio $\overline{Q}_{si-d} / \overline{Q}_{s-HS}$ at flow strengths A, B and C are 1.53, 0.62, and 1.43. $\overline{Q}_{s-HS}$ did not decrease with flow strength, which contradicts observations made during the experiments and $\overline{Q}_{si-d}$ estimates. This suggests that there may be more measurement-induced error in Q_{si-HS} than there is variation between the two methods used to determine Q_{si}. The ratio $\overline{Q}_{se-HS} / \overline{Q}_{se-d}$ ranged between 0.62 and 1.14. At three of the flow strengths, $\overline{Q}_{se-HS}$ and $\overline{Q}_{se-d}$ are within 15 % of each other. Because there are more samples during the equilibrium period of these flows, the effect of measurement error is diminished.

Figure 2.28 indicates the agreement between Q_{s-d} and Q_{s-ss} is also variable. Transport estimates are clustered about the 1:1 line and most Q_{s-ss} estimates are within a factor of 0.5 - 2× the Q_{s-d} estimate. Agreement is improved somewhat if only $\overline{Q}_{s-d}$ and $\overline{Q}_{s-ss}$ are compared. At flow strengths A, B and C, the ratio $\overline{Q}_{se-ss} / \overline{Q}_{se-d}$ ranged between 0.97 and 1.09 and the error bounds overlap, indicating that sediment movement over the dune back is essentially equivalent to the volume moved in the dune form.

At flow strengths D, E and E_A the ratio $\overline{Q}_{se-ss} / \overline{Q}_{se-d}$ is 1.80, 2.0 and 0.74 respectively. Results from flow strength E can be dismissed as the transport estimates are based on only 2 of 17 dunes and

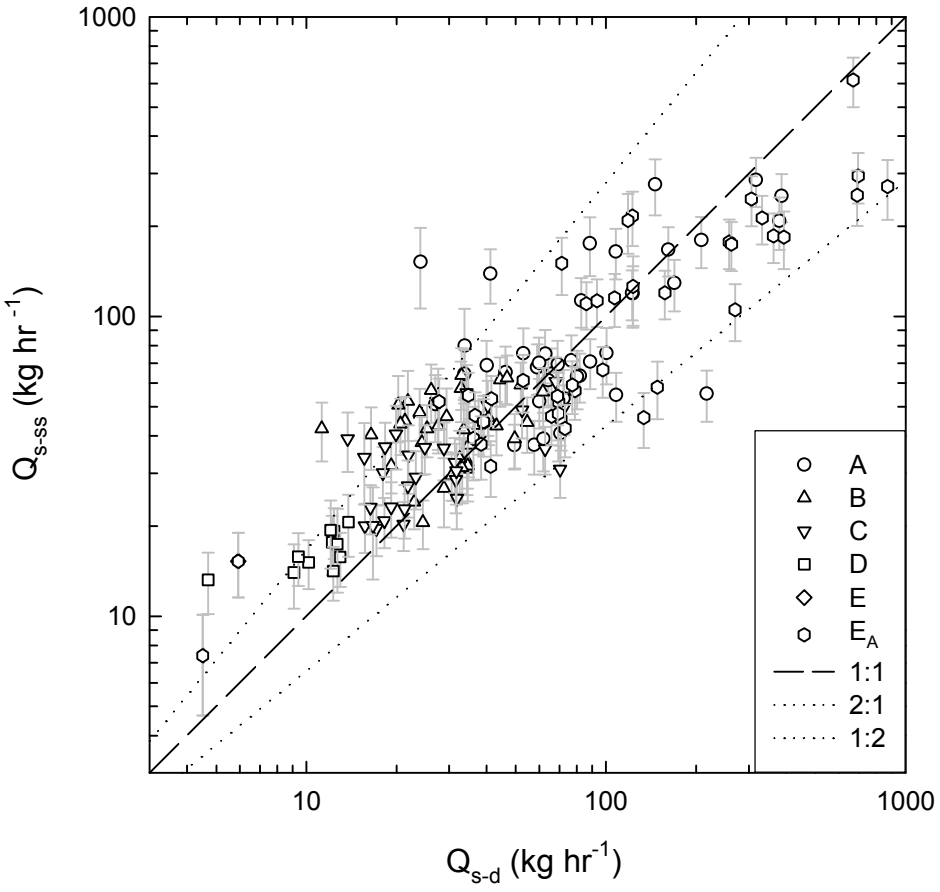

Figure 2.28: Agreement between the dune related transport rate, Q_{s-d}, and the sand sheet related transport rate, Q_{s-ss}. Sand sheet error bars are the standard error of the estimate.

only one of those points exceeds the range of Q_{se-d}. Similarly, the run at flow strength E_A can be dismissed as it did not reach equilibrium and so Q_{se} may not be a relevant statistic for comparison. It is interesting that the ratio Q_{s-ss}/Q_{s-d} calculated for individual dunes averages to ~1.0 for all dunes with sand sheets at flow strength E_A. Thus, there appeared to be some dunes with larger transport rates that did not have superimposed sand sheets.

However, for Run 29 (flow D), Q_{s-ss} is clearly much larger than Q_{s-d}. The ratio Q_{s-ss}/Q_{s-d} calculated for individual dunes averages to ~1.7 for all dunes with sand sheets. The poor agreement is confirmed in Figure 2.26, indicating there is more sediment moving over the dune back as sand sheets than is moving in the dune itself. Error bounds for Q_{s-ss} and Q_{s-d} do not overlap. More sediment appears to be recruited from the dune back than is moving over the dune crest. Thus, the bedforms where sheets were observed may have been growing. However, it is probable that the relation between R and R_{min}, derived from the run at flow strength B, is not applicable at the lower flow strengths and that extrapolation of this relation to flows D and E was too extreme.

2.7 Summary

A series of experiments was conducted in which a narrowly graded 0.5 mm sand bed was subjected to a 0.155 m deep, non-varying mean flow ranging from 0.30 to 0.55 m s^{-1} in a 1 m wide flume. Bed waveform morphology was monitored using overhead video and echo-sounders. Three basic waveforms were found in the channel, including long sediment pulses, dunes and sand sheets. Insufficient data are available to examine the long sediment pulses so investigation is limited to the two latter sandwave features.

The data presented here are inappropriate to examine initial bedform properties. Equilibrium height and length increase with flow strength. Growth in dune height and length are found to be approximately exponential through time. The dunes that are present during the equilibrium stage are morphologically similar to the initial forms present. Aspect ratios suggest that most of the forms

present are dunes according to the classification scheme of *Allen* [1968]. There is no obvious transition from small ripples at the beginning of the runs to dunes when the sandwaves become larger.

Several different crest and stoss morphologies are found for the dunes. In the most common crest morphology the slipface is decoupled from the bedform's minimum and maximum bed height. The second most common crest morphology has the dune trough co-existent with the slipface base. The most common types of stoss slope morphologies exhibit either a smooth, non-linear transition to the upstream dune trough or a pair of slope breaks defining a pan that holds the separation cell. These slope breaks also define a bedform crown where sand sheets develop.

Over equilibrium dunes, ~3 - 4 sand sheets were observed per 100 s. The sheets, many lacking slipfaces, form at ~0.5 m from the dune slipface, downstream of the reattachment point on the dune stoss slope. This distance is invariant with dune size, suggesting there is a necessary 'fetch' length needed for the sheets to begin to grow. The sheets have heights that are typically 0.1× the height of the dune upon which they are superimposed, migrate at 8-10× the dune rate, and have lengths that are nearly constant over the full range of dune lengths and flow conditions. Aspect ratios are generally < 0.1 with a mode of ~0.025, classifying them as low relief or incipient dunes.

Sediment transport rates measured with a Helley-Smith sampler and estimated from the morphology of both the dunes and the sand sheets are similar in magnitude. The measurement error associated with the Helley-Smith samples is too large to make a meaningful comparison between the samples and the morphological transport estimates. For the three runs with the largest flow strength, the transport rate estimated from the sand sheet morphology was approximately equal to the estimates from the dune morphology. This suggests that the material moving over the stoss slope of these dunes is equivalent to the material moved in the dune form. This counters arguments that only a portion of the dune form contributes to the transport rate. At one of the lower flow strengths there appears to be more material moving over the dune than is moved in the dune itself. This presents an interesting problem that needs further attention.

Chapter 3-The Initiation of Bedforms on a Flat Sand Bed

3.1 Introduction

The purpose of this chapter is to discuss the initiation of bedforms on an artificially flattened sand bed. The initial flow conditions over the flat bed, prior to bedform development, are investigated in order to establish that the flow agrees with standard models of flow and turbulence over hydraulically rough flat beds. This establishes that the bedforms are not developed by some aberrant flow condition. Bedform development is examined with and without artificially generated bed defects (small indentations or mounds of sediment). For both cases, a series of micro-scale grain movements and bed deformations are documented that lead to incipient dune crestlines. An attempt is made to link these bed deformations to some observable flow condition. A simple Kelvin-Helmholtz model of water-sand interface instability is introduced to explain the initiation and organisation of two-dimensional dunes. The model is used to predict incipient dune lengths.

3.2 Experimental Procedure

The experiments discussed in this chapter used the same apparatus, experimental design, and flow conditions as in Chapter 2. The runs were conducted at the same pump frequencies, f_p = 23.5, 22.5, 21.5, 19.0 and 17.0 Hz. The bulk flow hydraulics of each run can be found in Table 2.1. Several runs were conducted at each f_p to accomplish the goals in this chapter, so the same labels are assigned to each flow strength to streamline the text. Flow strength A refers all runs conducted at f_p = 23.5 Hz, B all runs at f_p = 22.5 Hz, C all runs at f_p = 21.5 Hz, D all runs at f_p = 19.0 Hz and E all runs at f_p = 17.0 Hz. Bedforms were initiated instantaneously during Runs A, B and C and by defect propagation processes during at flows D and E.

3.2.1 Video

Runs were video taped using the set up described in Chapter 2 with the Super-VHS video camera mounted above the flume and centred at ~10.30 m from the head box. Recall that the side lighting produced a glare-free image with light shadows that highlighted millimetre-scale changes in the bed structure. The video records were sub-sampled from the tapes using a frame grabber at a 10 s interval which produced series of images similar to those in Figure 2.12 which were subjected to further analysis. This video was taken during Runs 53 (A), 54 (B), 55 (E), 56 (E), 57 (C), 58 (D) and 59 (D).

In addition to these videotaped runs, another series of runs was conducted and recorded to determine grain paths and velocities on the bed. The sand surface was seeded with black glass beads (D =0.5 mm). A Plexiglas plate 25.4 mm (1 inch) thick, ~0.3 m wide and ~0.5 m long was suspended at the water surface with a bevelled edge that faced upstream. The plate surface was illuminated using two 500 W and four 100 W flood lamps such that light penetrated the glass and the view from above was free of distortions caused by the water surface. The overhead video camera was focused on a portion of the bed ~0.2 $\times$ 0.2 m. Video of the particle movements was acquired for each of the flow strengths as the bed developed from a flat condition. The video was then converted to ~30 s long image sequences with a frequency of 30 Hz. This video was taken during Runs 31 (A), 32 (B) and 34 (C).

Subsequent data analysis revealed that measuring grain paths over time periods greater than a few tenths of a second was nearly impossible due to the extreme variability in the grain movements and the video resolution. Particles moved along the bed spasmodically, sometimes moving though the entire field of view and other times moving only a few millimetres. As particles moved they were frequently buried, while new particles were constantly uncovered and activated. This variability could be quantified, but particles seemed to be extinguished as they moved through the video line boundaries. Video images are typically composed of several hundred horizontal lines that blend together to produce a continuous field when examined by the human eye. However, the lines have boundaries and particles were small enough that they could follow the space between two video lines.

In such cases, a particle was hidden during part of its transport. Therefore it became impossible to determine which particles were coming to rest or being activated by the transport process and which particles were simply obscured by the spaces between video image lines. This occurred despite the fact that the particles were roughly 1.5 - 2× larger than the width of the video lines. It would benefit future investigation to use digital images that are not composed of horizontal lines or to substantially increase the ratio of the grain size to the video line width or pixel size (i.e. increase to 10×).

In spite of this problem, the video could be used to quantify the movement of a limited number of the black particles over short time periods. An image viewer that could display the images grabbed from the video in rapid succession (100 Hz) was used to view 0.167 - 0.667 s sequences immediately after widespread particle transport had begun. Particle movements were then marked directly from the computer monitor onto a sheet of acetate. The acetate was then calibrated and digitised in a GIS program to determine the particle movement distances over the elapsed sequence time, allowing the calculation of particle velocity, U_p. Between 45 and 90 grain movements were identified at each flow strength to estimate grain velocity. In order to be recorded as a movement, a particle could not rest for any period of time during the measurement period and was required to be moving at the beginning and end of the sequence. The measurement period was varied between 5 and 20 s so as not to bias the mean towards longer movements. Only particles that did not become significantly obscured between video line spaces were accepted. It is important to note that the velocity measurements are for the top of the transport layer only and U_p must logically decrease to zero at some depth.

3.2.2 Echo-sounder Mapping

In addition to the video, the bed was mapped using the two acoustic echo-sounders used in the experiments discussed in Chapter 2. The sensors were mounted with a cross-stream separation of 0.45 m on the motion control system and the bed height was mapped. The motion control system is

composed of an instrument cart that rode on iron roundways installed on each side wall that were levelled to within ± 0.5 mm along the flume. A computer-controlled stepper motor, gear reducer and a sprocket riding on a motorcycle chain on the flume side wall drove the cart. Also installed on the cart was a ball-screw axis, driven by stepper-motors, that allowed instruments to be positioned in the cross-stream stream direction.

At the start of mapping, the sensors were placed at 0.05 and 0.50 m from the side wall, at the upstream edge of the working section. The motion control system was programmed so that the sensors could be moved: (1) across the flume 0.45 m, (2) downstream 5 mm, (3) across the flume in the opposite direction and (4) downstream 5 mm, all at 10 m s^{-1}. This motion was then looped up to 600 times. On either side of the flume, 25.4 mm (1 in.) wide, 3.66 m (12 ft.) long aluminium stock, extending 0.05 m from the side walls, was hung 5 mm below the sensor height. Each time the sensor reached the sidewalls, the sensor recorded zeros indicating the end of a cross-stream line of data. The echo-sounders were sampled at 25 Hz so that each sensor would collect ~90 data points on each traverse across the flume. The collected motion produced a grid of 180 × 600 data points that took ~28 - 29 minutes to complete. These could then be plotted as contour maps to give detailed snapshots of the bed topography.

Mapping was done before each run and approximately every hour during flume runs. The flume was not stopped during data acquisition so as not to disrupt the topography development. Subsequent analysis of the grids indicated that at the greatest three flow strengths (A, B and C) the rates of bedform development and migration were too fast to provide any useful information (i.e. the distortion of the bedforms was too great). In contrast, at the lowest two flow strengths, development was sufficiently slow so that distortion was quite minimal and the full developmental process could be monitored.

3.2.3 Laser data

Velocity profiles were obtained for all five flow stages (described above) over an initially flat bed using a 300 mW Dantec laser-Doppler anemometer (LDA) that measures two-component flow velocities (u and w) and has a reported precision of ± 0.1 mm s^{-1}, a focal length of 750 mm and a sampling volume of 20 × 0.2 mm [*Dantec Measurement Technology*, 1995]. The laser acquired data at 20 Hz near the bed, and up to 1 kHz in the upper part of the profiles when velocity measurements were collected coincidentally. Much larger sampling frequencies were obtained when velocity components were measured independently of each other. Measurements with a sampling frequency less than 20 Hz were discarded. The LDA was operated in backscatter mode with burst type detectors so the LDA collected velocity samples whenever there were particles available in the sampling volume. Data were not collected at prescribed time intervals and so the data are irregularly spaced in time.

The LDA probe head, connected to the laser via a fibre optic cable, was mounted on a 3-axis motion control system that consisted of three ball-axes, driven by stepper-motors, allowing the probe head to be adjusted quickly and with great accuracy (fractions of a millimetre). The motion control system was set so that the measuring volume was normal to the flume wall and offset 4 degrees from the vertical plane. This allowed the measuring volume to be placed in the centre of the flume, 5 mm above the bed, while still measuring velocity data on both components.

Rather short 60 s samples were collected at up to 15 points in the vertical plane for each profile. Previous research over dunes in this flume by *Venditti and Bennett* [2000] indicated that this sampling period is sufficient to acquire reliable estimates of mean flow and turbulence without bias using an acoustic Doppler velocimeter. Unfortunately, the sampling period could not be extended as the bed developed too quickly. Two sets of profiles were taken to ensure consistent results with the short sampling period. Each set consists of a profile at each flow strength. In profile set 2, an additional

velocity profile was taken at the largest flow strength (f_p =23.5) as the bed developed rapidly. Profiles were also acquired over artificially made bed defects, mounds or pits in the flat bed, at the two lowest flow strengths. At the beginning of the second set of profiles, a 600 s velocity sample was taken at 5 mm above the flat bed. These long time series were used to examine integral scales of flow and to provide accurate estimates of the near-bed flow properties.

3.3 Initial Flow Structure

Before discussing the initial bed features developed in the flume experiments, it is necessary to discuss the structure of the flow that was present as these features were initiated. The data set collected here is of further interest as it is somewhat unique. Flow over fixed flat sand beds has been examined extensively, as has flow over fixed and mobile sediment beds with bedforms. However, data of flow over a lower regime labile sand bed without bedforms are less common. It is of interest to determine how the flows used in these experiments compare with conventional models of flow over sediment beds.

3.3.1 Velocity Profile Data Analysis

Analysis of the velocity profiles began with calculation of mean and root-mean-square velocities. Time-averaged at-a-point streamwise, U , and vertical, W , velocities were calculated as

$$U = \frac{1}{n}\sum_{i=1}^{n} u_i \; ; \; W = \frac{1}{n}\sum_{i=1}^{n} w_i \qquad 3.1$$

where u_i and w_i are instantaneous velocities and n is the total number of measurements. The mean streamwise velocity, $\overline{U}$, of a roughly logarithmic velocity profile is U at $0.36d$. Root-mean-square velocities for the streamwise, U_{rms} , and vertical, W_{rms} , components, were calculated from

$$U_{rms} = \left[\frac{1}{n}\sum_{i=1}^{n}(u_i - U)^2\right]^{0.5} \; ; \; W_{rms} = \left[\frac{1}{n}\sum_{i=1}^{n}(w_i - W)^2\right]^{0.5} . \qquad 3.2$$

The Reynolds shear stress, t_{uw}, was determined using

$$\overline{u'w'} = \frac{1}{n}\sum_{i=1}^{n}(u_i - U)(w_i - W) \qquad 3.3$$

$$t_{uw} = -r_w\overline{u'w'} \qquad 3.4$$

where r_w is the fluid density.

The boundary shear stress was estimated for each profile using four methods. The first method uses the depth-slope product as in Chapter 2 (denoted t_S). A second method is based on the von Karman-Prandtl law of the wall. At-a-point U velocity profiles were plotted as a function of height above the bed, z, and least-squares regression was used to determine the roughness height, z_o, as the z intercept. The shear velocity is calculated from

$$\frac{U_z}{u_*} = \frac{1}{k}\ln\frac{z}{z_o} \qquad 3.5$$

where U_z is the mean velocity at z and k is the von Karman constant which is assumed to be 0.4. The boundary shear stress based on the law of the wall (denoted $t_{0.2}$) is determined from

$$t = r_w u_*^2 . \qquad 3.6$$

The law of the wall is strictly applicable only to the log-layer where the increase in U with z is logarithmic. In fully turbulent open channel flow, this region extends from a few mm above the bed to $0.2d$ (d is flow depth) [*Nezu and Nakagawa*, 1993]. As such, equation 3.5 is applied to only the lower 20 % of each profile.

A third method of determining boundary shear stress involves plotting t_{uw} as a function of z/d. For uniform flows

$$t_{uw} = t_R(1 - z/d) . \qquad 3.7$$

An estimate of t_R can be obtained by using a least-squares regression projected to z/d =0 [*see Nezu and Rodi*, 1986; and *Lyn*, 1991]. A final method is to use a measurement of t_{uw} at just above the

boundary as the boundary shear stress (denoted t_B) [cf. *Nelson et al.*, 1995]. In these experiments, the 600 s u and w velocity measurement was used to determine t_B using Equation 3.4. Estimates of u_* and z_o are obtained through the final two methods using Equations 3.5 and 3.6 respectively.

3.3.2 Boundary Shear Stress

Figure 3.1 plots the calculated boundary shear stress values as a function of velocity. Neither t_S nor t_B is based on the profiles so there is only one unique value of each. Both $t_{0.2}$ and t_R are based on the profiles so there are two values at each mean velocity (three at flow strength A). Error bars in Figure 3.1b and c are the standard error from the least-squares regression. Examination of Figure 3.1b and c indicate that estimates of the boundary shear stress are dramatically different for different profiles at the same flow strength, although many estimates are within the error bars associated with the estimate from the other profile set. The most serious deviations in $t_{0.2}$ between profile sets occur at flows C and D while for t_R the greatest deviation is at flow strength B. Perhaps a more significant problem than these deviations is that $t_{0.2}$ and t_R do not necessarily increase with flow strength when a profile set (1 or 2) is examined individually.

Examination of velocity profiles showed the mean and root-mean-squared velocities were well represented and little variation was observed between points measured at the same height during different profiles. Velocity covariance ($\propto t_{uw}$) also appeared to be well represented, but significant differences were observed between the measurement points at the same height but different profiles. This affected all subsequent calculations using the Reynolds stress profiles.

There are several reasons why discrepancies in the expected pattern of $t_{0.2}$ and t_R may occur while the averaged values seem to be in accordance, including measurement error associated with the LDA. *Voulgaris and Trowbridge* [1998] have previously noted problems with the LDA resolving turbulence while providing acceptable mean velocities. Another source of error may be the stage of

bed development. All profiles were taken while the bed appeared to be flat however, as will be discussed below, micro-scale bed deformations occur on the flat bed, so it is conceivable that the flow is responding to both grain roughness and form roughness [e.g. *Smith and McLean*, 1977]. Since the micro-scale deformations are growing with time, this may cause some variability in profiles.

Despite these considerations, the most likely cause of the error is the short sampling time used for the profiles. Given this uncertainty, calculated means, root-mean-sqaures, and covariances were averaged for points measured at the same height during different profiles for each flow stage. When averaging profiles, only points with two (or three) data points were averaged. When averaging U and W (U_{rms} and W_{rms}) profiles, data at nearly all the heights above the bed could be included. When averaging t_{uw} values, the sampling frequency of some near bed points was below 20 Hz and there were not two (or three) data points to average. Therefore, the combined t_{uw} profiles are truncated at $\sim 0.2d$.

The combined U and t_{uw} profiles produced more consistent profiles and a consistent increase in $t_{0.2}$ and t_R with flow strength (Figure 3.1b and c). One exception was the t_{uw} profiles taken during flow B that produced a t_R value that was inconsistent with the general pattern even after the averaging. This point, and the t_B value taken during profile set 2, are likely biased by some measurement error and are removed from further consideration.

By examining the increase in t_S, t_B, combined values of $t_{0.2}$ and t_R, it is clear that regardless of which calculation is used, the boundary shear stress increase with $\overline{U}$ is non-linear. The boundary shear is nearly the same at flow strengths D and E while at A-C the increase with $\overline{U}$ is more pronounced. Figure 3.2 displays the boundary shear stress plotted against $t_{0.2}$ for both the individual and combined profiles. Regardless of whether the individual or combined profiles are used, $t_{0.2} \approx t_R \approx t_B$. This is encouraging as it suggests that the flow does not differ significantly from other documented uniform flows. In contrast, $t_S \approx 2.24 t_{0.2}$. It is significant to note that t_S values

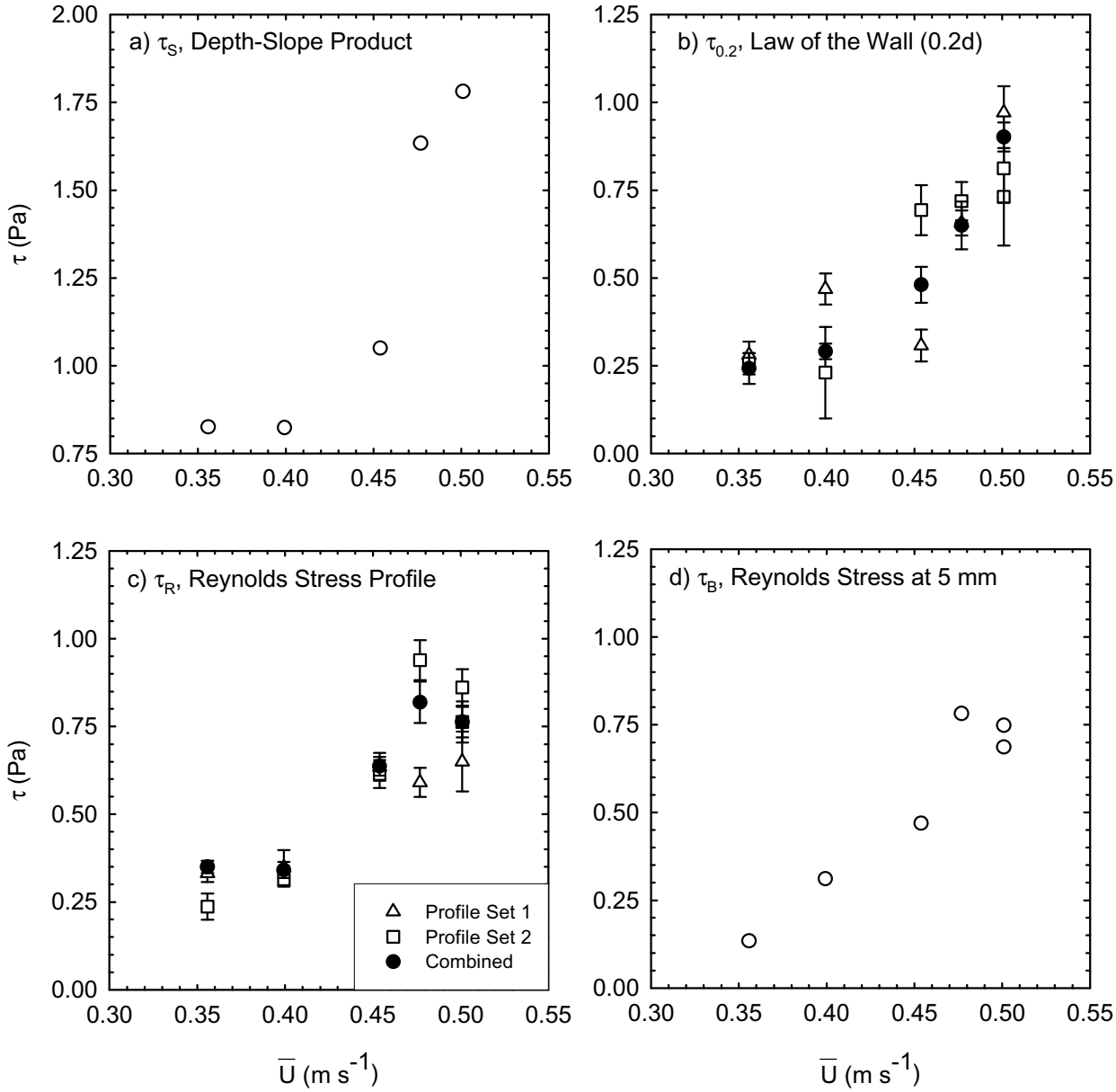

Figure 3.1: Calculated boundary shear stress plotted as a function of velocity, U. Note the different τ scale used for τ_S. Error bars are the standard error of the estimate.

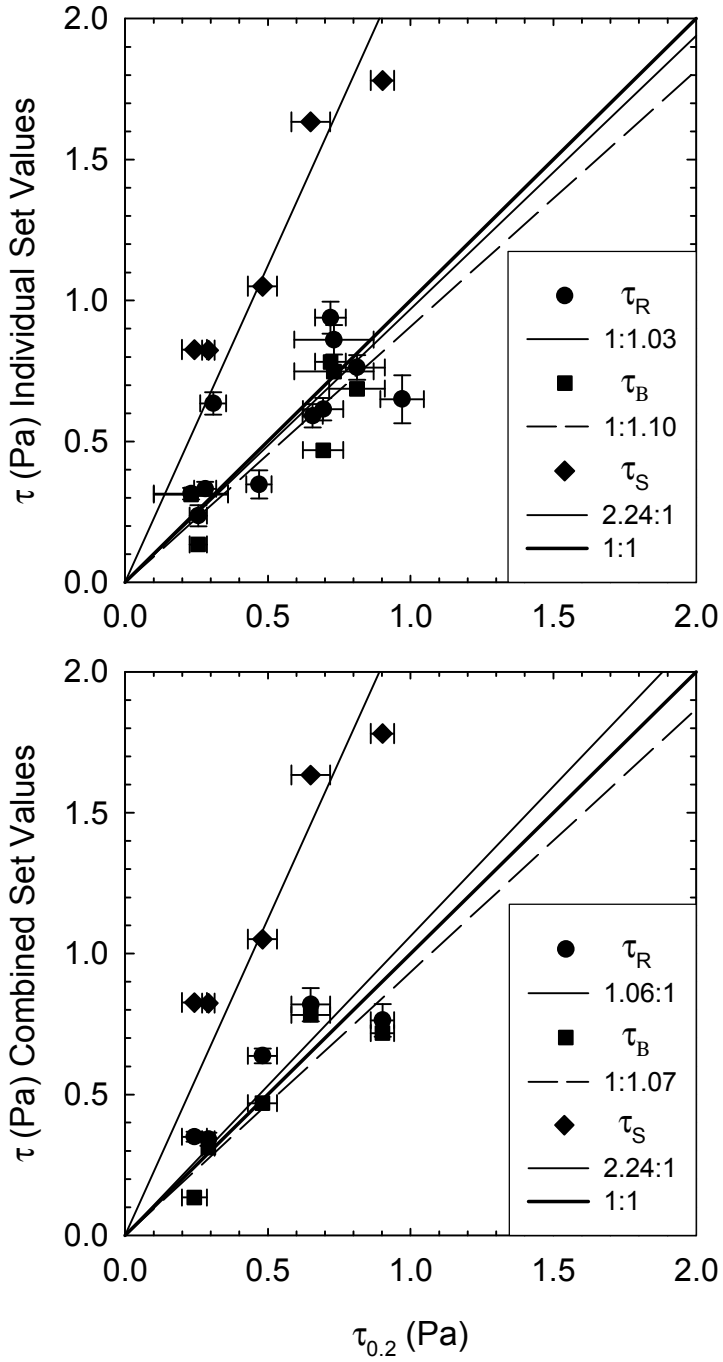

Figure 3.2: Measures of boundary shear stress, τ , plotted against the estimate based on the von Karman-Prandtl law of the wall estimate, $\tau_{0.2}$, for both the individual (top) and combined (bottom) profiles. Boundary shear estimates are based on the Reynolds stress profile, τ_R, the Reynolds stress at 5 mm above the bed, τ_B, and the depth-slope product, τ_S. Error bars are the standard error of the estimate.

represent a different type of boundary shear than $t_{0.2}$ and t_B which represent local shear, linked only to the bed roughness (primarily grain roughness). Shear estimates from the depth-slope product represent the total bed roughness, which may also include roughness induced by the bed topography and the sidewalls. Thus, some difference between the values produced by different methods is expected. However, t_R is based on the total profile and should be similar to t_S. The data do not reveal a strong correspondence between these values.

3.3.3 Mean and Turbulent Flow

Table 3.1 summarises the flow conditions from the experiments based on the combined velocity and stress profiles (including values based on t_S and t_B). The roughness height is variable depending on which method is used to determine the boundary shear stress. However, $z_{o0.2}$ ranged between 0.0064 and 0.0839 mm, an order of magnitude. This translates into equivalent sand roughness values, k_s, determined from

$$k_s = 30.2 z_o, \qquad 3.8$$

[*van Rijn*, 1993] that range between 0.19 and 2.53 mm using the $t_{0.2}$ estimate. *Yalin* [1992] suggests $k_s \approx 2D$ based on experiments with movable yet stationary grains. This relation yields $k_s \approx 1.0$ mm, which is within the range of observed k_s values.

The combined U profiles are presented in the top panels of Figure 3.3. The velocity profiles are linear through the lower $0.2d$, but there is a kink in the upper portion of the profiles at ~$0.5d$. This is not surprising as the profiles are expected to be linear only through the log-layer which is generally accepted to extend from a few mm above the bed to $0.2d$ [*Nezu and Nakagawa*, 1993].

The u and w turbulence intensities, calculated from

$$I_u = \frac{U_{rms}}{u_{*0.2}}, \; I_w = \frac{W_{rms}}{u_{*0.2}} \qquad 3.9$$

Table 3.1: Summary of flow parameters.

Flow Parameter	Flow A	Flow B	Flow C	Flow D	Flow E
f_p, Hz	23.5	22.5	21.5	19.0	17.0
d, m	0.1516	0.1517	0.1533	0.1530	0.1534
$\overline{U}$, m s^{-1}	0.5009	0.4768	0.4538	0.3993	0.3558
$U_{\max}$	0.5929	0.5588	0.5370	0.4556	0.4014
Fr	0.4107	0.3908	0.3700	0.3259	0.2900
Re	75936	72331	69568	61093	54580
Q, m^3 s^{-1}	0.0759	0.0723	0.0696	0.0611	0.0546
$S_{t=0} \times 10^{-4}$	12	11	7	5.5	5.5
Determinations based on depth-slope product					
u_{*S}, m s^{-1}	0.0422	0.0405	0.0324	0.0287	0.0288
t_S, Pa	1.7811	1.6337	1.0506	0.8239	0.8260
ff_S	0.0569	0.0576	0.0409	0.0414	0.0523
Determinations based on Law of the Wall using lower 20% of averaged profile					
$u_{*0.2}$, m s^{-1}	0.0301	0.0255	0.0219	0.0171	0.0156
$t_{0.2}$, Pa	0.9015	0.6498	0.4807	0.2911	0.2423
$z_{o0.2}$, mm	0.0839	0.0438	0.0225	0.0077	0.0064
$k_{s0.2}$, mm	2.5349	1.3235	0.6781	0.2338	0.1926
$ff_{0.2}$	0.0288	0.0229	0.0187	0.0146	0.0153
Determinations based on linear portion of the vertical Reynolds stress profile					
u_{*R}, m s^{-1}	0.0276	n/a	0.0253	0.0185	0.0187
t_R, Pa	0.7625	n/a	0.6369	0.3413	0.3496
z_{oR}, mm	0.0509	n/a	0.0526	0.0158	0.0219
k_{sR}, mm	1.5374	n/a	1.5899	0.4782	0.6629
ff_R	0.0244	n/a	0.0248	0.0172	0.0221
Determinations based on Reynolds stress measured at 5mm above bed (10 min average)					
u_{*B}, m s^{-1}	0.0268	0.0280	0.0217	0.0177	0.0116
t_B, Pa	0.7176	0.7822	0.4691	0.3114	0.1346
z_{oB}, mm	0.0433	0.0744	0.0221	0.0117	0.0005
k_{sB}, mm	1.3066	2.2477	0.6682	0.3534	0.0157
ff_B	0.0229	0.0276	0.0183	0.0157	0.0085

$Fr = \overline{U}/(gd)^{0.5}$, $Re = d\overline{U}/n$, $k_s = 30.2 z_o$, $ff = 8t / r\overline{U}^2$, $u_* = (t / r_w)^{0.5}$, z_{oR} or $z_{oB} = e^{(\ln z - U_z k / u_*)}$

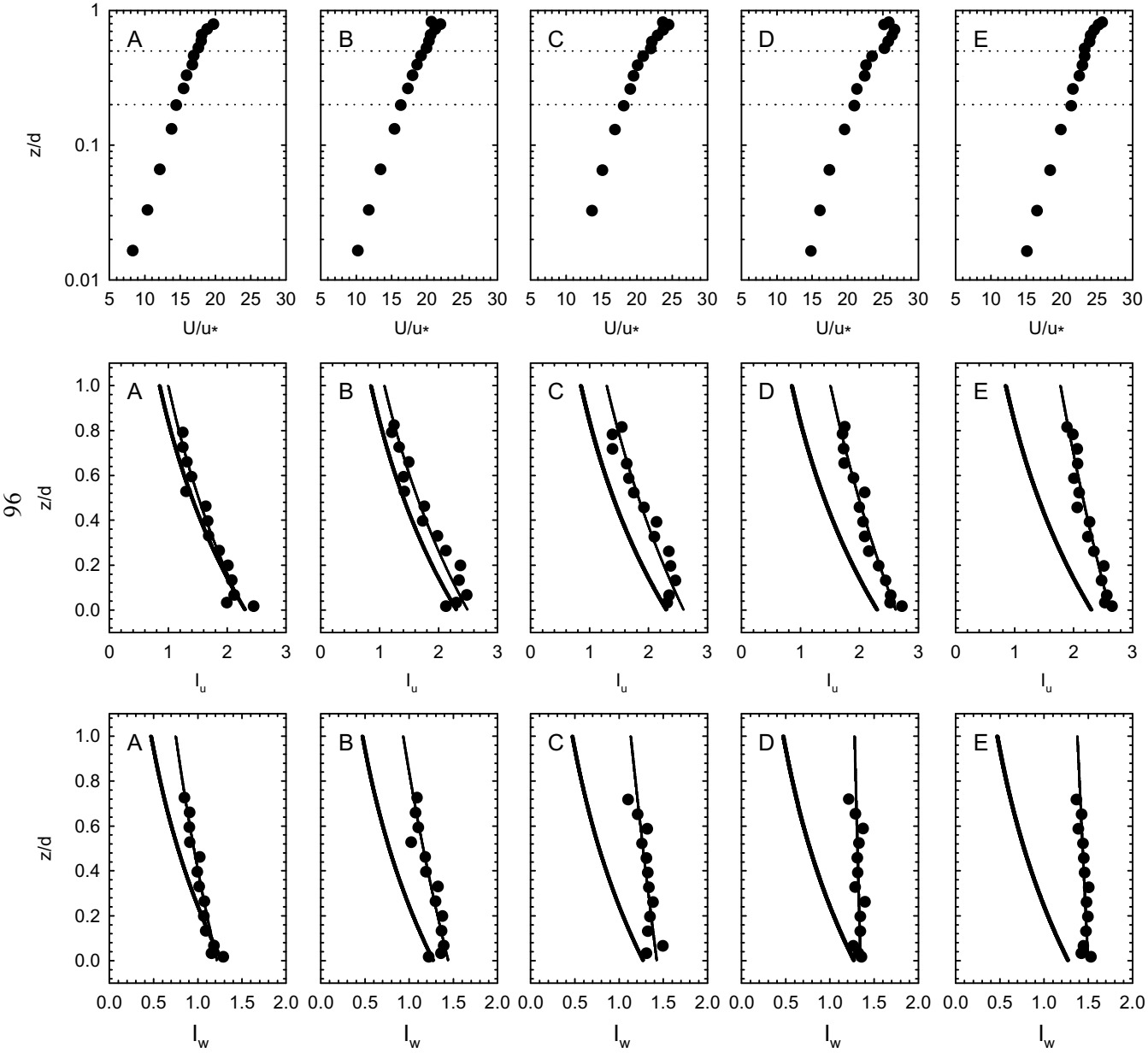

Figure 3.3: Profiles of mean streamwise velocity, U, streamwise turbulence intensity, I_u, and vertical turbulence intensity, I_w. Letters A-E refer to the flow strengths (see Table 5.1). U is normalised by shear velocity, u_*, calculated using the von Karman-Prandtl law of the wall. Height above the bed, z, is normalised by the flow depth, d. Thick lines are *Nezu and Nakagawa's* [1993] universal turbulence intensity functions (Equations 5.10 and 5.11) plotted using their coefficients. Thin lines are *Nezu and Nakagawa's* [1993] functions plotted using coefficients determined from least squares regressions that are provided in Table 3.2.

are plotted in Figure 3.3. Also plotted are the semi-theoretical, universal functions for turbulent intensity provided by *Nezu and Nakagawa* [1993], calculated as

$$I_u = D_u \exp(-C_{ku}\, z/d) \qquad 3.10$$

$$I_w = D_w \exp(-C_{kw}\, z/d) \qquad 3.11$$

where D_u, C_{ku}, D_w, and C_{kw} are empirical constants. These have been previously determined experimentally for laboratory open channel flows as 2.30, 1.0, 1.27, and 1.0 respectively [*Nezu and Nakagawa*, 1993]. These values are not universal constants but depend on bed roughness and, potentially, the presence of bedforms. For example, *Sukhodolov et al.* [1998] calculated a new set of constants for flow over a bedform field that were somewhat different from those provided above. In consideration of this, a new set of constants was calculated using least-squares regression for the flows in these experiments (Table 3.2). Values of D_u, D_w, and C_{ku} are similar to those calculated by *Nezu and Nakagawa* [1993], but C_{kw} values are significantly different. The distribution of I_w with z/d is nearly linear for the lower flow strengths and fitting an exponentially decreasing curve seems unwarranted.

The combined t_{uw} profiles appear in the top panels of Figure 3.4 and show a roughly linear decrease with z, as is expected for uniform flow. Also plotted in Figure 3.4 is the boundary layer correlation coefficient, R_{uw}, calculated as

$$R_{uw} = \frac{-\overline{u'w'}}{U_{rms} \cdot W_{rms}}. \qquad 3.12$$

The boundary layer correlation coefficient ($-1 \leq R_{uw} \leq 1$) is a normalised covariance that expresses the degree of linear correlation between u and w velocity fluctuations. As such, R_{uw} is a 'local' statistic that provides insight into the presence or absence of flow structure at a specific location. In flow over a flat bed, there is little streamwise variation in R_{uw} and values of ~0.5 are typical of the near-bed regions, while decreased values of 0.0 - 0.3 are found in the outer flow region [*Nezu and*

Table 3.2: Values of parameters in Equations 3.10 and 3.11 evaluated from measured profiles.

Flow	D_u	C_{ku}	D_w	C_{kw}	$C_{ku} + C_{kw}$
A	2.28	0.83	1.21	0.49	1.32
B	2.49	0.84	1.44	0.44	1.28
C	2.59	0.70	1.42	0.23	0.93
D	2.61	0.55	1.34	0.05	0.60
E	2.61	0.39	1.49	0.08	0.47
Mean	2.52	0.66	1.38	0.26	0.92

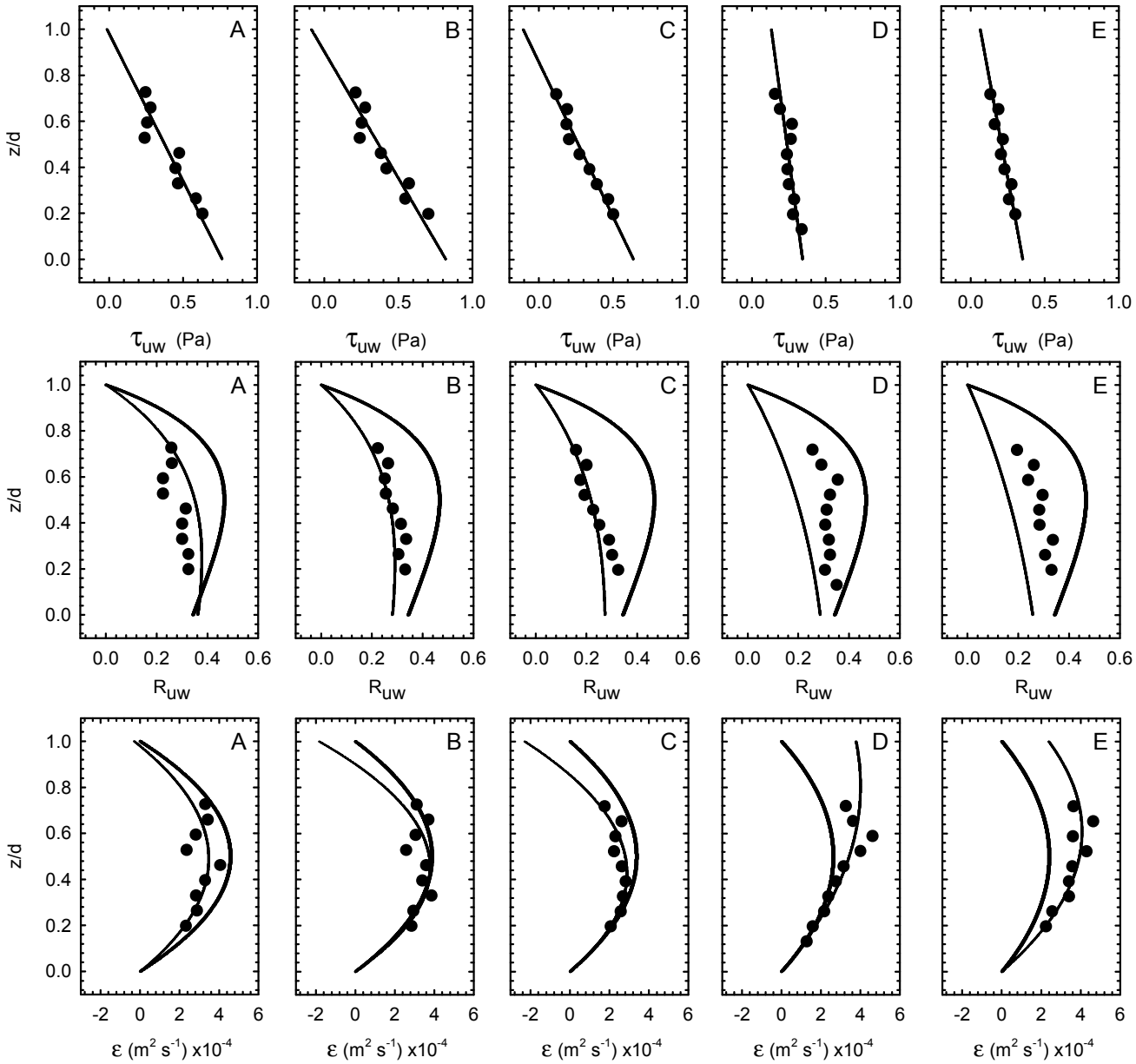

Figure 3.4: Profiles of Reynolds shear stress, τ_{uw}, boundary layer correlation coefficient, R_{uw}, and eddy viscosity, ε. Letters A-E refer to the flow strengths (see Table 5.1). Height above the bed, z, is normalised by the flow depth, d. Thick lines are functions for the vertical variation in R_{uw} (Equation 5.13) and ε (Equation 5.15) using coefficients provided by *Nezu and Nakagawa* [1993] and thin lines are the same functions plotted using the coefficients determined from least squares regressions that are provided in Table 3.2.

Nakagawa, 1993]. *Sukhudolov et al.* [1998] provide an expression based on Equations 3.10 and 3.11 for R_{uw} as a function of z/d,

$$R_{uw} = \frac{1 - z/d}{D_u D_w \exp\left(-(C_{ku} + C_{kw})\, z/d\right)} \qquad 3.13$$

that is plotted in Figure 3.4 using the constants derived by *Nezu and Nakagawa* [1993] and those derived here (Table 3.2). The *Nezu and Nakagawa* [1993] empirical constants provide R_{uw} values that are too large at all z/d. In contrast, the empirical constants derived here provide a decent fit to the data with the exception of the two lowest flow strengths. Here, the predicted R_{uw} values are too small at all z/d. This is likely because the distribution of I_w is not an exponentially decreasing function with height.

A final important characteristic of turbulent flow is the eddy viscosity e, as defined in the mixing-length concept, which is the strength or magnitude of the turbulent eddies within the flow and is defined as

$$e = \frac{-\overline{u'w'}}{dU/dz}. \qquad 3.14$$

If the entire velocity profile is assumed to be logarithmic

$$e = kU_* z\,(1 - z/d) \qquad 3.15$$

[*Nezu and Nakagawa*, 1993]. *Bennett et al.* [1998] note that, in flat-bed flows, the distribution of eddy viscosity is generally parabolic, reaching a maximum near $0.5d$. In order to calculate e, the absolute values of dU/dz needed to be used because in some places the local slope of the velocity profile was negative. Plots of e for each flow strength are given in Figure 3.4. Also plotted are curves that represent the fitted t_{uw} curve divided by the fitted U profile curve and equation 3.15. As would be expected, the fitted curves match the data nearly identically. These parabolic e curves reach a maximum between 0.4 and $0.6d$. However, at flow strength D the e curve reaches a maximum around $0.8d$, suggesting that the zone of maximum fluid diffusion is shifted upwards in

the vertical profile relative to other flows. This seems unlikely given the curves at other flow strengths. It is likely that the curve fits for U and t_{uw} deviate fortuitously to generate this result.

3.3.4 Effect of a Bed Defect

Most authors who have examined the development of sand bedforms have argued that the erosion in the lee of the initial features, the development of the scour pit and, ultimately, the propagation of the initial features is caused by the development of a flow separation cell [c.f. *Raudkivi*, 1966*; Southard and Dingler*, 1971; *Best*, 1992]. A velocity profile taken at flow strength E just downstream of a negative defect as it developed is characteristic of flow separation (Figure 3.5). The defect was ~10 mm deep and had a circumference of 30 mm at flow E. Profiles taken over the defect bed and over a flat bed match closely in the range z/d =0.2 - 1. However, below z/d = 0.2, U is dramatically reduced relative to its flat bed value and U_{rms} is increased, providing the turbulent energy to scour out the bedform lee.

3.3.5 Integral scales

Autocorrelations for the velocity time series were derived to determine integral time and length scales in the near bed region using the 600 s time series collected at 5 mm above the bed. An integral time scale is the time an eddy requires to pass a given point in the flow, and an integral length scale is the characteristic eddy dimension. The Eulerian integral time scale, T_E, is defined as

$$T_E = \int_0^k R(t)\mathrm{d}t \qquad 3.16$$

where $R(t)$ is the autocorrelation function, $\mathrm{d}t$ is the lag distance, and k is the time step at which $R(t)$ is no longer significantly different from zero [*Tennekes and Lumley,* 1972]. With a *Taylor* [1935] approximation, the Eulerian integral length scale, L_E, is defined as

$$L_E = T_E \cdot U \qquad 3.17$$

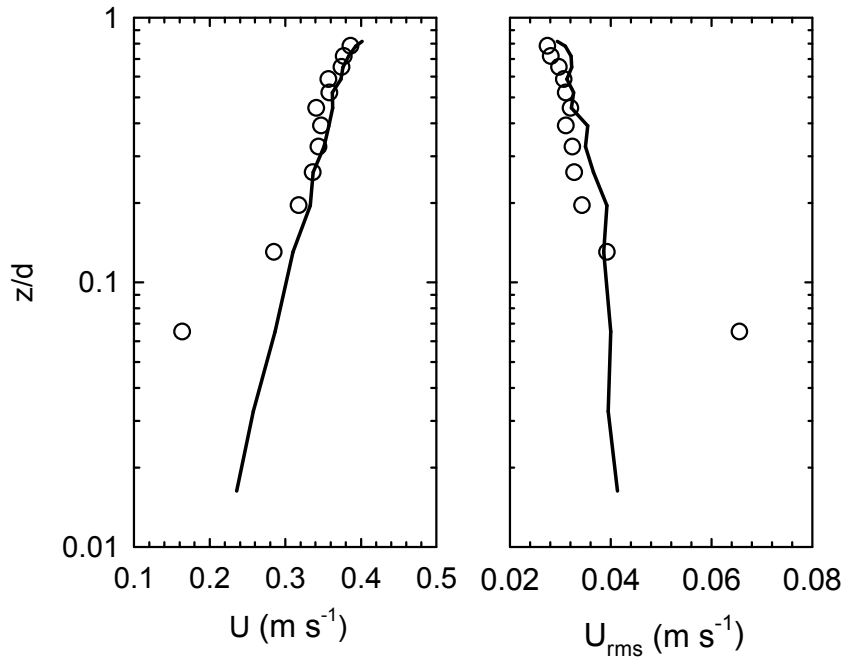

Figure 3.5 Profiles of mean streamwise velocity, U, over a negative defect at Flow E. Height above the bed, z, is normalised by the flow depth, d. Open circles are data measured over the defect and lines are profiles measured at the same flow strength without the defect.

where U is measured at-a-point.

Calculation of autocorrelations required that linear interpolation be used to convert the time series that had irregularly spaced data through time to regularly spaced time series. A sampling frequency of 75 Hz was selected for the new time series as that was the minimum observed file averaged sampling frequency for the 600 s time series. Mean and root-mean-square velocities were nearly identical between the regular and irregular time series. Each 600 s time series was divided into five 120 s sections that were detrended.

Sample autocorrelations for these 120 s time series are shown in Figure 3.6. In general, $R(t)$ approached zero asymptotically. In those cases when $R(t)$ approached and then oscillated about a zero value, k was determined when $R(t) = 0.01$. Table 3.3 presents the average streamwise T_E and L_E. Integral time scales do not vary greatly with flow velocity. Mean T_E varied between 0.225 and 0.271 s while mean L_E varied between 0.0620 and 0.0758 m. Thus, in the near bed region, the average or dominant eddy size is ~0.07 m.

3.5.6 Summary of Flow Conditions

Overall the velocity data suggest that flow over the lower stage plane beds at the beginning of the experiments is in accordance with conventional models of uniform flow over flat beds. With the exception of the depth-slope product calculations, estimates of the boundary shear stress derived from different methods are similar in magnitude and increase in a similar fashion with $\overline{U}$. The roughness heights are consistent with previous observations. The turbulence intensities and R_{uw} can be modelled by the semi-empirical functions provided by *Nezu and Nakagawa* [1993] with the exception of the vertical intensities at the low flow strengths. Finally, with few exceptions, the momentum exchange (t_{uw}) and fluid diffusion (e) conform with current formulations for fully turbulent, uniform, open channel flows over flat beds. Bed defects dramatically reduce the streamwise velocity

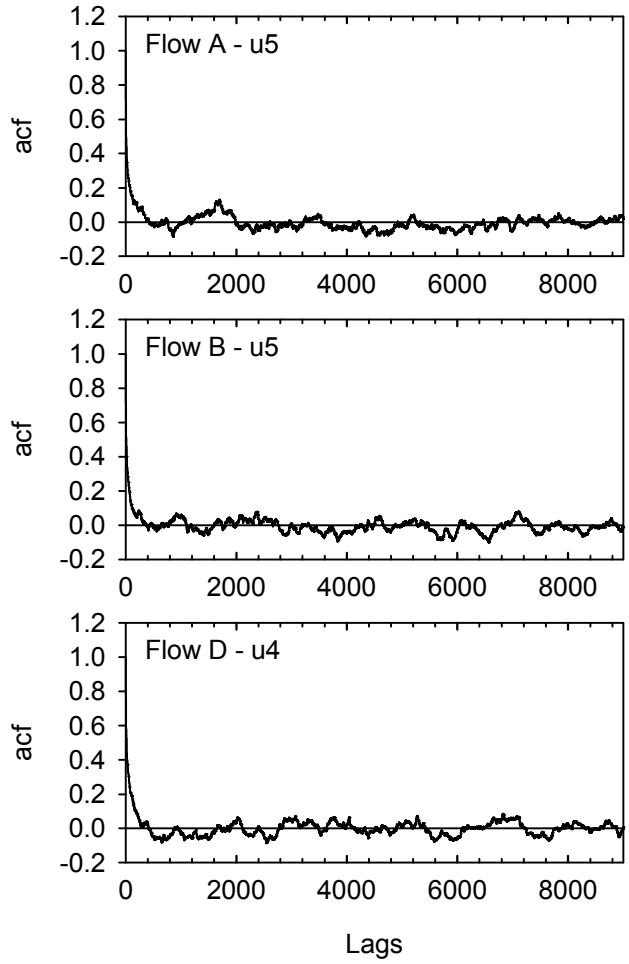

Figure 3.6: Sample autocorrelation functions (acf) for 120 s time series drawn from the 600 s velocity measurements. The displayed acf are for the fourth (u4) or fifth (u5) segments of the 600 s time series at flows A, B, and D.

Table 3.3: Integral time and length scales. Values are mean and standard deviation (brackets) of the five 120 s time series extracted from the 600 s time series.

Flow	$U_{0.5}$ (cm s^{-1})	T_E (s)	L_E (cm)
A-1	28.50 (1.29)	0.25 (0.03)	7.04 (0.78)
A-2	29.90 (1.15)	0.25 (0.07)	7.37 (2.14)
B	28.00 (0.97)	0.27 (0.04)	7.58 (1.09)
C	28.31 (0.91)	0.23 (0.04)	6.36 (1.06)
D	26.72 (0.34)	0.27 (0.06)	7.18 (1.59)
E	24.73 (0.55)	0.25 (0.06)	6.20 (1.44)

near the bed, increasing turbulence and providing the turbulent energy to scour out the bedform lee. Integral length scales are $\sim d/2$ in the near bed region.

3.4 Bedform Initiation modes

Two types of initiation were observed in the experiments: defect initiation and instantaneous initiation. At the two lowest flow strengths used in the experiment (D and E), a flat bed appears to be stable for long periods of time, even though the threshold of motion has clearly been exceeded. Many early researchers [e.g. *Menard*, 1950; *Simons and Richardson*, 1961; *Raudkivi*, 1963] have suggested that any sediment motion on a flat bed will lead to bedform development. However, others [*Liu*, 1957; *Bogardi*, 1959; *Southard and Dingler*, 1971] have reported stable flat beds with sediment transport and no bedform development. The flat beds observed here could not be maintained indefinitely. Sediment carried into the head box was ultimately deposited at the entrance to the channel that developed small mounds of sediment. Eventually, these mounds of sediment developed into bedform trains that propagated through the flume channel. At flow strength E the bedform fields took nearly three hours to migrate from the head box to the area where observations were being made (~9.8 m). At the second lowest flow strength (D) the bedform fields took ~35 - 45 min to migrate the same distance. As the bed was flattened, millimetre scale indentations or mounds of sediment (defects) formed at the sidewalls or occasionally in the channel. At flow strength D, these defects tended to propagate downstream forming bedform fields. Interestingly, not all defects developed into bedforms. If sediment entering the flume did not form mounds, it is possible that the stable flat beds could have existed indefinitely.

In contrast to this type of bedform development, at the greater flow strengths bedforms were observed to develop instantaneously over the entire bed. This type of development occurred within a few tens of seconds, with the initial appearance of the pattern that leads to bedform crestlines appearing after only a few seconds of flow. Hence, this type of bedform development cannot be

linked to defect propagation from the head box or sidewalls. In fact, where defects were observed on the flat bed, they were washed away as the initial bedform pattern was imprinted on the bed.

The threshold between the two types of initiation was just above $t_{0.2} = 0.29$ Pa. A practical threshold for the sand used in these experiments occurs at $t_{0.2} \approx 0.30$ Pa which corresponds to a dimensionless shear stress

$$q = \frac{t_{0.2}}{gD(r_s - r_w)} = 0.0371 \qquad 3.18$$

where D is the grain size (0.5 mm) and r_s is the grain density (2650 kg m^3). Both types of initiation are examined in greater detail below.

3.4.1 Defect Initiation

Following the work of *Southard and Dingler* [1971], who examined ripple propagation behind positive defects (mounds) on flat sand beds, the defect type of bedform development was examined from artificially made defects rather than examining bedform growth from random features on the bed. It seems likely that negative defects (divots) are also of interest in terms of bedform development. Therefore, both positive and negative bed defects were used in the experiments herein. The defects were generated by either sucking sand into or depositing sand from a large dropper until the desired defect size was attained. The dimensions of the defects in the runs discussed below are given in Table 3.4. The defects were cone shaped and ~30 mm in diameter. Negative defects were 8.2 - 9.4 mm below the mean bed elevation, $\bar{z}$ and positive defects were 8.2 - 10.4 mm above $\bar{z}$. *Southard and Dingler* [1971] noted that there was some effect of mound height on the development of ripples in their experiment. However, this conclusion is drawn from a series of runs using defects that varied in height between 2.5 and 50 mm. The effect of the variations in defect size here is probably insignificant.

Table 3.4: Defect Dimensions.

Flow	f_p (Hz)	Run	Defect Circumference (mm)	Defect Depth/Height Relative to $\bar{z}$ (mm)
D	19	22	28	+8.2
		58	30	+10.0
		21	33	-9.4
		59	26	-8.2
E	17	20	30	+8.5
		56	28	+10.4
		19	30	-8.2
		55	27	-8.5

The basic development pattern of the bedform fields can be observed in a series of bed maps displayed in Figure 3.7. Although maps were generated for positive and negative defects at flow strengths D and E, they were qualitatively similar at the coarse scale afforded by the bed mapping. Therefore, only one bedform field development sequence is displayed, that developed from a positive defect at flow strength E. Figure 3.8 displays the bed height along the field centre line. The first bedform map was taken without any flow and simply shows the positive defect (Figure 3.7a). The planar nature of the bed and the defect shape are evident in cross-section (Figure 3.8). Subsequent maps (Figure 3.7b-d) display the defect propagating downstream and developing new crests. The initial defect grew in H and L with each bed map while the rest of the field is composed of bedforms that decrease in H and L with distance downstream (Figure 3.8). As the bedform propagation progressed downstream, the bedform field widened at a regular rate until it reached the sidewalls, forming a triangular shape with the initial defect at its pinnacle (Figure 3.7e). In cross-section the bedforms began to take on a uniform H and L (Figure 3.8). The map in Figure 3.7f shows the triangular field continuing to modify the bed, forming larger bedforms. Bedforms developed at the inlet to the flume travelled into the mapped area and merged with the defect bedform field. This is particularly evident in cross-section where the lead bedforms from the head box are much smaller than those in the defect field. In the next bed map (Figure 3.7g) the two bedform fields have merged, but the defect field is still identifiable as larger bedforms. With subsequent bed mappings, the bedform field continues to merge and there is increasingly little observable effect of the original defect pattern (Figure 3.7g-i and Figure 3.8). The run was extended until equilibrium H and L were reached for this flow strength (Figure 3.7j).

As noted above, mapping of the bed took too much time to examine the development process in any detail and, for this purpose, the video data are examined. The way defects initially develop bedforms differs slightly between positive and negative defects and thus it is useful to describe them separately. Time-lapsed image sequence animations of bedform development from defects can be found in Appendix B. Figure 3.9 shows the development of the first eight bedforms from a negative

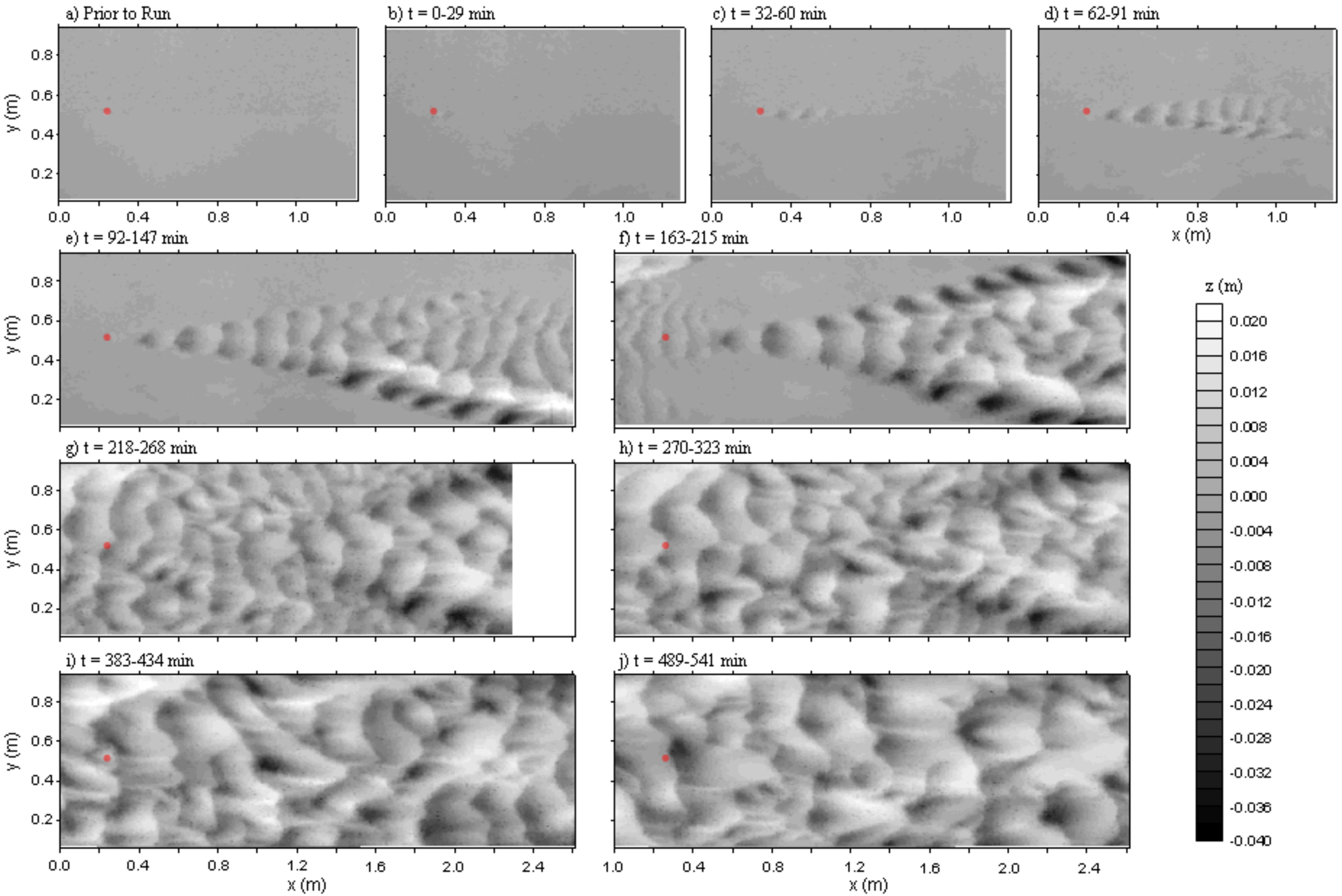

Figure 3.7: Maps of bed height as a bedform field develops from a positive defect at flow E (f_s = 17.0 Hz). The initial defect dimensions are given in Table 3.3. The maps begins at 8.45 m from the head box. The red dot indicates the location of the original defect. Flow is left to right.

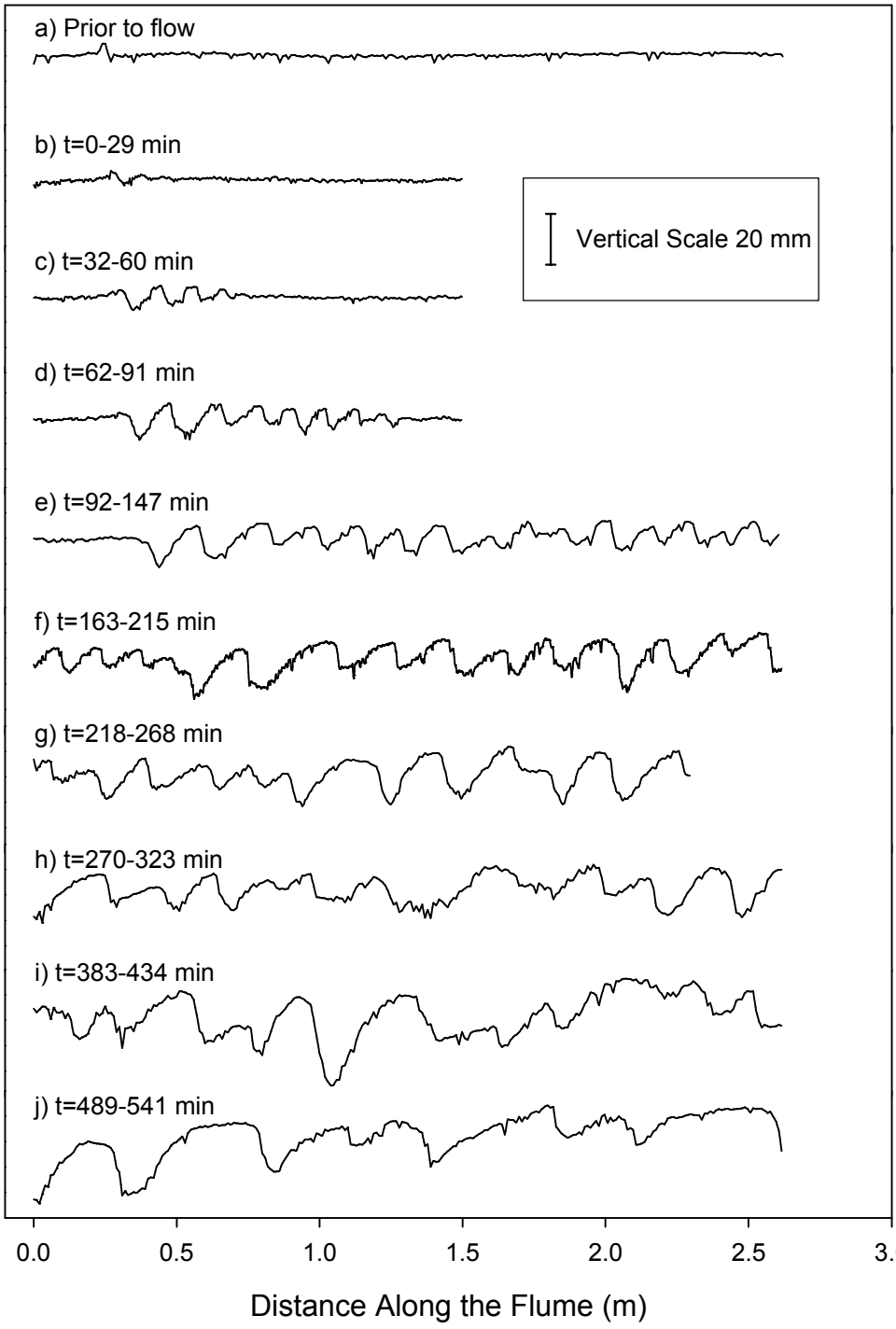

Figure 3.8: Cross-sections drawn along the centre line of Figure 3.7. The map begins at 8.45 m from the head box.

a) t = -60 s

b) t = 80 s

c) t = 250 s

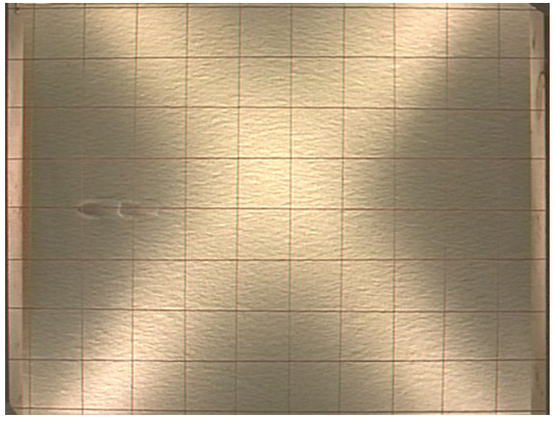

d) t = 600 s

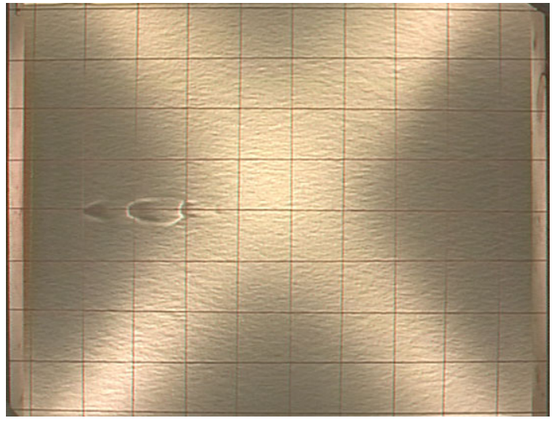

e) t = 1040 s

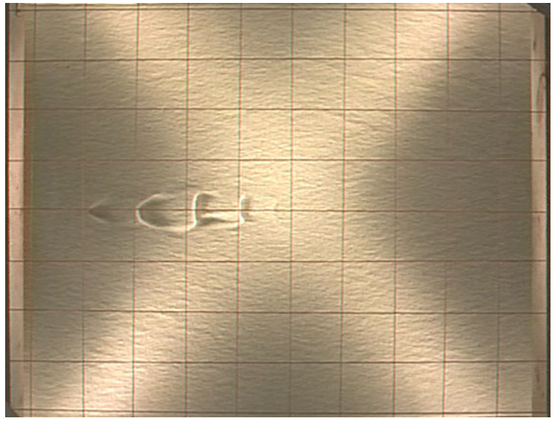

f) t = 1460 s

g) t = 1860 s

h) t = 2320 s

i) t = 2930 s

Figure 3.9: Evolution of bedforms from a negative defect at flow E. Prior to $t = 0$ s the discharge was being ramped up the desired flow strength. Flow is left to right.

bed defect at the lowest flow strength (E). As the flow is increased to the desired flow strength a negative defect undergoes the following deformations:

1a. Initial divot stretching in the downstream direction to develop a shallow scour pit (Figure 3.9b);

2a. Sediment eroded from the scour pit begins to accumulate at the downstream edge;

3a. The edge is squared off transversely as in Figure 3.9b;

4a. Erosion of the stoss slope of the new bedform building the crest in height;

5a. A new shallow scour pit develops at the downstream edge of the new bedform crest;

6a. Steps 2a - 5a are repeated to propagate the feature downstream, forming new bed features (Figure 3.9c-i).

Concurrent with this process, the original defect formed a chevron shape rather than developing into a bedform (Figure 3.9d). New incipient bed features tended to have crests that were transversely narrow for the first few crests (Figure 3.9c-f). The previously developed crests widened transversely, grew in height, and lengthened in the streamwise direction with time. As the upstream crests became wider, so did the subsequent forms. Interestingly, once the field grew to include five new crests, the whole field began to migrate downstream. This initial stability of the bedform field was also observed at the flow strength D, but the migration began after only two new bedforms appeared.

Figure 3.10 displays bedform L along the centre line of the video of the initial defect and the first five new bedforms as a function of time. The initial negative defect grew in length for a period of time and reached quasi-equilibrium. At the higher flow strength (D), L then decreased and the defect eventually disappeared as it was filled in from upstream. Each new bedform had approximately the same L and appeared to grow in a fashion similar to that observed in Chapter 2. Unfortunately, no data on H could be practically derived from the video and the maps were too infrequent to extract detailed information.

The development of a bedform field from a positive defect appears to differ in several respects. Figure 3.11 shows the development of the first bed feature from a positive bed defect at the lowest

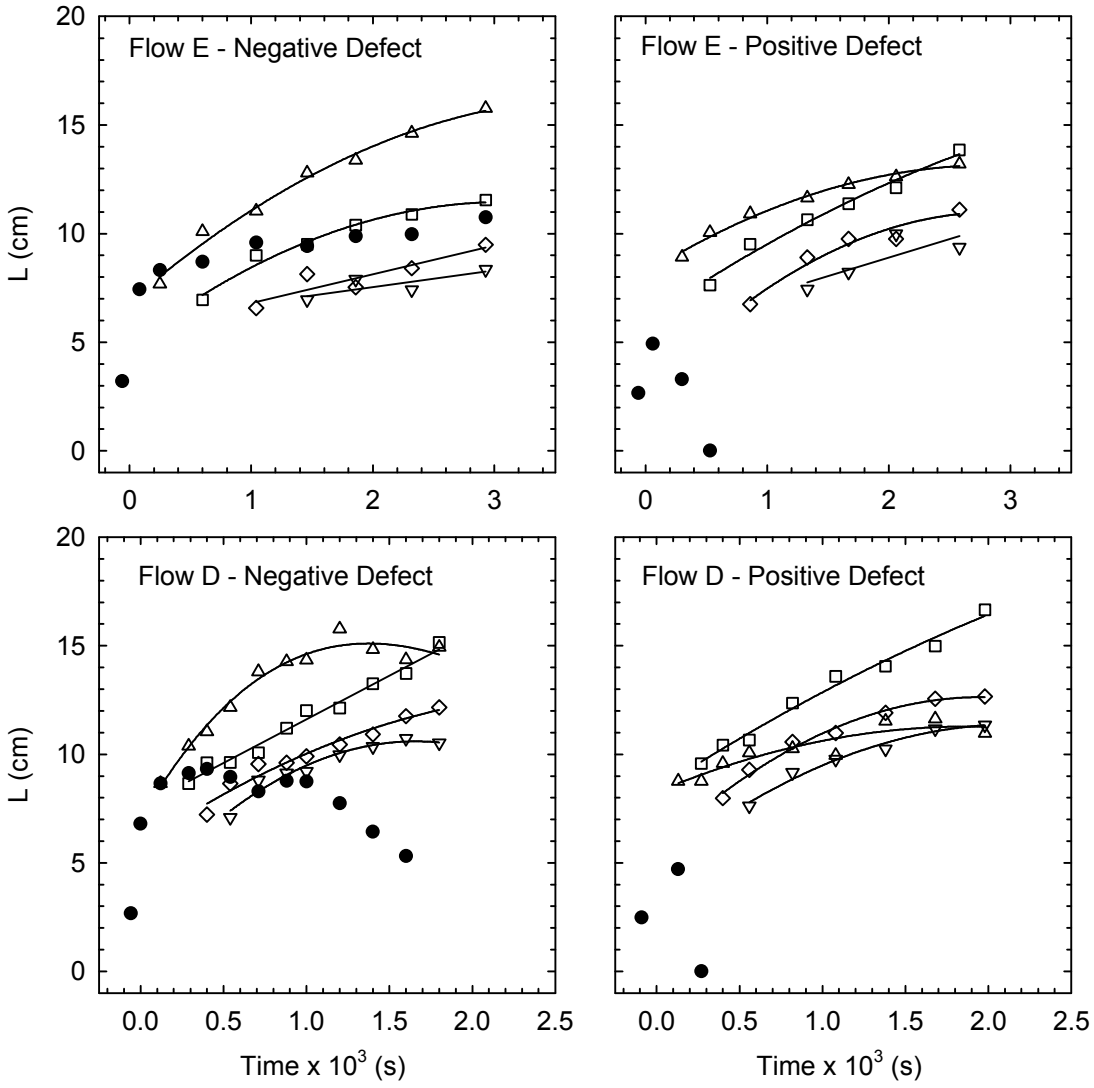

Figure 3.10: Bedform *L* for the first five new bedforms developed from negative and positive defects. The initial defect dimensions are given in Table 5.3. Initial defect length (closed circles); 1st new bedform (upward triangles); 2nd new bedform (squares); 3rd bedform (diamonds); 4th new bedform (downward triangles).

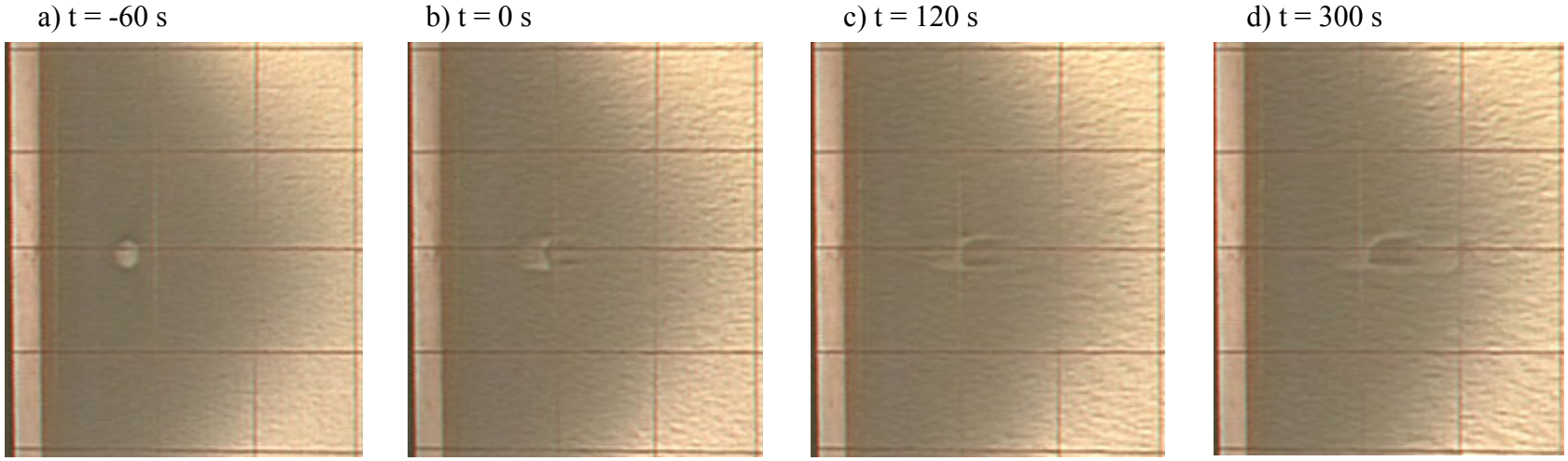

Figure 3.11: Evolution of a positive defect at flow strength E. Prior to *t*= 0 s the discharge was being ramped up the desired flow strength. Flow is left to right.

flow strength (E). In contrast to the process described for a negative defect, as the flow is increased to the desired flow strength, a positive defect undergoes the following deformations:

1b. Erosion of the stoss side of the initial defect, stretching, and streamlining the feature (Figure 3.11b);

2b. Concurrently, the edge is squared off transversely as in Figure 3.11b;

3b. The defect develops arms that stretch downstream forming a barchanoid feature (Figure 3.11c);

4b. Erosion in the lee of the defect forms a scour pit between the barchan arms;

5b. Once the scour pit is developed, steps 2a-5a are repeated to propagate the feature downstream forming new bed features as in Figure 3.11d.

Once a few new bedforms have developed, the initial positive defect is planed out to the mean bed elevation. This left only the scour pit that eventually developed into a chevron shape not dissimilar from the feature in Figure 3.9d-i. This also happens to the first new bedform after the initial positive defect is gone. This observation is interesting as it suggests that the positive defect is important only for generating the first scour pit and that it is the scour pits that are propagated downstream rather than the crests. This makes sense because the sediment that forms the ridges must be picked up from the pits. Thus, scour pits seem to be more stable features than the mounds that are generated at their downstream edge. Initial growth of the bedform field from this first scour pit is similar to growth from the initial negative defect.

Regardless of the defect form, bedform fields developed from negative (Figure 3.12a) and positive (Figure 3.12b) defects at flow strength E have approximately the same form, when the fields are composed of five or more bedforms. The observed processes were qualitatively similar at different flow strengths, but the development was much quicker at the larger flow strength (D). Bedform fields developed from negative (Figure 3.12c) and positive (Figure 3.12d) defects at flow strength D enveloped the field of view in only 20 min compared to 45 min at the lower flow strength. At both flow strengths, the positive field was slightly more developed than the negative field although

a) - defect at flow E (t = 45 min)

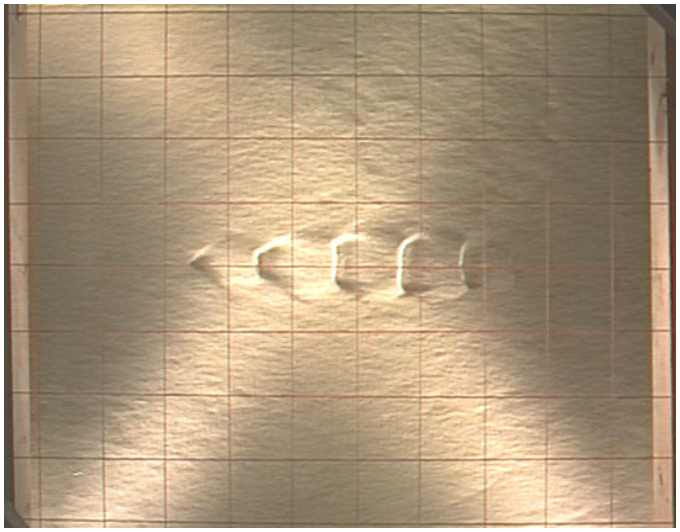

b) + defect at flow E (t = 45 min)

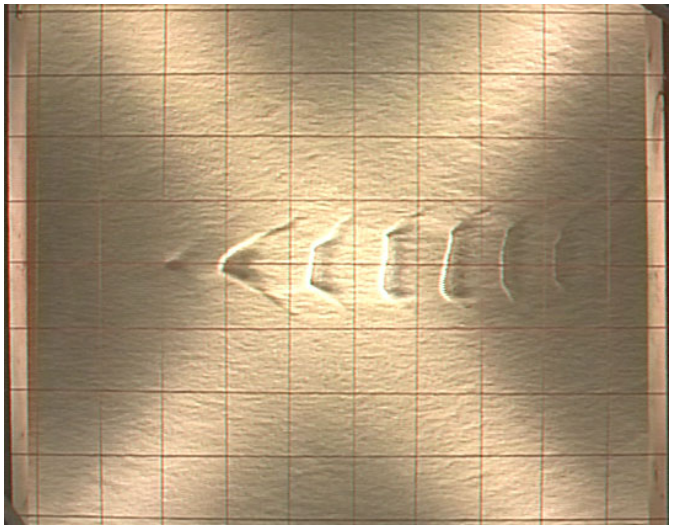

c) - defect at flow D (t = 20 min)

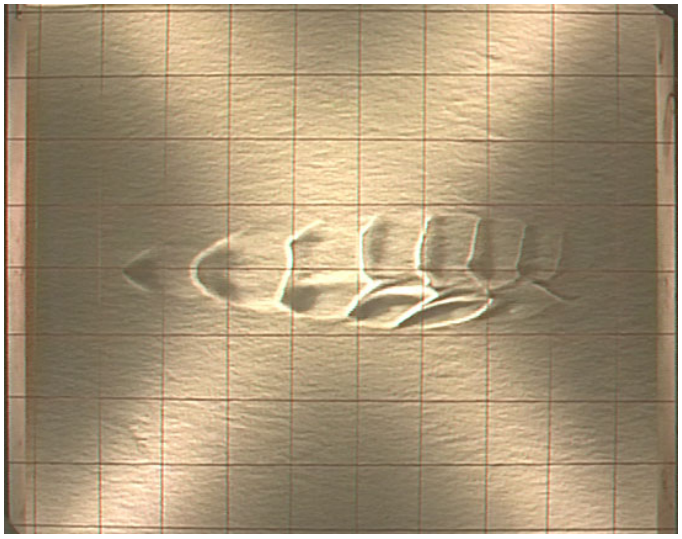

d) + defect at flow D (t = 20 min)

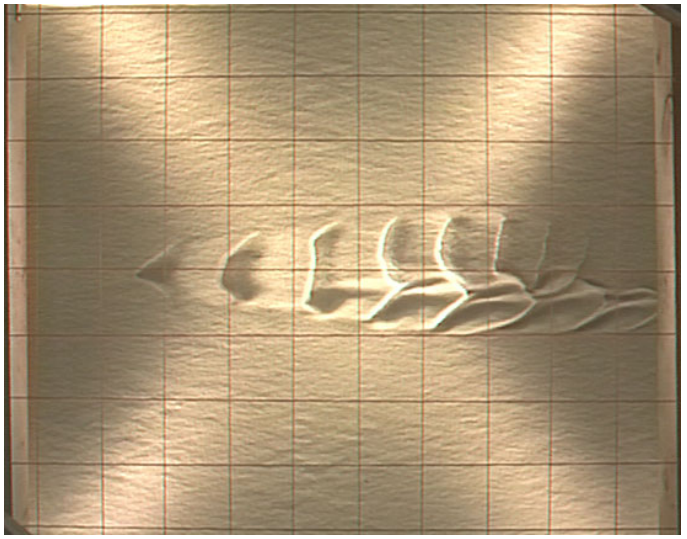

Figure 3.12: Positive and negative defect bedform fields developed at flow strengths D and E. Flow is left to right.

the effect was more pronounced for the larger flow. There was more sediment initially available in the positive case as a negative defect must excavate the sediments from the scour pit initially while the positive defect offers an ample supply of sediment above the mean bed elevation in the defect itself. The positive defect bed began developing with less energy expended and is more efficient in generating the first bedform. The positive beds developed more quickly because of this advantage.

Artificially made defects placed on the bed at the larger flow strengths (A, B and C) failed to persist. The defects were simply washed out and little or no remnant was observed only a few seconds after the flow was started.

3.4.2 Instantaneous Initiation

At flow strengths A, B and C, bedform initiation occurred spontaneously over the entire bed surface. The development of the bed from flat to two-dimensional dunes is documented by a series of video images in Figure 3.13. Initially, the bed was covered with lineated striations, oriented along the flow, with spacing approximately equivalent to the expected streak spacing $l_s = 100n/u_*$ [see review in *Best*, 1992] (Figure 3.14a). These linear streaks did not appear to play any significant role in further development of the bed. Instead, the bed undergoes the following deformations:

1. A cross-hatch pattern is imprinted on the bed (Figure 3.13b);
2. Chevron-shaped scallops develop at the nodes of the cross-hatch (Figure 3.13c);
3. Chevrons begin to migrate and organise into incipient crestlines (Figure 3.13d);
4. Crestlines straighten into two-dimensional features (Figure 3.13e-h);
5. Bedforms grow in height and length.

The time required to move through these developmental stages decreased significantly with increasing flow strength.

The cross-hatch pattern is composed of striations at oblique angles to the flume centre line (Figure 3.14a-c). Angles between the oblique striations and the flume centreline were measured from

a) t = -60 s

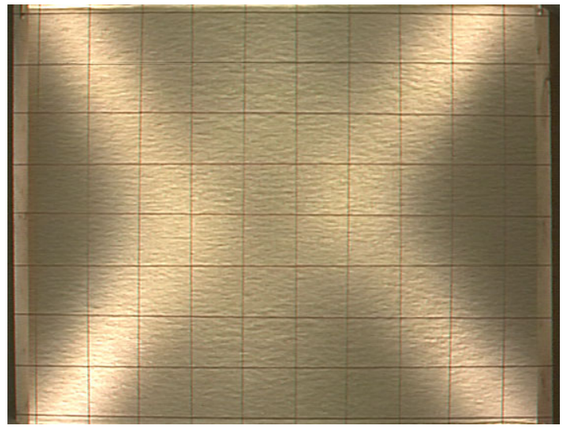

c) t = -20 s

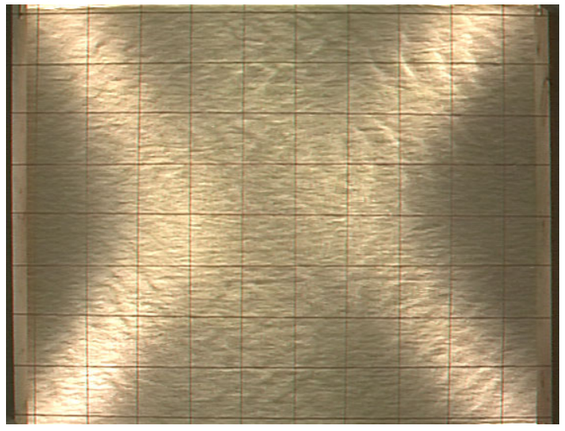

d) t = -10 s

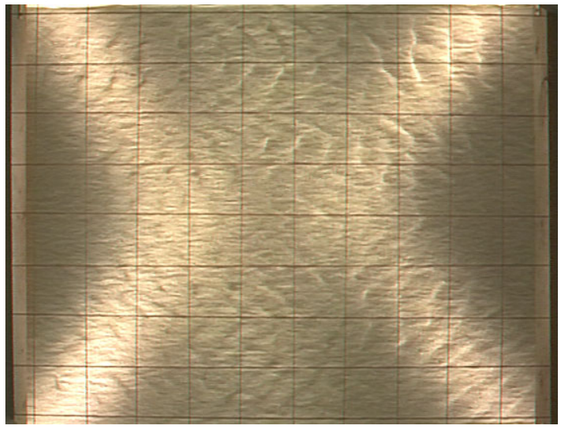

e) t = 10 s

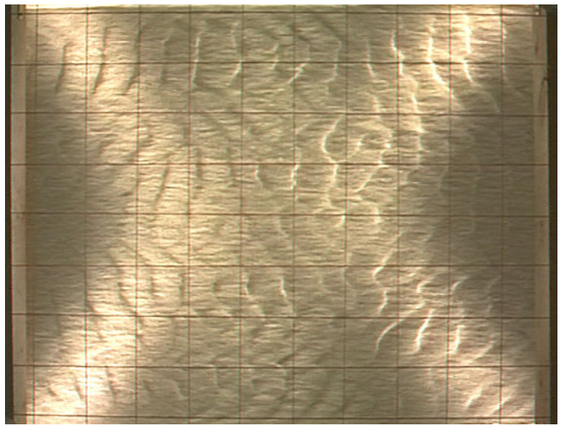

f) t = 30 s

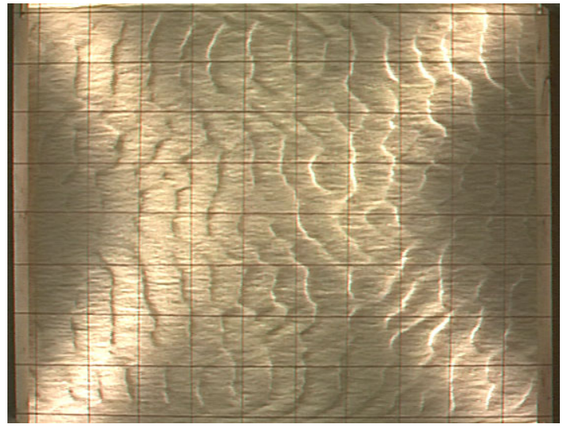

g) t = 50 s

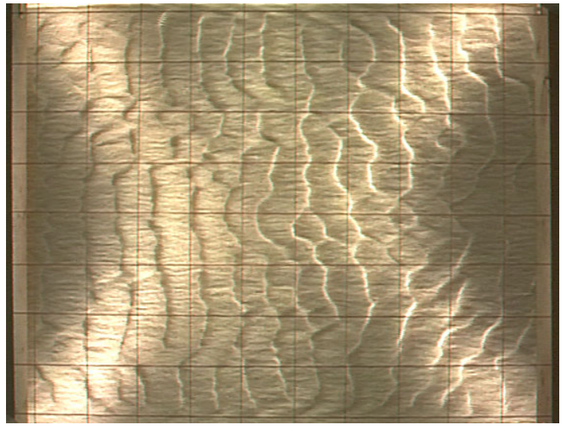

h) t = 80 s

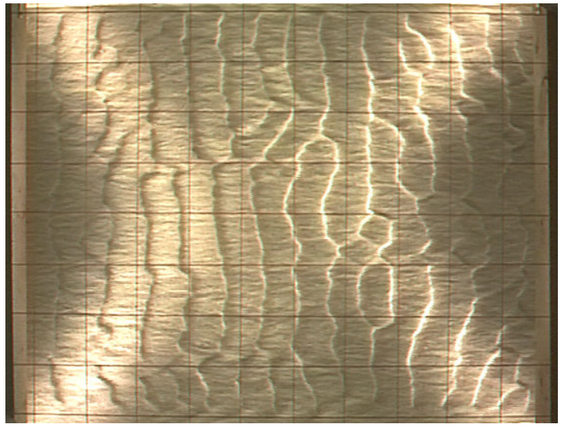

i) t = 240 s

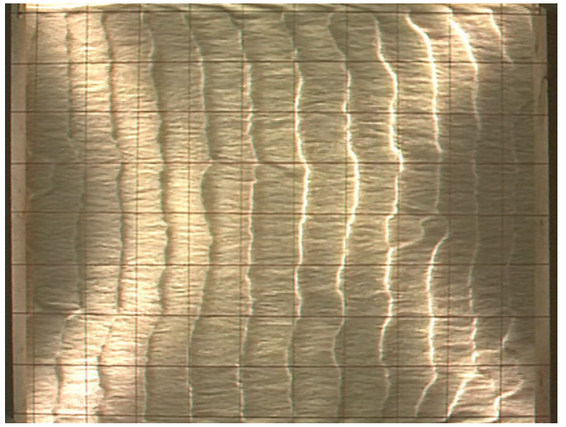

Figure 3.13: Evolution of a bed through instantaneous bedform initiation process at flow strength A. Prior to t = 0 s the discharge was being ramped up the desired flow strength. Flow is left to right.

a) t = -20 s during flow A

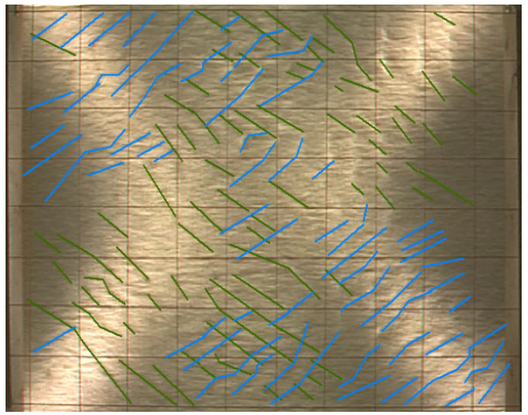

b) t = 1 s during flow B

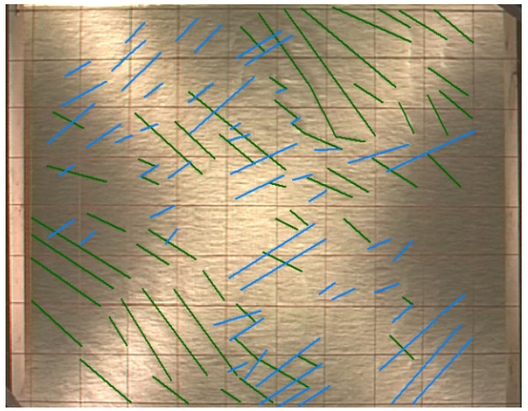

c) t = 30 s during flow C

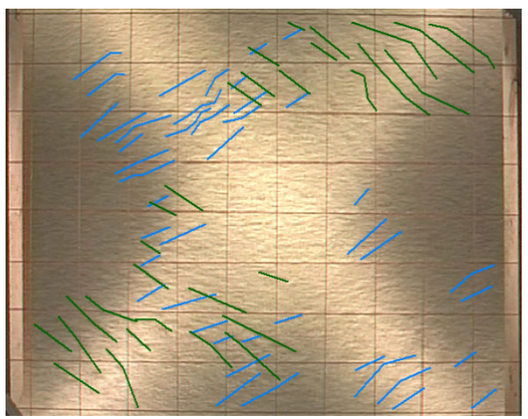

d) t = -20 s during flow A

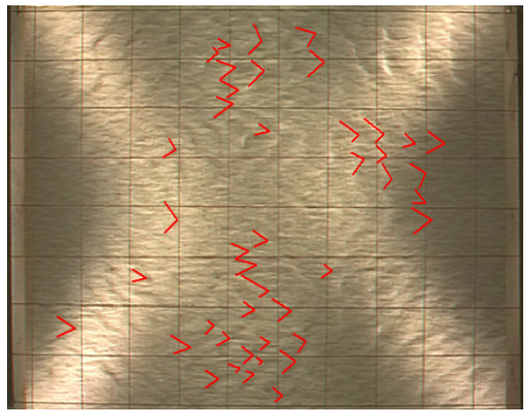

e) t = 1 s during flow B

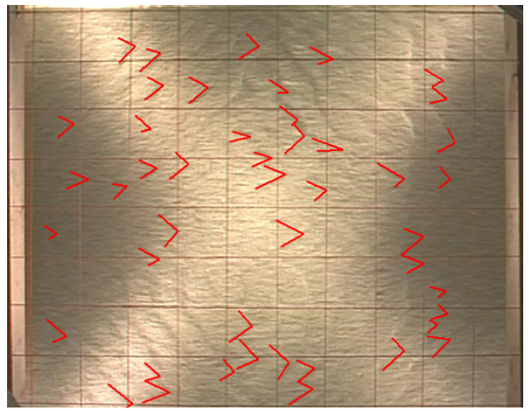

f) t = 30 s during flow C

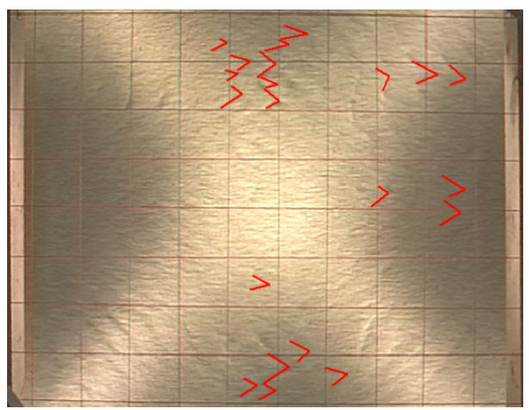

g) t = -15 s during flow A

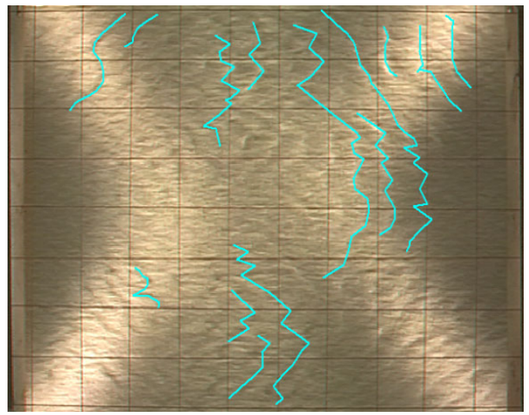

h) t = 1 s during flow B

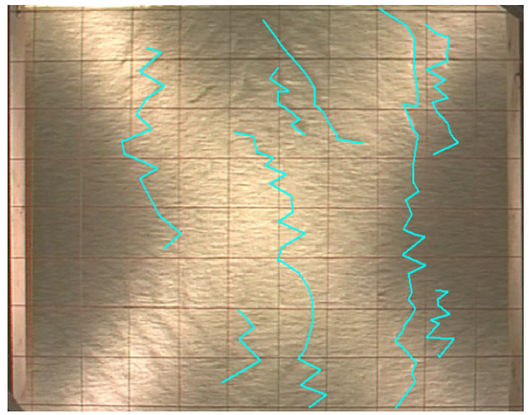

i) t = 120 s during flow C

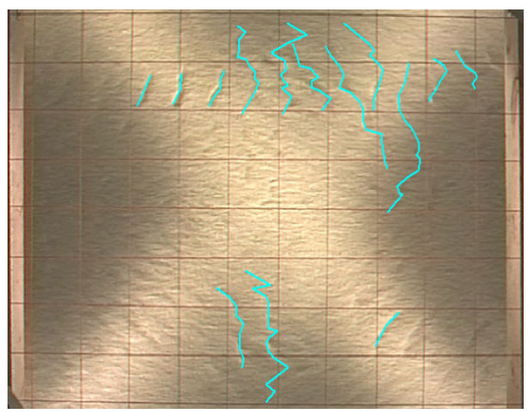

Figure 3.14: Cross-hatch patterns (a-c), chevrons (d-f), and incipient crestlines (g-i) developed during flows A, B and C. Prior to *t* = 0 s the discharge was being ramped up the desired flow strength. Flow is left to right.

the images in Figure 3.14a-c. The angles ranged between 10^o and 70^o, with a mean between 35 and 40^o for all three instantaneous initiation runs. The oblique striations were ~1 - 2 D in height. *Williams and Kemp* [1971] have indicated that flow separation occurs when

$$Re = u_* H / n > 4.5 . \qquad 3.19$$

Even when $H = D$, $Re > 4.5$. Therefore it is likely that some flow separation occurred over the striations.

It is difficult to measure the oblique striation spacing as the pattern on grabbed images is somewhat weak in spots (Figure 3.14). This is not an indication that the cross-hatch was not present in those areas. Lack of observations in some areas represents a limitation of the observation techniques. (The features are best observed by eye, on the video, or in time lapsed image sequences. Time lapsed image sequence animations for each run can be found in Appendix B.) Where the oblique striations were well represented on the grabbed images, their separation, L_{xy}, was ~0.045 - 0.048 m (Table 3.5). Assuming the cross-hatch angles were ~35 - 40^o, the streamwise separation of the nodes is ~0.064 - 0.067 m. Both separations are >> l_s.

Once the cross-hatch pattern was developed it began to migrate downstream, and in doing so, formed chevron shaped defects at the nodes of the cross-hatch (Figure 3.14d-f). These chevron shapes had a developing crestline that flared upstream. Similar features have been identified by *Gyr and Schmid* [1989] when the flow strength was increased quickly. The chevron shapes are also remarkably similar to rhomboid ripple marks [see discussion in *Allen*, 1986]. These features are commonly found on steep seaward-facing beaches or on bar faces where flow is shallow and temporary (transient). *Allen* [1986] notes rhomboid ripples are transitional to transverse ripples.

Gyr and Schmid [1989] attempted to link their observations to turbulent sweep events that are ubiquitous in turbulent flows and are characterised by $+u'$ and $-w'$ velocities. They noted that, in order for turbulent events to deform the entire bed, forming the chevron shapes, the events would need to be phase locked.

Table 3.5: Initial bedform length scales for instantaneous development runs. L_{xy} is measured from one image at the beginning of the run and L_i is measured from a single image taken at time, t_i.

Parameter	Flow A (Run 53)	Flow B (Run 54)	Flow C (Run 57)
L_{xy}, cm	4.51	4.84	4.69
t_i, s	60	120	330
$\overline{L}_i$, cm	8.27	8.56	9.08
$s\ L_i$, cm	1.63	1.45	1.47
L_{i-max}	13.78	12.08	12.53
L_{i-min}	4.27	5.64	5.18

The chevron features seem to differ from those described by *Williams and Kemp* [1971] and *Best* [1992] that are characterised by flow parallel ridges, flared at their downstream edges, with small accumulations of sediment at the mouth. *Best* [1992] also argued that these features were generated by coherent turbulent structures. *Grass* [1970] laid the foundation for this idea by noting that initial sediment transport is a product of 'sweep' impacts on flat sediment beds. The high-speed sweep structures alternate with low-speed streaks in the cross-stream direction, giving rise to hairpin vortices. Noting a significant difference between the size of the sweep structures and the size of initial bed defects, *Best* [1992] suggested that defects are formed by multiple hairpin vortices (composed of multiple sweeps), whose size is commensurate with the size of initial defects. *Best* [1992] also noted that burst events were concentrated over flow parallel ridges in experiments.

Regardless of the specific defect feature, it is widely accepted in the literature that sweep events generate the chevron shaped defects observed in the flume. While there is an increasing acknowledgement amongst the scientific community that the coherent structures examined by *Grass* [1970] and *Best* [1992] are organised, they are still considered to be rather random in space and time. In fact, data presented by *Best* [1992] seems to demonstrate a rather random distribution of grouped sweep structures without ridges installed in the flume. It is therefore difficult to imagine how the flow parallel ridges are established by random events in *Best's* [1992] experiments and how this might lead to the chevron patterns observed herein. It is not clear how random events could give rise to the regular cross-hatch pattern observed. Significant flow parallel ridges were not observed in the instantaneous development experiments. Unfortunately, without spatially detailed flow measurements the causal mechanisms of the cross-hatch pattern cannot be defined.

Once chevrons were migrating, they quickly began to organise transversely, forming flow perpendicular ridges at preferred along-stream spacing (Figure 3.14g-i). These incipient bedforms grew in size, with H increasing more quickly than L. In fact, L remained nearly constant until the crestlines were fairly well developed and two-dimensional (Figure 3.13). In the present experiments,

the initial bedform length, L_i, varied between 0.04 and 0.14 m and had a mode that varied between 0.08 and 0.10 m (Figure 3.15). Mean L_i decreased with increasing flow strength, as did the time required to develop the two-dimensional forms, t_i (Table 3.5). It should be noted that the specific value of $\overline{L}_i$ will vary slightly depending on when the measurement was taken.

While the origin of the chevron pattern is still open to debate, the organisation of the chevron pattern into crestlines has not before been addressed in any detail. The process of instantaneous bedform development and, in particular, the organisation of the chevrons appears similar to the expression of classic hydrodynamic instabilities [see *Lawrence et al.*, 1991]. If it is assumed that an interfacial instability is generated along the top of the sediment transport layer, the sheared density interface occurs between the water flow and the pseudo-fluid flow of the transport layer whose density is composed of both solid and fluid components.

A variety of hydrodynamic instabilities is defined in the Richardson number range $-3 \leq Ri \leq 1$ [*Lawrence et al.*, 1991]. The Richardson number is defined as

$$Ri = \frac{\Delta r}{r_2} \frac{gd}{\Delta u^2} \qquad 3.20$$

where Δr and Δu are the density and velocity differential, respectively, r_2 is the density of the lower, more dense fluid (the transport layer) and d is the thickness of the velocity interface. When $Ri < 0.07$ the Kelvin-Helmholtz instability dominates. In the flow system observed here $Ri < 0.02$ (using the definitions below). Therefore, it is of interest to test the theory of a Kelvin-Helmholtz instability to determine if the flow system envisioned above conforms to a classic hydrodynamic instability.

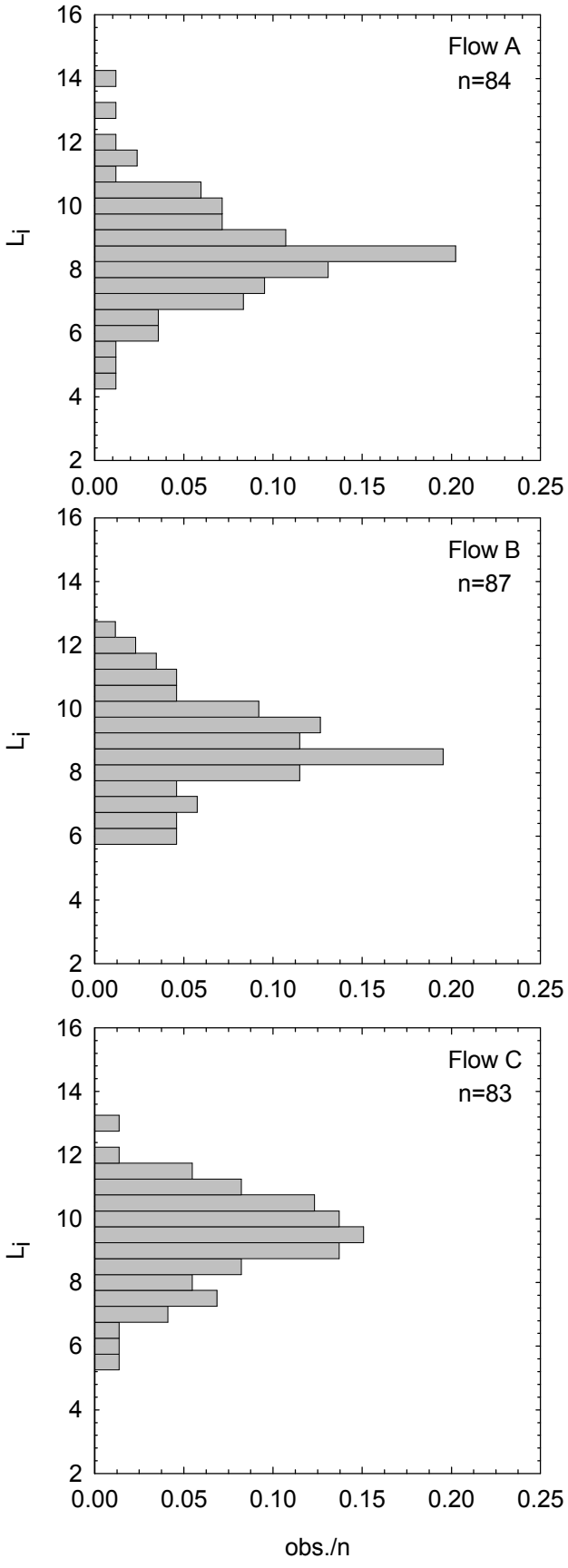

Figure 3.15: Histograms of initial bedform wavelength, L_i, for each instantaneous initiation run. Measurements are from images at $t = 60$ s (Flow A), $t = 120$ s (Flow B), $t = 330$ s (Flow C). Measurements are of all bedforms on the image, from crest to crest, along the streamwise direction only.

3.5 Kelvin-Helmholtz Instability Model

Liu [1957], drawing on presentations of theory presented in *Lamb* [1932], *Prandtl* [1952] and *Rouse* [1947], notes that an interface between two fluid of densities r_1 and r_2 moving at velocities u_1 and u_2 (Figure 3.16) will be stable if:

$$(u_1 - u_2)^2 < \frac{gL_{K-H}}{2p} \cdot \frac{r_2^{\,2} - r_1^{\,2}}{r_1 r_2}. \qquad 3.21$$

If the squared velocity difference exceeds the right-hand side of Equation 3.21, the interface is unstable and begins to undulate, forming a Kelvin-Helmholtz wave with a defined wavelength, L_{K-H}. An along-stream (streamwise) variation in velocity is generated as the waveform causes the streamlines to converge (increased velocity) and diverge (decreased velocity). According to the Bernoulli principle, a decrease in velocity is counteracted by an increase in pressure and an increase in velocity is counteracted by a decrease in pressure. The pressure variations are accentuated with time, which results in the concentration of vorticity at the crests of the waveforms and the generation of discrete vortices (Figure 3.16).

In the relation represented by Equation 3.21, it is assumed that: (1) flow is two-dimensional, (2) both fluids are moving in the same direction, (3) fluids are inviscid, (4) turbulence is not present or can be ignored, (5) both fluids have infinite depth and (6) only gravitational forces are acting on the fluids.

The wavelength at which the interface becomes unstable can be predicted by rearranging Equation 3.21 such that

$$L_{K-H} = (u_1 - u_2)^2 \cdot \frac{2p}{g} \cdot \frac{r_1 r_2}{r_2^{\,2} - r_1^{\,2}}. \qquad 3.22$$

Liu [1957] was first to suggest that this is a viable mechanistic explanation for the establishment of bedforms. He considered the less dense, faster moving layer to be flow in the viscous sub-layer and the denser, slower moving fluid to be the sediment bed. Unfortunately, difficulties in measuring the velocities and densities of each layer impeded acquisition of an arithmetic solution for Equation 3.22.

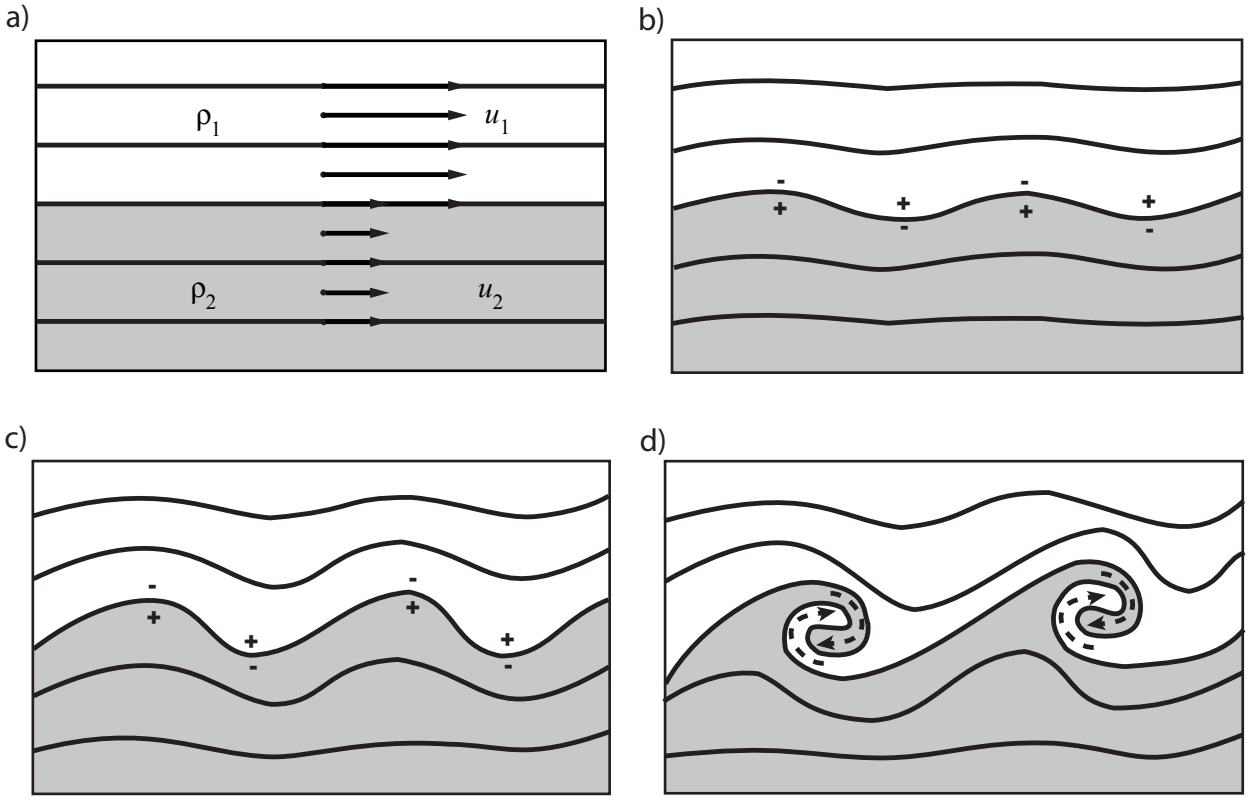

Figure 3.16: A definition sketch for a Kelvin-Helmholtz instability where fluid 1 has a lower density, ρ, and a larger velocity, u. Plus and minus signs indicate pressure relative to a mean value at the interface [Based on *Liu*, 1957].

Therefore, the seminal work of *Liu* [1957] relied on applying an instability index that contained information related to the sediment bed and the near bed flow, which was simply a Reynolds number calculated using u_* and D. The measurements taken during the present experiments allow the arithmetic solution to Equation 3.22 that eluded *Liu* [1957].

3.5.1 Scenario for K-H Model Testing

The interfacial instability scenario envisioned here is slightly different from that considered by *Liu* [1957]. In this conceptual model the upper fluid is considered to be the water column and is not restricted to the viscous sub-layer. The velocity of this upper layer is taken as the velocity measured at 5 mm above the bed, $U_{0.5}$, and the density is equal to r_w (Table 3.6). Using $u_1 = \overline{U}$ would be an oversimplification of the problem but it may be a valid approximation. The best way to approximate u_1 would be to incorporate the velocity profile through the log-layer ($z < 0.2\,d$) or even the entire d. This would greatly complicate Equation 3.22, and is not necessary for an initial test of the Kelvin-Helmholtz model.

The lower fluid depicted in Figure 3.16 is considered to be the active sediment transport layer. The velocity of particles at the surface of the transport layer (U_p) is measured from the video and generally varied between 0.010 and 0.075 m s^{-1}, depending on the run, and has a mode that varied between 0.015 and 0.035 m s^{-1} (Figure 3.17). As flow strength increased, mean particle velocity, $\overline{U}_p$, increased. If we assume U_p decreases linearly to zero at some depth, the depth averaged particle velocity is $U_{pd} = \overline{U}_p / 2$ (Table 3.6). Measurements made by *Paulos* [1998] suggest that the U_p profile is in fact linear and that this is a valid approximation of U_{pd}. As with the upper layer it would be useful to incorporate the grain velocity profile through the transport layer into an estimate of u_2, but this would also complicate Equation 3.22. Determining an appropriate value for r_2 is far more difficult than for r_1 as the lower layer is composed of solid and liquid components.

Table 3.6: Parameters used in the calculation of the Kelvin-Helmholtz model. Error ranges are ± the standard error for each parameter. Error analysis followed the general rules for the propagation of error when deriving a quantity from multiple measured quantities [*Beers*, 1957; *Parratt*, 1961]. Parameters marked with an asterisk (*) are measured quantities.

Parameter	Flow A	Flow B	Flow C
*Surface Particle Velocity, $\overline{U}_p$, cm s^{-1}	3.66 ± 0.22	3.40 ± 0.25	2.67 ± 0.21
Depth-averaged U_p, U_{pd}, cm s^{-1}	1.83 ± 0.11	1.70 ± 0.13	1.33 ± 0.11
*Flow velocity at z = 5 mm, $U_{0.5}$, cm s^{-1}	30.92 ± 0.03	29.52 ± 0.03	28.96 ± 0.02
*Shear Velocity, $u_{*0.2}$, cm s^{-1}	3.01 ± 0.07	2.55 ± 0.13	2.19 ± 0.11
Depth of Trans. Layer, d_{tl}, mm	0.99 ± 0.013	0.90 ± 0.028	0.82 ± 0.026
*Initial Dry-Mass Transport Rate, Q_{si}, kg s^{-1} x 10^{-3}	7.96 ± 0.51	5.76 ± 0.36	2.85 ± 0.41
Mass of Sand in Trans. Layer, M_s, kg x 10^{-3}	7.96 ± 0.51	5.76 ± 0.36	2.85 ± 0.41
Mass of Water in Trans. Layer, M_s, kg x 10^{-3}	15.19 ± 1.14	13.08 ± 1.24	9.27 ± 0.94
Volume of Active Layer, V_{tl}, m^3 x 10^{-5}	1.81 ± 0.11	1.53 ± 0.12	1.09 ± 0.09
Volume of Sand, V_s, m^3 x 10^{-5}	0.29 ± 0.02	0.22 ± 0.01	0.17 ± 0.02
Volume of Water, V_w, m^3 x 10^{-5}	1.52 ± 0.11	1.31 ± 0.12	0.93 ± 0.09
Combined Density, r_{tl}, Kg m^{-3}	1265 ± 104	1235 ± 130	1249 ± 142
Predicted Wavelength L_{K-H}, cm	10.04 ± 2.03	10.27 ± 2.65	9.85 ± 2.74
*Observed Initial Wavelength, L_i, cm	8.27 ± 0.18	8.56 ± 0.15	9.08 ± 0.16

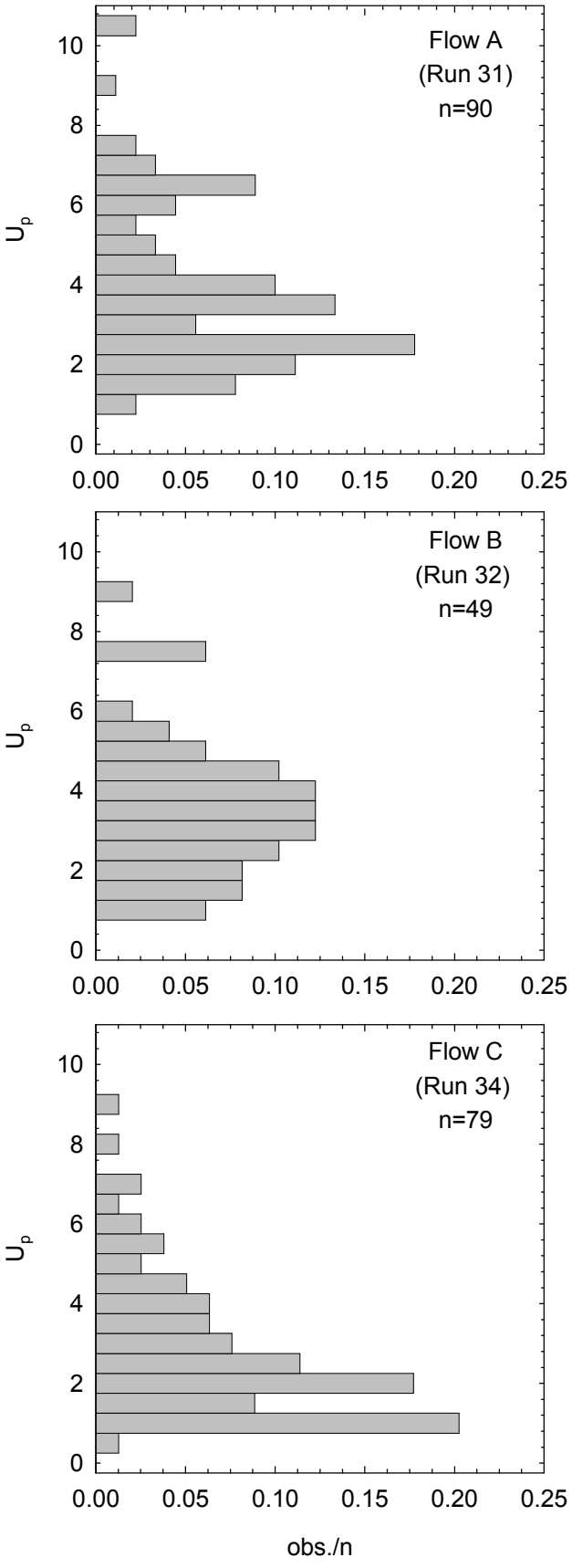

Figure 3.17: Histograms of surface particle velocity on the bed, U_p, for each instantaneous initiation runs. Measurements were made over the 30 seconds following the onset of widespread sand transport.

3.5.2 Depth and Density of the Active Layer

The density of the active sediment transport layer is calculated as the sum of the solid and liquid component masses per unit volume. A volume of the active layer, V_{tl}, can be determined as

$$V_{tl} = y_w \cdot d_{tl} \cdot \left(U_{pd} \cdot t\right) \qquad 3.23$$

where y_w is the flume width, t is some period of time (1 s in all calculations here), and d_{tl} is the depth of the transport layer. No suitable, systematic measurements of d_{tl} could be obtained during the experiments. However, limited observations indicated $d_{tl} = 2 - 3\ D$ and that d_{tl} increased with flow strength.

Depth of the active transport layer is an issue that has been debated in the literature, resulting in several relations to predict d_{tl} [see review in *Bridge and Bennett*, 1992]. *Einstein* [1950] suggested $d_{tl} \approx 2 - 3\ D$, in his seminal treatise on bedload transport. Other relations are based on the assumption that d_{tl} varies with t (or u_*). The most frequently referenced relations are those of *Bridge and Dominic* [1984], *Bagnold* [1973], and *van Rijn* [1984a], all of which are composed of an empirical fit between d_{tl} and some measure of the shear stress above its critical value for entrainment (Table 3.7). The *van Rijn* [1984a] relation also includes some measure of the sediment's submerged weight and the fluid viscosity.

Calculated values of d_{tl} in Table 3.7 indicate most values are within the range suggested by *Einstein* [1950] and the range observed during the experiments. The *Bridge and Dominic* [1984] relation provides a rather small depth estimate, which is not surprising as the empirical fit is based solely on the data of *Abbott and Francis* [1977]. Their study examined the motion of solitary particles (D = 6.4 - 8.2 mm) over a fixed bed composed of rounded pea-gravel D = 4.8 - 9.6 mm. Extension of the empirical relation to sand sized particles represents a radical extrapolation, and evidently produces erroneous results. *van Rijn* [1984a] and *Bagnold* [1973] back-calculated d_{tl}

Table 3.7: Depth of the transport layer estimates (in mm). In the *Bridge and Dominic* [1984] relation $V = 0.5$ for solitary grains moving over a bed and $V = 0$ in a bedload transport layer. The subscript *cr* represents critical values for the entrainment of sediment estimated from the Inman curve in *Miller et al.* [1977].

Source	Estimate	Flow A	Flow B	Flow C
Einstein (1952)	$d_{tl} = 2 - 3D$	1-1.5	1-1.5	1-1.5
Bridge and Dominic (1984)	$d_{tl} = (2.53(q - q_{cr})^{0.5} + V)D$	0.35	0.27	0.20
Bagnold (1973)	$d_{tl} = 1.4(u_* / u_{*cr})^{0.6} D$	0.99	0.90	0.82
van Rijn (1984a)	$d_{tl} = 0.3 {D_*}^{0.7} T^{0.5} D$	1.30	1.00	0.73

$D_* = D\left(\frac{g}{n^2}(r_s / r_w - 1)\right)^{\frac{1}{3}}$; $T = \frac{t_{0.2} - t_{cr}}{t_{cr}}$.

values from sand transport rates measured by *Williams* [1970] in which median D = 1.35 mm. Although either the *Bagnold* [1973] or *van Rijn* [1984a] relations can reasonably be used, the former is used in the calculation of V_{tl} here.

The mass of the sediment in V_{tl}, M_s, can be determined from the initial dry-mass transport rate, Q_{si}, as

$$M_s = Q_{si} \cdot t . \qquad 3.24$$

There are two candidate Q_{si} values for each run; that measured by the Helley-Smith sampler, Q_{s-HS}, and that determined from the nascent waveforms using the morphological method, Q_{s-d}. Unfortunately, there appears to be a larger amount of error associated with Q_{s-HS} (see discussion in Chapter 2). A value of Q_{s-d} is calculated using all bedforms observed during the first 10 min of the echo soundings. During this period H was generally less than 5 mm, which is fortuitous as the transport rate increased significantly when H exceeded 5 mm. These values of Q_{s-d} are similar to Q_{s-HS}, but with a reasonable increase in the transport with flow strength.

The mass of the water in V_{tl}, M_w, can be determined as

$$M_w = r_w(V_{tl} - V_s) \qquad 3.24$$

where V_s is the volume of sediment grains in the transport layer calculated as

$$V_s = \frac{M_s}{r_s} . \qquad 3.25$$

Using M_s and M_w, the density of the active transport layer can be calculated as

$$r_{tl} = \frac{M_s + M_w}{V_{tl}} . \qquad 3.26$$

Table 3.6 provides estimates of Q_{s-d}, M_s, M_w and r_{tl} for all three runs in which instantaneous bedform initiation was observed.

3.5.3 Error Analysis

Before proceeding with a discussion of agreement between predictions and observations, it is useful to review the error associated with the measured quantities and its propagation through the calculation of L_{K-H}. Error analysis followed the general rules for the propagation of error when deriving a quantity from multiple measured quantities [*Beers*, 1957; *Parratt*, 1961]. Standard errors of the estimate ($s/\sqrt{n}$) are given in Table 3.6 with each parameter. The error range associated with a parameter is 2× (or ±) the standard error.

All measured quantities used in the calculation of L_{K-H} have some associated error. The error associated with d_{tl} is derived from the error associated with the least-squares regression used to determine $u_{*0.2}$. The standard error of the estimate of $u_{*0.2}$ ranges between 0.69 and 1.64 mm s^{-1} and $u_{*0.2-err}/u_{*0.2}$ = 5 - 11 % (the subscript *err* indicates the error range). However, the error associated with the d_{tl} estimate from *Bagnold's* [1973] equation is not great, d_{tl-err}/d_{tl} is only 2.7 - 6.4 % because d_{tl} is determined from $(u_*/u_{*cr})^{0.6}$ and $u_* = (t/r_w)^{0.5}$. These power functions effectively reduce the effect of the error derived from $u_{*0.2}$.

The error associated with $U_{0.5}$ is excessively small because such large samples are used to determine mean velocity at z = 5 mm. This is not the case for the error range associated with $\overline{U}_p$ which is 4.21 - 5.05 mm s^{-1}. This translates into large errors in U_{pd} where U_{pd-err}/U_{pd} = 12 - 16 %. This is caused by relatively small sample size relative to the magnitude of variation in U_p.

The error range associated with r_{tl} is rather large (r_{tl-err}/r_{tl} = 16 - 23 %) as this calculation compounds errors associated with V_{tl}, M_s and M_w, which have large associated errors. The bulk of the error associated with V_{tl} is derived from the measurement of U_{pd}, as only errors associated with it and d_{tl} are combined in the calculation of V_{tl}. The error associated with M_s is also large and entirely derived from the error in Q_{si}. The number of samples used to determine Q_{si} was 21 for flow

A, 17 for flow B and 5 for flow C, resulting in an error range for Q_{si} that varied between 0.72×10^{-3} and 1.02×10^{-3} kg s^{-1}. Thus, Q_{si-err}/Q_{si} = 12 - 29 %. Since M_w is calculated as a function of V_{tl} and V_s ($\propto M_s$), its associated error is also large.

Applying Equation 3.22 compounds these measurement-related errors resulting in a relatively large degree of error in L_{K-H} where the error range is 40.6 mm for flow A, 53.1 mm for flow B and 54.9 mm for flow C. Ultimately, $L_{K-H-err}/L_{K-H}$ = 40 - 56 %. Nearly all the error is derived from error associated with Q_{si} and U_p. The error associated with Q_{si} could be reduced by significantly increasing the number of samples. The error in $\overline{U}_p$ could also be reduced by increasing the number of observations, but an improved technique is required to do so.

In contrast to the error associated with the prediction, the error range associated with the observed bedform length is 3.56 mm for flow A, 3.10 mm for flow B and 3.22 mm for flow C. So, $L_{i-err}/\overline{L}_i$ = 3.5 - 4.1 %. The error in the predicted L_{K-H} is much larger than the error in the observed $\overline{L}_i$.

3.5.4 Estimate Agreement

Predictions of L_{K-H} using Equation 3.22 are provided in Table 3.6. The predicted threshold for an unstable Kelvin-Helmholtz wave for this flow system ranges between 0.0985 and 0.1027 m, depending on the flow strength. Observed $\overline{L}_i$ is slightly smaller, 0.0827 - 0.0908 m, and so is median L_i, 0.08 - 0.10 m. Both mean and median lengths are within the error ranges associated with L_{K-H}. Predictions of L_{K-H} are extremely sensitive to the estimate of sediment transport rate. The ratio of $L_{K-H}/\overline{L}_i$ would be unity if Q_{si} was increased only 10 - 20 %.

It is interesting to note that when the bedform length becomes equivalent to L_{K-H}, the bedforms crestlines begin to breakdown and become three-dimensional. This suggests that the Kelvin-Helmholtz instability dominated the system through the two-dimensional stage.

3.6 The Development of Bedforms

Two types of bedform initiation have been described above: defect and instantaneous initiation. Initiation of a bedform field from a bed defect has been described previously in the literature [e.g. *Raudkivi*, 1966; *Southard and Dingler*, 1971; *Williams and Kemp*, 1971; *Leeder*, 1980; *Best*, 1992]. Negative defects on the bed initially grow downstream due to scour over the upstream lip of the defect. This piles sand grains scoured from the pit at its downstream edge, generating further downstream flow separation, which in turn generates a new scour pit and mound of sand grains at its downstream end. Through this process, negative defects grow downstream. After several pits are developed, the accumulation of sediment at the downstream end of the pits begins to square off and resemble bedforms. Each new scour pit is wider than the previous and, as the pits are propagated, the bedform field grows laterally. Through this process the initial defect is seen to generate a bedform field that covers the entire bed.

Positive defects differ in their response to the flow in that they are initially planed off. Concurrently, a scour pit develops in the lee of the defect. Propagation of the scour pits continues in the fashion of the negative defect. It appears that these scour pits are more stable features than positive defects which quickly decay if there is no scour pit upstream. Regardless of the defect form, bedform fields have approximately the same form when the fields are composed of five or more bedforms. Positive defect fields tend to develop more rapidly than negative fields, because there is more sediment initially available and exposed to flow in the mound.

The observed processes were geometrically similar at different flow strengths, but the development was much quicker at the greater flow strength. Beginning with *Raudkivi* [1966] most investigators have generally accepted that the driving mechanism behind defect propagation is flow separation. In fact, velocity profiles taken over the defects in these experiments demonstrate the characteristics of flow separation. It is therefore interesting that a separate initiation mode was observed in these experiments that was unrelated to defect initiation processes.

At the greater flow strengths, bedform initiation seemed to be instantaneous and defects are actually washed out. A cross-hatch pattern is first imprinted into the flat bed surface, which breaks up into individual chevrons that migrate independently. It has been suggested that the origin of these chevrons is linked to coherent turbulent flow structures that are ubiquitous in anisotropic shear flow [see *Gyr and Schmid*, 1989; *Best*, 1992]. This seems unlikely as one must argue that spatially and temporally random events must lock in place to generate the cross-hatch pattern. *Best* [1992] suggested that this may be the case if flow parallel ridges are developed because hairpin vortices tend to stabilise over this kind of topography. Lineated striations are observed over the bed, but these are not coincident with the scaling of the cross-hatch or chevrons. Unfortunately, the origin of the cross-hatch cannot be determined from the data herein, but its similarity to rhomboid ripple marks suggests its development may be linked to the sudden (transient) onset of flow and transport.

The organisation of the chevrons can be explained as a hydrodynamic instability that occurs at the shear interface between the sediment transport layer and the near-bed flow. Once sediment transport is initiated, the active sediment transport layer begins to act as a pseudo-fluid with a density that is composed of solid and fluid components. An instability develops at the interface of the fluid flow and the transport layer causing an oscillating along-stream pressure gradient. The pressure variations are accentuated with time and the waveform eventually breaks, generating localised sediment erosion and organisation of migrating features. When the waveform breaks, there is a concentration of vorticity at the crests of the waveform and the generation of discrete vortices [*Lawrence et al.*, 1991]. The integral scale, which is a measure of the average sized eddy in the flow, is within the error boundaries of L_{K-H} for two of the instantaneous initiation runs. Thus, the integral length scale is coincident with the length at which vorticity is concentrated in the Kelvin-Helmholtz instability.

Predictions from the theory of a Kelvin-Helmholtz instability are encouraging because $\overline{L}_i$ and median L_i are within the error range of L_{K-H}. This result has not been attained in the literature previously. Ultimately, it appears that the instantaneous initiation of bedforms is controlled by a

simple hydrodynamic instability. This is in direct contrast to theories of bedform development based purely on the motions of coherent turbulent eddy structures, but it statistically complements the observed regularity of the initial bedforms.

A more advanced solution than Equation 3.21 is necessary to take into account the velocity profiles in the near-bed region and through the sediment bed. Improved estimates of the initial transport rate, using more advanced technologies, are critical. There is also a need to examine the active layer through measurements in order to better characterise its depth and density. Finally, further research is needed to define the grain sizes, grain size distributions and transport intensities over which the two types of initiation processes described here dominate.

3.7 Summary

Bedform initiation was examined on a flat bed, composed of a homogeneous 0.5 mm sand. The bed was subjected to a 0.155 m deep, non-varying mean flow ranging from 0.30 to 0.55 m/s in a 1 m wide flume. Bed deformation was monitored using overhead video and echo-sounders. In order to confirm that the flows were typical steady, uniform flows, velocity profiles were taken using laser Doppler anemometry. Overall the velocity data suggest that flow over the lower stage plane beds at the beginning of the experiments was in accordance with conventional models of uniform flow over flat beds. With the exception of the depth-slope product calculations, estimates of the boundary shear stress derived from different methods are similar in magnitude, and increase in a similar fashion with $\overline{U}$. The roughness heights are consistent with previous observations. The turbulence intensities and R_{uw} can be modelled by the semi-empirical functions provided by *Nezu and Nakagawa* [1993], with the exception of the vertical intensities at the low flow strengths. With few exceptions, the momentum exchange (t_{uw}) and fluid diffusion (e) are typical of fully turbulent, uniform, open channel flows. Bed defects dramatically reduce the streamwise velocity near the bed, increasing turbulence and providing the turbulent energy to scour out the bedform lee.

Two types of bedform initiation are observed in the experiments. The first occurs at lower flow strengths and is characterised by the propagation of defects via flow separation processes to develop bedform fields. This type of bedform development has received some attention in the literature and widespread support in the earth sciences. The second mode of bedform initiation has received less attention. This form of bedform initiation begins with the imprinting of a cross-hatch pattern on the flat sediment bed, which leads to chevron shaped forms that migrate independently of the initial structure.

The chevron shapes are organised by a simple fluid instability that occurs at the sediment transport layer-water interface. Predictions from a Kelvin-Helmholtz instability model are nearly equivalent to the observations of bedform lengths in the experiments. It is likely that the instability model holds only for intense transport conditions when the bed constitutes a fluid layer, and is less applicable to situations where the active transport layer is discontinuous. Further research is needed to define the grain sizes, grain size distributions, and transport intensities over which the two types of initiation processes described here dominate.

Chapter 4: The Transition between Two- and Three-Dimensional Bedforms

4.1 Introduction

The purpose of this chapter is to examine the transition between two-dimensional (2D) and three-dimensional (3D) dunes. A definition of what constitutes a 3D bedform is provided using a statistic called the non-dimensional span or sinuosity of dune crests. A critical value of the non-dimensional span is proposed to divide bedforms with straight or slightly sinuous 2D crests from 3D bedforms. Video records are examined for patterns in the breakdown of dune crestlines that give insight to the physical mechanisms of the transition. The problem of whether 3D bedforms develop only at greater flow strengths will be addressed. Finally, a possible explanation is provided for why the transition occurs.

It is well known that sediment transport rates are dependent on the applied shear stress. A mechanism that reduces (or stabilises) the shear stress should also reduce (or stabilise) the sediment transport rate. Drag reduction is a mechanism that may protect the bed from erosion by reducing the applied shear stress. This can contribute to the stability of the bed and the channel by reducing susceptibility to degradation. In light of this idea, the shift from 2D to 3D morphology is examined as a mechanism that reduces drag. Drag coefficients and forces are examined as bedforms develop from 2D transverse ribs through to equilibrium 3D dunes.

4.2 Experimental Procedures

The experiments discussed in this chapter used the same apparatus, experimental design, and flow conditions detailed in Chapter 2. The runs were conducted at the same pump frequencies, f_p = 23.5, 22.5, 21.5, 19.0 and 17.0 Hz. The bulk flow hydraulics of each run can be found in Table 2.1. Several runs were conducted at each f_p to accomplish the goals in this chapter, so labels are again assigned to each flow strength to streamline the text. As before, flow strength A refers to all runs

conduced at f_p = 23.5 Hz, B all runs at f_p = 22.5 Hz, C all runs at f_p = 21.5 Hz, D all runs at f_p = 19.0 Hz and E all runs at f_p = 17.0 Hz. As discussed in Chapter 3, bedforms were initiated instantaneously during Runs A, B and C, and by negative defect propagation processes during flows D and E.

A short note on scaling is necessary before any discussion of 3D bedforms can be accomplished. If a dune is 1 m long in a 0.1 m wide flume, the sinuosity of the crest may be low. If that same dune is formed in a 2 m wide flume, the crest sinuosity is free to develop to larger values. The level of three-dimensionality of a bedform is certainly a function of L/y_w (L is bedform length and y_w is width of the flume). In the 1 m wide flume used for these experiments, only the longest bedforms had $L > y_w$, so this is probably not a problem. However, all observations discussed in this chapter need to be considered in this light.

4.2.1 Video

Experimental runs were recorded using the Super-VHS set up discussed in Chapters 2 and 3. Videotape records were sub-sampled with a frame grabber at an interval of 10 sec. This produced a series of images suitable for further analysis. The video was taken during Runs 53 (A), 54 (B), 55 (E), 57 (C) and 59 (D).

4.2.2 Water Surface and Bed Level Sensors

During the videotaped runs, changes in water surface level were monitored using two ultrasonic water level sensors built by Contaq Technologies Corporation. The water level sensors emit an ultrasonic signal toward a boundary (liquid or solid) and the signal return time is sensed and converted to a distance using hardware and software provided by the manufacturer. The minimum operational distance to a boundary is ~0.15 m and the reported resolution is 0.172 mm. The sensors

were mounted in the centre of the channel with a streamwise separation x_{wl} = 2.26 m at 8.66 and 10.92 m from the head box (see Figure 2.3). The video was taken towards the downstream end of this span. Instrument signals were sampled at ~2.5 Hz for 30 min periods through out the experiment. The signals appeared to be relatively free of signal contamination, but the high sampling frequency of the sensors produced far more detailed information than was necessary for the purposes of this investigation. As such, a 250 s running mean was calculated for the time series at 25 s intervals. This provided nearly continuous measurements of the water surface level and slope, S, determined as

$$S = \frac{z_{WS\,1} - z_{WS\,2}}{x_{wl}} \qquad 4.1$$

where $z_{WS\,1}$ and $z_{WS\,2}$ are the water levels at sensors 1 and 2 (Figure 2.3).

Echo-sounder bed height measurements are used in this chapter to determine the change in bed level surface with time. Records used are those discussed in Chapter 2 taken during runs 26 (A), 27 (B), 28 (C), 29 (D) and 30 (E). The sensors were deployed in the centre of the channel with a streamwise separation of 0.13 m at 10.36 and 10.50 m from the head box (Figure 2.3).

4.2.3 Arcview Analysis

In order to examine the morphology of the bed the video image series were analysed using a GIS software package. Figure 4.1 details the two sets of measurements made. In order to calculate an areally averaged bedform length, $L_a = A_b / y_b$, the area between two crestlines, A_b, was digitised and the distance that the bedform extended across the flume, y_b, was measured along the cross-stream axis of the flume. A_b could only be digitised when both crestlines were visible in the video view and within ~1.2 m of each other, placing a practical limit on L_a. The second set of measurements consisted of a measurement of the length along the bedform crest, L_c, and a measurement of the

a)

b)

c)

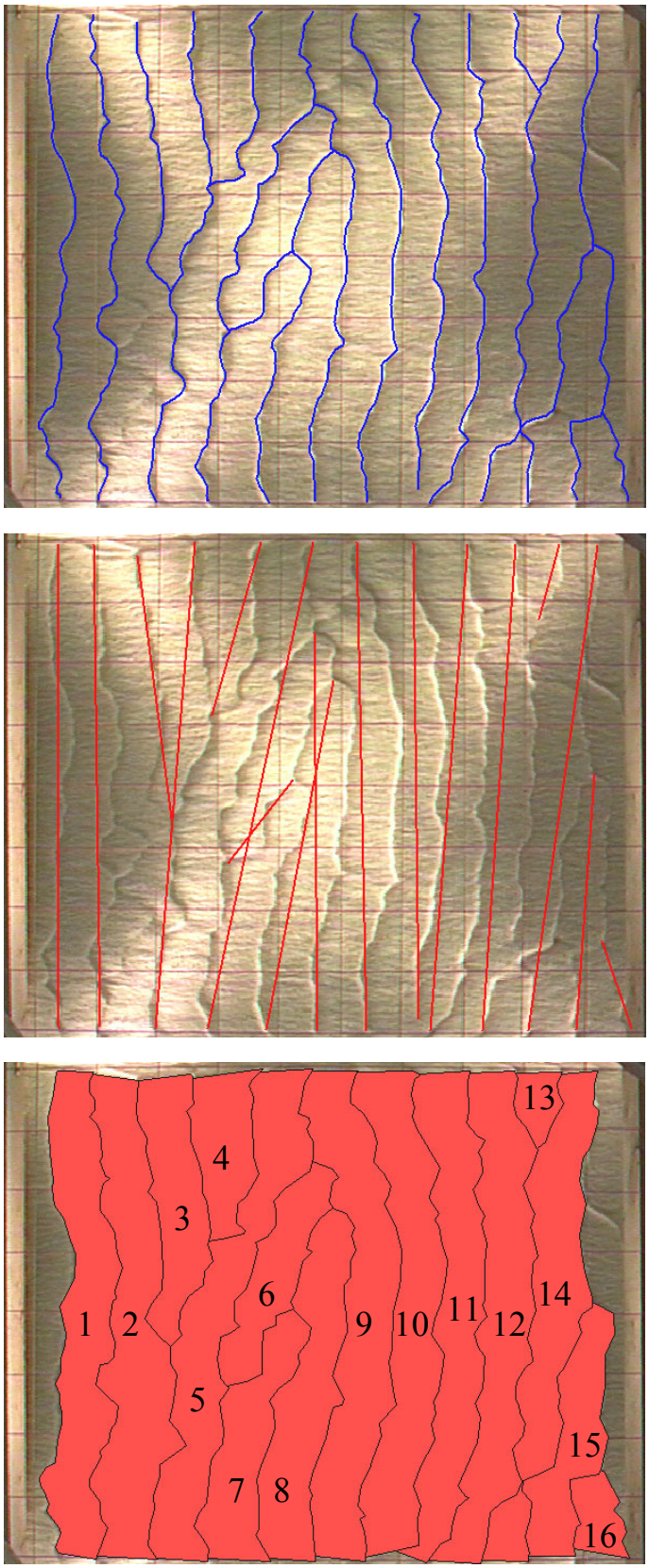

Figure 4.1: Measurements taken from video images: (a) Crestline length, L_c; (b) Linear crest length, L_y ; (c) Bedform area, A_d. Image is Run54-0031 (t = 240 s). Flow is left to right.

linear distance between the end points of the crestline, L_y which is measured according to the orientation of the bedform crestline. In nearly all cases, $y_b \neq L_y$.

Digitising data from video images is enormously time consuming so different measurement periods were used based on the rate of bedform change, which is a function of flow strength and, ultimately, the sediment transport rate. Measurement period also varied based on data requirements to answer the research questions. It was necessary to have extensive data at the beginning of the higher flow runs, when bedforms were initiated instantaneously, because these data were needed to define when the transition between 2D and 3D bedforms had occurred. The rest of the records were needed to examine the variability of measured quantities through time and so the data density was lower in all but one run.

For Run 54 (B), measurements of A_b, y_b, L_c and L_y were made at 60 s intervals throughout the 12 hour experiment, providing a complete data set of the variation in measured quantities. For Run 53 (A), at a slightly greater flow strength than 54, images were digitised at 60 s intervals for the first 4 hours. For Run 57 (C), at a slightly lesser flow strength than 54, measurements were made at 60 s intervals for the first 1 hour and at 120 s intervals when $t = 2$ - 4 hours. Images were digitised at 5 min intervals after 4 hours for Runs 53 and 57 to ensure the patterns were consistent with those observed during Run 54. Bedforms developed from negative (or positive) defects provide a fairly complex morphology before they extend across the whole channel (see Chapter 5). Therefore images were digitised after $t = 4$ hours. The rate of change for these bedforms was not great, so images were digitised at 5 min intervals.

All measurements were made with respect to the overhung grid in the video view. Due to distortion caused by the distance between the grid height and the bed height, all areas measured from the images are corrected by multiplying by 1.28 and all lengths are corrected by multiplying by 1.15. See Chapter 2 for details and justification of these corrections.

4.3 A Definition of 3D Bedform Morphology

Numerous researchers have examined the character of 3D dunes [e.g. *Allen*, 1968; *Ashley*, 1990], yet few of these researchers have attempted to define the three-dimensionality of a bedform numerically. Most researchers have instead relied on descriptive terms that characterise the crestlines of bedforms such as straight, sinuous, catenary, linguoid, cuspate and lunate [*Allen*, 1968]. These terms are typically applied to the whole bedform field. This approach to documenting bedform shape provides a necessary element of simplification in order to characterise bed structures in the rock record or general patterns in active rivers. However, the assignment of a particular term is somewhat subjective since a bedform field may be composed of bedforms with different degrees of three-dimensionality. Terms also vary widely in the literature, meaning that a single bedform field may legitimately have several terms that describe its morphology. In light of this, *Ashley* [1990] reviewed the literature and recommended that the terms 2D and 3D be used as primary descriptors of the bed morphology in lieu of the terms listed above. While this makes defining the areal morphology of a bedforms more universal, the final designation of descriptor is still somewhat subjective. It is therefore beneficial to define a criterion that uses actual bedform characteristics to define the level of three-dimensionality.

Allen [1968] was first to suggest a numerical measure of areal bedform morphology, defining the degree of 'waviness' of a crestline as

$$\Lambda_{Allen-a} = l_x / l_y \qquad 4.2$$

where l_y is the cross-stream distance between lobes of a sinuous, catenary, linguoid, cuspate or lunate crestline and l_x is the streamwise distance that the lobes extend downstream (Figure 4.2). In a later writing, *Allen* [1969] suggested bedform three-dimensionality could be characterised by the ratio

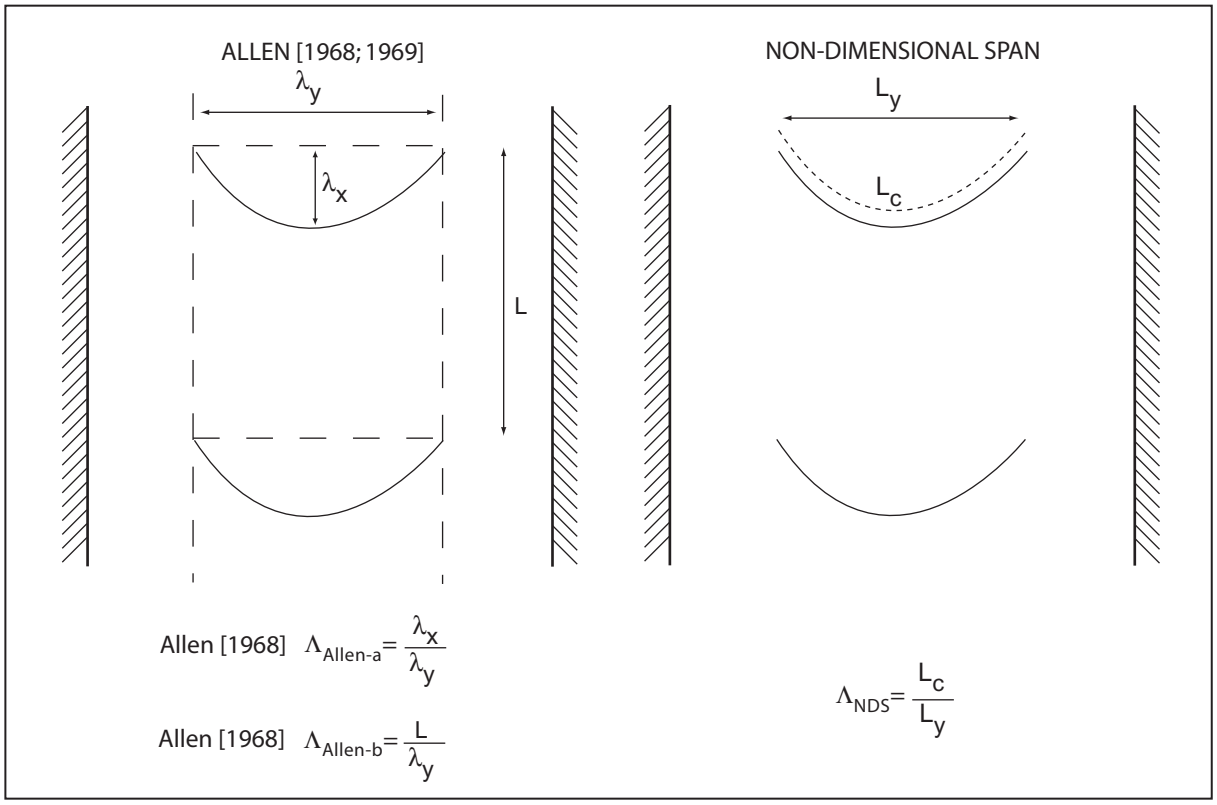

Figure 4.2: Measures of bedform crestline three-dimensionality.

$$\Lambda_{Allen-b} = L / l_y \qquad 4.3$$

(Figure 4.2). In fact, *Allen* [1969] attempted to functionally link $\Lambda_{Allen-b}$ to a Froude number. Unfortunately, both measures suggested by *Allen* [1968; 1969] require rather simple plan geometries of bedforms. If a bedform crest is composed of multiple lobes, it becomes inordinately difficult to define l_y, l_x and L. In this study, in particular, the streamwise extent of lobes is not uniform along a single crestline and it is difficult to break the bedforms into individuals. It may even be misleading to break a single crestline into several paired lobes.

An alternative to *Allen's* [1968; 1969] measures of crestline morphology is the non-dimensional span (or sinuosity) defined as

$$\Lambda_{NDS} = L_c / L_y \qquad 4.4$$

(Figure 4.2). This measure is ideal when the crests of bedforms can be linked into a continuous crestline. Even if the bedforms are isolated individuals on the bed, Λ_{NDS} can be defined as L_y is measured from the ends of the crestline. Figure 4.3 provides examples of Λ_{NDS} values averaged over the image, Λ_{NDS-im}. When $\Lambda_{NDS-im} = 1.02$, the minimum observed, the bed is composed of straight crested 2D dunes. At $\Lambda_{NDS-im} = 1.10$, the crestlines remain largely 2D but converge at several locations and the crestlines bend. When $\Lambda_{NDS-im} = 1.21$, the bed is composed of a mixture of highly sinuous and linguoid [in the terminology of *Allen*, 1968] bedforms. At the larger values of Λ_{NDS-im} in Figure 4.3 (1.29 and 1.39), the bed is largely composed of linguiod bedforms with some crestlines that are highly sinuous.

As will be discussed below, instantaneously developed bedforms provide a clear transition between 2D and 3D bedforms. Bedforms that develop from bed defects eventually become 3D, but lag effects complicate the transition process. Therefore only the greater flow strength runs are used to define a numerical criterion that divides 2D dune fields from 3D fields.

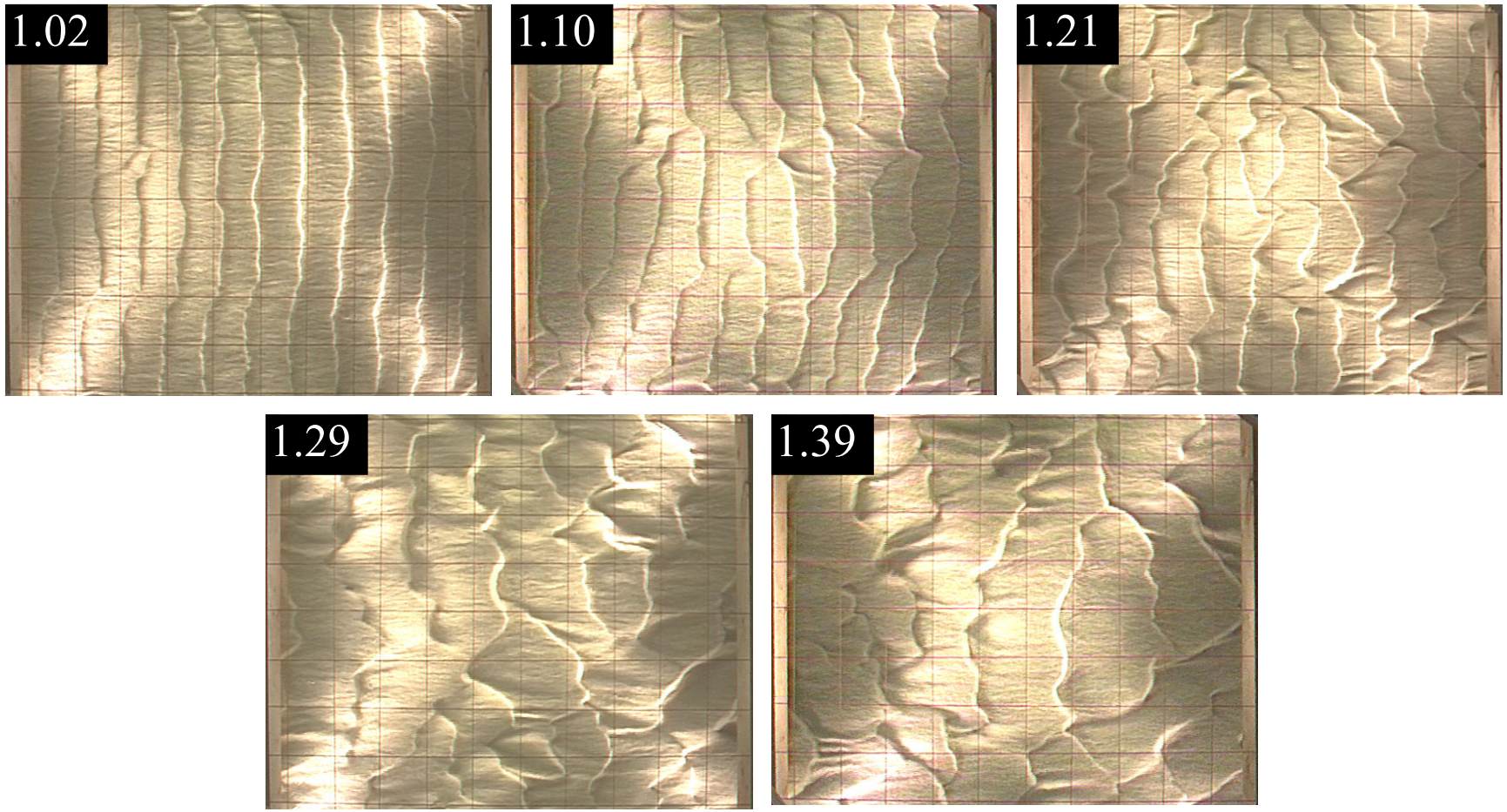

Figure 4.3: Examples of non-dimensional span averaged over each image. Clockwise from top left, images are 531-0037 (t = 300 s), 541-0073 (t = 660 s), 571-0106 (t = 1020 s), 541-0223 (t = 2160 s) and 531-0175 (t = 1680). Flow is left to right.

Figure 4.4 plots Λ_{NDS} as a function of time for the first hour of the experiments. There is considerable scatter in Λ_{NDS} which is reduced by excluding values where L_y does not exceed 0.7 m (as is done in Figure 4.3) which inordinately bias the image averages. A general trend can be observed in Λ_{NDS} values, but plots of Λ_{NDS-im} clarify the pattern. Initially, the majority of Λ_{NDS} values are in the range 1.1 - 1.3 with Λ_{NDS-im} = 1.1 - 1.2 when the bed is composed of organising chevron shapes. As the crestlines straighten and become 2D, Λ_{NDS-im} begins to drop approaching its definitional minimum of 1.0.

At flow strength B, crestlines that are continuous across the channel form at t_c = 120 s, while minimum values of Λ_{NDS} occur at t_{2D} = 420 s, ~5 min later (Table 4.1). Similar trends can be observed at flow strengths A and C where $t_{2D} - t_c \approx 300$ s and thus appear not to depend on flow strength. At t_{2D} there are several observations of $\Lambda_{NDS} \approx 1.00$, but Λ_{NDS-im} = 1.02, 1.08 and 1.07 at flows A, B and C, respectively. That Λ_{NDS-im} is much lower at flow strength A may be significant; at this flow the velocity gradient that leads to Kelvin-Helmholtz instabilities is the greatest and thus the concentration of vorticity may be greatest. However, this observation could be fortuitous as lower values of Λ_{NDS-im} may occur in between the sampled images at flows B and C.

Roughly 20 - 30 min beyond the minimum, Λ_{NDS-im} increased to values that were as large as 1.38-1.39 (Table 4.1). There was a nearly linear increase in Λ_{NDS-im} from 1.02 - 1.39 at flow A, after which Λ_{NDS-im} varied between 1.2 and 1.4 as the bedforms grew towards an equilibrium. The variability in Λ_{NDS} beyond the first hour is discussed later. The same near linear increase can be observed at Flows B and C, but from Λ_{NDS-im}=1.07 - 1.08 to 1.31 - 1.29, after which Λ_{NDS-im} approaches 1.4, defining a local maximum Λ_{NDS-im} at $t_{\max}$ (Table 4.1).

As crestlines begin to break up and become 3D, Λ_{NDS} rises until nearly all observations with L_y > 0.70 m are above a value of 1.2. The scatter about Λ_{NDS-im} also increases substantially

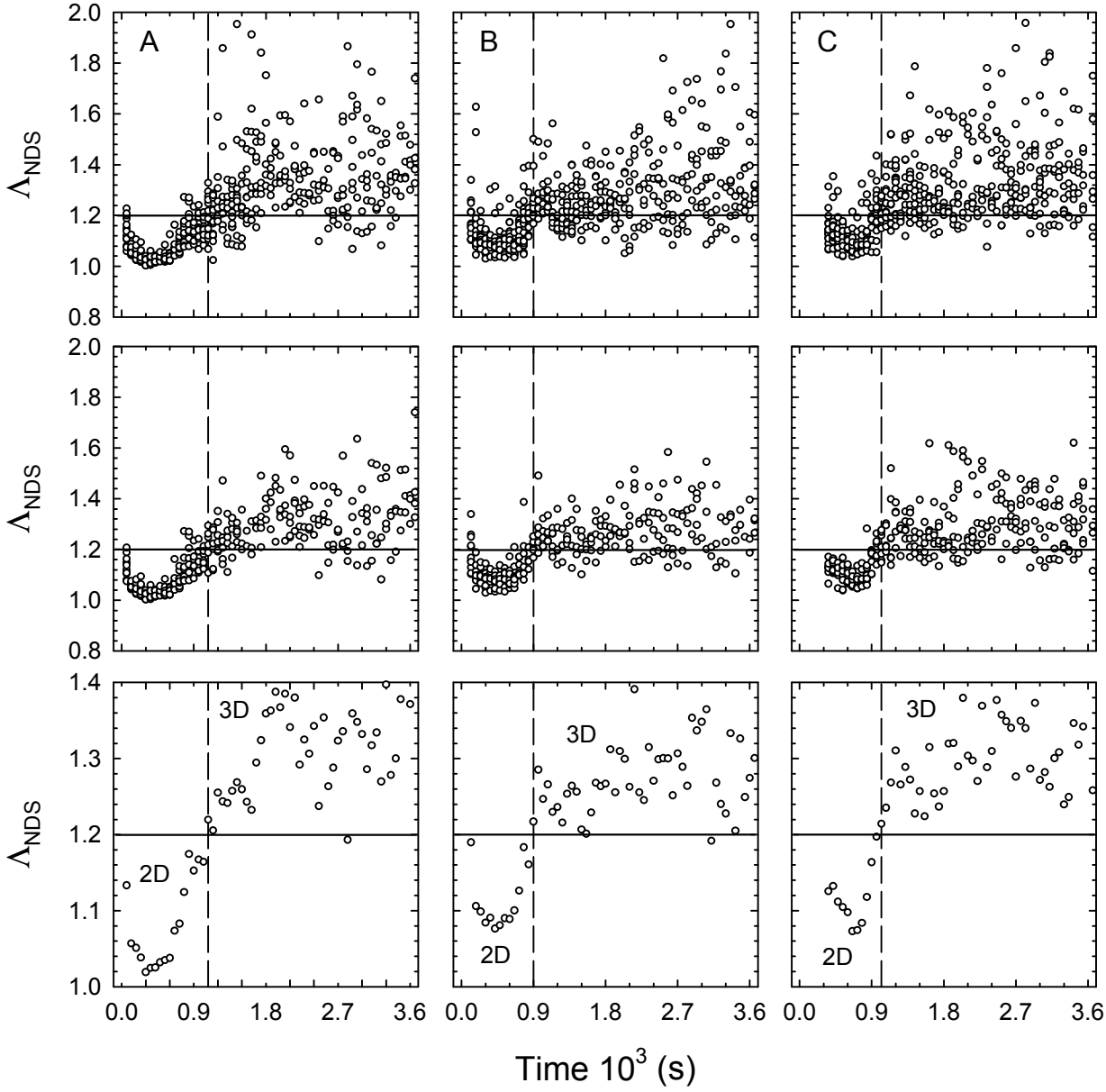

Figure 4.4: Non-dimensional span, Λ_{NDS}, during the first hour of experiments. All observations are plotted in top row of panels. Middle panels plot crests that exceed a cross-stream extent of 0.7 m and bottom panels are image means of data in middle row.

Table 4.1: Timing of critical non-dimensional span values over 2-3D transition.

Flow	Run	t_c (s)	Λ_{NDS}	t_{2D} (s)	Λ_{NDS}	t_{3D} (s)	Λ_{NDS}	$t_{\max}$ (s)	Λ_{NDS}
A	53	60	1.1332	300	1.0192	1080	1.2195	1920	1.3873
B	54	120	1.1895	420	1.0764	900	1.2169	2160	1.3909
C	57	360	1.1256	660	1.0730	1020	1.2141	2040	1.3795

compared to when Λ_{NDS} was less than 1.2 because the bed is composed of bedforms with varying degrees of three-dimensionality. Given these observations and the description associated with $\Lambda_{NDS-im} = 1.21$ in Figure 4.3, it seems logical to assert that when Λ_{NDS} is less than 1.20 a crestline is 2D, and when Λ_{NDS} exceeds 1.20 a crestline is 3D.

4.4 Observations of the Transition between 2D and 3D Bedforms

Before proceeding with a discussion of the processes involved in the 2-3D transition, it is useful to simply note that the ultimate bedform morphology was 3D. This answers an important question raised in Chapter 1: do 3D dunes develop at larger flow strengths than 2D dunes? As noted in Chapter 2, *Baas* and collaborators [*Baas et al.*, 1993; *Baas*, 1994; *Baas*, 1999] have demonstrated that, given enough time, ripples will always transform from a 2D to a 3D morphology. This also appears to be true for dunes as 2D dunes were observed to be temporary and transitional features.

Southard and Boguchwal [1990] provide the most extensive bedform phase diagrams and plotting methodology in the literature to date. All the observations made during the present experiments plot in the 2D dune fields (Figure 2.2). The idea that 2D features develop at lower flow strengths than 3D dunes [*Costello and Southard*, 1981; *Southard and Boguchwal*, 1990] does not seem valid, at least for the grain size employed in the experiment.

The 2-3D dune transition was observed to occur shortly after the features developed for all experimental runs. The transition is far more pronounced when the 2D bed is developed instantaneously, rather than from a bed defect, and so it is useful to discuss the two sequences separately.

4.4.1 Bed Defect Developed Fields

It is difficult to define distinct 2D and 3D phases for the bedform field developed from defects at flows D and E. The bedform field developed from defects is initially 2D and then undergoes a

transition to 3D morphology with time. Also, newly developed crests can have a 2D form that undergoes a later transition to 3D. Figure 3.9a-e demonstrates that the features developed from a defect are straight crested. However, a disturbance in the crestline appears in Figure 3.9f and is amplified with time in Figure 3.9g-i. The defect bedform field that appears in Figure 3.9h has some features that would be considered 2D and others that would be considered 3D. In Figure 3.9g-i the third and fourth crests and the top portion of crests 5 - 8 crestlines are approximately 2D while the rest of the field is approximately 3D.

This kind of mixed morphology can also be observed throughout the sequence of maps presented in Figure 3.7. Bedforms that migrate from the head box are generally 2D but become 3D as they interact with the defect field. Once the defect-developed field is overtaken by bedforms developed at the head box, the entire field becomes 3D (see Figure 3.7g). However, since sediment transport rates are low for the defect- developed bed, the 2-3D transition may lag behind at newly developed portions of the bed. Essentially, the transition between 2D and 3D bedforms occurs at different times and at different locations in the bedforms field. Nevertheless, once the defect pattern and head box developed bedforms have interacted and the dunes are fully developed, their morphology is 3D as in Figure 3.7h-j. Given the complicated lag in the 2-3D transition at flows D and E, it is best to examine the processes in which the transition occurs quickly and entirely.

4.4.2 Instantaneously Developed Fields

Figure 4.5 depicts a series of morphological changes that the 2D bed undergoes during the transition to 3D when the bed is developed instantaneously. Time-lapsed image animations of the 2D-3D dune transition can be found in Appendix B.

Once organised by the Kelvin-Helmholtz instability, the bed is composed of straight or slightly sinuous crested dune features (Figure 4.5a). The crestlines begin to bend along their cross-stream length and become convex downstream during the greatest flow strength examined (A) (Figure 4.5b).

a) t = 300 s

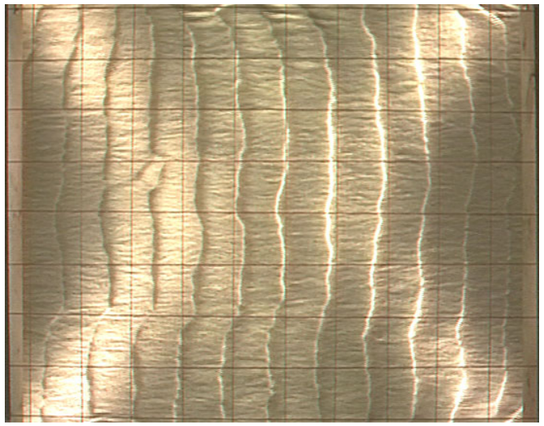

b) t = 660 s

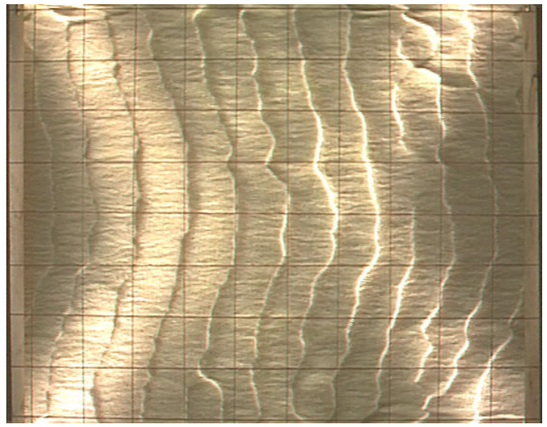

c) t = 780 s

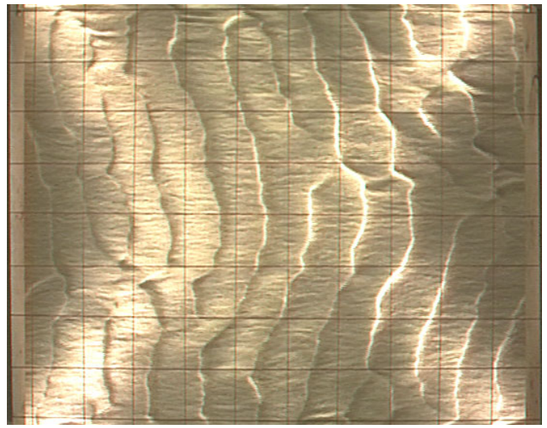

d) t = 900 s

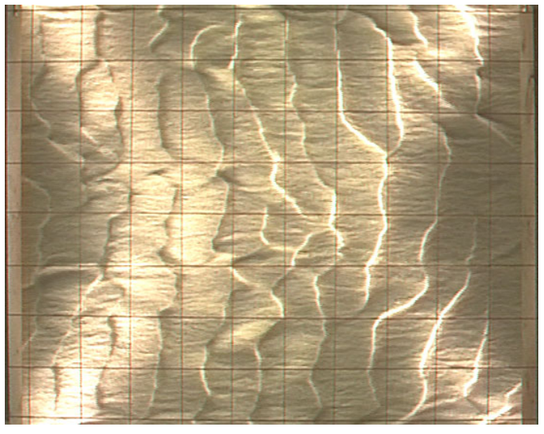

e) t = 1020 s

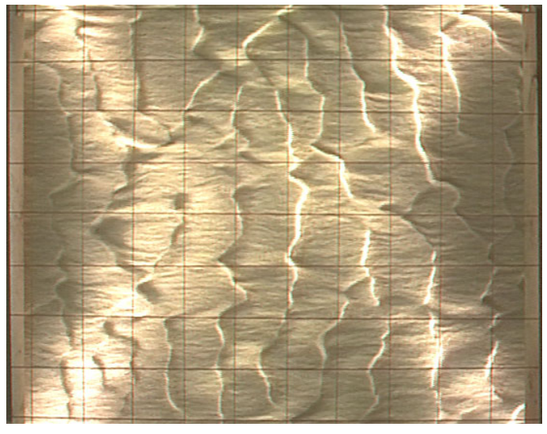

f) t = 1140 s

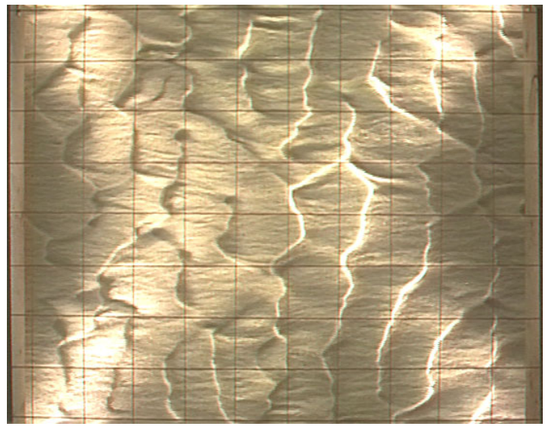

Figure 4.5: Transition between instantaneously initiated 2D and 3D dunes at flow strength A. Flow is from left to right.

At flow B bending is less perceptible, and does not occur at flow C, the lowest instantaneous initiation flow strength. Presumably this phenomenon is caused by side wall drag, where the wall fluid is moving slightly slower compared to fluid in the centre of the flume. The cross-stream gradient is strongest at the greatest flow strengths.

As the 2D bed (and 2D bed with bending crests) persists, crest defects sporadically form, which are minor, transient excesses or deficiencies of sand in the crestline. Figure 4.6 shows several crest defects developed in the 2D field that appear similar to dune blowouts observed along coastal sand dunes formed by sea breezes [*Hesp and Hyde*, 1996]. Crest defect development can probably be linked to turbulent busting over the 2D bed, but the measurements taken herein are inappropriate to test this hypothesis.

Crest defect features are passed from crest to crest and can be seen to migrate though the dune field (Figure 4.7). When the defect is formed a volume of sediment is generated downstream causing a convex downstream bulge in the crestline in-line with the defect. The parcel of sand that composes the defect is elongated downstream, flattening it. The dune crestline acts as a barrier to flow. Once it is removed in the form of a crest defect, the downstream crestline is exposed to a greater flow velocity than the rest of the downstream crest and another blowout is formed in line with the previous defect. The defect sand parcel is thus cleaved from the crestline and passed to the downstream crest.

Crest defect features move through the bedform field at a velocity ~2× the dune migration rate. The defects in Figure 4.6 moved at an average rate of 2.9 mm s^{-1} while the bedforms were moving at only 1.5 mm s^{-1}. The larger defects, such as A and F, moved through the dune field more quickly than the others, with velocities of 3.6 and 3.5 mm s^{-1} respectively. Smaller defects, such as D and B, tend to move slowly; both moved at a velocity of 2.5 mm s^{-1}.

Crest defects are of little consequence when the bed is composed of straight or slightly sinuous dunes. Defects are successfully passed from one crestline to the next without altering the

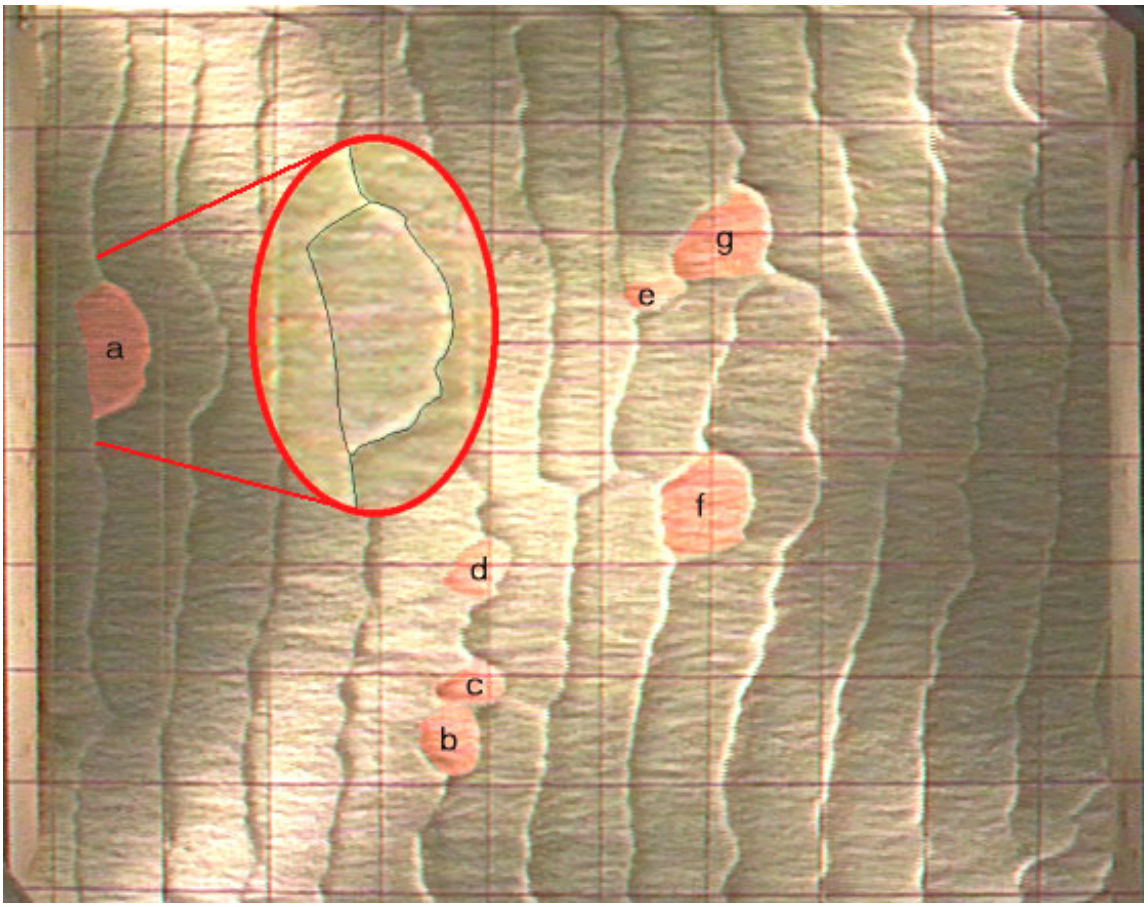

Figure 4.6: Crest defects developed during Run 54 at $t = 320$. $\Lambda_{NDS} \approx 1.1$. The area in the red oval is defect 'a' magnified by 200 %. Flow is left to right.

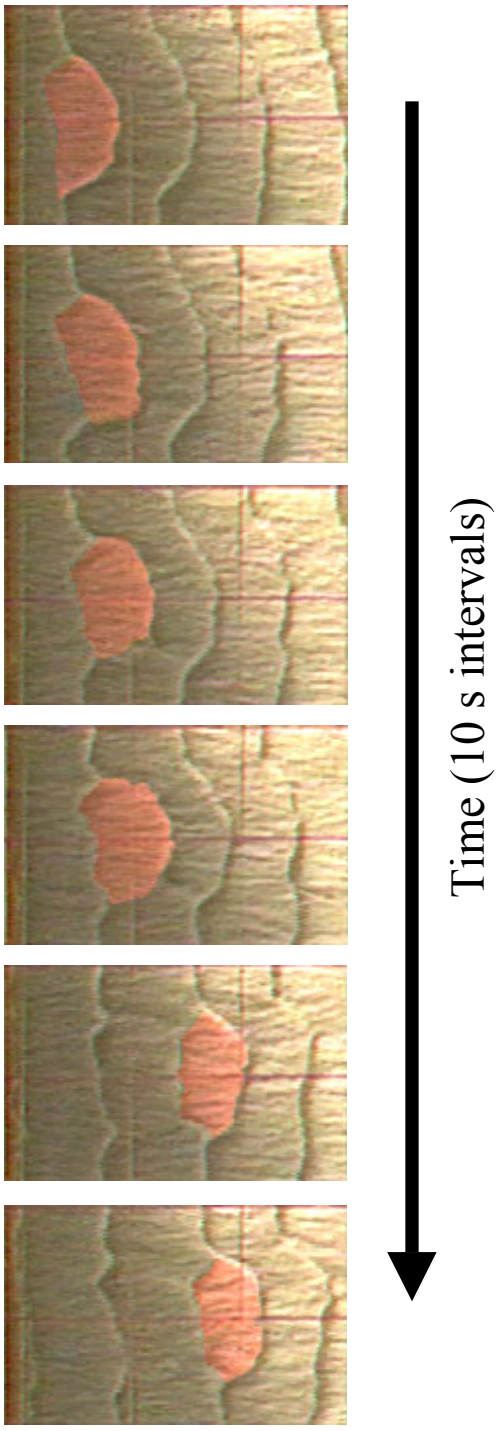

Figure 4.7: Progression of defect ‘a’ from Figure 4.6 as it migrates from one crest to the next (t = 320-370 s). The area highlighted red is the parcel of sand passed from one crest to another. Note the effect of defect progression on the downstream crest before it cleaves from the upstream crestline. Flow is left to right.

morphological characteristics of the crest (Figure 4.7). Crest defects are generally passed through a few crestlines and then disappear when the bed is 2D and so the field appears able to 'swallow' a limited number of defects. However, the number of crest defects increases with time and the 2D field is eventually overwhelmed (Figure 4.5c-d). When this occurs, crest defects slow their downstream march and eventually stop, causing permanent changes in the crestline. The defects interact and the bed falls into a cycle where the 3D bed is maintained, indefinitely.

4.4.3 Operation and Maintenance of the 3D Bed

Allen [1973] provided a description of the mechanisms associated with a 3D bed that *Baas* [1994; 1999] aptly called ripple 'birth-and-death processes'. According to *Allen* [1973], death can occur by a number of different processes. Rapid deceleration of a ripple or crest can occur if the crestline becomes strongly concave downstream which leads to a concentration of the lee side vortex and a deep scour pit. The increased erosion can accelerate the next crest's (crests') downstream migration, starving downstream crests of material and allowing the accelerating ripple to overtake the downstream ripples. Increasing the local height of a ripple may also lead to downstream features being planed off, and one or more crestlines being destroyed by the efficiency of the separation vortex.

Allen [1973] indicated that new ripples may be developed by a crestline splitting along its cross-stream length at spurs, which are ridges of sand on dune backs perpendicular to crestlines. Alternatively, a new ripple of limited height may be generated on an existing ripple back that grows in height and splits the original ripple length. *Allen* [1973] noted that all these processes are at work on the bed at any one time. Only in exceptional cases did these processes lead to the generation or extinction of a ripple.

Most of *Allen*'s [1973] description focused on what was happening to produce or destroy bedforms along a streamwise transect cut into the bed (a 2D plane). This is appropriate because

Allen's [1973] primary interest was in explaining certain types of cross-stratification that are typically examined in a 2D plane of the rock record. All the processes that *Allen* [1973] described are occurring; in a 2D plane however, these processes are secondary to a dominant processes observed to maintain the 3D bed.

This process is the growth of crestline lobes that extend downstream (Figure 4.8). Lobe extension is caused by localised increases in bedform height across the flume and erosion of a scour pit in the lee of the bedform. As the increased available sediment extends the lobe, it will sometimes stop and be planed out. Frequently the lobe will begin to locally starve the downstream crestline of sediment while the rest of that crestline continues to move (Figure 4.8b). Eventually, the upstream and downstream crestlines will meet and two fragments will join (Figure 4.8c) forming a new crestline and two bifurcations (Figure 4.8d). Concurrent with this process, local crestline heights are increased in downstream dunes forcing new crest lobe growth downstream. As long as H and L vary across the channel, this process of lobe extension will continue, inevitably maintaining the 3D bed. Once the bed becomes 3D it cannot become 2D again without some external driving force, such as a change in flow rate. During flow E, when the flow rate was increased (see Chapter 2), 2D dunes briefly re-established themselves, but became 3D a short time later.

Given these observations, it is necessary to ask if there really is a birth-and-death process that occurs on the 3D bed. A simple answer is 'no' because new bedforms are rarely created or destroyed when the bed is examined in plan. There is a constant rearranging of crestlines that gives the appearance of the birth and death process in the 2D plane. This observation may have eluded previous investigators as their research was conducted in flumes where the ratio L/y_w was too small, inducing scale effects on planimetric dune morphology.

As discussed in Chapter 2, *Raudkivi and Witte* [1990] have suggested that bedforms actually grow in length through the birth and death cycle by the coalescence of smaller bedforms, because smaller bedforms have larger migration rates, R, and can overtake the larger features on a bed.

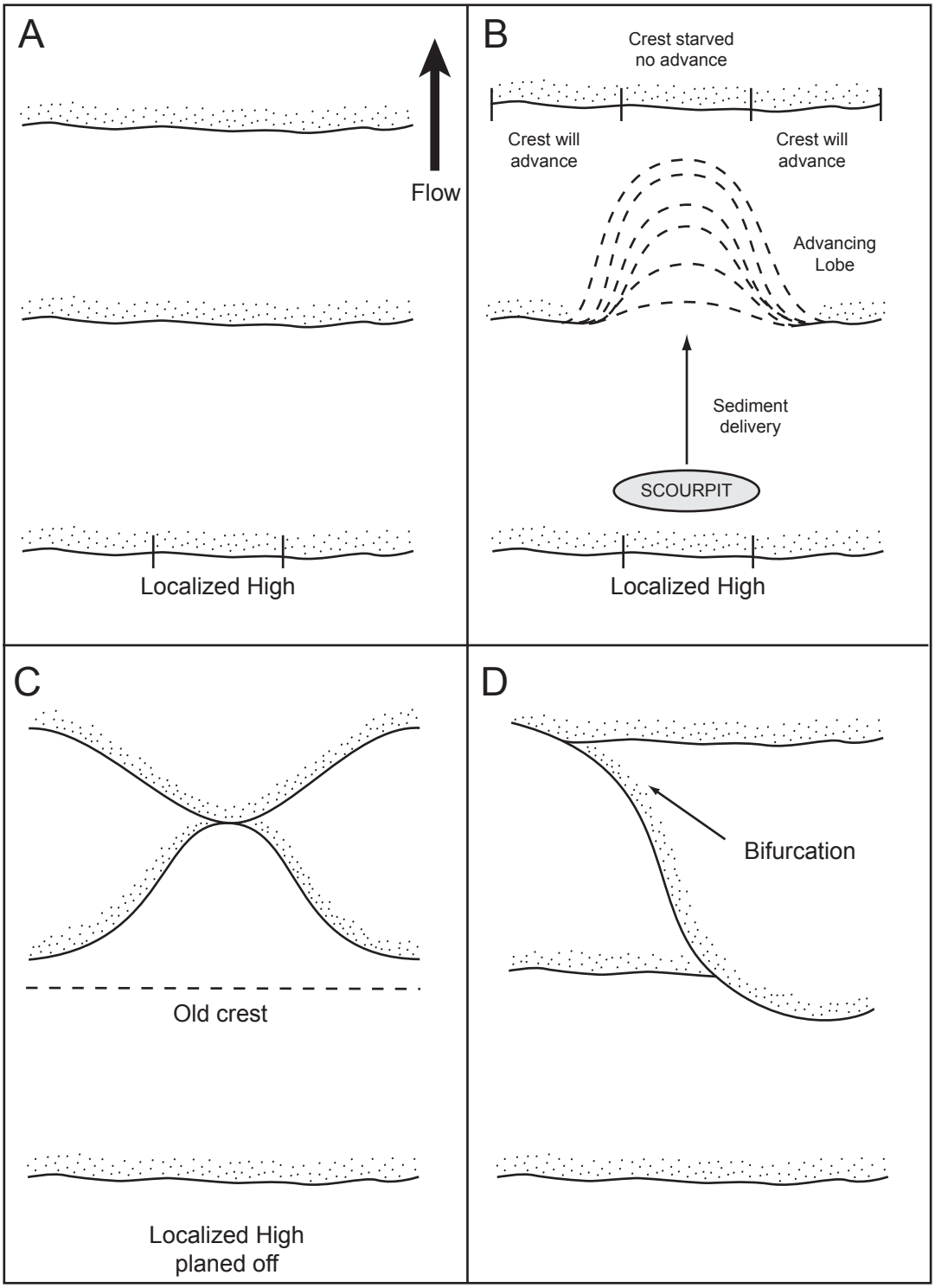

Figure 4.8: Schematic of an advancing crestline lobe as it joins with the downstream crestline and generates bifurcations.

Ditchfield and Best [1990] argued against this idea, indicating that there is no relation between bedform size and the migration rate, R. They also suggested that bedforms may both grow or attenuate without interaction with other bedforms, or alternatively, they may coalesce as they migrate.

In contrast to *Ditchfield and Best* [1990], a strong relation was observed between L and R for some runs (see Figure 2.8). Bedform coalescence was observed during the experiments, but it was limited to the sand sheets combining with the dune crestline. This was equilibrium process that maintained transport over the dune and did not cause dune growth. Widespread bedform coalescence did not occur amongst the dune population; rather, crest realignment by the growth of scour induced crest lobes dominated. It appears that the bedform unification models advocated by *Raudkivi and Witte* [1990] and by *Coleman and Melville* [1992] need to be re-examined.

4.5 Drag Reduction Mechanisms

Recent advances in the aerodynamics literature have suggested that surface drag can be significantly altered by the arrangement of perturbations on otherwise flat surfaces. *Sirovich and Karlsson* [1997] examined flow over 'riblets' (basically the opposite of dimples in a golf ball) in an effort to determine what sort of riblet patterns would be effective in reducing drag on airplane surfaces. This research demonstrated that a strictly 2D aligned pattern of riblets (Figure 4.9a) produced a larger drag than a smooth surface while an out-of-phase random pattern (Figure 4.9b) produced a lower drag than a smooth surface. Hydraulic drag can be reduced by up to 20 % by changing the arrangement of perturbations. The researchers demonstrated that random orientations of riblets effectively modulate the burst-sweep cycle, reducing boundary shear stress.

The work of *Sirovich and Karlsson* [1997] may have profound implications for sandy bedform evolution in river channels. The aligned pattern of riblets can be considered analogous to 2D bedforms while the random orientation of riblets is analogous to the random 3D linguoid

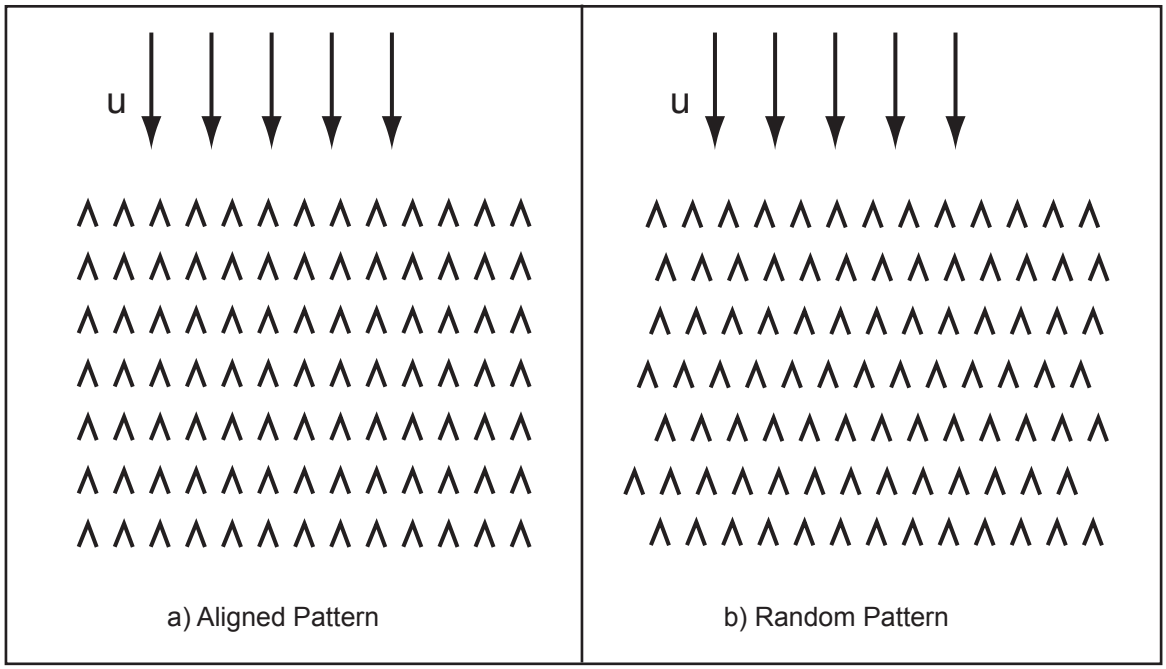

Figure 4.9: Plan view of strictly two-dimensional aligned pattern and out-of-phase random pattern of riblets examined by Sirovich and Karlssen (1997).

morphology, identified as the equilibrium bed morphology here and in other studies [see references above]. Thus, a sediment bed composed of randomly arranged bedforms, as opposed to straight crested 2D bed features, may reduce or stabilise the shear stress. Transport and erosion rates are strongly dependent on the shear stress. Therefore decreasing or stabilising shear stress can contribute to the stability of the bed by reducing the likelihood of degradation. In order to test these ideas, it is necessary to examine the behavior of drag as changes in bed morphology occur, which requires the calculation of a time dependant drag coefficient, C_D, and drag force, F_D.

4.5.1 Calculating Drag Coefficients and Drag Force

The standard form of the drag coefficient is

$$C_D = 2\left(u_* / \overline{U}\right)^2 \qquad 4.5$$

where u_* is the shear velocity and $\overline{U}$ is the mean channel velocity. The drag force is calculated from

$$F_D = \frac{1}{2} C_D \, r_w \overline{U}^2 A_b \qquad 4.6$$

where r_w is the density of water and A_b is the effective cross-sectional area of a body [*Roberson and Crowe*, 1993]. For dunes, $A_b = H \cdot L_y$, where H is dune height.

It is important to note that F_D, and the associated C_D, represent the total drag. Following *Einstein and Barbarossa* [1952] the total drag force F_{tot} is the sum of the skin drag, F_{sf}, which is related to the resistance to flow offered by the sediment grains, and form drag, F_{form}, which is resistance to flow offered by the bedform morphology. It is widely thought that the transport rate over a dune stoss slope is related only to F_{sf}.

Based on an approach to divide these quantities by *Smith and McLean* [1977], *Nelson et al.* [1993] present equations that may be used to calculate F_{sf} and F_{form} separately. Unfortunately, the

calculations require detailed velocity profiles downstream of the reattachment point, for each bedform, which are not available, but this problem can be circumvented. One grain size was used in all experiments, so the grain related roughness remained approximately the same for all the bedforms observed, whether 2D or 3D. Some variation in F_{sf} may be caused by the intensity of sediment transport over different bedforms but that is, arguably, another component of F_{tot} [*Wiberg and Nelson*, 1992].

Since direct calculation of F_{sf} and F_{form} is not possible, this investigation is primarily concerned with the variation of F_{tot} (and the associated C_D). Under the assumption that F_{sf} is near constant, most of the change in F_{tot} is related to change in F_{form} which is thought to be unrelated to the transport rate over a dune stoss slope. This complicates the idea that drag reduction can decrease or stabilise transport rates. However, this should not be a problem because when a bedform field is considered as a whole, the transport rate increases with the total applied shear force (F_{tot}).

In order to calculate $C_D(t)$ and $F_D(t)$, u_* and $\overline{U}$ must be calculated as a function of time. The shear velocity can be calculated from its definition

$$u_*(t) = \sqrt{\frac{t_S(t)}{r_w}} \qquad 4.7$$

where

$$t_S(t) = r_w g S(t) d(t) \qquad 4.8$$

and r_w is the density of water, g is acceleration due to gravity, d is flow depth. Because S has been measured continuously, only d need be estimated from measurements, which as a function of time is

$$d(t) = d_{st} - z_{bed}(t) + z_{WS}(t) \qquad 4.9$$

where d_{st} is its initial value at the beginning of the experiment, z_{bed} is the change in the mean bed level and z_{WS} is the change in the water surface. The mean velocity can be adjusted as a function of time using $d(t)$ such that

$$\overline{U}(t) = Q/\left(d(t) \cdot y_w\right) \qquad 4.10$$

where Q is the discharge and y_w is the channel width.

4.5.2 Flow Depth and Velocity as a Function of Time

The first step in calculating $C_D(t)$ and $F_D(t)$ is to determine z_{bed}. Unfortunately, bed level could not be monitored while the video and water level sensors were being operated – the echo-sounders disturbed the water surface. However, bed level erosion as a function of time can be estimated from echo-soundings collected during other experimental runs. Thus, the echo soundings discussed in Chapter 2 are used to determine best-fit curves through crest heights, z_C, and trough heights, z_{Tr} and the mean bed level as a function of time is

$$z_{bed}(t) = \frac{z_C(t) + z_{Tr}(t)}{2}. \qquad 4.11$$

The height of dune crests increases exponentially to an asymptote and can be expressed by

$$z_C(t) = c_C + a_C\left(1 - e^{-b_C t}\right) \qquad 4.12$$

while the height of dune troughs decrease exponentially to an asymptote and can be expressed by

$$z_{Tr}(t) = c_{Tr} + a_{Tr} e^{-b_{Tr} t} \qquad 4.13$$

where a, b and c are coefficients determined from least-squares regression (Figure 4.10 and Table 4.2). As with the exponential fits to the growth in L and H in Chapter 2, r^2 values varied but were generally lower for the lesser flow strength runs where there are fewer observations. All but one of the regression fits are significant at the 95 % confidence interval. Only the z_C model fit at flow E is not significant, but there is an apparent visual fit of the curve to the data (Figure 4.10). At flow C,

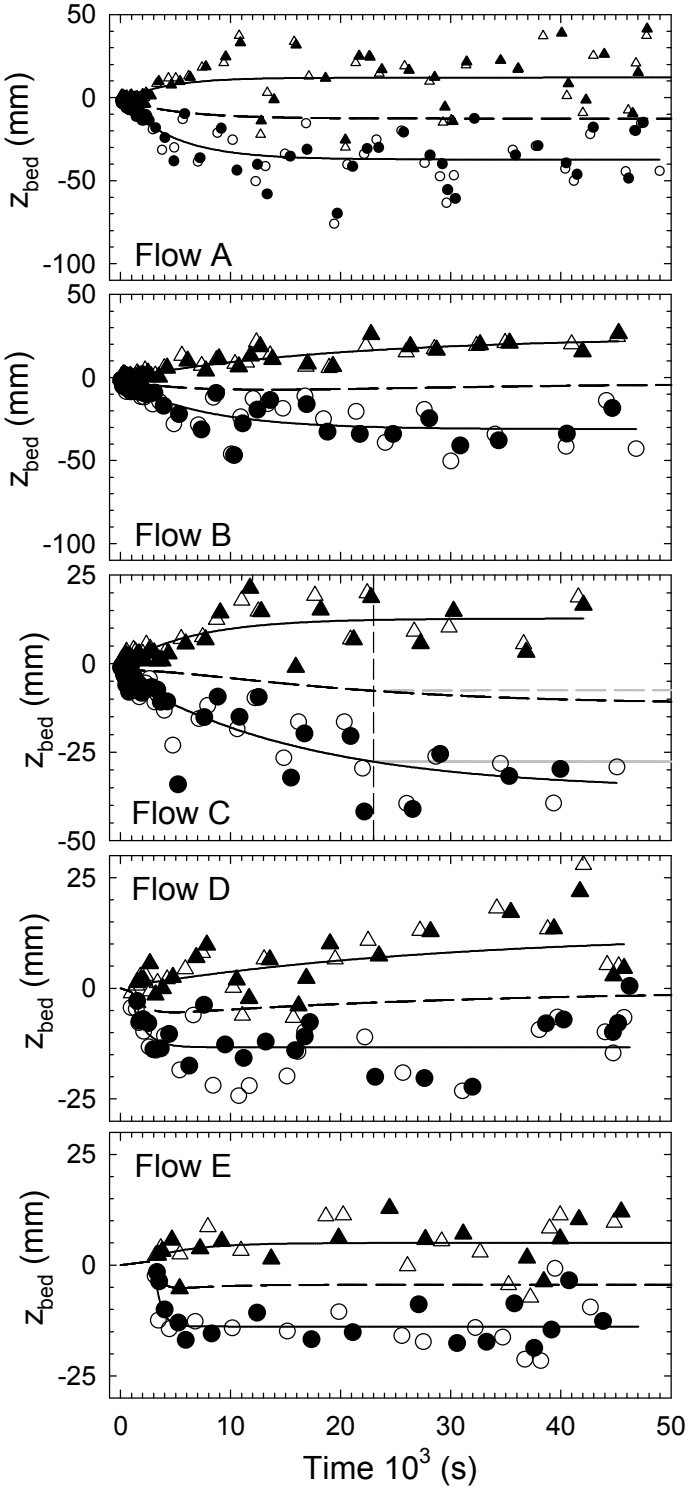

Figure 4.10: Change in bed level. Triangles are the heights of dune crests, z_C, and circles are heights of dune troughs, z_{Tr}, measured using the echo-soundings discussed in Chapter 2. Open symbols are data from echo-sounder 1 and closed symbols are data from echo-sounder 2 (see Figure 2.3). Solid lines are exponential least-squares regressions through the crests or troughs (coefficients are in Table 4.1). Dashed lines are the change in the mean bed level, $z_{bed} = (z_C + z_{Tr})/2$. The vertical line in the middle panel at $t = 23000$ s is where $z_{Tr}(t)$ was forced to a constant value. The effects of this adjustment are shown by the gray lines.

Table 4.2: Model fitted results for crest height and trough height.

Flow	Run	c_C mm	a_C mm	b_C $\times 10^{-4}$	r^2 z_C	$p - z_C$	c_{Tr} mm	a_{Tr} mm	b_{Tr} $\times 10^{-4}$	r^2 z_{Tr}	$p - z_{Tr}$
A	26	-2.123	14.205	2.488	0.18	<0.001	-37.240	36.463	2.117	0.68	<0.001
B	27	-0.650	24.971	0.506	0.85	<0.001	-31.072	28.313	1.322	0.68	<0.001
C	28	-0.255	12.994	1.500	0.58	<0.001	-35.778	32.469	0.603	0.77	<0.001
D	29	0.174	12.421	0.338	0.30	0.001	-13.348	25.069	8.396	0.18	<0.001
E	30a	-1.485	6.498	2.450	0.04	0.567	-13.873	2315.1	16.780	0.30	0.015

$z_{Tr}(t)$ does not reach an asymptote, which becomes problematic later in the analysis. Therefore, after 23000 s $z_{Tr}(t)$ is forced to a constant value.

The next step in calculating $C_D(t)$ and $F_D(t)$ is to determine $z_{WS}(t)$. The rise in the water surface was measured at ~10.9 m from the head box (sensor 2 in Figure 2.3) which is just downstream of where the measurements that went into estimates of z_{bed} were taken. Initially z_{WS} dropped several millimetres when flow was initiated. However, within a few minutes bedforms developed that increased resistance to flow, causing a rise in the water surface that varied amongst runs, but generally decreased with flow strength (Figure 4.11). With growing bedform size, z_{WS} continued to increase. It is expected that $z_{WS}(t)$ would increase asymptotically and reach an equilibrium value, z_{WSe}, after some time (subscript e indicates an equilibrium value). Beyond this point, no significant increases or decreases in z_{WS} would be expected. Slope of the $z_{WS}(t)$ curves all tended toward zero after some time period. While some records achieved what appears to be equilibrium, others displayed a gradual increase over the remaining hours of the experiment. It is likely that this gradually increasing portion of the records represents an equilibrium state. The water level rise in these records was < 2 mm. Slight changes in the volume of water in the flume, changes the volume of sediment available for transport along the channel, or potentially, a large water temperature change could cause a gradual increase in the trend of z_{WS}. Keeping this in mind, values of z_{WSe} increase with flow strength.

The variability in z_{WS} about z_{WSe} also increased with flow strength. At flow strength A, minimum and maximum running averages of z_{WS}, after z_{WSe} is reached, are separated by 8 mm while at flow E, this separation is < 1 mm. Not all the variation in z_{WS} is associated with the increased resistance to flow; some of it is related to the progression of the dunes. According to Bernoulli's principle, the water surface will fall over the dune crest due to accelerated flow and rise over the

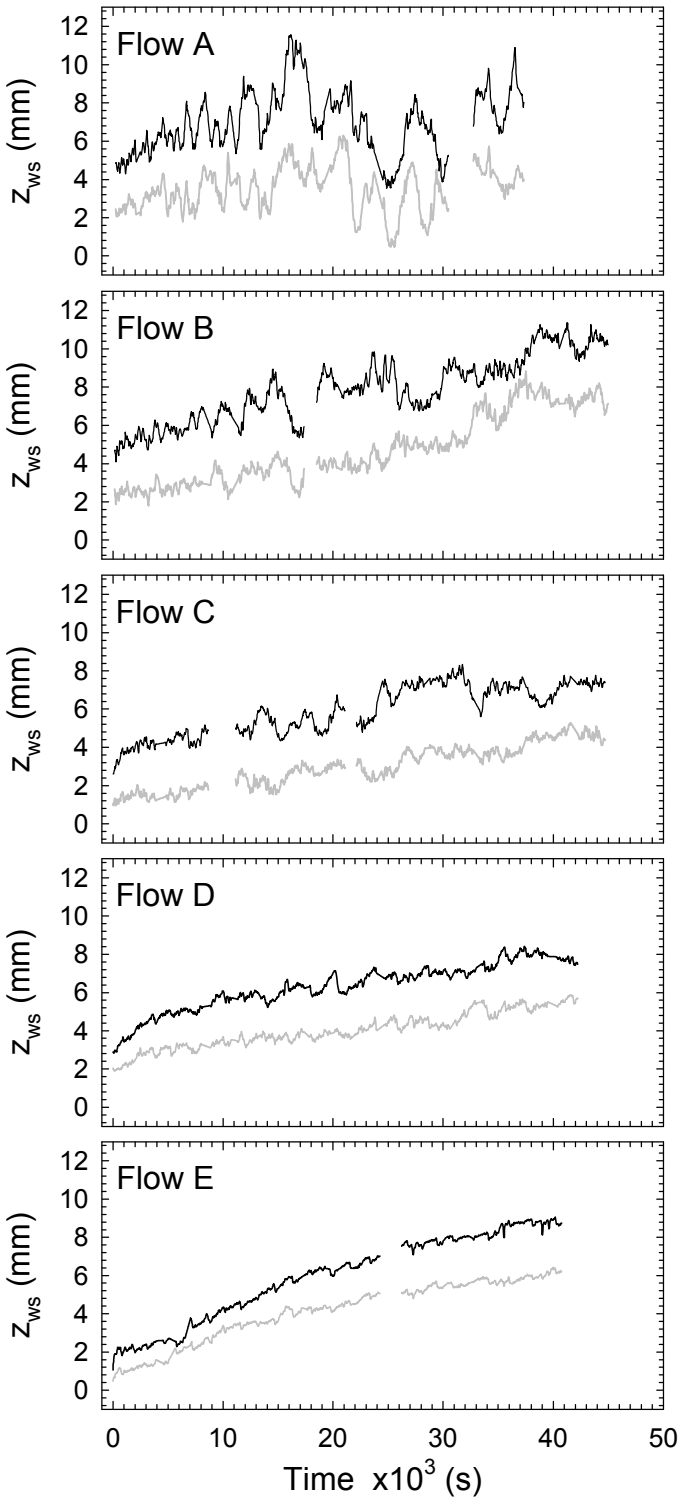

Figure 4.11: Water surface level records. Black lines are data from water level sensor 1 and gray lines are data from water level sensor 2 (see Figure 2.3). The datum is the flat water surface before the experiment started.

dune trough due to decelerated flow. When the dunes are large, as at flow A, the rise and fall of the water level over the dune crest and trough is several mm about the mean for that bedform. As equilibrium bedform size decreases with flow strength (see Chapter 2), this variability is reduced.

Figure 4.12 displays $d(t)$, calculated using Equation 4.9. Flow depth increases asymptotically towards a maximum for all runs and $\overline{U}(t)$ responds by decreasing asymptotically. Note that had the original $z_{Tr}(t)$ function at flow C been used, $d(t)$ would have been a continuously increasing function and $\overline{U}(t)$ would have been a continuously decreasing function, which would have been counter to observations during the run. Interestingly, in flows D and E, both d and $\overline{U}$ only begin to change significantly when bedforms migrate into the field of view from the head box. Obviously, these cross-channel bedforms have a dramatically different effect on resistance to flow than the bed defect developed fields.

4.5.3 Shear Stress as a Function of Time

Both $S(t)$ and $t_S(t)$ are displayed in Figure 4.13. Generally, S underwent an initial period when it increased after the flow was established and then varied about what appears to an equilibrium value after equilibrium 3D bedforms were established. At flow E, S does not appear to reach an equilibrium value, which is not surprising given the increasing trends in the water surface level sensor records at this flow. Initial water surface slope, S_i, is of the order 10^{-3} and increases with flow strength (Table 4.3).

Once equilibrium 3D bedforms have developed, mean slope, $\overline{S}_e$, increases substantially. At flow strengths A, B, and C the increase is 30.6 - 45.7 %. At the lower flow strengths, $\overline{S}_e$ is up to 109.4 - 154.5 % S_i (Tables 4.3 and 4.4). Variability in equilibrium values of parameters is quantified using the coefficient of variation, CV, which is the standard deviation divided by the mean. The variability in S_e is relatively large compared with the early portions of the record

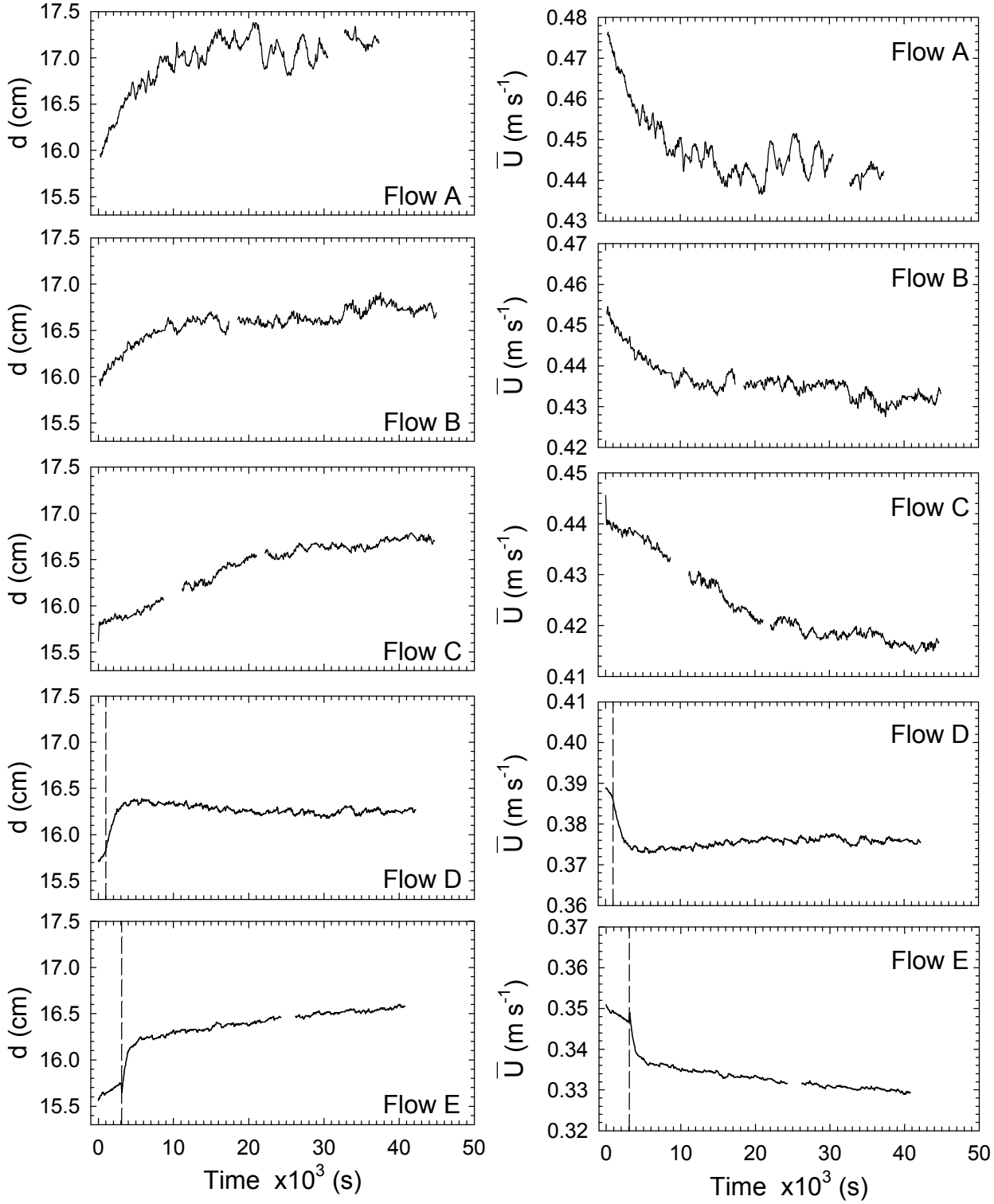

Figure 4.12: Flow depth, d , and mean flow, U , calculated as a function of time. Vertical lines indicate when bedforms developed at the head box migrated into the measurement section at flows D and E.

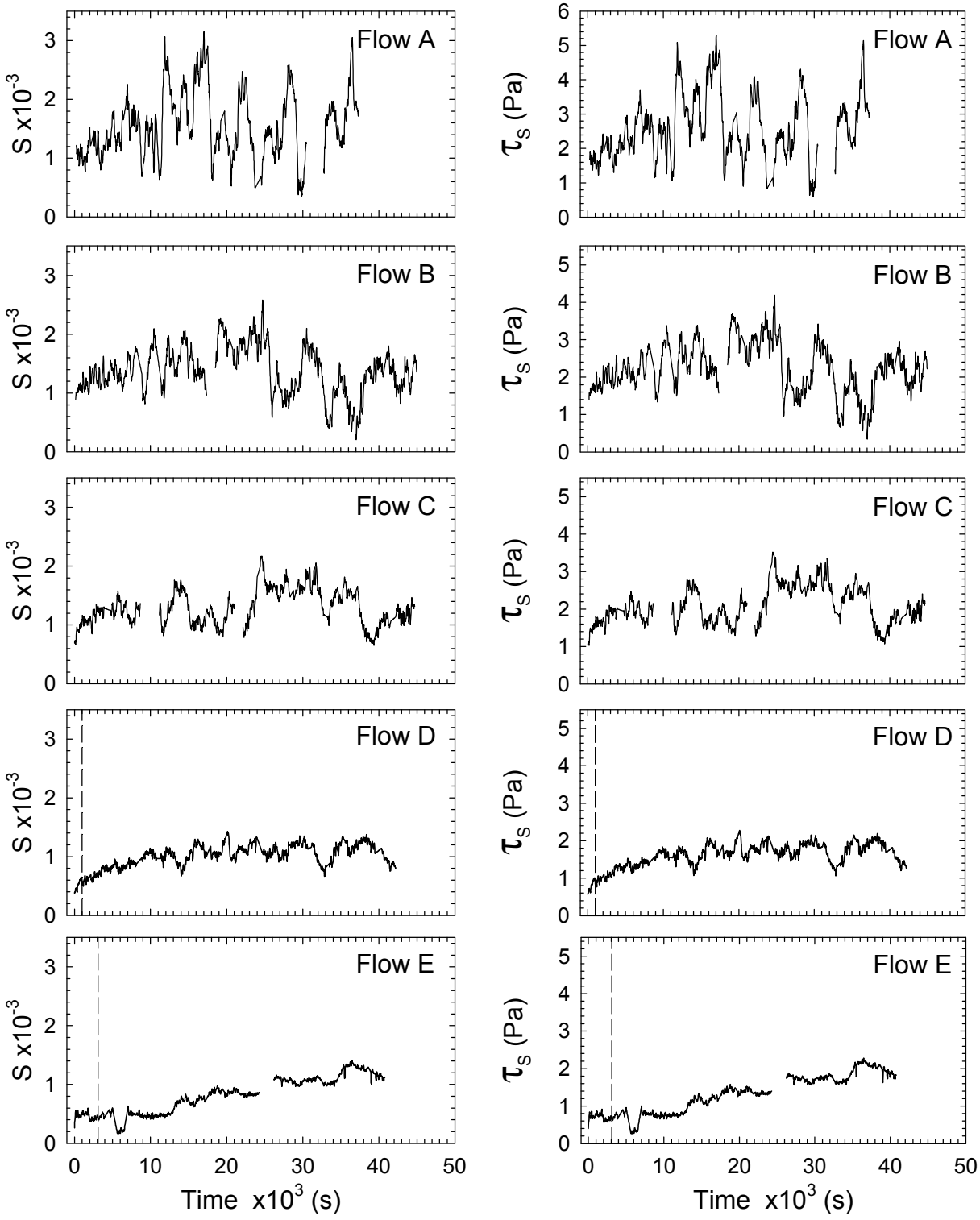

Figure 4.13: Measured water surface slope, S, and shear stress calculated from the depth slope product, τ_S, as a function of time. Vertical lines indicate when bedforms developed at the head box migrated into the measurement section at flows D and E.

Table 4.3: Initial values of parameters used to calculate C_D and F_D calculated at $t = 300$ s.

Flow	Run	d_i (m)	$\overline{U}_i$ (m s^{-1})	$S_i \times 10^{-4}$	t_i (Pa)	C_{Di}	F_{Di} (N)
A	53	0.1593	0.4763	12.18	1.9043	0.0168	3.24
B	54	0.1593	0.4540	9.60	1.4992	0.0145	4.55
C	57	0.1580	0.4404	9.39	1.4562	0.0150	2.09
D	59	0.1574	0.3883	4.26	0.6569	0.0087	1.04
E	55	0.1561	0.3497	4.49	0.6875	0.0112	0.90

(CV_{Se} = 13.2 - 38.1 %) and is largest at the greatest flow strengths. Some of this variability may be related to changes in bedform morphology, but a large portion is related to the rise and fall of the water surface with position over the dune, which is considerably enhanced or damped in the calculation of slope. The slope is enhanced when sensor A is over a dune trough and sensor B is over a dune crest. Slope is damped when the opposite positioning occurs. Since the water level deviation over a dune increases with bedform size and dune size increases with flow strength, variability in S increases with flow strength (Table 4.4).

Bulk shear stress calculated using Equation 4.8, is strongly dependent on S and follows the same pattern, increasing from an initial value and then varying about an equilibrium value. Initial shear stress values, t_{Si}, varied between 1.90 and 0.66 Pa, decreased with flow strength and were in accordance with values reported in Chapter 2. Note that t_{Si} at flows D and E are for defect developed fields and not full width fields that later encroached upon the measurement section from the head box. Mean equilibrium shear stress, $\bar{t}_{Se}$, is 40.1 - 52.3 % larger for flows A, B, and C while at flows D and E, $\bar{t}_{Se}$ is 163.2 - 120.9 % larger. Variation in t_{Se} is similar to that observed for equilibrium slope; CVt_{Se} is within $\pm$ 1 % of CV_{Se}. The only fluctuating properties in the calculation of C_D and F_D are d, S and $\overline{U}$, which are already strongly interrelated. Therefore, the variability in equilibrium C_D and F_D, will be the same as for t_{Se}.

4.5.4 Drag Coefficients and Force as a Function of Time

Figures 4.14 and 4.15 display $C_D(t)$ and $F_D(t)$, respectively, with H overlain for reference. It is useful to make a brief comment related to C_D before proceeding with a discussion of its variability or any interpretation of patterns. The drag coefficient is often treated as a constant for a given body, but C_D tends to increase with body size [*Halliday et al.,* 1993]. In fluid mechanics, C_D for a given body is widely accepted to decline with increasing Reynolds Number, $\mathrm{Re} = \ell U_b / n$ (ℓ is a

Table 4.4: Equilibrium values (after 10000 s) of parameters used to calculate C_D and F_D.

Flow	Run	$\overline{d}_e$ (m)	$\overline{U}_e$ (m s^{-1})	$\overline{S}_e$ 10^{-4}	$s\,S_e$ 10^{-4}	$\overline{t}_e$ (Pa)	$s\,t_e$ (Pa)	$\overline{C}_{De}$	$s\,C_{De}$	$\overline{F}_{De}$ (N)	$s\,F_{De}$ (N)
A	53	0.1711	0.4437	15.91	6.07	2.6685	1.0148	0.0271	0.0103	120.45	44.93
B	54	0.1665	0.4343	13.99	4.27	2.2836	0.6921	0.0242	0.0072	110.65	33.19
C	57	0.1655	0.4206	13.22	3.09	2.1466	0.5033	0.0243	0.0057	86.69	23.15
D	59	0.1626	0.3758	10.84	1.43	1.7291	0.2264	0.0245	0.0032	37.99	5.19
E	55	0.1645	0.3319	9.40	2.33	1.5187	0.3815	0.0276	0.0071	30.80	8.19

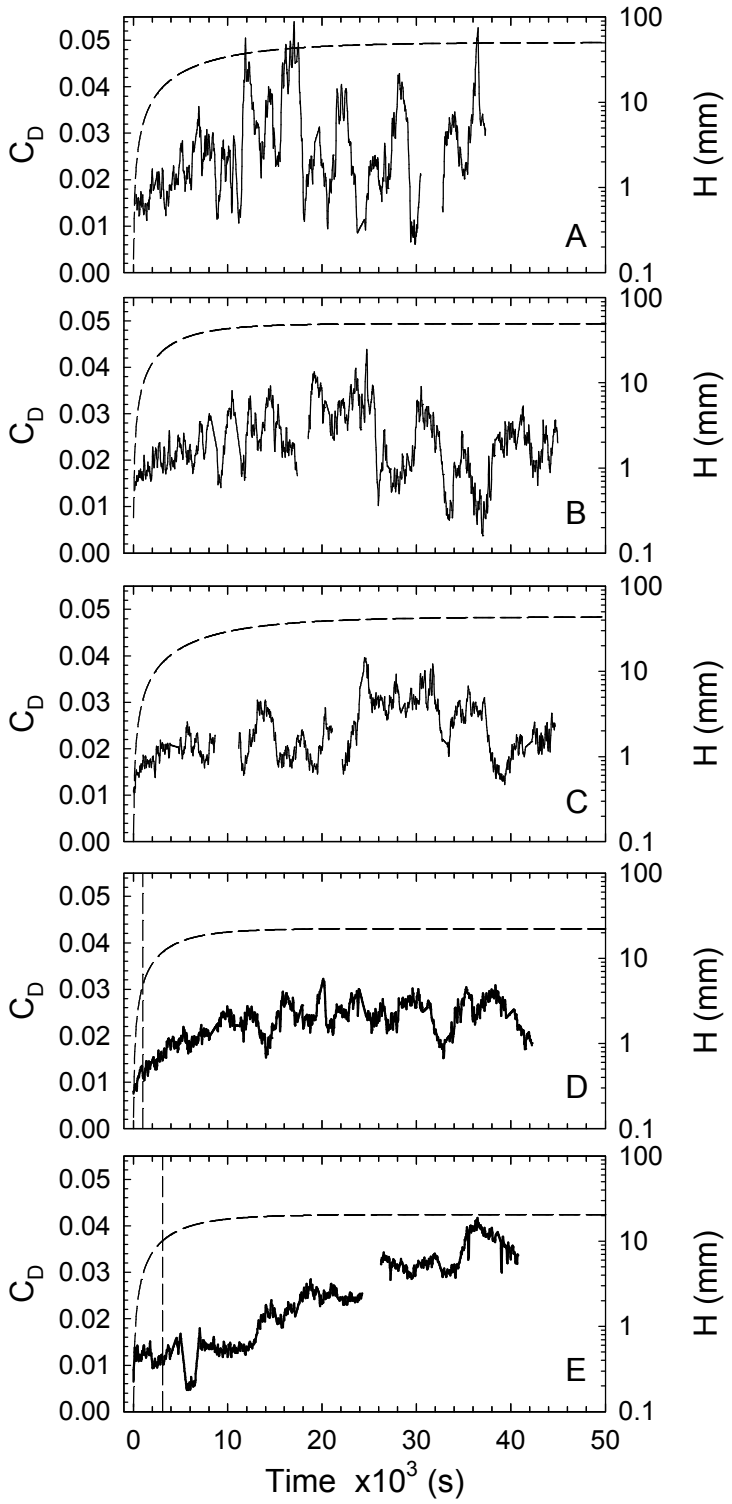

Figure 4.14: Drag coefficient, C_D, calculated as a function of time (solid line). The exponential increase in dune height, H, from Figures 2.6 and 2.7 are overlaid for reference (dashed line). Vertical lines indicate when bedforms developed at the head box migrated into the measurement section at flows D and E.

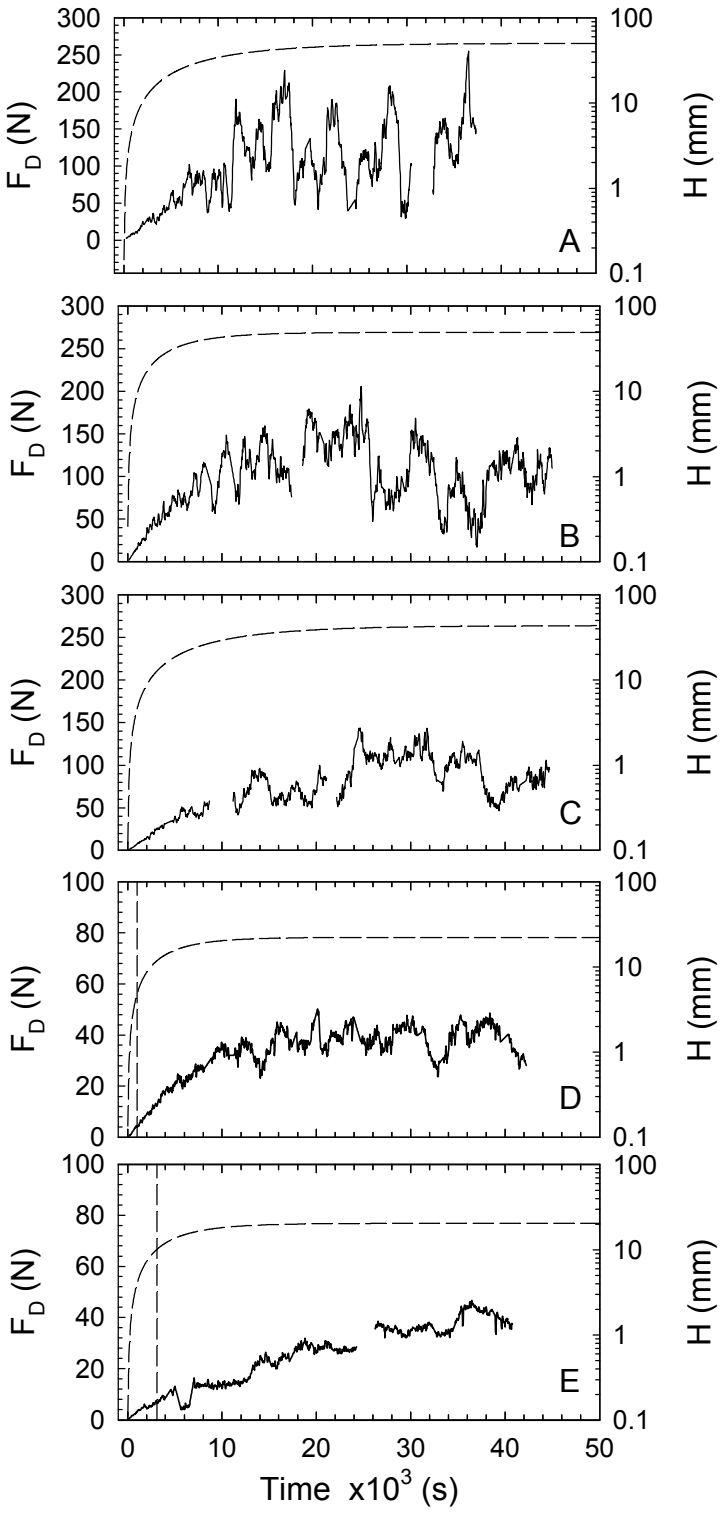

Figure 4.15: Drag force, F_D, calculated as a function of time (solid line). The exponential increase in dune height, H, from Figures 2.6 and 2.7 are overlaid for reference (dashed line). Vertical lines indicate when bedforms developed at the head box migrated into the measurement section at flows D and E.

characteristic length of the body, U_b is the relative velocity of the body to the fluid and n is the kinematic viscosity of the fluid) [*Roberson and Crowe*, 1993]. In sediment transport studies, it has been accepted for some time that sediment particle C_D decreases towards an equilibrium value, regardless of shape or density, with increasing Re [*Rouse*, 1946]. The reason for this change in C_D has been conclusively linked to changes in the boundary layer structure over particles at higher flows [*Stringham et al*., 1969]. It is significant to note that this experimentally determined relation holds only for particle sizes less than a few centimeters because C_D will increase with the body size at a constant flow. A larger body, such as a bedform, will generate a greater level of turbulence and hence a larger value of u_* than a smaller body. The increase in turbulence will decrease $\overline{U}$, but this occurs disproportionately because boundary layers develop. In separated flows, as over dunes, a dramatic increase in u_* with bedform size occurs with relatively modest decreases in $\overline{U}$ (as is demonstrated above). In summary, C_D should increase with dune size at a constant flow.

The drag coefficient experiences a general increase with bedform size (represented by H) until an equilibrium H is reached, after which C_D varied about an equilibrium value, $\overline{C}_{De}$. Values of $\overline{C}_{De}$ are similar for all runs, varying between 0.024 and 0.027 and, unlike $\overline{S}_e$ (or $\overline{t}_{Se}$), $\overline{C}_{De}$ shows no variation with flow strength (Table 4.4). Initial values of the drag coefficient, C_{Di}, at flows A, B and C are similar (0.014 - 0.017) and $\overline{C}_{De}$ is 61.3 - 66.9 % greater than C_{Di}. At flows D and E, C_{Di} is smaller (0.009 -0.011) and $\overline{C}_{De} >> C_{Di}$ (146.4 - 181.6 %) when compared to flows A, B and C. This is because C_{Di} at the lesser flow strengths is computed for the bed defect fields where part of the bed remains smooth. C_D increases when a defect field is overtaken by bedforms developed at the head box.

Figure 4.16 plots C_D against the areal bedform length (L_a) measured from the video (plots of L_a as a function of time can be found in Appendix C). The relation has a strict linear upper limit,

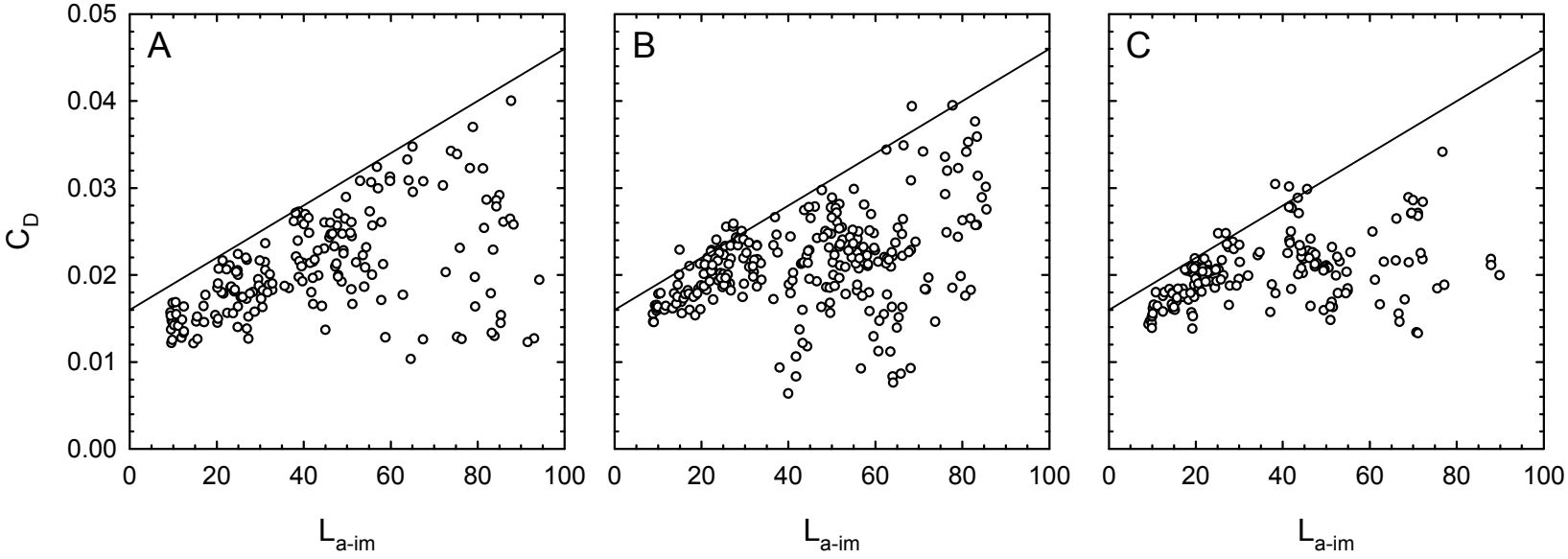

Figure 4.16: Drag coefficient, C_D, plotted against the areally averaged dune length, L_{a-im}.

but there is considerable scatter for some of the large bedforms where C_D is often less than expected. Some of this scatter is probably related to drag reduction. However, S and ultimately C_D are most strongly affected by fluctuations in z_{WS} associated with the bedforms when the dunes are large. Overall, C_D does appear to increase with dune size as expected.

The drag force is calculated using Equation 4.6 where H is estimated from the least-squares regressions calculated in Chapter 2 (see Figures 2.6 and 2.7 as well as Table 2.3). It is assumed that $L_y = y_w$. The drag force experiences a strong increase with bedform size. When H increases exponentially, all other variation in F_D is damped. This compromises the use of F_D as an indicator of drag reduction as the bedform size increases. However, F_D can be used when equilibrium H has been reached. Initial values of the drag force, F_{Di}, varied between 0.90 and 4.55 N and equilibrium drag force, $\overline{F}_{De}$, varied between 30.80 and 120.45 N. Both show a decrease with flow strength (Tables 4.3 and 4.4). There is a dramatic 23 - 36X increase in $\overline{F}_{De}$ over F_{Di} during the experiments.

4.5.5 Drag Reduction and Bedforms

Image-mean non-dimensional span is plotted as a function of time in Figure 4.17 (plots of raw Λ_{NDS} and Λ_{NDS} > 0.70 m data are in Appendix C). Descriptive statistics for Λ_{NDS} after $t_{\max}$ are presented in Table 4.5. For the 3D stage, Λ_{NDS-im} = 1.34 - 1.43 and $CV_{\Lambda_{NDS-im}}$ = 7 - 15 %. For the instantaneous development runs, minimum $\Lambda_{NDS-im} < 1.2$ and $\Lambda_{NDS-im} \approx 1.2$ for the lower flow strength runs during the 3D stage. Individual crests were observed where minimum $\Lambda_{NDS} < 1.05$ (Table 4.5). Maximum $\Lambda_{NDS-im} > 1.6$ for all runs, but the greater flow strength maximums are generally larger (Λ_{NDS} = 1.8 - 2.3) than the lesser flow strength maximums. Individual crests were observed where Λ_{NDS} was as high as 10, but the maximum for most runs was in the range 2 - 5 (Table 4.5).

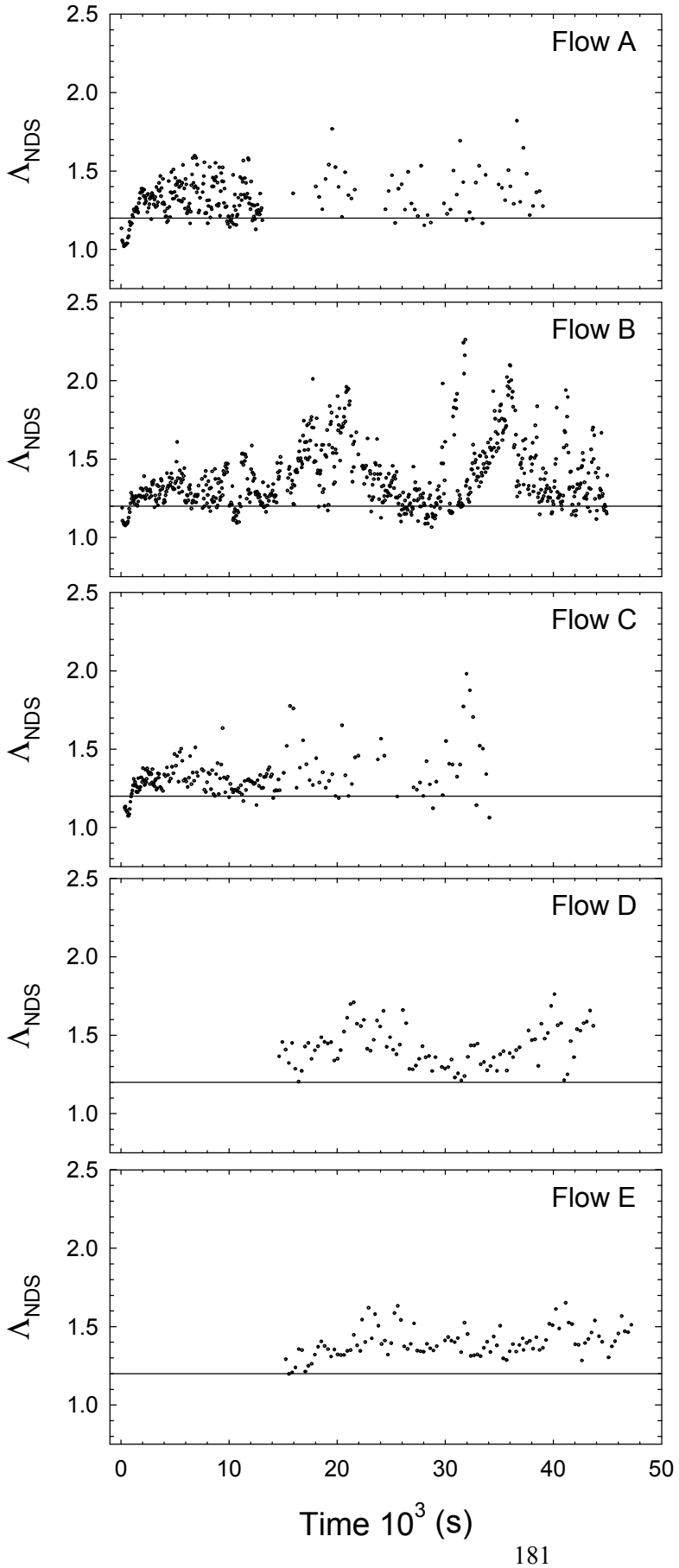

Figure 4.17: Non-dimensional span, Λ_{NDS}, time series. Data are image averages of crests whose cross-stream extent exceeds 0.7 m.

Table 4.5: Descriptive statistics for non-dimensional span of 3D bedforms.

Flow	Run	Image Mean				Raw Data	
		$\overline{\Lambda}_{NDS-im}$	$s\ \Lambda_{NDS-im}$	Max Λ_{NDS-im}	Min Λ_{NDS-im}	Max Λ_{NDS}	Min Λ_{NDS}
A	53	1.3422	0.1187	1.8204	1.1277	3.2395	1.0457
B	54	1.3971	0.2088	1.2617	1.0650	4.9570	1.0623
C	57	1.3355	0.1318	1.9810	1.0617	10.1481	1.0413
D	59	1.4256	0.1274	1.7608	1.2033	3.3540	1.0390
E	55	1.3986	0.0925	1.6510	1.1986	4.4790	1.0470

The most detailed Λ_{NDS} record was generated for Flow B, where there is clear evidence of at least two dramatic increases in the three-dimensionality of the bedforms in the video view, separated by ~4.5 hours, at 5.5 and 10 hours. There is no relevant time scale associated with the flow or the flume that might cause this. However, low relief bars are known to develop in flumes. Indeed, the long sediment pulses described in Chapter 2 seem to be evidence of them. It is easy to envision a scenario that might lead to changes in the flow velocity and depth, as a bar form passes, that could account for this increase in Λ_{NDS}.

In order to determine if drag reduction is occurring during the 2-3D dune transition, it is necessary to compare the Λ_{NDS} to C_D and F_D time series. Figure 4.18 plots the first hour of the C_D and F_D time series with a line indicating 2D and 3D stages determined when $\Lambda_{NDS} < 1.2$ and > 1.2 respectively. As noted above, the F_D time series is strongly dependent on H, which obscures any other patterns when H is increasing exponentially. There is no dramatic reduction in C_D after the dunes have become 3D; there is actually a 15-27 % increase (see Table 4.6). The C_D time series also occurs against a background of increasing bedform size, so it would be expected that it would increase like F_D, but this is not the case.

There is a minor increase in C_D after bedforms are initiated, between $t = 0$ s and t_c for Flows B and C (no C_D data are available before t_c at Flow A). Following this period, C_D remains stable at ~0.015, and then begins increasing, closer to where $t_{\max}$ occurs (when Λ_{NDS} increases to ~1.4). This has an important consequence. When C_D should be increasing, it is not, suggesting that indeed the change in morphology is reducing drag. Based on the dune H data from the echo-sounders presented in Chapter 2, there is an increase of 1129 (Flow A), 567 (Flow B) and 439 % (Flow C) in H between t_c and $t_{\max}$. Image averages of areal bedform length increase 413 (Flow A), 244 (Flow B) and 186 % (Flow C) over the same time period. This occurs with relatively little change in C_D.

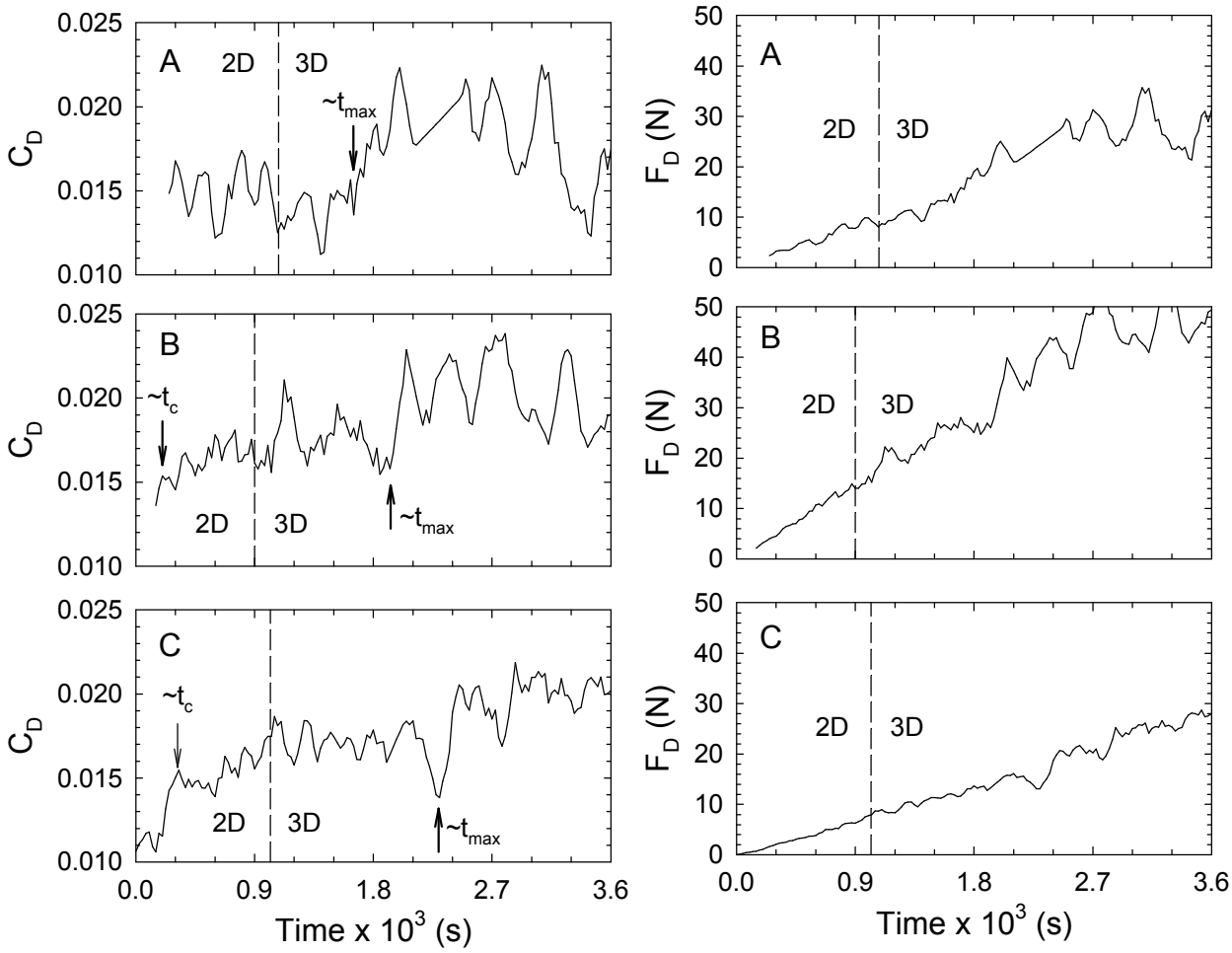

Figure 4.18: Drag coefficient, C_D, and drag force, F_D, calculated as a function of time over the first hour of the experiment. Vertical dashed lines indicate when the transition between two- and three-dimensional bedforms occurred in Figure 4.4. The time when dunes extend across the entire flume is t_c and $t_{\max}$ is when the non-dimensional span approaches 1.4 for the first time.

Table 4.6: Mean 2D and 3D C_D.

Flow	Run	2D t (s)	2D $\overline{C}_D$	3D t (s)	3D $\overline{C}_D$	2D/3D (%)
A	53	0-1080	0.0150	1080-3600	0.0172	15
B	54	0-900	0.0162	900-3600	0.0191	18
C	57	0-1020	0.0144	1020-3600	0.0183	27

Another way of examining whether drag reduction occurs with increases in Λ_{NDS} is to compare Λ_{NDS} and C_D records to determine if they are out of phase. If an increase in Λ_{NDS} causes a decrease in C_D the two are dynamically linked. In order to further examine this possibility, Λ_{NDS} and C_D time series were correlated. It is important to note that there are increasing and equilibrium portions of some of the time series. These portions need to be separated. The increasing portions of the Λ_{NDS} and C_D time series will inevitably produce positive correlations which betray the true nature of the phase relation. Therefore, at flows A, B and C, time series were split into stages when H was increasing (prior to 5000 s) and when H was in equilibrium (after 10000 s). At flows D and E, Λ_{NDS} data are already restricted to the equilibrium portions of the record.

The first step in the correlation analysis was to determine if Λ_{NDS} and C_D are normally distributed using a Kolmogorov-Smirnov Normality Test. If the normality test p value exceeds 0.05, at the 95 % confidence level, the distribution is normal. Table 4.7 demonstrates that few of the selected time series portions are normally distributed, so Pearson Product Moment Correlation is inappropriate. Spearman's Rank Order Correlation does not assume the data are normally distributed and, therefore, was used for the analysis.

For the equilibrium portions of runs at flows A, B and D, the correlation coefficients, r, are negative, as expected, but none are statistically significant (Table 4.7). At flow strength C, r is positive but the result is not significant at the 95 % confidence interval. At flow strength E, r is positive and the result is significant at the 95 % confidence interval. These results are surprising as visual inspection of the time series suggests that there are portions where Λ_{NDS} and C_D are clearly out of phase (Figure 4.19; full records are in the Appendix C). Most other portions show no relation or are poorly in phase. Of the two dramatic increases in Λ_{NDS} at roughly 5.5 and 10 hours during the run at Flow B, C_D is significantly lower than the mean for one and higher than the mean for the other.

Table 4.7: Results of Spearman Rank Order correlations between Λ_{NDS} and C_D. Normality test p-values are given for both Λ_{NDS} and C_D, separated by a slash.

Flow	Run	Normality Test p	n	r	p
A	53	0.004/ 0.020	103	-0.132	0.182
B	54	<0.001/ 0.418*	549	-0.036	0.397
C	57	0.388*/ 0.093*	91	0.072	0.494
D	55	<0.001/ <0.001	90	-0.060	0.575
E	59	0.388*/ 0.093*	85	0.258	0.017*

*Statistically significant at the 95% confidence interval

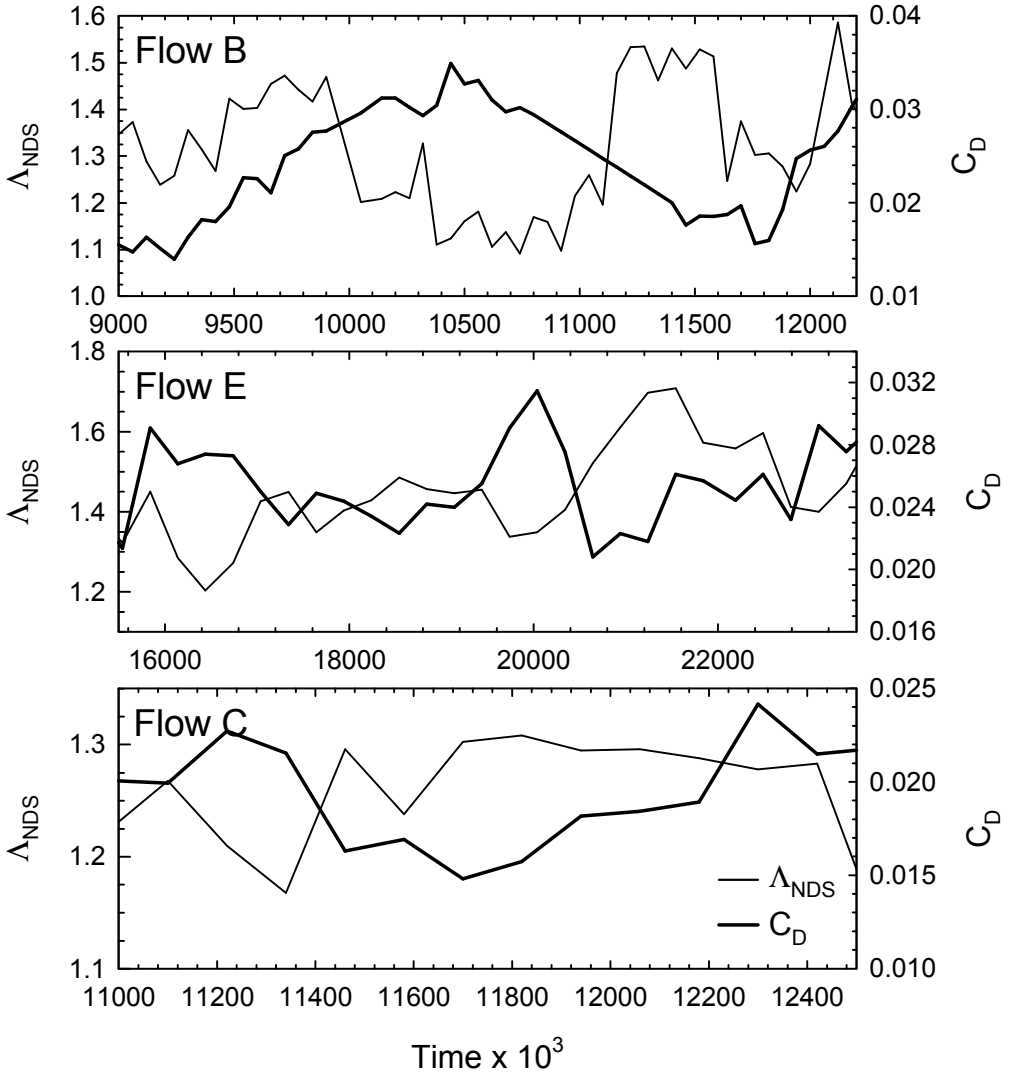

Figure 4.19: Examples of when the drag coefficient, C_D, and the non-dimensional span, Λ_{NDS}, are out of phase with one another.

There may be a simple explanation for this outcome. Nearly all the variation in the C_D time series is derived from the water surface slope and level. It is assumed in the derivation of Equation 4.8 that S is equivalent to the energy grade. Given that a portion of z_{ws} and S is dependent on the passage of bedforms, it is not clear that this assumption is satisfied. This is particularly true during the equilibrium phase of the experiments when bedform position can cause several millimetre variations in z_{ws}. Unfortunately, it would be nearly impossible to remove this effect from the current data set. Another significant impediment to finding a strong out-of-phase relation between Λ_{NDS} and C_D is that Λ_{NDS} is estimated for only a 1 m long section of the flume. Water surface slope is estimated over 2.26 m of the flume, so there is a large portion of the bed that may not have a similar Λ_{NDS}.

It would appear from C_D, calculated over the first hour of the experiments, that drag reduction does play an important role in the 2-3D transition. The drag coefficient fails to increase against a background of increasing bedform size. Increasing the level of three-dimensionality may also serve to reduce drag once 3D bedforms have been established. Portions of Λ_{NDS} and C_D time series are out of phase. However, the nature of the data set, in particular whether the slope can be linked to the energy grade, precludes any confident statements in this regard.

In light of this another experiment was designed to examine the turbulence structure and the form drag over fixed 2D and 3D dunes. The dunes, modelled after those observed in the experiments discussed here, were 0.45 m in length and 25 mm in height. Only the shape of the crestline was varied between runs, providing a data set where C_D could be accurately known for 2D and 3D bedforms. These data are described in the next chapter and are more suitable to determine if the 2-3D dune transition is linked directly to drag reduction processes.

4.6 Summary

The transition between 2D and 3D dunes in a homogeneous 0.5 mm sand was examined. A flat sand bed was subjected to a 0.155 m deep, non-varying mean flow ranging from 0.30 to 0.55 m/s in a 1 m wide flume. Changes in the planimetric configuration of the bed were monitored using high-resolution video. A video capture card was used to yield a series of 10 s time lapsed digital images. The images reveal that, once 2D dunes are established, minor, transient excesses or deficiencies of sand are passed from one crestline to another. The bedform field appears capable of 'swallowing' a small number of such defects but, as the number grows with time, the resulting morphological perturbations produce a transition in bed state to 3D forms that continue to evolve, but are pattern-stable.

All the observations made during the experiments plot as 2D dune fields on conventional bedform phase diagrams, despite the observation that the ultimate dune morphology is 3D. Stable 2D dunes were not observed in this calibre sand, which calls into question the reliability of bedform phase diagrams using crestline shape as a discriminator.

The idea that 3D arrangements of bed roughness elements passively reduce drag, when compared to smooth or 2D arrangements, was examined as a possible explanation for why the transition occurs. A defined increase in the drag coefficient is lacking during the early stages of the experiment and during the 2-3D dune transition, suggesting that passive drag reduction processes may be at work. Further, an out of phase relation between the drag coefficient and the non-dimensional span suggests these quantities may be dynamically linked at certain times. However, correlation analysis fails to reveal a relation between the drag coefficient and the non-dimensional span. Changes in the drag are somewhat obscured by other processes – primarily dune growth – as the transition occurs. Also problematic is that the measured water surface slope may not be representative of the energy gradient. Unfortunately, these problems cannot be resolved here. Thus, another experiment was conducted using fixed bedforms with varying crestline shapes. Dunes were scaled to the live bed

experiments discussed here, had the same size and were subjected to the same flow conditions. These experiments are discussed in Chapter 5.

Chapter 5-Aspects of Turbulent Flow over Two- and Three-Dimensional Dunes

5.1 Introduction

The purpose of this chapter is to discuss a set of experiments designed to examine the turbulent flow over fixed dunes with different crest shapes but constant wavelengths and heights. Flow is examined over a fixed flat bed and six dune morphologies including (1) straight-crested, two-dimensional (2D), (2) full-width saddle (crestline bowed upstream), (3) full-width lobe (crestline bowed downstream), (4) sinuous crest, (5) regular staggered crest and (6) irregular staggered crest. The flow structure is discussed in the context of recent experiments that have elucidated the flow structure over 2D dune morphologies. The effects of three-dimensional (3D) morphology on momentum transfer, mixing and energy exchanges from the mean flow to turbulent frequencies are discussed. Spatially averaged flow characteristics are presented for each morphology and drag reduction over 3D dunes is examined.

5.2 Experimental Procedure

The experiments were conducted in the Civil Engineering Hydraulics Laboratory at the University of British Columbia using a tilting flume channel, 17 m long, 0.515 m wide and 1 m deep. The head box exit was fitted with a honeycomb of 0.025 m (1 in.) PVC pipe that was 0.3 m (1 ft.) long to ensure quasi-uniform flow out of the head box. A Styrofoam float damped water surface waves. An adjustable sluice gate at the rear of the flume controlled the width of exiting flow and, ultimately, flow depth. Flume slope was adjusted by a pair of hydraulic jacks at the rear of the flume. In order to generate flow in the flume channel, water was pumped to the head box tank ($1.5 \times 2 \times 3$ m) from an underground tank via an axial pump driven by a constant speed electric motor. Flow rate was controlled by a screw valve installed on the inflow pipe that dumped water into the head box from above. Flow rate was measured with an acoustic pipe flow meter, mounted upstream of the control valve. Discharge was maintained by the valve to within $\pm 3.3 \times 10^{-4}$ m^3 s^{-1}.

5.2.1 Fixed Bedform Design

Bedforms were constructed from 14 pressure treated 16 ft 2×4 planks. A predetermined bedform shape was carved into each 2×4 plank eleven times and the boards were bolted together to form bedforms that spanned the flume channel. The accuracy of the carved bedform heights was approximately ± 1 mm.

The template used for bedform shape was based on the earlier experiments at NSL-USDA (discussed in Chapters 2-4). The along-stream and vertical locations of bedform features, identified in Figure 2.11 for crest type C3 and stoss type S1, were determined at flow strength B. These dimensions were normalised by the bedform height, H, and length, L, to derive dimensionless bedform morphology for a dune at flow B. Dimensionless morphology is averaged to produce a dimensionless scale model. By selecting a desired H or L, a corresponding L or H value can be calculated from the average bedform aspect ratio, H / L, for flow B. The dimensionless scale model is converted to actual dimensions by multiplying through by H and L.

It was decided that, since the transition between 2D and 3D dunes occurred during the exponential increase in bedform size (i.e. in H and L), the model bedform dimensions should be less than equilibrium size for the flow strength. Ideally, bedforms should be the precise size they were when the 2D-3D transition occurred. Unfortunately, at the transition $H \approx$ 10-15 mm and $L \approx$ 0.2 - 0.3 m. The bedforms would be too small to take measurements over using the available instrumentation (an acoustic Doppler velocimeter or ADV). In light of this, L = 0.45 m was selected as a desired length. This provided that at least 10 bedforms could be carved into the 16 ft planks. With L = 0.45 m and average H / L = 0.05 for flow B, the corresponding H = 22.5 mm. A smaller H would have been too difficult to carve into the planks and the ADV sampling volume, ~0.9 cm^3, would have been roughly the same size as the step height. The resulting morphology appears in Figure 5.1. The variability in H across the 11 bedforms was < 5 %.

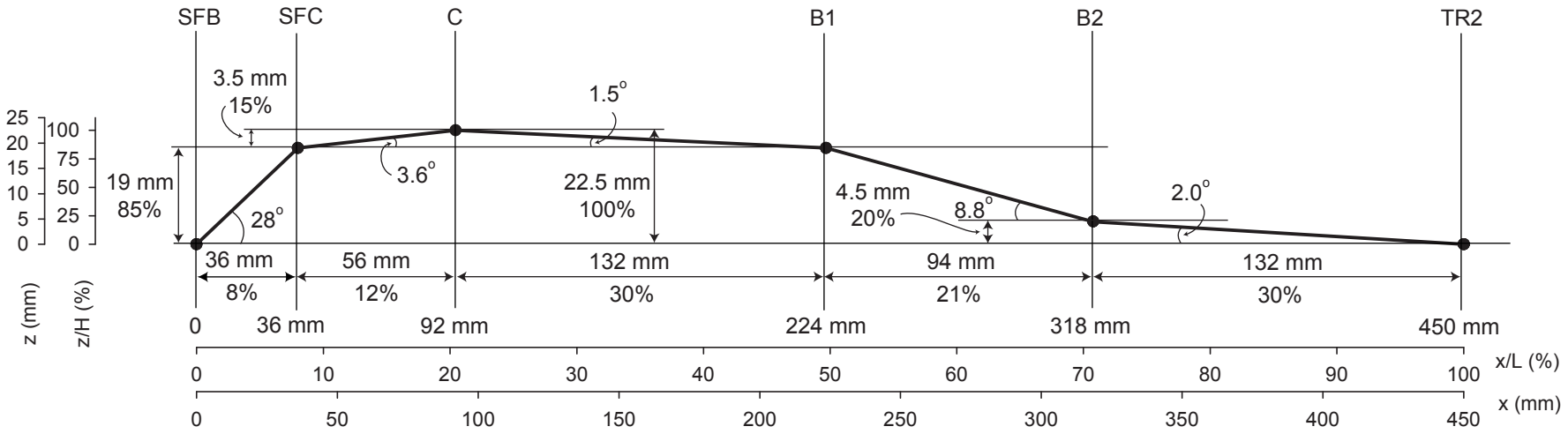

Figure 5.1: Dune morphology determined from active transport experiments. Distances along the dune and the height of dune features (slipface base, *SFB*, slipface crest, *SFC*, crest, *C*, stoss slope breaks, *B1* and *B2* and the upstream trough, *Tr2*) were calculated from the dune dimensions observed at flow strength B (see Chapter 2). Crest data were collated for crest configuration C3 and stoss data were collated for configuration S1 (see Chapter 2 for definitions of C3 and S1). These dune dimensions were normalised by the bedform height, H, and length, L, to obtain dimensionless dune morphology. Vertical height above the dune trough, z, and distance along the dune, x, were obtained by multiplying the dimensionless heights and lengths by the desired H (22.5 mm) and L (0.45 m).

By staggering the alignment of the boards, various dune crestline configurations could be generated. Six different crestline configurations were designed (Figure 5.2). A straight crested 2D dune (2D) was created by lining up the crests carved in the wooden planks. With the understanding that *Sirovich and Karlsen* [1997] examined flow over regular and irregular shapes (see Chapter 4), a set of regular and irregular crested 3D bedforms was designed. The regular crested dune morphology had the boards staggered at 92 mm relative to one another (the dune trough lined up with its neighbouring board's crest). This is an extreme example of a regular dune crest. Practically, it is unlikely that a dune with lobes and saddles so tightly spaced could occur naturally. Staggering of the boards for the irregular dune morphology was essentially random. The irregular crest could form naturally and similar morphologies were observed during the active transport runs discussed in Chapter 4. The regular and irregular features had $\Lambda_{NDS} \approx 2.4$ (Table 5.1). Recall from Chapter 4, $\Lambda_{NDS} = L_c / L_y$ where L_c is the crestline and L_y is the linear distance between the crest endpoints.

More conventional 3D dunes were designed with crestlines that bowed downstream over the whole flume width; these are referred to as full-width lobes (FWL) (Figure 5.2). Another set was designed with crestlines that bowed upstream; these are referred to as full-width saddles (FWS) (Figure 5.2). For both configurations, the two centreboards were staggered at 35 mm relative to the next and the other boards are staggered at 45 mm relative to the next. The full-width bedforms had a non-dimensional span, $\Lambda_{NDS} = 1.43$.

A sinuous crested bedform was composed of two lobes, one saddle in the centre of the flume and two half saddles at the side walls with approximately the same Λ_{NDS} as the full-width bedforms (Table 5.1). For the sinuous crest, the boards were staggered by 35 mm from the next (Figure 5.2). Measurements were taken over a sinuous lobe (SNL) and a sinuous saddle (SNS). Once measurements over the sinuous crested bedform were complete, the crestline was smoothed with wood filler to remove the jagged edge, producing a new bed morphology, a sinuous and smooth

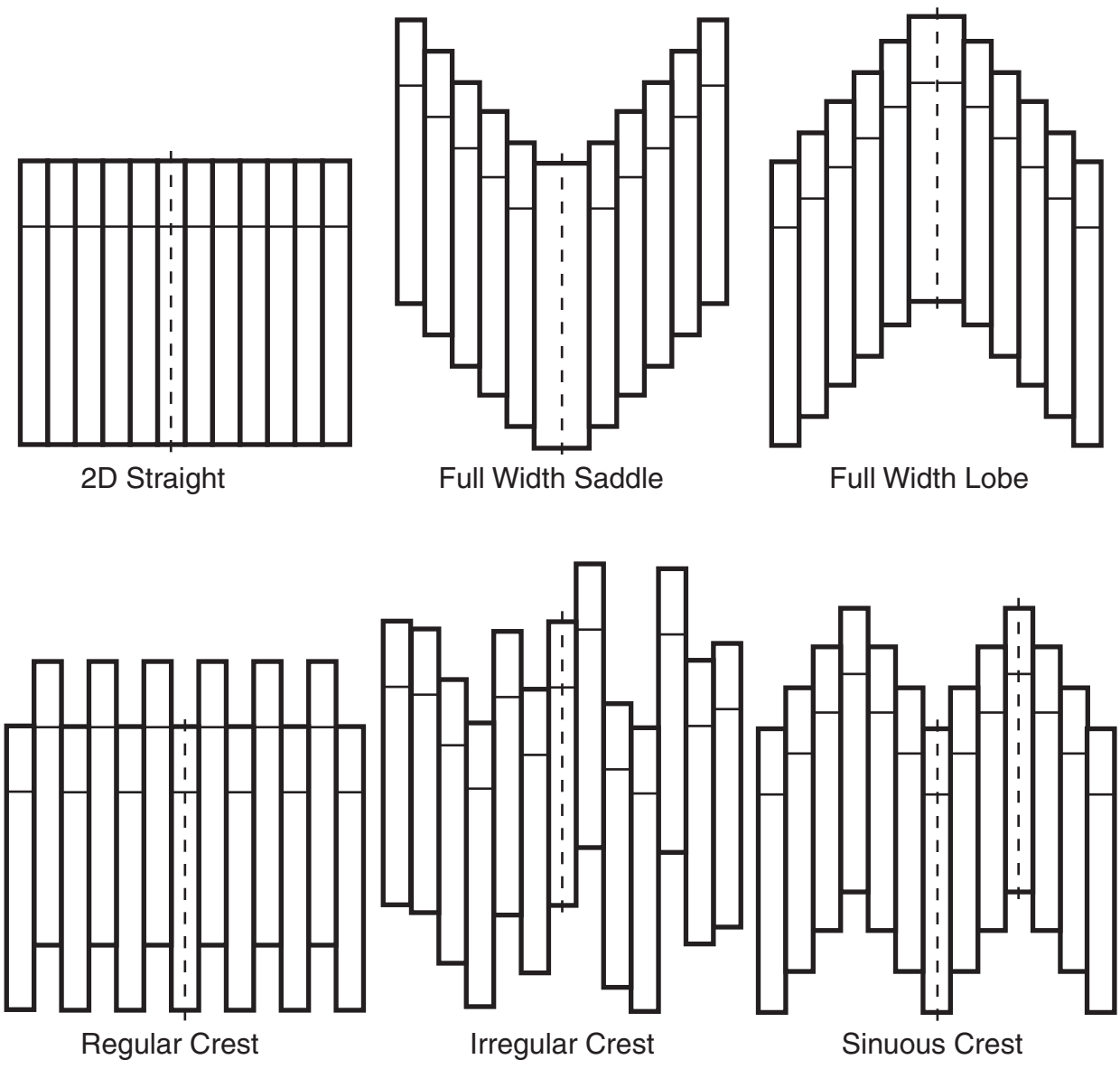

Figure 5.2: Dune morphologies tested. Thin horizontal lines indicate the location of the dune crest on each plank. Lines down the centre (and along the right lobe of the sinuous crest) indicate where the profiles were taken. Flow was from bottom to top.

Table 5.1: Summary of flow parameters. Shear stresses are corrected for side wall effects using the relation supplied by *Williams* [1970].

Flow Parameter	Flow B	Flat	2D	FWL	FWS	REG	IRR	Sinuous	Sinuous-Smooth
Λ_{NDS}	--	--	1.0	1.43	1.43	2.59	2.31	1.33	1.33
Q, $m^3 s^{-1}$	0.0723	0.0376	0.0376	0.0376	0.0376	0.0376	0.0376	0.0376	0.0376
d_{min}, m	--	--	0.1394	0.1412	0.1413	0.1442	0.1458	0.1438	0.1448
d_{max}, m	--	--	0.1640	0.1632	0.1623	0.1660	0.1696	0.1657	0.1683
$\overline{d}$, m	0.1517	0.1535	0.1507	0.1520	0.1533	0.1561	0.1569	0.1549	0.1562
$\overline{U}$, $m s^{-1}$	0.4766	0.4756	0.4846	0.4803	0.4763	0.4679	0.4653	0.4713	0.4674
Fr	0.39	0.39	0.40	0.39	0.39	0.38	0.38	0.38	0.38
Re	72300	73010	73010	73010	73010	73010	73010	73010	73010
$S \times 10^{-3}$	1.06	0.767	1.43	1.41	1.59	1.49	1.33	1.27	1.16
Determinations based on depth-slope product									
U_{*S}, $m s^{-1}$	0.0405	0.0323	0.0437	0.0436	0.0465	0.0454	0.0430	0.0417	0.0400
t_S, Pa	1.6337	1.0447	1.9072	1.9052	2.1610	2.0571	1.8507	1.7422	1.6028
ff_S	0.0560	0.0370	0.0651	0.0662	0.0763	0.0753	0.0685	0.0628	0.0588

saddle (SSS). This provided an opportunity to examine the effect of the jagged dune face on shear stress estimates.

Upstream and downstream of the dune configured bed, a flat bed section was installed at the level of the first dune trough. The flat bed extended ~6.5 m downstream from the head box and ~3 m downstream of the dune field.

The use of fixed bedforms is problematic. As discussed below, an active bedload layer has been shown to increase turbulence [*Best et al.* 1997]. Fixed beds eliminate the migration of the bedform that theoretically increases the resistance to flow. Also, the solid boundary offered by wood bedforms eliminates the exchange of fluid between the interstitial space within the bedform and the fluid flow. However, recent work by *Venditti and Bauer* [in review] suggests that these conditions may affect the turbulence structure over a dune only nominally. A more easily corrected problem is that a smooth bedform does not have the same grain roughness as a natural bedform. To reduce this problem, the flat and dune field portions of the bed were painted with contact cement to which a layer of 0.5 mm sand was adhered.

5.2.2 Flow Conditions

Since the dune morphology was based on dunes observed during flow strength B, the experiments were run at the same discharge, Q=0.0723 $m^3 s^{-1}$, corrected for the smaller width of the flume, 0.0376 $m^3 s^{-1}$. The initial flow depth, d, at flow strength B was 0.152 m and the initial slope, S, was 1.06×10^{-3}. An attempt was made to set d and S to these values by adjusting the sluice gate and the flume tilt to provide constant depths over the upstream flat portion of the bed. The flow depth established was 0.153 m. Unfortunately, the flume tilt was found to be slightly different than S over the flat bed portion of the bed (i.e. at a flume tilt of zero, $S \neq 0$). Thus, S was not perfectly matched between the model and the prototype. Bed slope over the flat portion was ~72 % of S at flow B and shear stress, $t_S = r_w g \bar{d} S$, was ~64 % of t_S at flow strength B (r_w is water density and g is

gravitational acceleration). In spite of this, the velocities, $\overline{U} = Q/(\overline{d} \cdot y_w)$, were nearly identical (Table 5.1) and the flow was uniform in both cases.

Best et al. [1997] suggest that a transport layer modulates turbulence by increasing roughness heights and near-bed turbulence intensities while reducing mixing lengths. It is likely that this is part of the reason why the fixed flat bed data yield a lower value of t_S than flow B, but the same d and $\overline{U}$. However, turbulence modulation is not sufficient to account for the entire deviation. The fixed flat bed data will be used to examine the vertical structure of the boundary layer. Thus, the difference in t_S, between the active transport and fixed bed conditions, will not affect the results greatly. However, care is needed when using t_S in some of the spatially averaged flow calculations below.

Over the 2D dune bed, the sluice gate opening and S were readjusted so that d over the crests was similar to d over the crests of dunes with H =22.5 mm at flow B. Quasi-equilibrium flow was achieved by adjusting the slope to obtain the same depth (±1 mm) over five successive bedform crests. Over subsequently tested dune configurations, the sluice gate opening was maintained so that only the flume tilt was adjusted to attain quasi-equilibrium flow. As such, d and $\overline{U}$ are a function of flume tilt (ultimately S) and crestline configuration.

Table 5.1 summarises the bulk hydraulic conditions for each crest configuration. Only one set of hydraulic conditions is presented for the sinuous crests (SNS and SNL). The mean flow depth, $\overline{d}$, was calculated as

$$\overline{d} = d_{min} + H(1 - b) + \frac{z_{WS-max} - z_{WS-min}}{2} \qquad 5.1$$

where d_{min} is the minimum depth (over the crest), b is the bedform shape factor, z_{WS-max} is the maximum water surface over the dune length and z_{WS-min} is the minimum water surface over the dune length. Recall from Chapter 2, $b = A/(HL)$ where A is the cross-sectional area of the bedform.

The minimum depth was calculated over the same 4-5 dunes that were used to establish quasi-equilibrium flow.

Mean flow depth over the dunes varied between 0.151 and 0.157 m depending on the bed configuration. Mean flow velocity, calculated using $\overline{d}$, varied accordingly, between 0.484 and 0.465 m s^{-1}. Over the 3D beds, $\overline{d}$ is larger ($\overline{U}$ smaller) than over the 2D bed, but $\overline{d}$ was largest ($\overline{U}$ smallest) when Λ_{NDS} was greatest (IRR and REG) and when the crestline was complicated (sinuous crests). Depths and velocities were nearly identical over the 2D bed and simple 3D forms (FWL and FWS).

Froude numbers, $Fr = \overline{U} / \sqrt{g\overline{d}}$, were ~0.38-0.40 and the Reynolds number, $Re = \overline{U}\,\overline{d} / n$ was 73010 (n is the kinematic viscosity) demonstrating that the flow is both sub-critical and fully turbulent. Bed slope varied between 1.16×10^{-3} and 1.59×10^{-3}, was greatest over the full-width saddle and regular crestlines, intermediate over the 2D and full-width lobe crestlines and lowest over the IRR and sinuous crests. Bulk shear stress was corrected for side wall effects using the relation proposed by *Williams* [1970] and varied between 1.6 and 2.1 Pa. Values of t_S follow the same patterns as S. Corresponding shear velocities, $u_{*S} = \sqrt{t_S / r_w}$, varied between 0.040 was 0.046 m s^{-1} and corresponding friction factors, $ff = 8t_S / r_w \overline{U}^2$, varied between 0.059 and 0.076.

5.2.3 Measurements and Analysis

Velocity measurements were obtained using an ADV that measured three-component flow velocities (streamwise, u, cross-stream, v, and vertical, w) at 50 Hz. The ADV has a reported precision of ±0.1 mm s^{-1} and a focal length of ~0.05 m. ADV signals are affected by Doppler noise, or white noise, associated with the measurement process [*Lohrmann et al.*, 1994]. The presence of this noise at high frequencies may create an aliasing effect in frequencies greater than the Nyquist frequency (herein f_n =25 Hz). To remove possible aliasing effects, a Gaussian low-pass filter with a

half-power frequency of 25 Hz was applied to the velocity time series, removing all variance at frequencies above f_n [*Biron et al.,* 1995; *Lane et al.*, 1998].

The ADV manufacturer provides signal quality information in the form of a correlation coefficient, r_{ADV}. The manufacturer suggests that when r_{ADV} does not exceed 0.7 the signal is dominated by acoustic noise and, as a rule of thumb, that at-a-point measurements should be discarded when r_{ADV} does not exceed 0.7 for more than 70 % of the record [*Sontek*, 1997; *Lane et al.*, 1998]. However, recent work by *Martin* [2002] has suggested that signal quality is reduced in highly turbulent regions of flow and suggested that the threshold r_{ADV} may be < 0.7. *Martin* [2002] conducted sensitivity analyses that revealed accurate mean velocities could be obtained when r_{ADV} exceeded 0.4 and accurate Reynolds stresses could be determined when r_{ADV} exceeded 0.7.

The measurements presented here also indicated that low r_{ADV} values occurred in highly turbulent regions of flow. Near the bed, along the lee slope and in the separation zone, r_{ADV} was frequently less than 0.7 for < 70 % of the record. Low r_{ADV} values appear to be distributed randomly in these records (i.e. low correlations do not appear to be related to a specific turbulent motion).

In recognition of these observations, a filter was designed to remove data points in the time series when r_{ADV} did not exceed 0.7. Then at-a-point measurements were removed from the data set in which r_{ADV} did not exceed 0.7 for > 70 % of the record. When the measurement was near the bed, along the lee slope or in the separation zone, at-a-point measurements were accepted when r_{ADV} exceeded 0.7 for > 40 % of the record. At a sampling rate of 50 Hz, a record in which only 40 % is retained is still sampled at a nominal rate of 20 Hz. In this respect, the data can be viewed as having been collected in a ‘burst sampling’ mode rather than a 'continuous' time-dependent sampling mode.

A test section was defined over the eighth dune, 9.5-10.0 m downstream of the flume entrance. A total of 35-37 profiles of velocity were taken along the flume centre line and spaced at 0.014 to 0.018 m apart. Each profile consisted of 10-15 vertical measurement locations sampled for 90 s. Figure 5.3

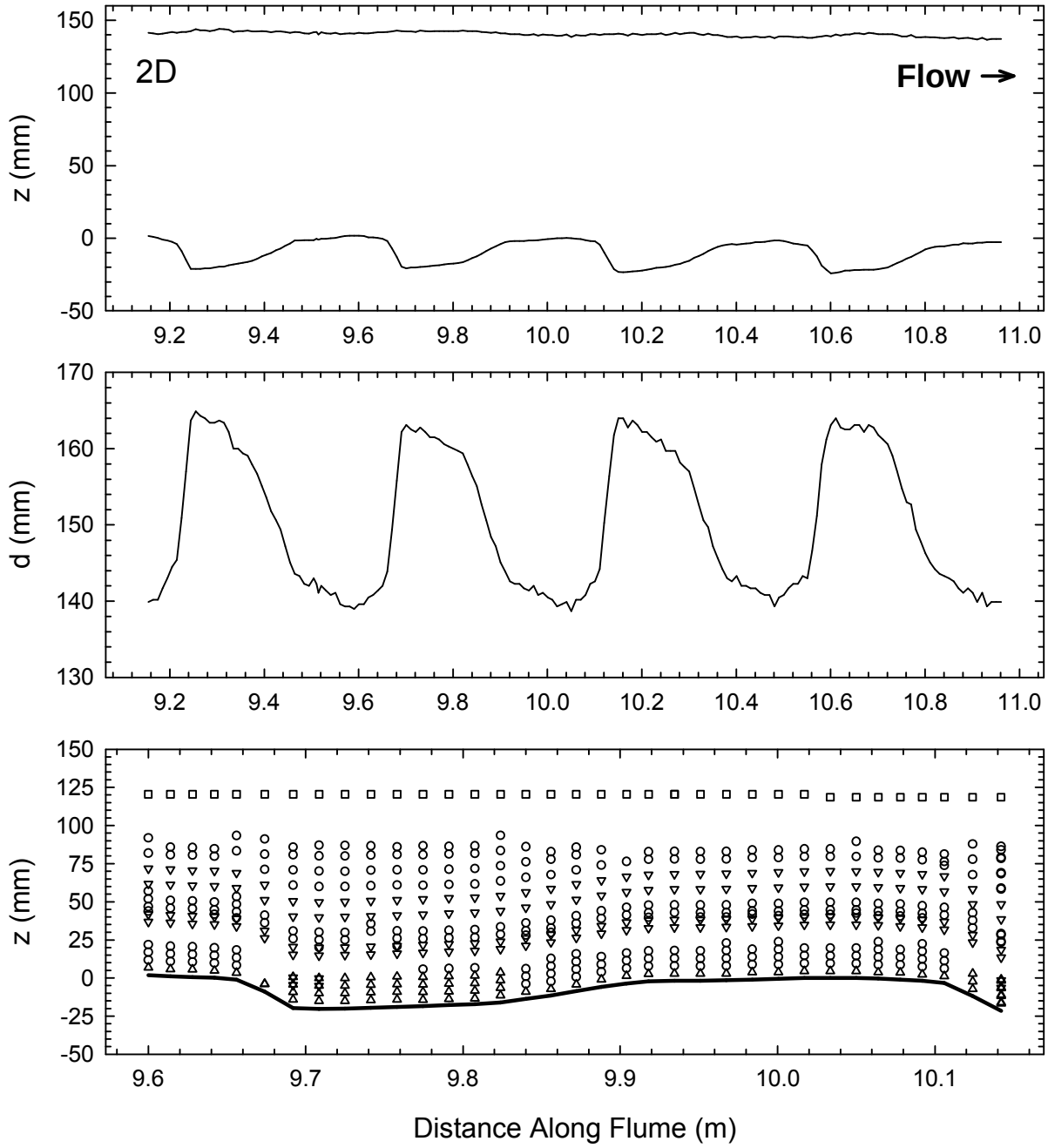

Figure 5.3: Example of bed and water surface profiles over bedforms 5-9 (top) and corresponding flow depths (middle) for the 2D dune configuration. Profiles were taken over the 8th downstream dune at the locations noted in the bottom panel. See Appendix E for similar diagrams for the other dune configurations. Circles indicate where the probe was mounted in the 0^o position. Down oriented triangles indicate the probe was in the 45^o position. Squares indicate the probe was in the 90^o position. Up oriented triangles indicate the probe was in the 0^o position but that the lower threshold for data retained after filtering was 40% as opposed to the 70 % retention threshold used for the rest of the data.

shows the location of the velocity measurements over the 2D dunes. Locations were similar over the other dune configurations (see Appendix D for velocity measurement location diagrams for all configurations).

Over the sinuous crestline, the centre line profiles were over a saddle (SNS). An additional set of profiles was taken nearer to the side wall over a lobe (SNL) (Figure 5.2). Only one set of hydraulic measurements was taken over the sinuous (ragged crest) configuration. In addition to the profiles over the dunes, 6 profiles were taken over the flat bed at 0.10 m intervals between 5.0 and 5.5 m.

For most measurements, the ADV probe head was oriented towards the bed at 0^o. The lowest point in each velocity profile was at a height of ~0.005 m above the bed and highest point was at ~0.08-0.11 m, depending on the position over the dune. Poor data quality caused by acoustic feedback was observed at several heights above the bed. This is a common feature of ADV measurements [see *Lane et al.*, 1998]. In order to obtain data at these heights, the ADV probe head was rotated 45^o in the cross-stream plane to reduce the feedback. To augment the velocity profiles, the ADV probe head was also rotated 90^o in the cross-stream plane to obtain a measurement that was typically 0.11-0.12 m above the dune crests.

Data collected when the probe head was at 45^o and 90^o needed to be rotated into the vertical plane. The streamwise velocity has the same magnitude and direction, regardless of whether the probe was in the 0^o, 45^o, or 90^o positions. Thus, the data need to be rotated only in the v - w plane. The v and w velocity components were rotated according to the following convention

$$\begin{aligned} v_{rp} &= v_m \cos j + w_m \sin j \\ w_{rp} &= -v_m \sin j + w_m \cos j \end{aligned} \qquad 5.2$$

where subscripts m and r refer to the measured and rotated velocity frames, respectively, and j is the angle of the probe head (0^o, 45^o or 90^o). The subscript p indicates the rotation is necessary for realignment when the probe is in the 45^o or 90^o position.

Care was taken in orienting the probe head so it was aligned with the maximum streamwise

velocity in the 0^o, 45^o, or 90^o positions. However, small misalignments were still common, which presented the possibility of having slightly different planes of reference for the measurements in different configurations. This is a potentially serious problem when different probe head alignments are used. Therefore, rotations are necessary in the u-v and u-w plane. A u and v rotation follows the convention

$$\begin{aligned} u_{ra} &= u_m \cos\gamma + v_{rp} \sin\gamma \\ v_{ra} &= -u_m \sin\gamma + v_{rp} \cos\gamma \end{aligned} \qquad 5.3$$

where γ is a misalignment angle in the u-v plane and the subscript a distinguishes this rotation from the realignment necessary when the probe is in the 45^o or 90^o position. A u and w rotation follows the convention

$$\begin{aligned} u_{ra2} &= u_{ra} \cos\phi + w_{rp} \sin\phi \\ w_{ra} &= -u_{ra} \sin\phi + w_{rp} \cos\phi \end{aligned} \qquad 5.4$$

where ϕ is a misalignment angle in the u-w plane and the subscript 2 indicates that this is the second rotation of the u component.

In order to estimate the rotation angles γ and ϕ, calibration files were taken each time the probe was readjusted at 0.06 and 0.09 m above the flat bed portion of the flume at 5.0 m from the head box, where v and w components of velocity could be expected to average to zero. By assuming the mean v_{ra} velocity is zero, Equations 5.3 can be rearranged such that

$$\gamma = \tan^{-1} \frac{V_{rp}}{U_m} \qquad 5.5$$

(capital u, v and w represent mean at-a-point velocities). In order to estimate ϕ, the data need to be rotated by applying Equations 5.3. Then, assuming mean w_{ra} velocity is zero, Equations 5.4 can be rearranged such that

$$\phi = \tan^{-1} \frac{W_{rp}}{U_{ra}} . \qquad 5.6$$

Calibration files were used to estimate g and f, which were averaged between the two heights. Values of g and f varied between -4° and 3° but were typically smaller. Data collected over the dunes are then rotated by g and f using Equations 5.3 and 5.4, placing the entire data set in the same plane of reference. By approaching the rotations in this manner, deviations in the mean vertical and cross-stream velocities over the dunes are accepted as real.

5.3 Empirically Derived Structure of Flow over Flat and 2D Dune Beds

The mean and turbulent flow structures over fixed 2D dunes have been described previously [*Nelson et al*., 1993; *McLean et al*., 1994; *Bennett and Best*, 1995; *Venditti and Bennett*, 2000; *Best and Kostaschuk*, 2002]. Figure 1.3 shows the main characteristics of the flow are (1) convergent, accelerating flow over the dune stoss, (2) flow separation at the dune crest, (3) flow reattachment at ~3.5 - 5 *H* [*Engel*, 1981; *Bennett and Best*, 1995; *Venditti and Bennett*, 2000], (4) a turbulent wake and shear layer originating at the crest, extending and expanding downstream, (5) an internal boundary layer (IBL) that grows from the reattachment point downstream beneath the wake towards the crest, and (6) an outer, overlying wake region. Of particular interest here is the shear layer and wake region and their turbulence characteristics. The wake region resembles flow behind a cylinder [*McLean*, 1990], and three-dimensional rollers, kolks, and internal boils occur along the shear layer, dominating the macroturbulent flow structure (See chapter 1 for a more complete description of flow over 2D dunes).

The flow field over the 3D dunes is examined empirically via several simple yet informative turbulence and velocity relations. Contour maps for all flow and turbulence parameters were constructed, but only selected results are presented here. Calculation methods for the mean and turbulence parameters are presented below, followed by a description of how each has been observed to vary over flat beds and 2D dunes in previous research. The descriptions of flow over 2D dunes are based on work by *Nelson et al.* [1993], *McLean et al*. [1994], *Bennett and Best*, [1995] and *Venditti*

and Bennett [2000], unless otherwise indicated. The focus of each of these studies is different, but descriptions of the flow field are consistent.

Figures 5.4 and 5.5 show contour maps of time-averaged streamwise, U, and vertical, W, flow velocities defined as

$$U = \frac{1}{n}\sum_{i=1}^{n} u_i \text{ and } W = \frac{1}{n}\sum_{i=1}^{n} w_i \qquad 5.7$$

where u_i and w_i are instantaneous velocities and n is the total number of measurements. Over a flat bed, U and W should not show any along flow variation, unless the flow is non-uniform. Flow over a 2D dune is highly non-uniform, accelerating over the dune stoss slope due to convergence and decelerating over the dune trough due to expansion. The vertical velocity responds with flow directed towards the bed downstream of the lee slope and water surface directed flow up the stoss slope from reattachment towards the crest. Mean cross-stream flow, V, is negligible across 2D crestlines but this does not indicate that eddies do not have a significant cross-stream extent. Over the 3D dunes considered, V will probably be negligible as profiles are taken over symmetric crestlines, with the exception of the irregular bed. Here, V will not necessarily average to zero along the dune profile.

Streamwise root-mean-square velocity, U_{rms}, was calculated from

$$U_{rms} = \left[\frac{1}{n}\sum_{i=1}^{n}(u_i - U)^2\right]^{0.5} \qquad 5.8$$

and the streamwise turbulence intensity, displayed in contour maps for each bed in Figure 5.6, was calculated as

$$I_u = \frac{U_{rms}}{u_{*S}}. \qquad 5.9$$

The pattern of I_u over a dune is a reflection of the pattern in U_{rms}. Recall from Chapter 3 that, over a flat bed, I_u decreases exponentially towards the bed following *Nezu and Nakagawa's* [1993] semi-theoretical universal functions. Previous research suggests that, over 2D dunes, maximum U_{rms}

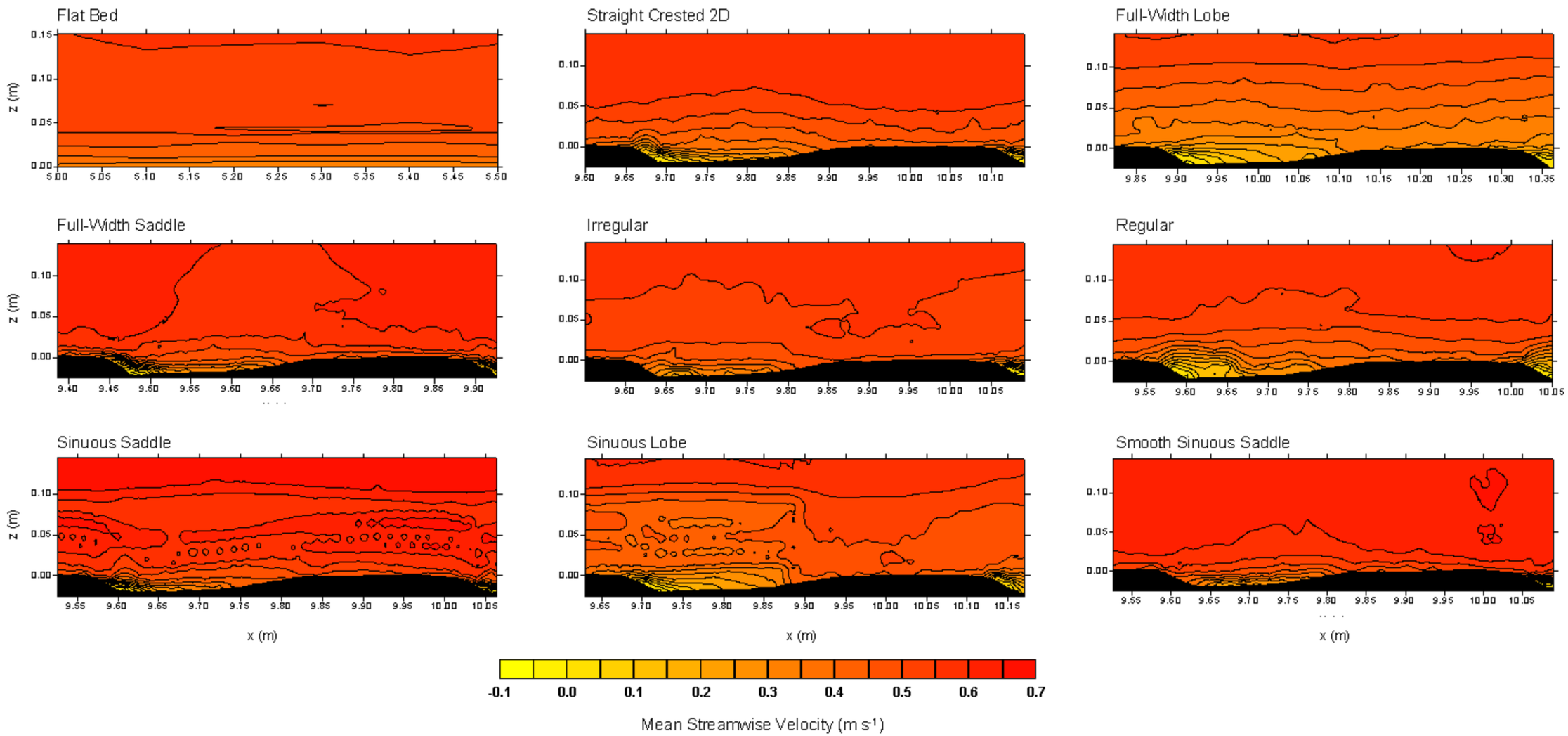

Figure 5.4: Mean streamwise velocity (z is height above the crest and x is distance along the flume). Note that after profiles were taken between $x = 9.630$ and 9.855 m over the sinuous lobe, the ADV probe was replaced by another probe which lead to an apparent disruption in the pattern of U. Only the sinuous lobe measurements are affected. Flow is left to right.

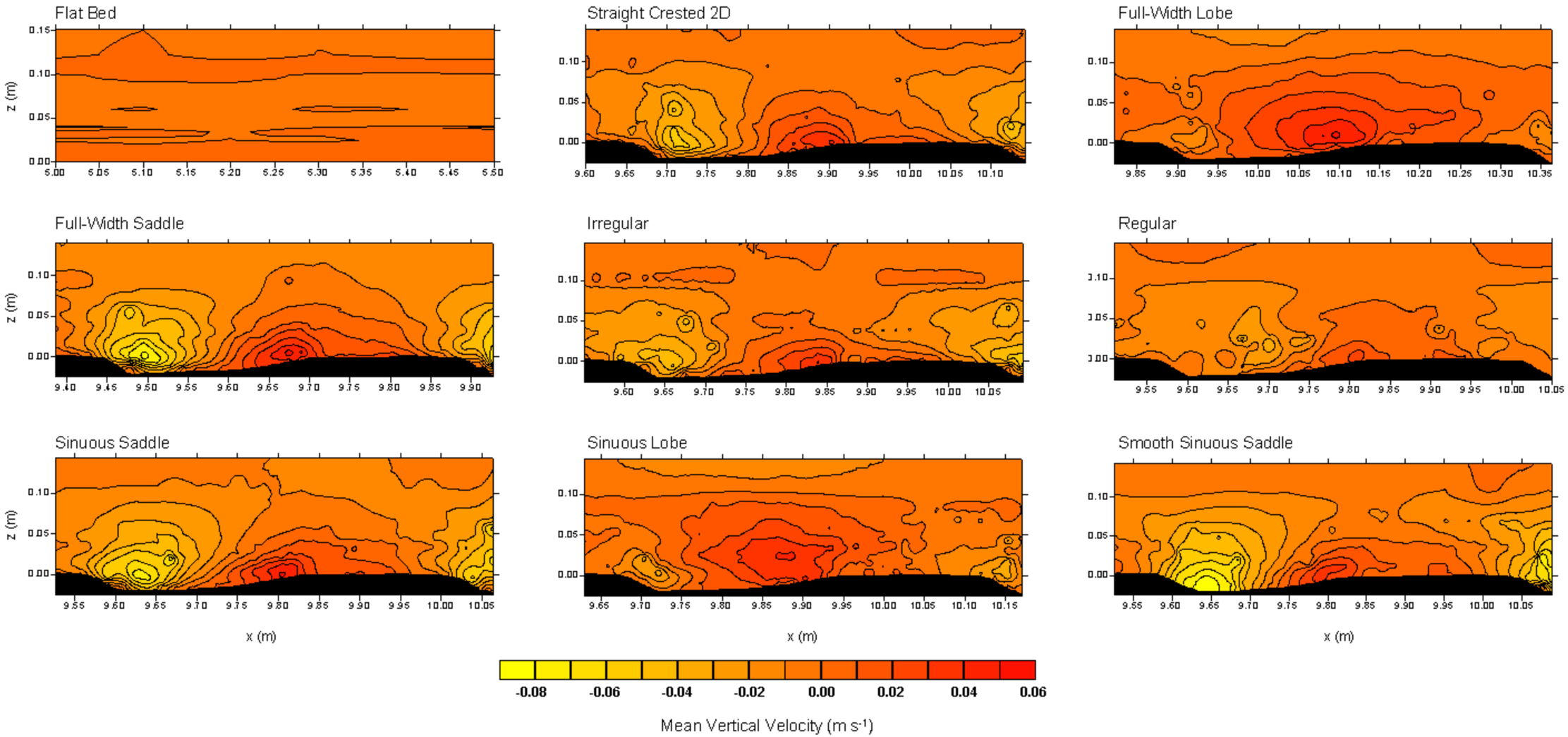

Figure 5.5: Mean vertical velocity (*z* is height above the crest and *x* is distance along the flume). Flow is left to right.

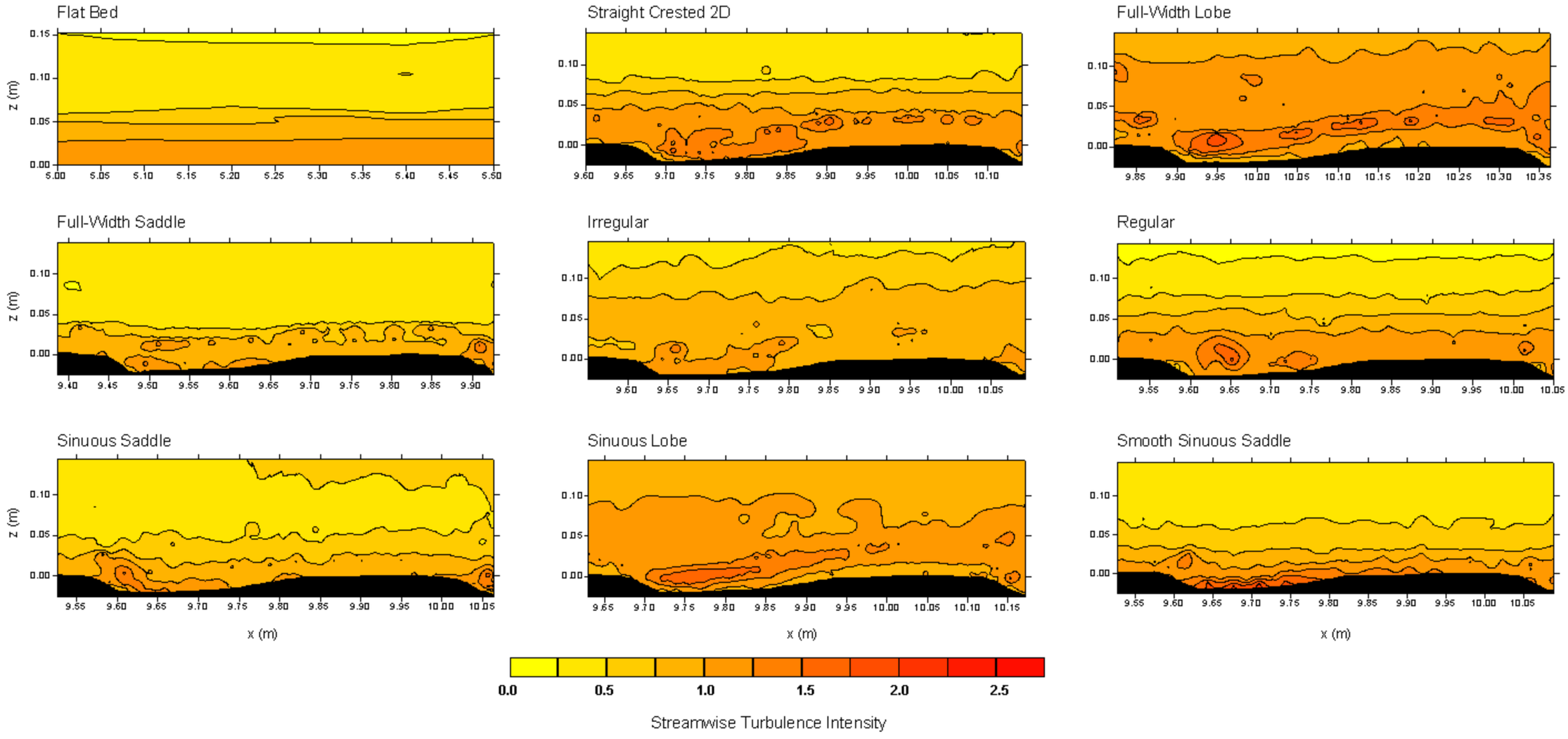

Figure 5.6: Streamwise turbulence intensity (z is height above the crest and x is distance along the flume). Flow is left to right.

values occur just downstream of reattachment and local highs occur within and just downstream of the separation cell. Elevated U_{rms} values occur in the highly turbulent wake region.

The Reynolds shear stress, t_{uw}, is plotted in contour maps displayed in Figure 5.7 and was determined using

$$\overline{u'w'} = \frac{1}{n}\sum_{i=1}^{n}(u_i - U)(w_i - W) \qquad 5.10$$

$$t_{uw} = -r_w \overline{u'w'}. \qquad 5.11$$

Recall from Chapter 3 that, for flow over a flat sand bed, t_{uw} should increase linearly from near zero at the water surface to a maximum at the bed with no along-stream variation. Maximum values of t_{uw} over 2D dunes occur at, and just downstream, of the reattachment zone and along the shear layer. Large t_{uw} values extend downstream of the dune crest, defining the wake and the IBL below. t_{uw} should tend towards zero (or even be slightly negative) moving up in the water column. Some authors have observed large Reynolds stresses in the IBL upstream of the dune crest [e.g. *Smith*, 1970; *Nelson et al*., 1993]. However, others have failed to observe this pattern [*Bennett and Best*, 1995; and *Venditti and Bennett*, 2000], probably because of insufficient measurements near the bed. It is unlikely this phenomenon could be observed here using the ADV technology.

The boundary layer correlation coefficient, R_{uw}, is plotted in Figure 5.8 and was calculated as

$$R_{uw} = \frac{-\overline{u'w'}}{U_{rms} \cdot W_{rms}}. \qquad 5.12$$

Recall from Chapter 3 that the boundary layer correlation coefficient ($-1 \leq R_{uw} \leq 1$) is a normalised covariance that expresses the degree of linear correlation between u and w velocity fluctuations. As such, R_{uw} is a 'local' statistic that provides insight into the presence or absence of flow structure at a specific location. In flow over a flat bed, there is little streamwise variation in R_{uw} and values of ~0.5 are typical of the near-bed regions, while decreased values of 0.0 - 0.3 are found in the outer

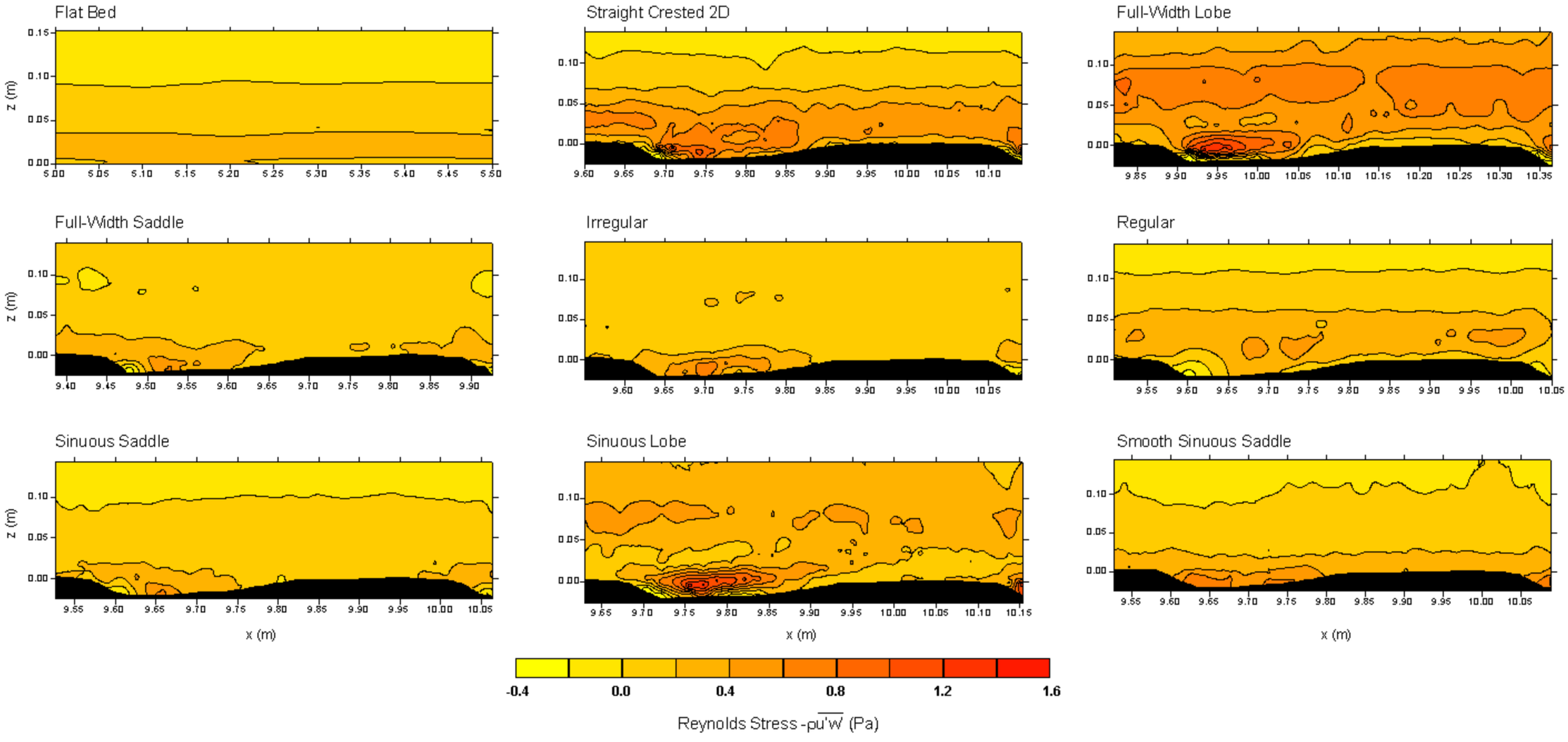

Figure 5.7: Vertical and streamwise components of the Reynolds stress (*z* is height above the crest and *x* is distance along the flume). Flow is left to right.

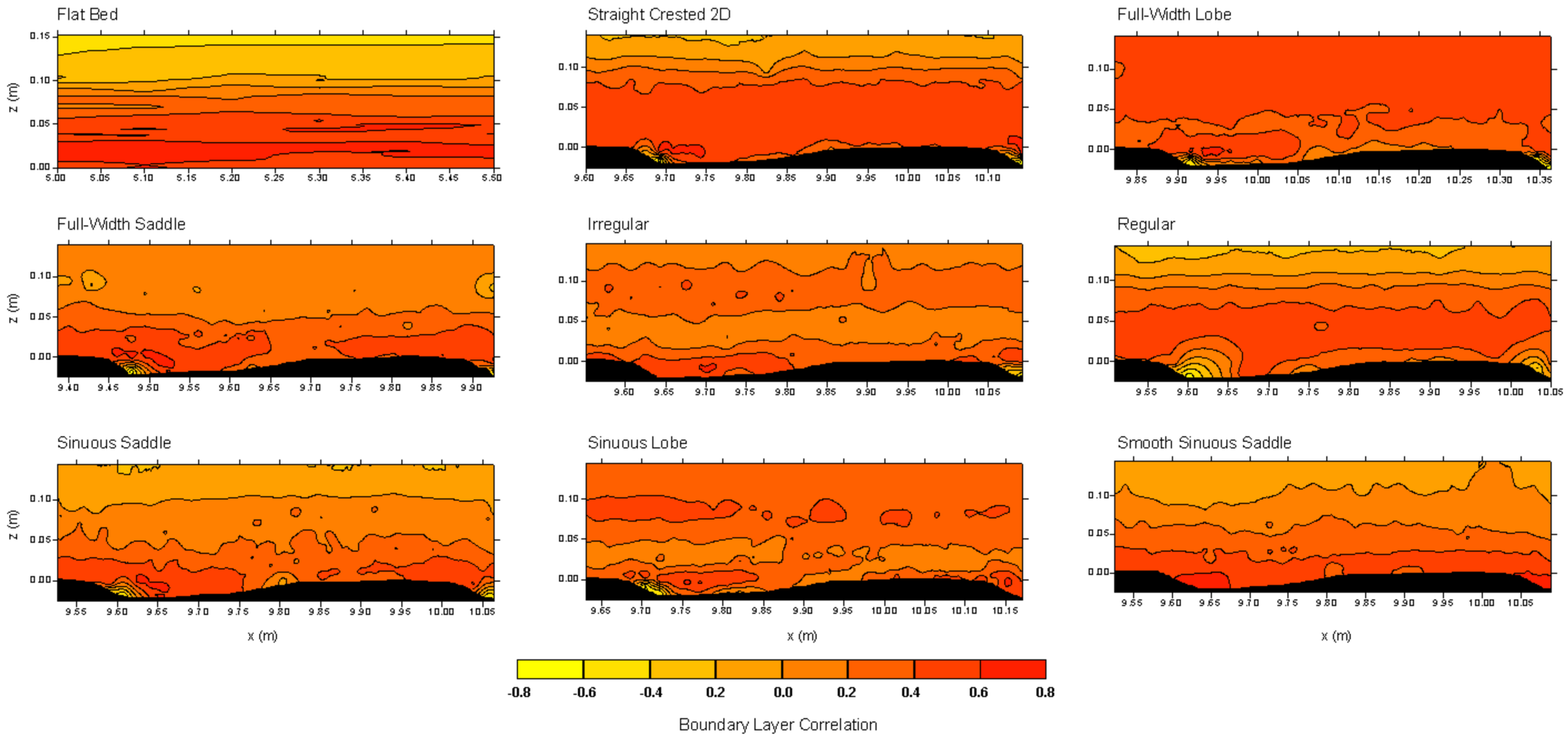

Figure 5.8: Correlation between vertical and streamwise velocity components, also known as the boundary-layer correlation coefficient (z is height above the crest and x is distance along the flume). Flow is left to right.

flow region [*Nezu and Nakagawa*, 1993]. Over a 2D dune, R_{uw} is largest in the separation cell (~0.7) and elevated along the wake where values are typically > 0.5. Low R_{uw} values (< 0.4) are observed in the IBL and outer layer.

The turbulent kinetic energy per unit volume is plotted in contour maps in Figure 5.9 and is calculated as

$$TKE = \frac{1}{2} r_w \left(\overline{u'^2} + \overline{v'^2} + \overline{w'^2} \right). \qquad 5.13$$

where $v' = v_i - V$ and v_i is an instantaneous velocity. TKE represents the energy extracted from the mean flow by the motion of turbulent eddies (*Kline et al.*, 1967; *Bradshaw*, 1977). TKE production involves interactions of the Reynolds stresses with mean velocity gradients and, ultimately, TKE dissipation occurs via viscous forces after being passed through the inertial subrange of the turbulence spectrum [*Tennekes and Lum*ley, 1972]. Since most turbulence production occurs at the boundary [*Kline et al.*, 1967], TKE can be expected to be largest near the bed for the flat bed case and decrease towards the water surface. Over a 2D dune *Venditti and Bennett* [2000] indicated that TKE defines the wake structure and reaches a maximum at reattachment. Elevated levels are common in the separation cell.

5.4 Flow Structure Empiricism and Resolution of the ADV

Before examining the results of the experiments it is useful to consider the turbulent scales that can usefully be resolved using the ADV technology. The ADV is a somewhat coarse instrument to examine fine scale turbulence structures. The use of the ADV probe in this experiment is predicated on several assumptions. The first is that only the larger scale eddies are of interest. At a sampling rate that varied between 20 and 50 Hz, it is not reasonable to expect eddy frequencies in the viscous subrange to be resolved. Further, a large degree of averaging occurs within the sampling volume of the ADV which is ~0.9 cm^3. The probe can only practically resolve eddies that are larger than the sampling volume. Both these constraints (sampling frequency and sampling volume) suggest that

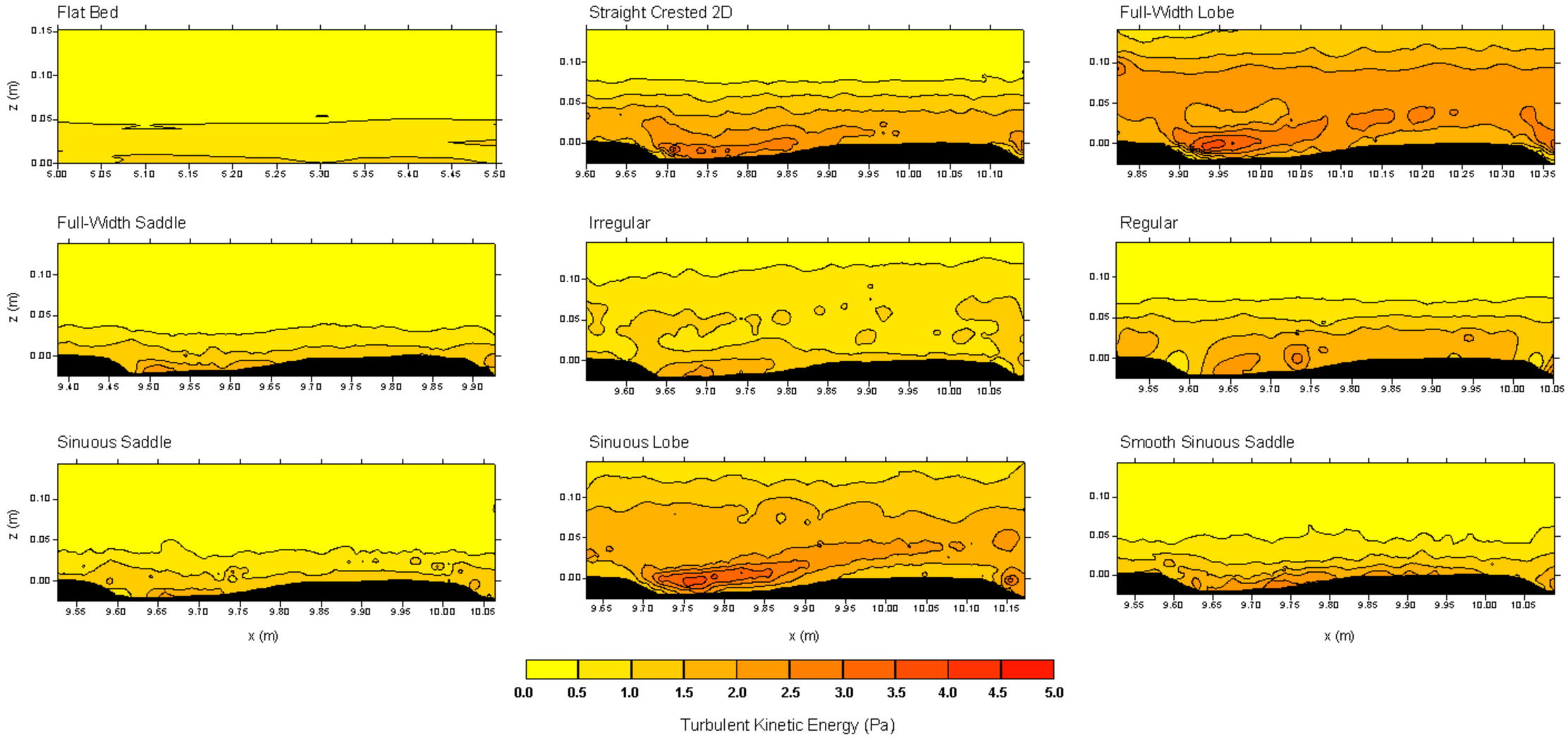

Figure 5.9: Turbulent kinetic energy per unit volume (z is height above the crest and x is distance along the flume). Flow is left to right.

only those eddies in the productive subrange (coherent structures) can reasonably be resolved. This should not preclude comparison of the results with measurements made using technologies that do not suffer from these limitations (i.e. hot wire (or film) and laser Doppler anemometry). However, some care must be taken before absolute comparisons can be made.

In light of this, it should be noted that some of the turbulence structure cannot practically be resolved over the low relief dunes observed here, because the bedforms are only 2.5× the height of the ADV sampling volume and the instrument cannot be operated within 0.005 m of the boundary. If the separation cell is small or weakly defined as a result of the 3D morphology of the dune, it may not be observable at all. Also, because the ADV cannot be operated within 5 mm of the boundary, a component of the flow must extend vertically beyond this height in order to be observed. Components of the flow such as the separation cell, reattachment point and the IBL stress maximum may not be observable over all dunes.

Given these limitations, the character of the turbulence structure will be considered in a relative sense. For example, if the separation cell is observable over one dune morphology and not over another, it must be small or weakly defined over the latter. Its absence in the contour plots should not be interpreted as an indication that flow separation is not occurring over the dune. As such, most of the conclusions drawn about how the turbulence structure interacts with various 3D morphologies will be focused on readily observable components of the flow field (i.e. wake, IBL, separation cell and outer layer). More advanced technologies need to be applied to flow over the dunes in order to resolve the fine scale turbulent flow properties. Fortunately, such resolution is not central to the present purpose.

5.5 Mean and Turbulent Flow Fields over 3D Dune Beds

5.5.1 Flat bed

Flow over the flat bed does not vary significantly from the empirical model reviewed above. Figure 5.10 displays U and U_{rms} profiles over the flat bed. Flow over the fixed flat bed is similar to flow over the active transport layer bed at flow B. The mean velocity profiles are log-linear through the lower $0.2\,d$ and U_{rms} profiles increase exponentially towards the bed conforming to the general form of *Nezu and Nakagawa's* [1993] semi-theoretical universal functions. The difference between the profiles is largely a result of the larger shear stress at flow strength B with the active transport layer. The mean velocity profile is slightly steeper and U_{rms} is larger, which is in accordance with *Best et al.*'s [1997] observations of how a transport layer affects the flow.

Contour maps of U, W and the turbulence parameters over the flat bed show no along-stream variation, indicating the flow is indeed uniform. Near the bed (up to ~$0.33\,d$), $t_{uw} \approx$ 0.2-0.4 Pa, R_{uw} exceeds 0.4 and TKE ranges between 0.5 and 1.5 Pa closest to the bed. In the middle flow region, between ~0.33 and $0.66\,d$, t_{uw} and R_{uw} decrease towards zero and eventually become negative above ~$0.66\,d$, indicating the decoupling of u and w motions and the absence of momentum exchange. TKE tends towards zero above ~$0.33\,d$ indicating there is little or no energy transfer from the mean flow (turbulence production) away from the bed.

5.5.2 2D Dunes

Flow over the 2D dunes displays most of the features described in previous research. Figure 5.10 displays U and U_{rms} profiles over the trough, stoss slope and crest of the 2D dunes and over the flat bed for comparison. A shear layer is observable in velocity profiles (Figure 5.10). Flow is generally decelerated over the dune trough and accelerated over the dune crest when compared to the fixed flat bed profiles. Over the dune trough, U is decelerated and U_{rms} is increased in the separation cell. Contour maps indicate there is an upstream directed flow near the slipface and that the shear layer

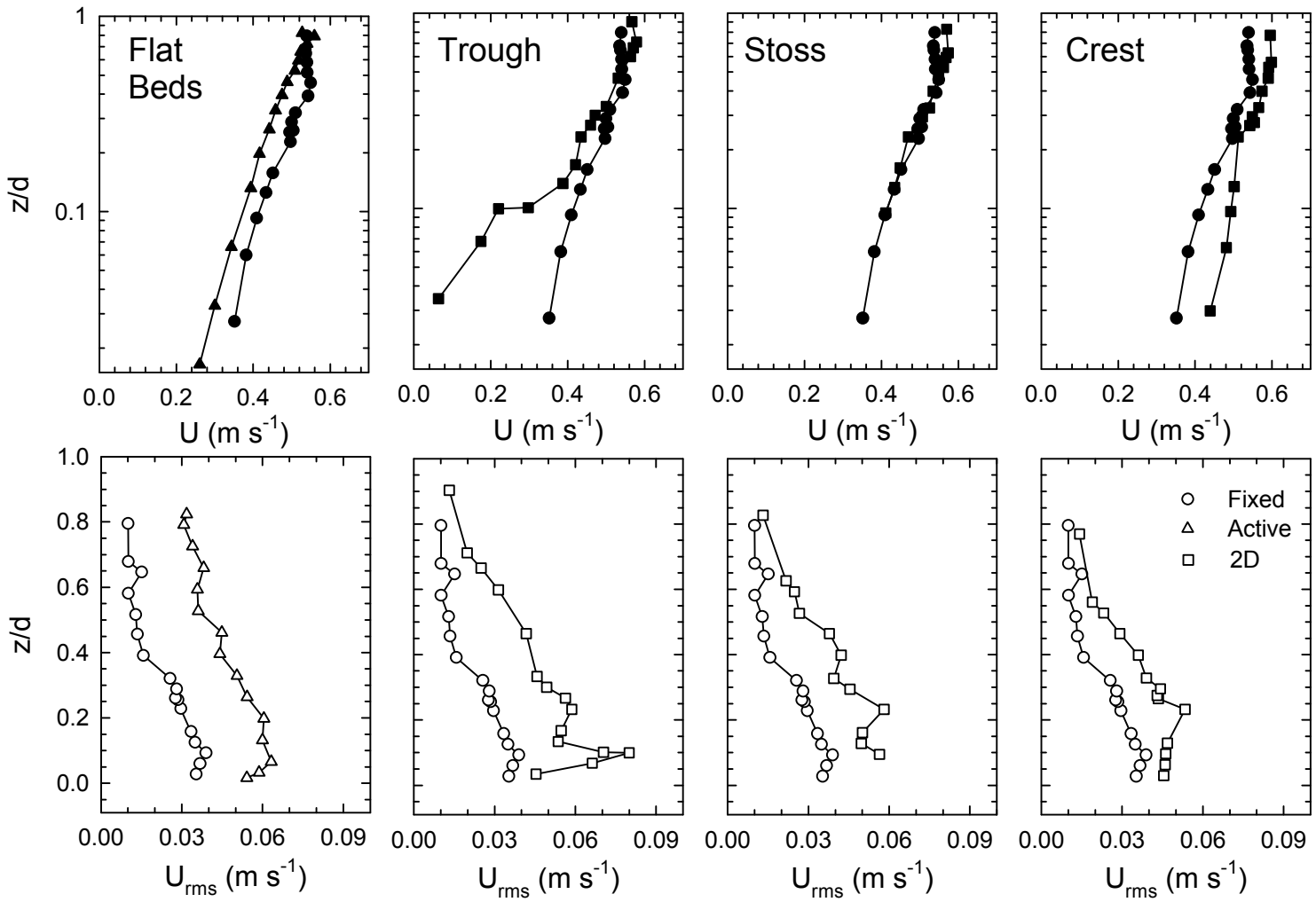

Figure 5.10: Select profiles of mean streamwise velocity, U (solid symbols), and streamwise root-mean-square velocity, U_{rms} (open symbols), over the flat bed and the 2D dune configuration. In the context of Figure 5.3 the profiles over the 2D dunes are the 8th (trough), 18th (stoss) and 28th (crest) from the left. Flat bed data was collected during flow strength B (see Chapter 5) with active transport and over the fixed flat bed without transport. The fixed flat bed data are the same in the trough, stoss and crest panels.

extends from *SFB* to *B2* (see Figure 5.1 for definitions). Mean streamwise flow over the stoss slope is nearly identical to that over the flat bed with the exception that the turbulence intensities are larger, which is the case over the whole 2D dune profile. Mean w contour maps show plunging vertical flow over the dune lee slope and water surface directed flow between *B2* and *B1*. Near the crest, mean vertical flow is negative (towards the bed).

There is a well-defined wake structure observable in the I_u - 1.25 and *TKE* - 2 Pa isolines that extend from the lee slope through the trough region and up over the downstream crest. An IBL seems to develop at *B1* and extend towards the crest. Reynolds stress reaches a maximum ($t_{uw} \approx 1.0$ - 1.2 Pa) in the separation cell and is elevated through the trough region and in the wake structure. Large positive R_{uw} occurs in the separation zone, but is large over most of the lower portion of the flow. As was observed over the flat bed, R_{uw} decreases towards negative values in the upper $0.33\,d$ of the flow. The reattachment point and IBL maximum stress are not observed, but this is likely due to limited resolution of the ADV.

5.5.3 Full-Width Lobe (FWL) and Saddle (FWS)

Mean u profiles over the full-width lobe (Figure 5.11) indicate that flow is retarded over the entire bedform when compared to the 2D dune, presumably due to increased flow resistance. There is no apparent shear layer observable in the dune trough profile; instead a smooth increase in U with height above the bed is observed. The contour map of U suggests there is a larger decelerated flow zone downstream of the dune crest over the trough to *B1*. This decelerated zone extends well above the dune crestline and confirms that no distinct shear layer is present. Compared to the 2D dune, there is an extensive zone where $U < 0$ occurs, abutting the slipface. Vertical flow plotted in the W map shows a much weaker plunging flow in the lee of the dune but a strong and extensive vertical current above *B2-B1*. A weak vertical flow component persists downstream of this zone and even over the dune crest.

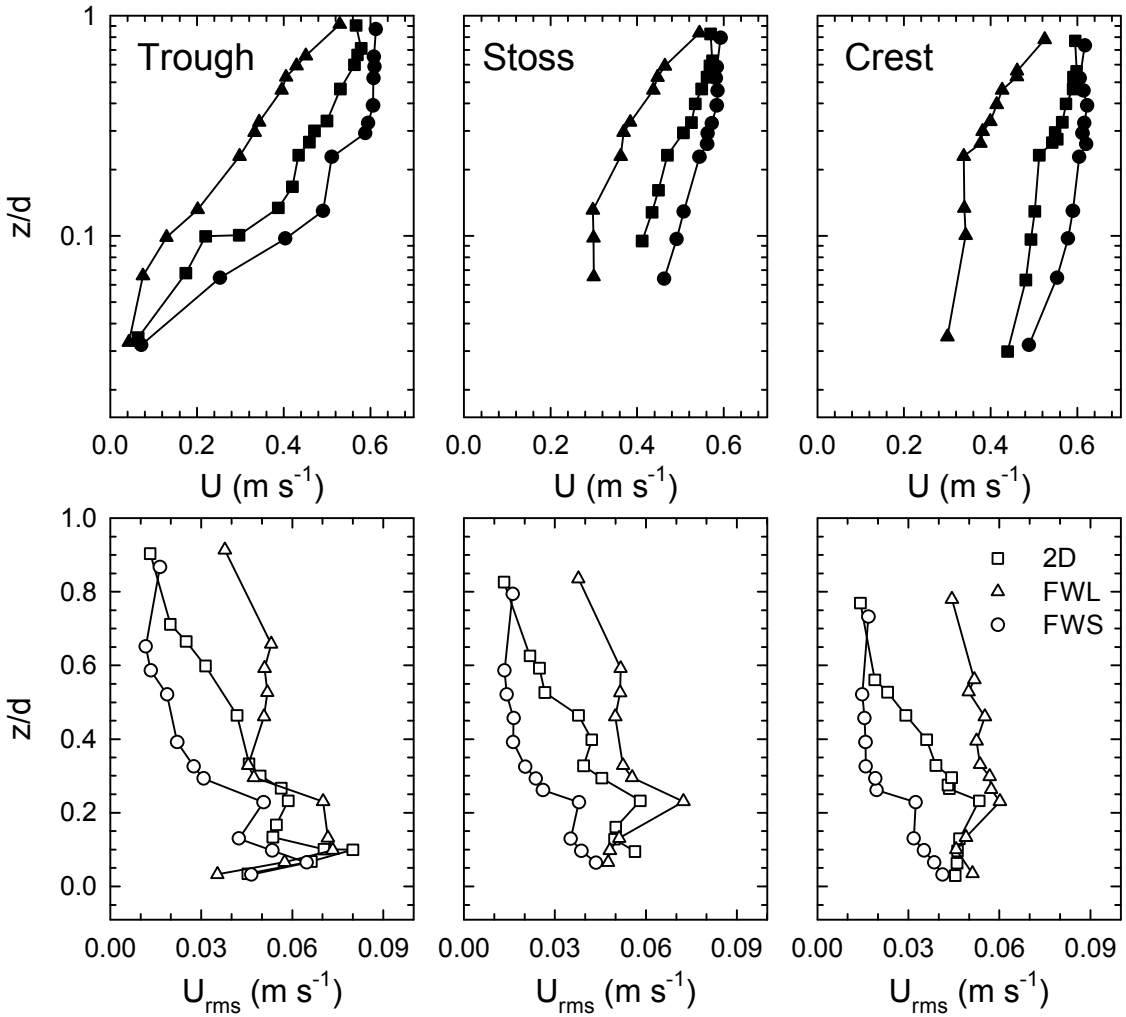

Figure 5.11: Select profiles of mean streamwise velocity, U (solid symbols), and streamwise root-mean- square velocity, U_{rms} (open symbols), over the full-width lobe (FWL), full-width saddle (FWS) and 2D dune configurations. In the context of Figure 5.3 the profiles over the 2D dunes are the 8th (trough), 18th (stoss) and 28th (crest) from the left. Height above the crests, z, is normalised by the dune height, d.

Turbulence appears to be enhanced over most of the full-width lobe bedform when compared to the 2D dune. Profiles of U_{rms} (Figure 5.11) reveal larger turbulence intensity in the upper portions of the flow but similar values near the base, although U_{rms} is larger at the trough profile, owing to more vigorous mixing in the separation cell. Contour maps of I_u and t_{uw} reveal low values in the upper and lower portions of flow with a strong core of elevated values that occupy ~0.33 d. The wake structure extends from the upstream lee slope downstream over the next dune crest, as defined by the I_u - 1.25 and TKE - 2.5 Pa isolines, and is somewhat stronger than in the lee of the 2D dune. In fact, it is likely that the core of more turbulent flow is composed of stacked wakes from upstream bedforms as suggested by *Nelson and Smith* [1986]. Low I_u, t_{uw}, R_{uw} and TKE values indicate there is an IBL beneath the wake on the stoss slope that is thicker than over the 2D dune. The separation cell is well defined and appears as an elongated zone where t_{uw} exceeds 0.6 Pa. Over most of the dune, $R_{uw} \approx$ 0.6-0.8, except in the IBL where R_{uw} is near zero, and in the separation zone abutting the lee slope, where R_{uw} is negative.

Mean u profiles over the full-width saddle indicate larger velocities over the dune profile compared to a 2D dune (Figure 5.11), presumably due to decreased flow resistance. There is some evidence of a shear layer in the U profile over the trough, but it is not as pronounced as over the 2D dune. The U contour map suggests a low velocity zone where $U < 0$ occurs near the lee slope. However, this zone is not extensive and the shear layer is diminished at one step height downstream of *SFC*. The W contour map indicates a strong plunging flow over the dune lee slope compared to the 2D dune bed and a responding surface directed flow between *B2* and *B1*. Vertical flow over the crest is negligible.

Turbulence appears to be suppressed over most of the full-width saddle bedform. Profiles of U_{rms} (Figure 5.11) reveal diminished turbulence intensity in the centre portion of the flow. Values of U_{rms} are similar over the 2D dune and the full-width saddle at the base and surface of the profiles.

This observation is confirmed by the contour maps of I_u which is < 0.5 over most of the flow field. I_u is larger in the lower $0.5d$ but is less than over the 2D dune. Interestingly, there is no apparent wake structure and consequently no observable IBL in any of the contour maps. The separation cell is small, absent, or only weakly defined. I_u, t_{uw}, R_{uw} and *TKE* are somewhat larger in the trough area bounded by *SFC* upstream and *B1* downstream, suggesting some turbulence is generated over the dune but not on the scale of the 2D dune.

5.5.4 Sinuous Lobe (SNL), Saddle (SNS) and Smooth Saddle (SSS)

Mean u over the sinuous crest follows essentially the same pattern as over the full-width lobe and full-width saddle (Figure 5.12). Flow velocity (U) is retarded over the sinuous lobe and enhanced over the sinuous saddle when compared to flow over a 2D dune. However, the magnitude of the retardation or enhancement is smaller over the sinuous lobe and saddle when compared to the full-width bedforms. Although this pattern persists over the whole bedform, the U velocity differential between the lobe or saddle and the 2D dune is less pronounced over the stoss slope and crest compared to the trough profiles.

There is no apparent shear layer developed in either the lobe or saddle profiles, which agrees with observations over the full-width bedforms (Figure 5.12). Over the sinuous lobe and saddle trough, there is a smooth decrease in U towards the bed. A contour map of U indicates there is a large decelerated zone over the sinuous lobe that is similar to the full-width lobe, but not as extensive. Negative U velocities are observed near the lee slope. Over the sinuous saddle, the decelerated zone is quite limited and there are no negative U velocities observed. A short shear layer diminishes $\sim 1H$ from the upstream *SFC*.

Contour maps of W indicate that plunging flow occurs with a surface directed return flow at *B1* over both the sinuous lobe and saddle. In agreement with observations over the full-width lobe and saddle, the magnitudes of the plunging and return flows are greater over the lobe. The magnitude of

these flows is similar to those over the full-width bedforms, indicating that this feature is unaffected by the width of the saddle or lobe. Over the sinuous lobe crest , vertical flow is negligible while, over the sinuous saddle crest, flow is directed towards the bed.

The characteristics of the turbulent flow over the sinuous bedforms also bear strong similarity to the full-width bedforms. Over the sinuous lobe, the upper portion of the U_{rms} profile is larger than over the 2D dune (Figure 5.12). Over the sinuous saddle, turbulence is suppressed in the central core of the flow but similar U_{rms} values are observed at the top and base of the profiles (Figure 5.12).

Over the sinuous lobe, contour maps reveal a central core region that has larger I_u and t_{uw} values compared to flow above and below. This region is less pronounced over the sinuous lobe when compared to the full-width lobe. The wake structure is well defined by the I_u - 1.25 and TKE - 2.0 Pa isolines and is better defined over the sinuous lobe than over the full-width lobe. This suggests that the width of the lobe tends to concentrate the strength of the wake over lobes. The central core is not as turbulent as over the full-width lobe; this may be attributed to the neighbouring saddle, which has no observable wake, interfering with the maintenance of mixing and the development of stacked wakes higher up in the flow. Low values of I_u, t_{uw}, R_{uw} and TKE indicate that there is an IBL beneath the wake on the stoss slope of the sinuous lobe that is similar in depth to the IBL over the full-width lobe. The separation cell is quite pronounced over the sinuous lobe trough and is of similar magnitude compared to the full-width lobe. In the elongated separation cell, $t_{uw} \approx$ 1.4 - 1.6 Pa.

Since there is no wake developed over the stoss slope of the sinuous saddle there is no apparent IBL. Further, the separation cell is weakly defined or non-existent. t_{uw} reaches a maximum of only ~0.6 Pa. Interestingly, the flow structure over the smoothed sinuous saddle is nearly identical to that over the ragged edged sinuous saddle, suggesting that the effect of the ragged edge is relatively minor.

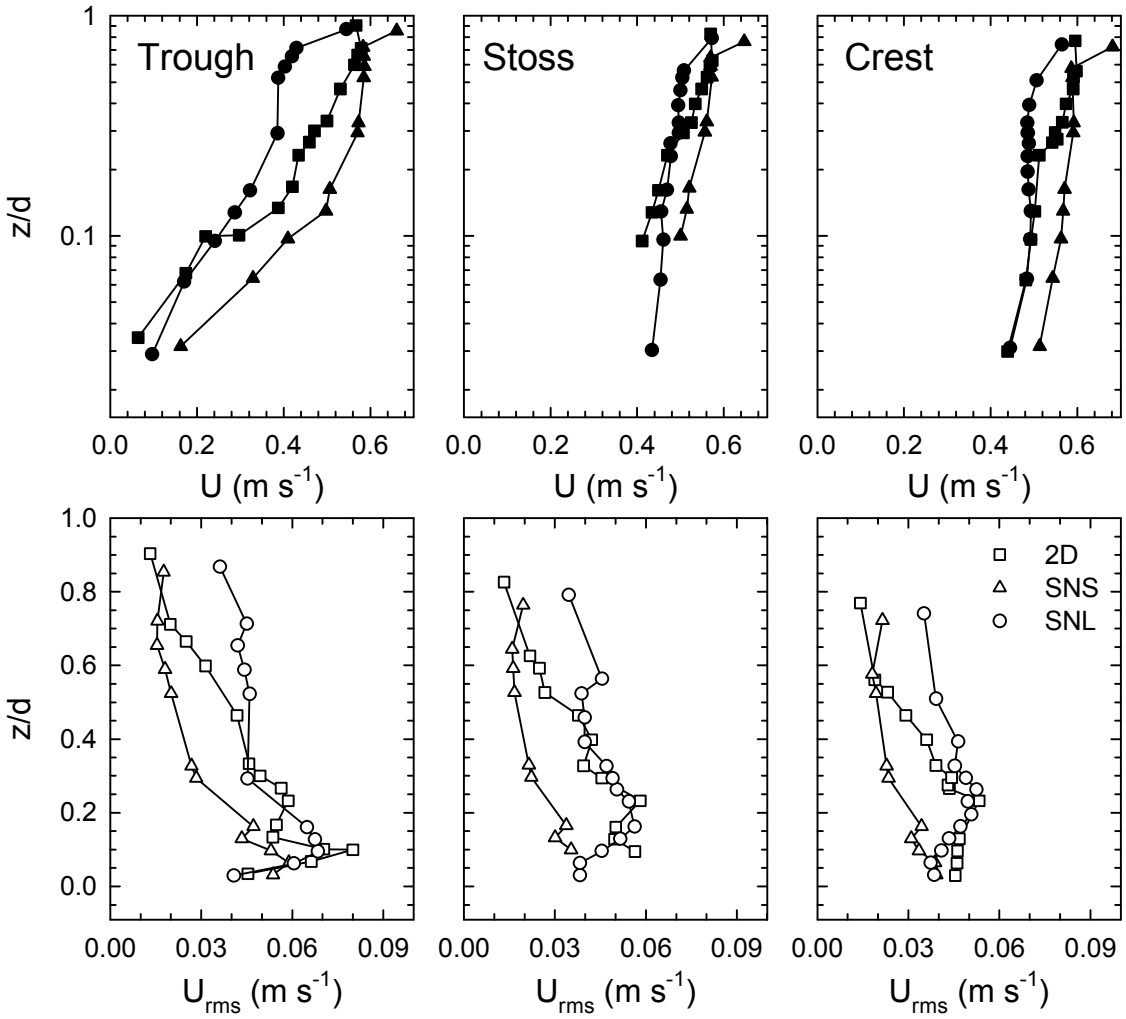

Figure 5.12: Select profiles of mean streamwise velocity, U (solid symbols), and streamwise root-mean- square velocity, U_{rms} (open symbols), over the sinuous lobe (SNL), sinuous saddle (SNS) and 2D dune configurations. In the context of Figure 5.3 the profiles over the 2D dunes are the 8th (trough), 18th (stoss) and 28th (crest) from the left. Height above the crests, z, is normalised by the dune height, d.

Recall from Figure 5.2 that the sinuous crest is composed of two lobes, one saddle in the centre of the flume and two half saddles at the side walls. If a single estimate of the level of turbulence (based on any of I_u, t_{uw}, R_{uw} and TKE) over the sinuous dunes was made, it would be logical to average the results over the lobe and the saddle. Since the sinuous lobe appears to have a slightly higher turbulence level than the 2D dune and the sinuous saddle a significantly lower turbulence level than the 2D dune, it is likely that an average would produce an equal or lower turbulence level when compared to the 2D dune.

5.5.5 Regular (REG) and Irregular (IRR) Crests

Before discussing the effect of the regular morphology on the flow structure, it is necessary to note that the regular crest morphology is not realistic. Recall from Figure 5.2 that the regular measurements were made over a saddle where the trough was recessed to the neighbouring crestline. It is unlikely that a crestline could develop with a lobe and saddle within $< 0.1\,L$. However, this morphology was included as an end member test of the theory of *Sirovich and Karlsen* [1997] (see Chapter 4). In light of this, the flow structure associated with the regular morphology will be discussed briefly. The irregular bed deserves more attention because it is perfectly likely that this bed morphology could develop. In fact, much of the equilibrium morphology in the active transport experiments resembled the irregular form with asymmetric lobes and saddles as a constantly varying component of the bed morphology.

Mean u profiles over the 2D and regular dune morphologies are identical above the dune height and U decreases substantially below crest height (Figure 5.13). The combination of the dune step and the hollow created by neighbouring crests generates a strong shear layer. There is no significant difference in U profiles over the stoss and crest of the regular and 2D dune morphologies, suggesting that the effect of the 3D form is localised to the trough region. Vertical flow inferred from the

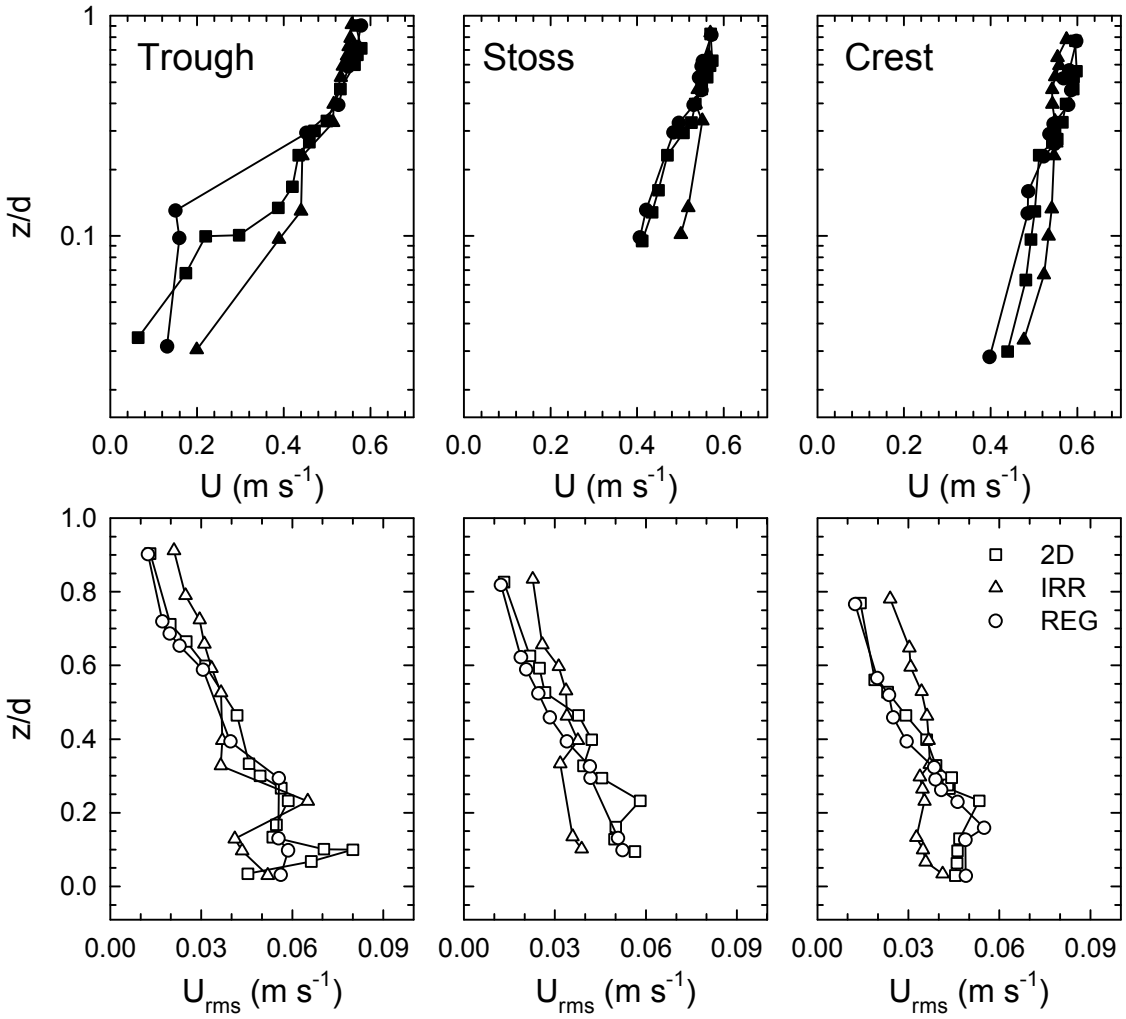

Figure 5.13: Select profiles of mean streamwise velocity, U (solid symbols), and streamwise root-mean- square velocity, U_{rms} (open symbols), over the regular (REG), irregular (IRR) and 2D dune configurations. In the context of Figure 5.3 the profiles over the 2D dunes are the 8th (trough), 18th (stoss) and 28th (crest) from the left. Height above the crests, z, is normalised by the dune height, d.

W contour map is negative in this trough region. Weak plunging flow occurs at the streamwise extent of the neighbouring lee slopes and a return flow occurs at *B1*.

There is no significant difference between the U_{rms} profiles over the regular and 2D dune morphologies except there is no increase in U_{rms} in the hollow at the lee slope in the regular dune trough profile. This is probably because there is no significant circulation in this region. A contour map of I_u indicates that a weak recirculation cell develops at the position of the neighbouring lee slopes. There is no strongly defined wake over the regular morphology but elevated values of I_u, t_{uw} and TKE occur between the upstream *SFB* and the upstream crest. Thus, the wake does not appear to have a lower boundary. Low t_{uw} and R_{uw} over the stoss slopes may indicate an IBL, but this is difficult to assess. In other respects the patterns of I_u, t_{uw} and TKE do not vary significantly over the regular and 2D dune morphologies.

Recall from Figure 5.2 that profiles over the irregular dune were taken where the neighbouring crests were staggered upstream and downstream. The crestline in the centre of the flume formed an asymmetric lobe. Profiles of U over irregular and 2D dunes are identical above the dune height. Below this point U is larger than over the 2D dune morphology (Figure 5.13). There is no shear layer observable in the trough profile and this is confirmed by examining the U contour map for the irregular morphology. In fact, the reduction in U is quite minimal in the trough zone and no upstream-directed flow is observed. The pattern of W velocities is similar over the irregular dune and the 2D dune. Plunging flow occurs over the dune crest with an upward directed return flow at *B1*. A significant difference in the mean flow quantities over the irregular and other morphologies is that there is a noticeable mean cross-stream velocity over the lobe, especially in the dune trough where V exceeds 0.08 m s^{-1} at the bed.

There is no observable wake, IBL or separation cell developed over the irregular dunes. However, there is a zone of more turbulent flow, observable in t_{uw} and TKE contour maps, in the

bedform trough that means some separation induced mixing must be occurring. Turbulent intensities are moderately larger in the outer layer over the irregular dune than over the 2D dune configuration but, near the bed, I_u is much less.

5.6 Effect of 3D morphology on Momentum Exchange and Energy Transfers

Over a flat bed, momentum exchange and mixing, as indicated by the distribution of t_{uw}, decreases with distance from the bed. Energy transfer from the mean flow, as indicated by the distribution of *TKE* , is confined to the lower $0.33\,d$. The presence of a 2D dune dramatically alters these distributions. The separation cell dominates momentum exchange but mixing is strong along the wake layer. As over a flat bed, little mixing occurs between $0.66\,d$ and the surface, because momentum exchanges at the bed have little impact. Similarly, the wake structure and separation cell dominates energy transfer from the mean flow. Turbulent energy is negligible above $0.66\,d$ of flow.

Introduction of three-dimensionality to the 2D crestline changes these distributions by rearranging the flow structure. Over a lobe, energy transfer from the mean flow (*TKE*) is dominated by the wake structure. When compared to a 2D dune, a greater amount of energy is transferred from the mean flow to turbulent flow, resulting in a slower mean flow velocity. Momentum is diffused laterally over the topographic high (Figure 5.14) and upwards into the flow column and a larger level of mixing is maintained over the whole dune field (Figure 5.7). Over a saddle, momentum is concentrated in the hollow (Figure 5.14) formed by the crestline, which results in less energy extraction from the mean flow and less mixing in the lee of the bedform (Figure 5.7). Therefore, flow velocity is enhanced as less energy is being extracted for mixing.

5.7 Spatially Averaged Flow over 3D Dunes

In order to make a final assessment of *Sirovich and Karlsen's* [1997] theory it is necessary to calculate a drag coefficient, $C_D = 2\left(u_*/U\right)^2$, and a drag force, $F_D = 0.5\,C_D\,r\,\overline{U}^2 A_b$ associated with

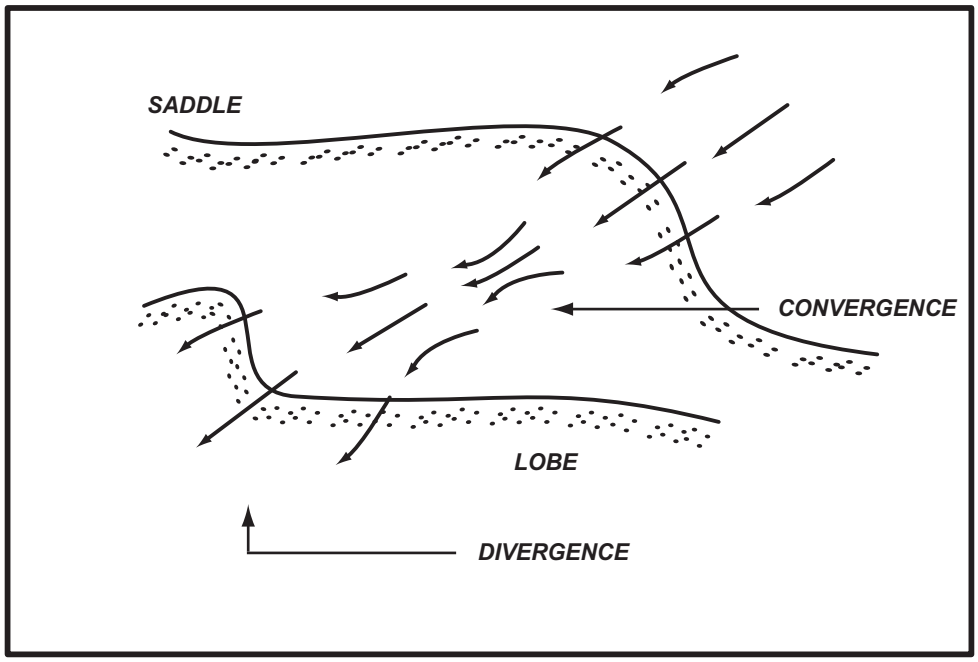

Figure 5.14: Lateral convergence or divergence of momentum and turbulent energy over lobe and saddle crestlines.

the dunes on each bed (A_b is the effective cross-sectional area of a body). For dunes A_b is the product of the dune width and H. Calculation of these quantities require the calculation of u_* for each bed morphology. Individual measurements of Reynolds stress or individual profile based estimates of shear stress are relatively meaningless over a dune as u_* varies tremendously across a dune surface. Therefore, spatially averaged u_* values must be estimated. These data can also be used to determine how 3D morphology affects the skin and form stress components of the total applied shear stress.

5.7.1 Theory

Over dunes the total spatially averaged shear stress, t_{tot}, is composed of a skin friction component, t_{sf}, and a form drag component, t_{form}, so

$$t_{tot} = t_{form} + t_{sf} \qquad 5.14$$

[*Einstein and Barbarossa*, 1952; *Smith and McLean*, 1977; *McLean et al.*, 1999]. The skin friction component is related to the resistance to flow offered by the sediment grains and the form drag component is resistance to flow offered by the bedform morphology. An additional component, the friction associated with the transport layer, can be added to t_{tot} when there is sediment transport [*Wiberg and Nelson*, 1992].

Evaluating the shear stress components can be a difficult enterprise and theoretical models have varying degrees of success when applied to real data. Thus, estimates of the shear stress components will be made using measurements.

There are two general approaches to estimating components of t_{tot}. The first method involves the calculation of t_{tot} over a flat bed with the same grain roughness as over the dunes formed at the same flow strength. Over a flat bed, $t_{tot} \approx t_{sf}$ because there is no form drag (assuming channel shape effects can be ignored). *van Rijn* [1984b] and *Yalin* [1992] have both proposed models in

which $t_{sf} \propto f(\overline{U}, r_w, C_{D-skin})$ and $C_{D-skin} \propto f(\overline{d}, k_s)$. Thus, assuming $\overline{U}$ and $\overline{d}$ are similar over the dune stoss slope and the flat bed, t_{sf} over the dune stoss slope is roughly equivalent to t_{sf} over the flat bed (t_{flat}). However, t_{sf} over a dune is not equivalent to t_{flat} because skin friction is only relevant between the reattachment point and the slipface crest. Thus, t_{sf} over a dune is related to the total stress over a flat bed by

$$t_{sf} = t_{flat}\left(\frac{L - x_R}{L}\right) \qquad 5.15$$

where x_R is the reattachment length. Equation 5.15 assumes that the width of flow over the flat bed and the dune bed is the same. The form drag can be estimated from Equation 5.14 (i.e. $t_{form} = t_{tot} - t_{sf}$).

Total shear stress can be determined by any number of methods. Assuming the water surface slope can be accurately determined, t_{tot} can be determined from the depth-slope product

$$t_S = r_w g \overline{d} S . \qquad 5.16$$

Alternatively, t_{tot} can be determined by plotting t_{uw} as a function of z/d. Over 2D dunes there is typically a region of approximately linear decrease with height above the bed. Through this region,

$$t_{uw} = t_R(1 - z/d) . \qquad 5.17$$

An estimate of t_R can be obtained by using a least-squares regression, through the linear decrease region, projected to the dune height [*Lyn*, 1993; *Nelson et al.*, 1993; *McLean et al.*, 1999]. This value of t_R should reflect t_{tot} [*McLean et al.*, 1999].

Another method of estimating the stress components in Equation 5.14 is based on the idea that spatially averaged velocity profiles over dunes are concave-down. *Smith and McLean* [1977] proposed that these velocity profiles can be divided into two log-linear segments, where the upper profile represents the total drag and the lower profile represents the skin friction component. Shear

velocities for the upper and lower portions of the velocity profile can be estimated from the von Karman-Prandtl law of the wall

$$\frac{U_z}{u_*} = \frac{1}{k} \ln \frac{z}{z_o} \qquad 5.18$$

where U_z is the velocity at some z and k is the von Karman constant which is assumed to be 0.4. The roughness height, z_o, is the intercept of the velocity profile plotted as a function of height above the bed. Shear stress for each profile segment can be determined from $t = r_w u_*^2$.

McLean et al. [1999] recently criticised this method for estimating total boundary shear stress, noting topographic effects are felt throughout the water column unless the flow is much deeper than the bedform height. Errors in t_{tot} can be up to ± 30 %. They note that local velocity profiles near the dune crest will underestimate t_{tot} and those in the dune trough will overestimate t_{tot}. They further suggested that a profile over the stoss slope between the two points may be as accurate as a spatial average. *Nelson et al.* [1993] and *McLean et al.* [1999] also note that lower velocity profiles should encompass measurements in only the IBL. If a spatial average uses measurements near the upstream dune crest, portions of the wake and the separation cell will be included, leading to erroneous estimates of t_{sf}. The message appears to be that spatial averages should be constructed in consideration of these problems and regarded with caution.

5.7.2 Depth Slope Product Measurements

Table 5.2 shows side wall corrected t_{S-tot} determined from the depth slope product (Equation 5.16) using $\bar{d}$ and S values presented in Table 5.1. Over the flat bed, t_{S-tot} = 1.0 Pa.

Applying Equation 5.15 to determine t_{sf} over the dunes is complicated because x_R could not be measured from flow maps as in other investigations [e.g. *Bennett and Best*, 1995; *Venditti and Bennett*, 2000]. Assuming $x_R \approx 3.5$ - $5\,H$ yields a separation length of 0.08 - 0.11 m, which may be

Table 5.2: Total, skin and form drag coefficient and force. Shear stresses are corrected for side wall effects using the relation supplied by *Williams* [1970]. Drag coefficients and forces are calculated based on the total shear stress. Values in brackets are for the central segment of spatially averaged Reynolds stress profiles.

Parameter	Flat	2D	FWL	FWS	REG	IRR	SNS	SNL	SSS
Determinations based on depth-slope product									
t_{S-tot}, Pa	1.0447	1.9072	1.9052	2.1610	2.0571	1.8507	1.7422	n/a	1.6028
t_{S-sf}, Pa	1.0447	0.6540	0.6540	0.6540	0.6540	0.6540	0.6540	n/a	0.6540
t_{S-form}, Pa	0.0000	1.2532	1.2512	1.5070	1.4031	1.1968	1.0883	n/a	0.9489
C_{DS}	0.0092	0.0163	0.0165	0.0191	0.0188	0.0171	0.0157	n/a	0.0147
F_{DS}, N	0.0120	0.0219	0.0219	0.0248	0.0236	0.0212	0.0200	n/a	0.0184
Determinations based on spatially averaged velocity profiles									
t_{*-tot}, Pa	0.5944†	1.1097	4.4905	0.0246	0.8915	0.0941	0.0859	0.1764	2.1953
t_{*-sf}, Pa	0.5944†	0.3577	0.1490	0.7115	0.4836	0.2464	0.8008	0.2311	0.4833
t_{*-form}, Pa	0.0000	0.7520	4.3415	-0.6869	0.4078	-0.1522	-0.7149	-0.0547	1.7120
C_{D*}	0.0052	0.0100	0.0393	0.0002	0.0080	0.0009	0.0008	0.0016	0.0213
F_{D*}, N	0.0068	0.0122	0.0515	0.0003	0.0102	0.0011	0.0010	0.0020	0.0252
Determinations based on spatially averaged Reynolds stress profiles									
t_{R-tot}, Pa	0.3679	0.9555	1.4066	0.0630 (0.2880)	0.6242	0.4226	0.0835 (0.2047)	1.0601	0.1642 (0.3751)
t_{R-sf}, Pa	0.3679	0.2303	0.2303	0.2303	0.2303	0.2303	0.2303	0.2303	0.2303
t_{R-form}, Pa	0.0000	0.7252	1.1763	-0.1673 (0.0577)	0.3939	0.1923	-0.1468 (-0.0256)	0.8298	-0.0661 (0.1448)
C_{DR}	0.0033	0.0081	0.0122	0.0006 (0.0025)	0.0057	0.0039	0.0018	0.0095	0.0015 (0.0034)
F_{DR}, N	0.0042	0.0110	0.0161	0.0007 (0.0033)	0.0072	0.0048	0.0023	0.0122	0.0019 (0.0043)

†Based on lower $0.2\,d$ of velocity profile (see Chapter 3 for explanation).

an accurate estimate over the 2D dune, but over the 3D morphologies, contour maps of the flow structure suggest x_R may vary. Based on the size of the separation cell, it appears that the reattachment length would be longer over the lobes and shorter over saddles when compared to a 2D dune. Without measurements, the reattachment length used in Equation 5.15 cannot be adjusted for different dune morphologies. However, it is likely that the skin friction contribution to the total shear stress is not great upstream of *B2* because of the dune topography. Therefore, x_R will be assumed to be the distance from the upstream dune *SFB* to *B2* or 0.13 m. Based on this assumption, t_{sf} = 0.65 Pa over the dunes.

Over the 2D dune, t_{S-tot} = 1.91 Pa ($t_{S-sf} = 0.34\, t_{S-tot}$) and t_{S-form} = 1.25 Pa ($0.66\, t_{S-tot}$). For a 2D dune with an aspect ratio of 0.05, *Smith and McLean* [1977] suggest the ratio of skin to total shear stress should be ~0.4, which is near the value observed over the 2D dune here.

Despite the fact that I_u and t_{uw} are substantially reduced over the full-width saddle and the regular bed, $t_{S-tot} \approx$ 2 Pa ($t_{S-sf} \approx 0.30$ - $0.32\, t_{S-tot}$). Over the irregular dune, where turbulence was greatly suppressed, t_{S-tot} and t_{S-form} are nearly equivalent to values for the 2D bed. The same is true of t_{S-tot} and t_{S-form} over the full-width lobe where I_u and t_{uw} are substantially enhanced. Only over the sinuous beds is t_{S-tot} reduced below its value over the 2D dune. Here t_{S-tot} = 1.6 - 1.7 Pa ($t_{S-sf} \approx 0.38$ - $0.41\, t_{S-tot}$). As expected, the sinuous dunes with the smoothed crest produced a lower total boundary shear stress.

When this array of t_{S-tot} values is used to calculate u_* and ultimately C_D and F_D, the same groupings appear. For the 2D, full-width lobe, irregular and sinuous lobe morphologies $C_D \approx 0.016$ and $F_D \approx$ 0.022 N. For the full-width saddle and the regular dunes the drag is moderately larger (C_D $\approx$ 0.019 and $F_D \approx$ 0.024 N) and for the smoothed sinuous crest, drag is reduced (C_D = 0.015 and F_D = 0.018 N.

The most substantial problem with these estimates of the shear and the drag is that they do not reflect the flow structure. The depth-slope product may simply be too coarse a measure. Spatial averaging is used below in an attempt to alleviate this problem.

5.7.3 Spatially Averaged Velocity Measurements

Spatial averages of velocity were calculated along constant heights above a datum. Over the flat bed the datum is the bed and over the dunes the datum was the dune crest. In order to avoid biasing the inner velocity profiles by velocities collected in the separation zone or the wake near the dune crest, averages of U were constructed over the dune back, between *B1* and the dune crest. The vertical rise in between these two points on the dune is minimal (~3 mm), so whether the inner profiles are constructed at constant heights above the bed, or constant heights above a datum, does not affect the profiles (see Appendix E).

It can be argued that the total shear stress should be based on a spatially averaged profile over the whole dune and not just over the portion where the skin stress contributes. Thus, two sets of profiles were constructed. The first set were the upper portion of the inner profiles over *B1* and the dune crest. The second set was averaged over the whole dune length. Whether the outer profiles are constructed at constant heights above the bed or, constant heights above a datum, does not affect the profiles significantly (see Appendix E). There was no significant difference between the outer profiles averaged over the whole dune and those averaged over the stoss slope (see Appendix E or Figure 5.15). The outer profiles discussed below are averaged over the stoss slope of the dunes.

Constructing the inner and outer profiles in this fashion should mitigate some of the concerns expressed by *McLean et al.* [1999]. However, the results will be considered in light of the fact that values of t_{tot} could vary by ± 30 % about their true value.

Figure 5.15 presents the spatially averaged velocity profiles over the flat, 2D dune and 3D dune beds. Tables 5.3 and 5.4 provides least-squares regression results that were used to estimate the slope

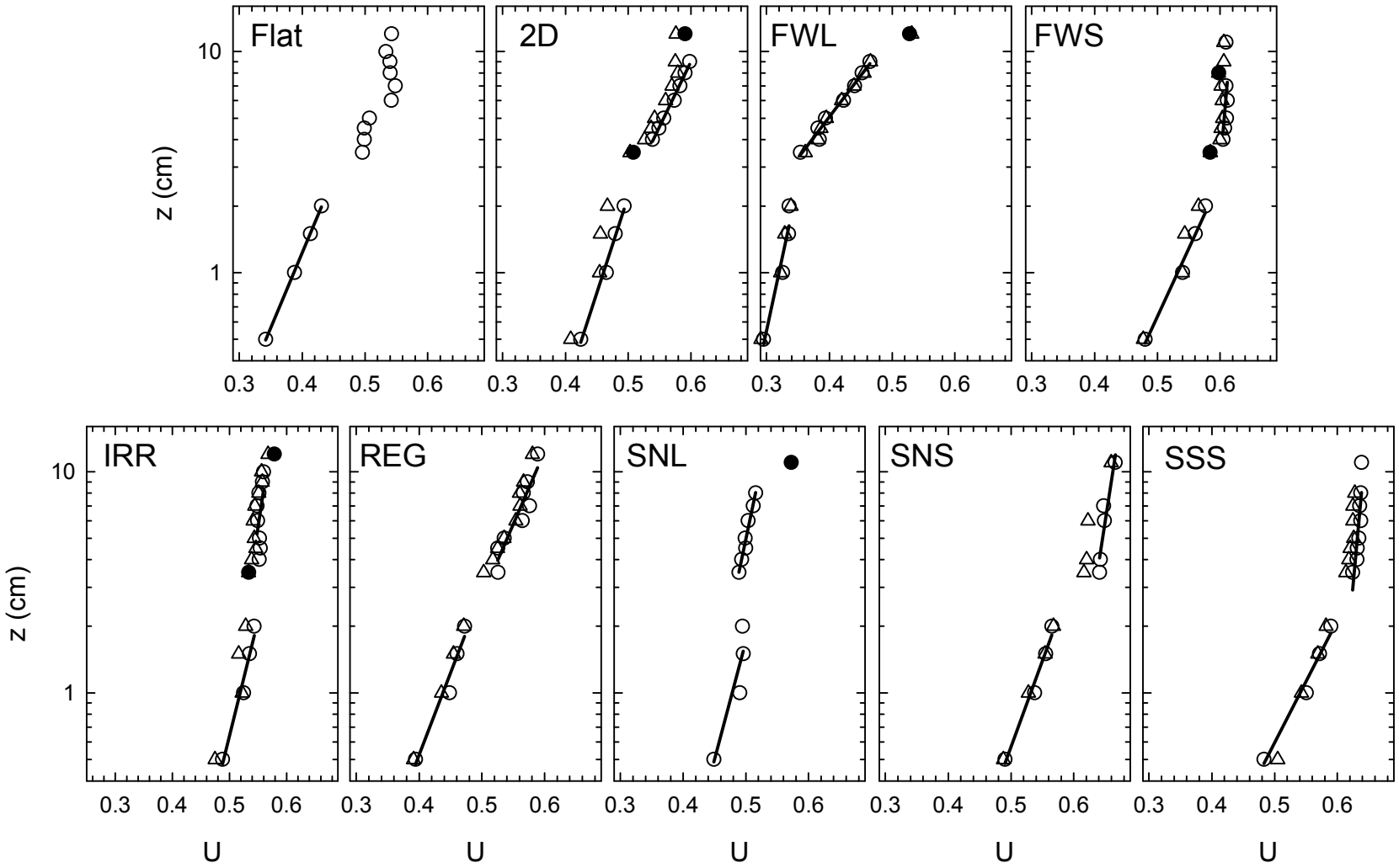

Figure 5.15: Spatially averaged streamwise velocity, U, profiles. Circles are averages of data between B1 and the crest (profiles 18-28 in Figure 5.3) and triangles are averages of all data between successive crestlines (profiles 1-28 in Figure 5.3). Regressions are based on the former set of averages. Inner profile regressions are based on the lower four data points and outer profiles include all points above 0.03 m. Solid symbols denote data points omitted from the regressions in order to improve the fit. Profiles using data from profiles 1-28 in the averages over the sinuous lobe were distorted because of the probe change and are not plotted.

Table 5.3: Least-squares regression of inner and outer velocity profiles constructed using profiles taken between *B1* and the crest. b_0 is the intercept and b_1 is the slope.

Parameter	Flat	2D	FWL	FWS	REG	IRR	SNS	SNL	SSS
				Inner Profile					
b_0	-2.62	-4.01	-4.24	-3.27	-3.25	-5.42	-3.00	-5.08	-4.13
b_1	6.77	8.71	13.27	6.15	7.42	10.45	5.55	10.61	7.77
r^2	1.00	0.99	0.92	0.98	0.96	0.97	0.98	0.84	0.98
				Outer Profile					
b_0	--	-2.59	-0.78	-19.99	-2.89	-9.04	-11.25	-6.06	-1.94
b_1	--	5.90	3.72	34.11	6.63	17.79	18.50	13.52	31.81
r^2	--	0.99	0.98	0.27	0.87	0.22	0.88	0.97	0.75

Table 5.4: Least-squares regression through linear portions of the Reynolds stress profiles. Values in brackets are for the central segment of spatially averaged Reynolds stress profiles. b_0 is the intercept and b_1 is the slope.

Parameter	Flat	2D	FWL	FWS	REG	IRR	SNS	SNL	SSS
b_0	7.49	8.65	16.71	9.05 (5.35)	8.76	14.11	10.58 (6.11)	14.65	8.50 (5.48)
b_1	-20.36	-9.06	-11.88	-143.64 (-18.56)	-14.03	-33.39	-126.83 (-29.86)	-13.82	-51.74 (-14.62)
r^2	0.99	0.98	1.00	0.87 (0.98)	0.99	0.92	0.90 (0.99)	1.00	0.94 (0.99)

and intercept of the upper and lower velocity profile segments. Over a flat bed, profiles are similar to those presented in Chapter 3 with a linear increase in U with log z. $t_{*tot} \approx 0.6\, t_{S-tot}$ (the subscript * indicates a value derived from a spatially averaged velocity profile), which should not be surprising. A similar trend was observed in Chapter 3 and attributed to the footprint of the lower portion of the velocity profile. The depth-slope product is dependent on side wall resistance in addition to bed resistance.

Profiles over the 2D dunes have two log-linear segments and upper segments have a lower slope (i.e. higher shear rate) (Table 5.3). Thus, $t_{*tot} > t_{*sf}$ and $t_{*form} > 0$ (Table 5.2). Over the 2D dune, $t_{S-tot} > t_{*tot}$ and $t_{*sf} \approx 0.32\, t_{*tot}$, near the t_{*sf} / t_{*tot} value (0.4) suggested by *Smith and McLean* [1977].

Values of t_{*sf} produced from the lower segment of the velocity profiles are of the same order of magnitude as t_{*tot} over the flat bed, but varied between 0.15 and 0.80 Pa over the different dune morphologies. There is no relation between t_{*sf} and $\overline{U}$. In the absence of more information, it is difficult to assess whether this is a problem in the method used to split the skin and form components of the total stress, or real variation.

Values of t_{*tot} also show confusing variation. Over the full-width lobe dunes, there are two log-linear segments and the upper segment has a lower slope than the inner segment, as was observed over the 2D dune (Table 5.3). However, t_{*tot} is much greater than its value over the 2D bed (t_{tot-2D}) at 4.5 Pa (t_{*sf} =0.033 t_{*tot}). This observation is in agreement with expectations based on the turbulent flow structure over the full-width lobe dune. Over the full-width saddle and the sinuous saddle (smoothed and ragged) crestlines there are two log-linear segments, but the upper segment has a lower slope (Table 5.3), indicating a lesser shear stress. For these profiles, $t_{*tot} < t_{*sf}$ and t_{*form}, by difference, is less than 0 (Table 5.2). Profiles over the irregular, regular and sinuous lobe crestlines have weakly defined slope breaks, where the upper and lower profiles have approximately

the same slope (Table 5.3). Over these dunes, $t_{*tot} \leq t_{*sf}$ and $t_{*form} \approx 0$ (Table 5.2). As is discussed below, it is not unreasonable to have $t_{*form} \approx 0$ when there is no evidence of strong separation or a wake structure. However, it is not clear how $t_{*form} < 0$ could occur under any circumstance. The suggestion by *McLean et al.* [1999], that the outer log-linear portions of the spatially averaged velocity profile may not accurately reflect t_{tot}, appears to be particular relevant over 3D bedforms.

5.7.4 Spatially Averaged Reynolds Stress Measurements

Figure 5.16 presents the spatially averaged t_{uw} profiles. Reynolds stress was averaged along constant planes above a datum. Over the flat bed the datum was the bed and over the dunes, the datum was the crest. Averages include all positive t_{uw} values observed between two successive crestlines. Profiles will differ if t_{uw} is averaged along equidistant lines above the boundary (Appendix E). However, the spatially averaged t_{uw} profile should only be linear well above the bedform where values are not directly affected by flow separation. Thus, the more meaningful profile is from averages at constant planes above the dune crest [see *Nelson et al.*, 1993 and *McLean et al.*, 1999].

Over the flat bed, profiles are similar to the profiles observed in Chapter 3 over the flat beds with active transport, except at the boundary. There is a linear increase in t_{uw} with decreasing z, but near the bed (z < 0.02 m or z/d < 0.15), t_{uw} decreases slightly. This is not surprising as the flat beds discussed in Chapter 5 had active sediment transport which would have increased t_{uw} in this region [see *Best et al.*, 1999].

Over the 2D dune, a substantial portion of the spatially averaged t_{uw} profile is linear and similar to those presented by *Wiberg and Nelson* [1992], *Nelson et al.* [1993], *Bennett and Best* [1995] *McLean et al.* [1999] and *Venditti and Bennett* [2000]. At a height of ~0.04 cm ($z/d \approx 0.25$), there is

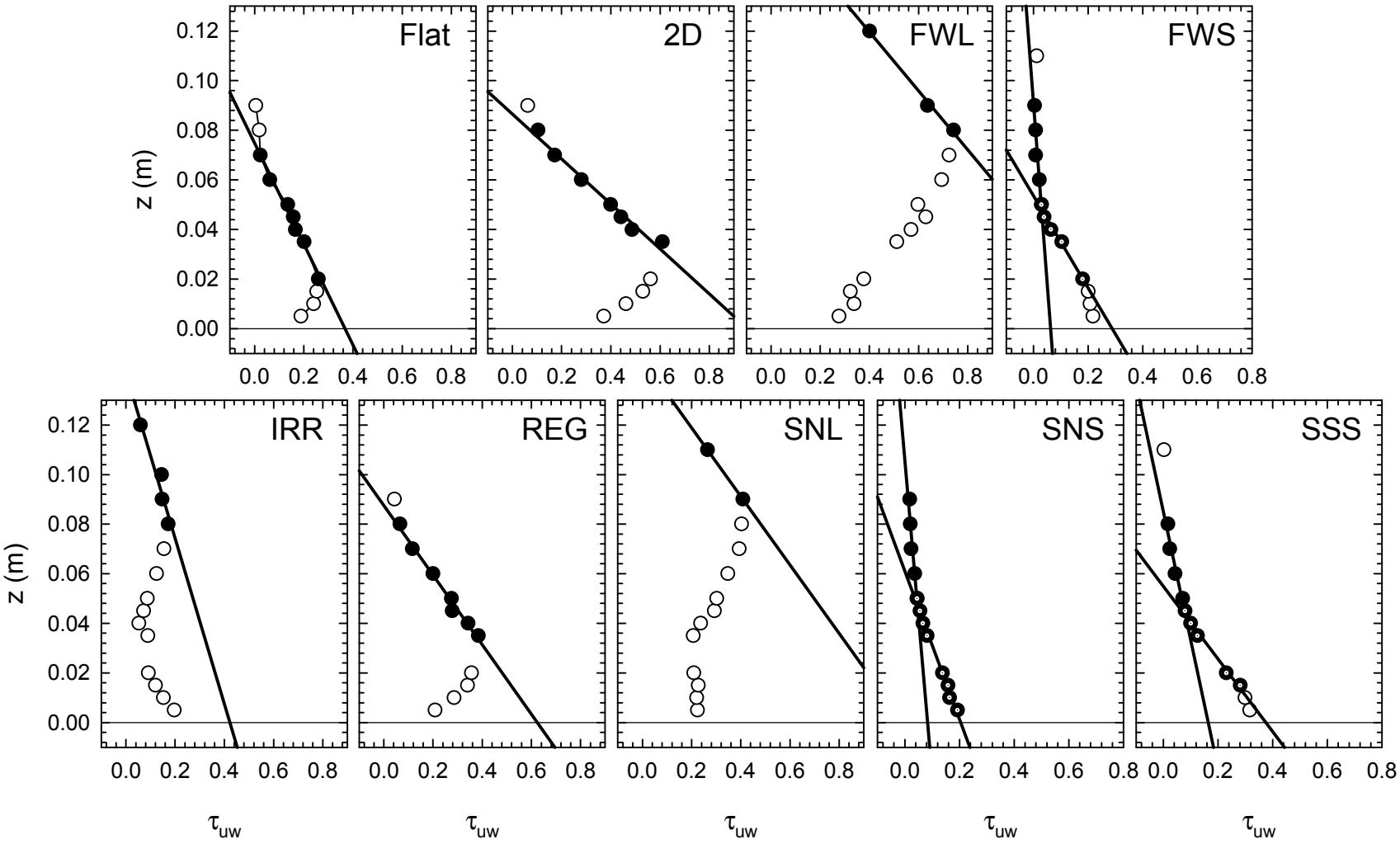

Figure 5.16: Spatially averaged Reynolds stress (τ_{uw}) profiles. Averages include all positive τ_{uw} values observed between two successive crestlines. Circles are averages along constant heights above a datum that was the crest over the dunes and the bed over the flat bed. Only closed circles were used in the least-squares regressions (thick lines). Two regressions were calculated for FWS, SNS and SSS profiles. The first uses the closed circles and the other uses the closed circles with centre dots.

an inflection in the curve and t_{uw} decreases in both vertical directions. The spatially averaged profile over the regular dune morphology has essentially the same form, which is not surprising. Apart from the fact that the regular dune lacked a well-defined wake, the distribution of I_u and t_{uw} over the 2D and regular dune morphologies were substantially similar.

Over the full-width lobe, there is an inflection in the t_{uw} profile that occurs at ~0.08 m ($z/d \approx$ 0.53) and, as over the 2D dune, t_{uw} decreases in both vertical directions. Profiles of spatially averaged t_{uw} over the sinuous lobe and irregular beds are composed of three segments (recall that profiles over the irregular bed were taken along the flume centre line over a minor lobe). As over the full-width lobe, an inflection occurs in the centre core of the flow at ~0.09 m ($z/d \approx$0.60) over the sinuous lobe and ~0.08 m ($z/d \approx$0.53) over the irregular lobe. Spatially averaged Reynolds stress decreases in both vertical directions about the inflection. Another inflection occurs at the base of the profile, ~0.04 cm ($z/d \approx$0.25), where t_{uw} increases in both vertical directions. The magnitude of t_{uw} at the inflections is largest over the full-width lobe, intermediate over the sinuous lobe and lowest over the irregular lobe.

Spatially averaged t_{uw} profiles over saddles are also composed of three segments, but all three segments show decreasing t_{uw} with increasing z. There are breaks in the slope of the curve at ~0.03 and 0.05 m ($z/d \approx$0.20 and 0.33). Top and bottom portions of the profiles have similar slopes that differ in magnitude over the various saddles.

It is a relatively simple task to identify the linear portions of the spatially averaged t_{uw} over the flat, 2D, regular and full-width lobe morphologies, allowing an estimate of t_R using Equation 5.17. Appropriately, t_{tot} (t_R) increases through flat - 2D dune - full-width lobe morphologies. Unfortunately, it is not obvious which portion of the spatially averaged t_{uw} profiles provide a reasonable estimate of t_{tot} over the other bed morphologies. It is assumed that the uppermost

segment of the three-segment profiles represent the total boundary shear stress when extended to the bed. Results of least-squares regression through these portions of the profiles are presented for all bed morphologies in Table 5.3 and estimates of t_R can be found in Table 5.2.

The side wall corrected, spatially averaged, boundary shear stress over the flat bed, t_{R-flat}, was 0.37 Pa or ~0.33 t_{S-tot}. Again, this pattern where $t_R < t_S$ was observed in Chapter 3. As noted above for depth slope product estimates of shear stress, t_{R-sf} is not equivalent to t_{R-flat} and Equation 5.15 needs to be applied using the assumption that x_R can be approximated as the distance from the upstream dune *SFB* to *B2*. Based on this assumption, t_{R-sf} = 0.23 Pa over the dunes.

Over the 2D dune, t_{R-tot} = 0.96 Pa (t_{R-sf} = 0.24 t_{R-tot}) and t_{R-form} = 0.73 Pa (0.76 t_{R-tot}). The ratio of skin to total shear stress is less than the value (0.4) suggested by *Smith and McLean* [1977]. Over the full-width lobe, t_{R-tot} = 1.41 Pa (t_{R-sf} = 0.16 t_{R-tot}) which is greater than its value over the 2D bed (t_{tot-2D}). Over the sinuous lobe, $t_{R-tot} > t_{tot-2D}$. Over the regular and irregular dune morphologies, $t_{R-tot} < t_{tot-2D}$. Irregular bed t_{R-tot} is less than regular bed t_{R-tot}. The ratio of skin to total shear stress varied between 0.16 and 0.54 over these dunes.

Spatially averaged t_{uw} profiles over saddles are more complex and pose a substantial impediment to determining stress values. Regressions extended to the boundary through the upper segments of these profiles indicate $t_{R-tot} < t_{R-sf}$. Regressions though the lowest segment produce similar results. Regressions through the steeper central profile provide greater t_{R-tot} values of 0.29 Pa (FWS), 0.20 Pa (SNS) and 0.38 Pa (SSS), which are either greater than or roughly equivalent to t_{R-sf}. One of two possibilities can explain these results. Either the model upon which 5.17 is based upon breaks down over saddle shaped features due to momentum convergence, or these bed morphologies are so effective at reducing form drag that this component of the stress is not felt throughout the profile and skimming flow is generated. Both possibilities are interrelated.

The basic assumption that underlies Equation 5.17 is that all turbulence production occurs at the boundary. Over a flat bed, discrete, coherent structures are generated that break down and cascade turbulent energy to smaller scales. With distance from an obstacle or rougher patch of the boundary, fluctuations in velocity and hence the turbulence, are reduced. Naturally, this also occurs with distance above a boundary, resulting in a reduction in the turbulent stresses with increasing height. Over dunes, most turbulence production occurs not at the boundary, but in the separation zone, and this turbulence is dissipated along the flow and vertically [*Nelson et al.*, 1993; *Venditti and Bennett*, 2000]. Applying a spatial average assumes that the turbulence is dissipated along-stream and that an average will remove the spatial non-uniformity over one bedform length [*McLean et al.*, 1999].

Over saddles, separation occurs but wake generation is inhibited. Thus, there is no strong along-stream dissipation of energy, and so the saddle shaped dune beds are acting like flat beds in that the lower portion of Reynolds stress profiles respond to skin friction over the stoss slope and crest. Minimal contributions to t_{R-tot} are made by t_{R-form}. This idea deserves further examination.

5.8 Drag over 3D Dunes

The effect of the 3D dune morphology on drag can be examined using drag estimates based on spatially averaged Reynolds stress profiles. Overall these results are consistent with the observations of I_u and t_{uw} over the dune. Values of C_D and F_D indicate that over the 2D dunes, C_{DR} = 0.008 and F_{DR} = 0.011 N. Lobes generally enhance drag while saddles cause significant drag reduction. The change in drag (enhancement or reduction) is measured as

$$\frac{C_{DR} - C_{DR-2D}}{C_{DR-2D}} \qquad 5.19$$

where the subscript $2D$ indicates a measurement over the 2D dune and + values indicate enhancement while - values indicate reduction.

The degree of drag enhancement is dependent on the cross-stream extent of the lobe. Compared with the drag over a 2D dune, sinuous lobes that occupy half the flume width increase total drag by ~17 % while full-width lobes increase total drag by ~50 %. The apparent reason for the enhancement is an increase in the form drag caused by the lateral and vertical divergence of momentum and turbulent energy over lobes. The degree of drag reduction over saddle forms does not depend on their cross-stream extent, as form drag does not contribute significantly to the total stress. This appears to be caused by the lateral and vertical convergence of momentum towards a small area in the lee of the bedform.

As discussed in Chapter 4, *Sirovich and Karlsen* [1997] theorise that drag is reduced by random or irregular distributions of roughness elements. A final test of whether this theory can be applied to bedforms can be made by examining the drag generated by the 2D, regular and irregular bedforms. Compared with the drag over a 2D dune, the regular dune morphology reduces total drag by ~30 % by reducing the form drag component. As noted above, the regular dune is an end member case for examination of the *Sirovich and Karlsen* [1997] theory. It is useful to examine the more probable regular 3D dune morphology (i.e. the sinuous case).

Recall from Figure 5.2 that the sinuous crest is composed of two lobes, one saddle in the centre of the flume and two half saddles at the side walls. If a single estimate of C_{DR} is made, it would be logical to average the results over the lobe and the saddle which gives $C_{DR} \approx 0.006$. Thus, total drag is reduced by ~30% over the sinuous crested dune.

The irregular bed morphology reduced total drag by ~52 %, even though measurements were taken over a lobe. Lobes appear to increase drag when they are full-width forms or are in a regular morphology, but if in an irregular morphology, drag is reduced over a lobe. The apparent reason is that the wake is prevented from developing and there can be no significant divergence of momentum. Thus, the form drag component is reduced.

The original idea behind the investigation of drag reduction was to determine if a shift 2D to 3D bed morphology reduced or stabilised the shear stress, and in doing so, reduced the transport rate, imparting greater stability the bed (see Chapters 1 and 4). The reduction in the total stress observed is caused by a reduction in the form component. It is often assumed that sediment transport rates over dune stoss slopes are related to the skin friction component. Thus, it is not clear how a reduction in the form drag will affect the transport rate at the individual bedform scale. However, at the scale of the bedform field, the reduction in the total drag should reduce transport rates leading to greater stability of the bed.

5.9 Summary and Conclusions

A set of experiments was designed to examine the turbulent flow over fixed dunes with different crest shapes but constant wavelengths and heights. Laboratory measurements of turbulent fluctuations in clear water over fixed flat, 2D and 3D dune beds were obtained in a 17 m long, 0.515 m wide flume. Flow over nine bedform morphologies is examined: (1) flat bed, (2) straight-crested 2D dunes, (3) full-width saddle (crestline bowed upstream), (4) full-width lobes (crestline bowed downstream), (5) sinuous crest (saddle portion), (6) sinuous crest (lobe portion with a ragged crest), (7) sinuous crest (lobe portion with a smooth crest), (8) regular staggered crest and (9) irregular staggered crest. Measurements of velocity were made at a sampling rate of 50 Hz using an acoustic Doppler velocimeter at 350-500 points over a dune in each morphology.

The time averaged turbulence structure over the fixed flat bed is dynamically similar to flow over a flat bed with active sediment transport. The observed flow field over the 2D dune agrees well with an empirically derived model of flow over mobile and fixed bedforms.

Three-dimensional bedforms appear to modify the flow field over a dune significantly. Lobe shaped dune crestlines appear to enhance the level of turbulence producing a better defined wake structure and more vigorous mixing in the separation cell than observed over 2D dunes. This causes lateral and vertical divergence of momentum and turbulent energy. Whether the lobe exists in a

regular configuration (i.e. sinuous crestline) or an irregular configuration seems to be relevant. Irregular lobes seem to affect the flow in the same fashion as saddle shaped dune crestlines where the separation cell is only weakly defined and the wake does not appear to be a significant component of the flow field. This causes the lateral and vertical convergence of momentum and turbulent energy to a small area in the lee of the dune.

Spatially averaged flow over the bedforms was examined in order to estimate the total, form and skin drag over the dune morphologies. Estimates of the shear and the drag from the depth-slope product do not reflect the turbulence structure. Spatially averaged velocity profiles over 2D dune beds show the characteristic outer and inner log-linear profiles that can be successfully linked to the total and skin related shear. Flow over the 3D dunes differs from flow over the 2D dune significantly enough that inner and outer profile segments cannot be consistently defined. The suggestion by *McLean et al.* [1999] that the outer log-linear portions of the spatially averaged velocity profile may not accurately reflect t_{tot} appears to be particular relevant over 3D bedforms. Using the inner and outer log-linear portion of spatially averaged velocity profiles to estimate total, skin and form drag over 3D dunes can produce erroneous results.

Spatially averaged Reynolds shear stress profiles appear to be the most accurate way to estimate the total boundary shear. Skin friction can be estimated from shear stress measurements over the flat bed allowing calculation of the form drag. Compared to flow over a 2D dune, lobe shaped crestlines enhance form drag while saddle shaped forms reduce form drag. Total shear stress over saddle shaped crestlines is nearly equivalent to the skin friction suggesting that, when there is no significant separation cell and wake, the form drag is rather insignificant.

Irregular crestline morphologies passively reduce drag more effectively than regular configurations. A regularly sinuous crested bedform reduced drag by ~30%. In contrast, an irregular crest morphology that resembled the 3D beds discussed in Chapter 4 reduced drag by ~52 %. These results suggest that drag reduction does occur during the transition between 2D and 3D dunes. The

ideas of *Sirovich and Karlsen* [1997] concerning drag reduction over aligned and randomly oriented surface roughness elements are relevant for dunes. Further work is required to determine what implications this finding has on sediment transport processes in sand-bedded river channels.

Chapter 6: Conclusions

6.1 The Initiation of Bedforms

The first aim of this study was to examine the processes that lead to the development of two-dimensional (2D) dunes in river channels. A specific goal was to examine a conceptual model termed herein the flow structure approach. The model indicates that bedforms are generated from random turbulent events that generate bed defects. These defects are propagated downstream by flow separation processes and eventually develop into bedforms. This model has received some attention in the literature and widespread support in the earth sciences yet there are two major problems with it. The first is that there is a large discrepancy between the time scales of bed development and turbulence. The second problem is that it is not clear how random turbulent events can produce one of the most regular forms observed in nature.

In order to examine this problem a series of experiments was designed to examine bedform development in homogeneous 0.5 mm sand in a 1 m wide flume. The sand bed was flattened to remove all variation greater than 1 mm and subjected to a 0.155 m deep, non-varying mean flow ranging from 0.30 to 0.55 m s^{-1}.

The initial flow conditions over the flat beds, prior to bedform development, were examined using laser Doppler anemometry to establish that the flow agrees with standard models of flow and turbulence over hydraulically rough flat beds. With the exception of the depth-slope product calculations, estimates of the boundary shear stress derived from different methods are similar in magnitude and increase in a similar fashion with mean flow strength. The roughness heights are consistent with previous observations. The turbulence intensities and boundary layer correlation can be modelled by the semi-empirical functions provided by *Nezu and Nakagawa* [1993], with the exception of the vertical intensities at the low flow strengths. With few exceptions, the momentum exchange and fluid diffusion are typical of fully turbulent, uniform, open channel flows. This establishes that the bedforms are not developed by some aberrant flow condition.

Two types of bedform initiation are observed in the experiments. The first occurs at lower flow strengths and is characterised by the propagation of defects via flow separation processes to develop bedform fields. This type of bedform development is in accordance with the flow structure approach described above. However, the defects examined here were artificially made because the flat bed seemed capable of remaining flat in their absence. Thus, a perturbation was introduced to the system and not internally generated by the flow structure (or random turbulence).

The second type of bedform initiation observed differs quite substantially from the flow structure approach to bedform development and has received less attention. This mode of bedform initiation begins with the imprinting of a cross-hatch pattern on the flat sediment bed which leads to chevron shaped forms that migrate independently of the initial structure. The chevron shapes are organised by a simple fluid instability that occurs at the sediment transport layer-water interface. Predictions from a Kelvin-Helmholtz instability model are nearly equivalent to the observations of bedform lengths in the experiments. It is likely that the instability model holds only for fully mobile bed conditions because the bed constitutes a fluid layer that would be less applicable to situations where the active transport layer is discontinuous.

Thus, neither type of bedform development observed here support the conceptual model based on turbulent flow structures. The observed defect propagation confirms that flow separation is a viable mechanism for bedform development. However, it is not clear that turbulent events can generate the initial defects. The fluid instability model of bedform development operates without external perturbation of the system and is capable of producing the regularity observed in bedform fields.

6.2 Development of Bedforms

The experiments in which bedform initiation was examined were extended to determine how the initial forms evolved. It was also of interest to determine what the equilibrium bedform dimensions and dynamics are at these flow stages. Three basic waveforms were found in the channel, including

long sediment pulses, dunes and sand sheets. Insufficient data was available to examine the long sediment pulses so investigation was limited to the dune and sand sheet waveforms.

The initial 2D bedforms developed by the Kelvin-Helmholtz instability developed into dune features that grew exponentially towards equilibrium dimensions. The instability scaling is not preserved because the presence of bedforms leads to a further mutual adjustment of the flow and the bed geometry. Dune heights and lengths increased with flow strength while their migration rate decreased. The dunes that are present during the equilibrium stage are morphologically similar to the initial forms present. Aspect ratios suggest that all the forms present are dunes according to the classification scheme of *Allen* [1968]. There is no obvious transition from small ripples at the beginning of the runs to dunes when the sandwaves are larger.

Smaller bedforms, termed sand sheets, developed over the stoss slope of the dunes. Interestingly, both the dunes and the sand sheets were observed to be in equilibrium at the same time, meaning both bedforms were active sediment transport agents. The sheets, many lacking slipfaces, form at approximately 0.5 m from the dune slipface, downstream of the reattachment point. This distance is invariant with dune size, suggesting there is a necessary 'fetch' length needed for the sheets to begin to grow. Approximately 3-4 sand sheets were observed per 100 s. The sheets have heights that are typically 0.1× the height of the dune upon which they are superimposed, migrate at 8 - 10× the dune rate, and have lengths that are nearly constant over the full range of dune lengths and flow conditions. Aspect ratios are generally < 0.1 with a mode of ~0.025, classifying them as low relief or incipient dunes.

Sediment transport rates, measured with a Helley-Smith sampler, and estimated from the morphology of both the dunes and the sand sheets, are similar in magnitude. Unfortunately, the measurement error associated with the Helley-Smith samples is too large to make a meaningful comparison between the samples and the morphological transport estimates. However, for the larger flow strengths the material moving in sand sheets over the stoss slope of the dunes is equivalent to the material moved in the dune form.

6.3 Transition Between 2D and 3D Dunes

One of the primary characteristics of the dunes observed during these experiments was that they were distinctly three-dimensional (3D) after an initial 2D stage that ended when the bedform lengths extended beyond the Kelvin-Helmholtz wavelength. Thus, a second aim of the study was to examine the 2-3D dune transition in river channels. The primary goals in this portion of the research were to determine what constitutes a 3D bedform, how they develop and why they develop.

A definition of what constitutes a 3D bedform was provided using a statistic called the non-dimensional span or sinuosity of dune crests, which is the distance along the bedform crestline divided by the distance across the channel between crest endpoints. A critical value of 1.2 is proposed to divide bedforms with straight or slightly sinuous 2D crests from highly 3D bedforms.

Overhead video records were examined for patterns in the breakdown of 2D dune crestlines that gave insight to the physical mechanisms of the transition. The video revealed that, once 2D dunes are established, minor, transient excesses or deficiencies of sand are passed from one crestline to another. The bedform field appears capable of 'swallowing' a small number of such defects but, as the number grows with time, the resulting morphological perturbations produce a transition in bed state to 3D forms that continue to evolve, but are pattern-stable.

A possible explanation for why the transition occurs is provided by examining recent advances in the aerodynamics literature that have suggested that surface drag can be significantly altered by the arrangement of perturbations on otherwise flat surfaces. Aligned (2D) arrangements of roughness elements were found to increase drag while random (3D) arrangements of roughness elements greatly reduced drag. Thus, the shift from 2D to 3D dune morphology was examined as a mechanism that reduces drag.

Time dependent drag coefficients were calculated using continuous records of water surface slope and bed elevation. A defined increase in the drag coefficient is lacking during the early stages of the experiment and during the 2-3D dune transition, suggesting that passive drag reduction processes may

be at work. However, changes in the drag are somewhat obscured by other processes, primarily dune growth, as the transition occurs. An out of phase relation between the drag coefficient and the non-dimensional span suggests that these quantities may be dynamically linked at certain times. However, correlation analysis fails to reveal a relation between the drag coefficient and the non-dimensional span because the measured water surface slope may not be representative of the energy gradient. Unfortunately, these problems could not be resolved through these data. Thus, another experiment was conducted using fixed bedforms with varying crestline shapes.

6.4 Drag Reduction Processes

A series of experiments was designed to examine turbulent flow over fixed dunes with different crest shapes, but constant wavelengths and heights. Laboratory measurements of turbulent fluctuations in clear water over fixed flat, 2D and 3D dune beds were obtained in a 17 m long, 0.515 m wide flume. The bedform dimensions and the corresponding flow conditions were identical to one flow stage in the experiments described above.

Flow over nine bedform morphologies was examined: (1) flat bed, (2) straight-crested 2D dunes, (3) full-width saddle (crestline bowed upstream), (4) full-width lobes (crestline bowed downstream), (5) sinuous crest (saddle portion), (6) sinuous crest (lobe portion with a ragged crest), (7) sinuous crest (lobe portion with a smooth crest), (8) regular staggered crest and (9) irregular staggered crest. Measurements of velocity were made at a sampling rate of 50 Hz using an acoustic Doppler velocimeter at 350-500 points over a dune in each morphology.

The time averaged turbulence structure over the fixed flat bed is dynamically similar to flow over a flat bed with active sediment transport. The observed flow field over the 2D dune agrees well with an empirically derived model of flow over mobile and fixed bedforms.

Three-dimensional bedforms appear to modify the flow field over a dune significantly. Lobe shaped dune crestlines appear to enhance the level of turbulence producing a better defined wake structure and more vigorous mixing in the separation cell than observed over 2D dunes. This causes

lateral and vertical divergence of momentum and turbulent energy. Whether the lobe exists in a regular configuration (i.e. sinuous crestline) or an irregular configuration seems to be relevant. Irregular lobes seem to affect the flow in the same fashion as saddle shaped dune crestlines where the separation cell is only weakly defined and the wake does not appear to be a significant component of the flow field. This causes lateral and vertical convergence of momentum and turbulent energy towards a small area in the lee of saddle shaped dunes.

Spatially averaged Reynolds shear stress profiles appear to be the most accurate way to estimate the total boundary shear. Skin friction can be estimated from shear stress measurements over the flat bed allowing calculation of the form drag. Compared to flow over a 2D dune, lobe shaped crestlines enhance total drag by increasing form drag and saddle shaped crestlines reduce total drag by decreasing form drag. Total shear stress over saddle shaped crestlines is nearly equivalent to the skin friction suggesting that, when there is no significant separation cell and wake, the form drag is rather insignificant.

Irregular crestline morphologies passively reduce drag more effectively than regular configurations. A regularly sinuous crested bedform reduced drag by ~30%. In contrast, an irregular crest morphology reduced drag by ~52 %. The ideas of *Sirovich and Karlsen* [1997] concerning drag reduction over aligned and randomly oriented surface roughness elements are relevant for dunes.

These results have important implications for the stability of a sand bed. Most of the bedforms observed during the active sediment transport experiments were 3D and similar in shape to the irregular bed configuration. If these bedform fields were composed of 2D bedforms, it is likely that total drag would have been greater. It is well known that sediment transport rates are strongly dependent on the applied shear stress. When the bed transforms from a 2D configuration to a 3D irregular configuration, drag is reduced. It is likely that transport rates would respond by either decreasing or at least stabilising. Thus drag reduction and the 2-3D transition are mechanisms that contributes to the stability of the bed by reducing the susceptibility to erosion.

References

Abbott, J.E., and R.D. Francis, Saltation and suspension trajectories of solid grains in a water stream, *Proceedings of the Royal Society of London, Series A*, *284*, 225-254, 1977.

Allen, J.R.L., *Current Ripples*, North Holland Publishing Company, Amsterdam, 1968.

Allen, J.R.L., *Sedimentary Structures: Their Character and Physical Basis,* Elsevier, Amsterdam, 1982.

Allen, J.R.L., Some recent advances in the physics of sedimentation, *Proceedings of the Geologists' Association*, *80*, 1-42, 1969.

Allen, J.R.L., Features of cross-stratified units due to random and other changes in bed forms, *Sedimentology*, *20*, 189-202, 1973.

Allen, J.R.L., and J.D. Collinson, The superimposition and classification of dunes formed by unidirectional aqueous flows, *Sedimentary Geology*, *12*, 169-178, 1974.

Anderson, A.G., The characteristics of sediment waves formed in open channels, in *Proceedings of the Third Mid-Western Conference on Fluid Mechanics, University of Missouri, Missoula*, pp. 397-395, 1953.

Ashley, G.M., Classification of large-scale subaqueous bedforms: A new look at an old problem, *Journal of Sedimentary Petrology*, *60*, 160-172, 1990.

Baas, J.H., A flume study on the development and equilibrium morphology of current ripples in very fine sand, *Sedimentology*, *41*, 185-209, 1994.

Baas, J.H., An empirical model for the development and equilibrium morphology of current ripples in fine sand, *Sedimentology*, *46*, 123-138, 1999.

Baas, J.H., A.P. Oost, O.K. Sztano, P.L. de Boer, and G. Postma, Time as an independent variable for current ripples developing towards linguoid equilibrium morphology, *Terra Research*, *5*, 29-35, 1993.

Bagnold, R.A., The nature of saltation and of "bed-load" transport in water, *Proceedings of the Royal Society of London, Series A*, *332*, 473-504, 1973.

Beers, Y., *Introduction to the Theory of Error*, Addison-Wesley Publishing Company, Don Mills, Ontario, 1957.

Bennett, S.J., and J.L. Best, Mean flow and turbulence structure over fixed, two-dimensional dunes: implications for sediment transport and bedform stability, *Sedimentology*, *42*, 491-513, 1995.

Bennett, S.J., and J.L. Best, Mean flow and turbulence structure over fixed ripples and the ripple-dune transition, in *Coherent Flow Structures in Open Channels*, edited by S.J.B. P.J. Ashworth, J.L. Best, and S.J. McLelland, pp. 281-304, John Wiley and Sons Ltd., 1996.

Bennett, S.J., and J.S. Bridge, The geometry and dynamics of low-relief bed forms in heterogeneous material in a laboratory channel, and their relationship to water flow and sediment transport, *Journal of Sedimentary Research*, *A65*, 29-39, 1995.

Bennett, S.J., J.S. Bridge, and J.L. Best, Fluid and sediment dynamics of upper stage plane beds, *Journal of Geophysical Research*, *103*, 1239-1274, 1998.

Best, J., S. Bennett, J. Bridge, and M. Leeder, Turbulence modulation and particle velocities over flat sand beds at low transport rates, *Journal of Hydraulic Engineering*, *123*, 1118-1129, 1997.

Best, J.L., On the entrainment of sediment and initiation of bed defects: insights from recent developments within turbulent boundary layer research, *Sedimentology*, *39*, 797-811, 1992.

Best, J.L., and R.A. Kostaschuk, An experimental study of turbulent flow over a low-angle dune, *Journal of Geophysical Research*, *107*, 3135 (1-18), 2002.

Biron, P., A.G. Roy, and J.L. Best, A scheme for resampling, filtering, and subsampling unevenly spaced laser Doppler anemometer data, *Mathematical Geology*, *27*, 731-748, 1995.

Bogardi, J., Hydraulic similarity of river models with movable bed, *Acta Techn. Acad. Sci. Hung.*, *24*, 417-445, 1959.

Bradshaw, P., *An Introduction to Turbulence and its Measurement*, Pergamon Press, Toronto, 1971.

Bridge, J.S., *Rivers and Floodplains: Forms, Processes, and Sedimentary Record*, Blackwell Publishing, Malden, MA, 2003.

Bridge, J.S., and S.J. Bennett, A model for the entrainment and transport of sediment grains of mixed sizes, shapes and densities, *Water Resources Research*, *28*, 337-363, 1992.

Bridge, J.S., and D.F. Dominic, Bedload grain velocities and sediment transport rates, *Water Resources Research*, *20*, 476-790, 1984.

Bucher, W.H., On ripples and related sedimentary surface forms and their paleogeographic interpretation, *American Journal of Science*, *47*, 149-210 and 241-269, 1919.

Coleman, S.E., and B.W. Melville, Bed-form development, *Journal of Hydraulic Engineering*, *120*, 544-560, 1994.

Costello, W.R., and J.B. Southard, Flume experiments on lower-regime bedforms in coarse sands, *Journal of Sedimentary Petrology*, *51*, 849-864, 1981.

Dantec, *Fiber Flow, Installation and User's Guide*, Dantec Measurement Technology, Skovlunde, Denmark, 1995.

Ditchfield, R., and J.L. Best, Development of bed features: Discussion, *Journal of Hydraulic Engineering*, *116*, 647-650, 1990.

Einstein, H.A., *The Bedload Function for Sediment Transportation in Open Channel Flows*, United States Department of Agriculture, Washington D.C., 1950.

Einstein, H.A., and N. Barbarossa, River channel roughness, *Transactions of the American Society of Civil Engineers*, *117*, 1121-1146, 1952.

Emmett, W.W., A field calibration of the sediment-trapping characteristics of the Helley-Smith bed load sampler, *USGS Professional Paper*, *1139*, 1-44, 1980.

Engel, P., Length of flow separation over dunes, *Journal of the Hydraulic Division of American Society of Civil Engineers*, *107*, 1133-1143, 1981.

Engelund, F., Instability in erodible channels, *Journal of Fluid Mechanics*, *42*, 225-244, 1970.

Flemming, B.W., Zur klassifikation subaquatistischer, stromungstrans versaler transportkorper, *Boch. Geol. U. Geotechn. Arb.*, *29*, 44-47, 1988.

Fredsoe, J., On the development of dunes in erodible channels, *Journal of Fluid Mechanics*, *64*, 1-16, 1974.

Gilbert, G.K., The transport of debris by running water, *USGS Professional Paper*, *86*, 1-263, 1914.

Grass, A.J., Initial instability of fine sand, *Journal of the Hydraulic Division of American Society of Civil Engineers*, *96*, 619-632, 1970.

Guy, H.P., D.B. Simons, and E.V. Richardson, Summary of alluvial channel data from flume experiments, 1956-1961, *USGS Professional Paper*, *462-I*, 1-96, 1966.

Gyr, A., and A. Schmid, The different ripple formation mechanism, *Journal of Hydraulic Research*, *27*, 61-74, 1989.

Halliday, D., R. Resnick, and J. Walker, *Fundamentals of Physics*, Wiley, Toronto, 1993.

Hesp, P.A., and R. Hyde, Flow dynamics and geomorphology of a trough blowout, *Sedimentology*, *43*, 505-525, 1996.

Jackson, R.G., Large scale ripples of the lower Wabash River, *Sedimentology*, *23*, 593-623, 1976.

Jackson, R.G., Sedimentological and fluid-dynamic implications of the turbulent bursting phenomenon in geophysical flows, *Journal of Fluid Mechanics*, *77*, 531-560, 1976b.

Kennedy, J.F., The mechanics of dunes and anti-dunes in erodible channels, *Journal of Fluid Mechanics*, *16*, 521-544, 1963.

Kim, H.T., S.J.W. Kline, and W.C. Reynolds, The production of turbulence near a smooth wall in a turbulent boundary layer, *Journal of Fluid Mechanics*, 133-160, 1971.

Kline, S.J.W., W.C. Reynolds, F.A. Schraub, and P.W. Rundstadler, The structure of turbulent boundary layers, *Journal of Fluid Mechanics*, *30*, 741-773, 1967.

Kostaschuk, R.A., and M.A. Church, Macroturbulence generated by dunes: Fraser River, Canada, *Sedimentary Geology*, *85*, 25-37, 1993.

Kostaschuk, R.A., and P. Villard, Flow and sediment transport over large subaqueous dunes: Fraser River, Canada, *Sedimentology*, *43*, 849-863, 1996.

Lamb, H., *Hydrodynamics*, Dover Publications, New York, 1932.

Lane, S.N., P.M. Biron, K.F. Bradbrook, J.B. Butler, J.H. Chandler, M.D. Crowell, S.J. McLelland, K.S. Richards, and A.G. Roy, Three-dimensional measurement of river channel flow processes using acoustic doppler velocimetry, *Earth Surface Processes and Landforms*, *23*, 1247-1267, 1998.

Lapointe, M., Burst-like sediment suspension events in a sand bed river, *Earth Surface Processes and Landforms*, *17*, 253-270, 1992.

Lapointe, M.F., Frequency spectra and intermittency of the turbulent suspension process in a sand-bed river, *Sedimentology*, *43*, 439-449, 1996.

Lawrence, G.A., F.K. Browand, and L.G. Redekopp, Stability of a sheared density interface, *Physics of Fluids*, *A3*, 2360-2370, 1991.

Leeder, M.R., On the stability of lower stage plane beds and the absence of ripples in coarse sand, *Journal of the Geological Society of London*, *137*, 423-429, 1980.

Leliavsky, S., *An Introduction to Fluvial Hydraulics*, Constable and Co. Ltd, London, 1955.

Liu, H.-K., Mechanics of sediment-ripple formation, *Journal of the Hydraulic Division of American Society of Civil Engineers*, *83* (HY2), 1-23, 1957.

Livesey, J.R., S. Bennett, P.J. Ashworth, and J.L. Best, Flow structure, sediment transport and bedform dynamics for a bimodal sediment mixture, in *Gravel-Bed Rivers in the Environment*, edited by P.C. Klingman, R.L. Beschta, P.D. Komar, and J.B. Bradley, pp. 149-176, Water Resources Publications, LLC, Highlands Ranch, Colorado, 1998.

Lohrmann, A., R. Cabrera, and N.C. Kraus, Acoustic-Doppler Velocimeter (ADV) for laboratory use, in *Proceedings of Fundamentals and Advancements in Hydraulic Measurements and Experimentation*, American Society of Civil Engineers, Buffalo, NY, 1994.

Lyn, D.A., Turbulence measurements in open-channel flow over bedforms, *Journal of Hydraulic Engineering*, *119*, 306-326, 1993.

Martin, V., *Hydraulic Roughness of Armoured Gravel Beds: The role of Grain Protrusion*, Ph.D. thesis, University of British Columbia, Vancouver, 2003.

Matthes, G.H., Macroturbulence in natural stream flow, *Transactions of the American Geophysyical Union*, *28*, 255-262, 1947.

McLean, S.R., The stability of ripples and dunes, *Earth Science Reviews*,, *29*, 131-144, 1990.

McLean, S.R., J.M. Nelson, and R.L.Shreve, Flow-sediment interactions in separating flows over bedforms, in *Coherent Flow Structures in Open Channels*, edited by P.J. Ashworth, S.J. Bennett, J.L. Best, and S.J. McLelland, pp. 203-226, John Wiley and Sons Ltd., 1996.

McLean, S.R., J.M. Nelson, and S.R. Wolfe, Turbulence structure over two-dimensional bedforms: Implications for sediment transport, *Journal of Geophysical Research*, *99*, 12729-12747, 1994.

McLean, S.R., S.R. Wolfe, and J.M. Nelson, Spatially averaged flow over a wavy boundary revisited, *Journal of Geophysical Research*, *104*, 15743-15753, 1999.

Menard, H.W., Sediment movement in relation to current velocity, *Journal of Sedimentary Petrology*, *20*, 148-160, 1950.

Miller, M.C., I.N. McCave, and P.D. Komar, Threshold of sediment motion under unidirectional currents, *Sedimentology*, 24, 507-527, 1977.

Müller, A., and A. Gyr, On the vortex formation in the mixing layer behind dunes, *Journal of Hydraulic Research*, *24*, 359-375, 1986.

Nelson, J.M., S.R. McLean, and S.R. Wolfe, Mean flow and Turbulence over two-dimensional bedforms, *Water Resources Research*, *29*, 3935-3953, 1993.

Nelson, J.M., and J.D. Smith, Mechanics of flow over ripples and dunes, *Journal of Geophysical Research*, *94*, 8146-8162, 1986.

Nelson, J.M., R.L. Shreve, S.R. McLean, and T.G. Drake, Role of near-bed turbulence structure in bed load transport and bed form mechanics, *Water Resources Research*, *31*, 2071-2086, 1995.

Nezu, I., and H. Nakagawa, *Turbulence in Open-Channel Flows*, A.A. Balkema, Rotterdam, 1993.

Nezu, I., and W. Rodi, Open-channel flow measurements with a laser Doppler anemometer, *Journal of Hydraulic Engineering*, *112*, 335-355, 1986.

Parratt, L.G., *Probability and Experimental Errors in Science*, John Wiley and Sons, New York, 1961.

Paulos, Y.K., *Intense bedload transport in non-uniform flow*, Ph.D. thesis, University of British Columbia, Vancouver, British Columbia, 1998.

Prandtl, L., *Fluid Dynamics*, Hafner Publishing Company, New York, 1952.

Pretious, E.S., and T. Blench, *Final Report of Special Observations of Bed Movement in Lower Fraser River at Ladner Reach During 1950 Freshet*, National Resource Council of Canada, Fraser River Model, Vancouver, 1951.

Raudkivi, A.J., Study of sediment ripple formation, *ASCE, Journal of the Hydraulics Division*, *89*, 15-33, 1963.

Raudkivi, A.J., Bedforms in alluvial channels, *Journal of Fluid Mechanics*, *26*, 507-514, 1966.

Raudkivi, A.J., Ripples on a streambed, *Journal of Hydraulic Engineering*, *123*, 58-64, 1999.

Raudkivi, A.J., and H.-H. Witte, Development of bed features, *Journal of Hydraulic Engineering*, *116*, 1063-1079, 1990.

Roberson, J.A., and C.T. Crowe, *Engineering Fluid Mechanics*, John Wiley and Sons, Toronto, 1993.

Rouse, H., *Elementary Fluid Mechanics*, 376 pp., John Wiley and Sons, New York, 1946.

Saunderson, H.C., and F.P.J. Lockett, Flume experiments on bedforms and structures at the dune-plane bed transition, *Modern and Ancient Fluvial Systems, Special Publication #6 of the International Association of Sedimentologists*, *6*, 48-58, 1983.

Shields, A., *Anwendung der Ahnlichkeitmechanik and turbulenzforschung auf die geschiebebewegung*, Preussischen Versuchanstalt für Wasserbau und Schiffbau, No.26. Berlin, 1936 (English translation by W.P. Ott and J.C. Uchelen, California Institute of Technology, Pasadena, California).

Simons, D.B., and E.V. Richardson, Forms of bed roughness in alluvial channels, *Transactions of the American Society of Civil Engineers*, *128*, 284-302, 1961.

Simons, D.B., and E.V. Richardson, Resistance to flow in alluvial channels, *USGS Professional Paper*, *422-J*, 1-61, 1966.

Simons, D.B., E.V. Richardson, and M.L. Albertson, Flume studies using medium sand (0.45 mm), *USGS Professional Paper*, *1498-A*, 1-76, 1961.

Simons, D.B., E.V. Richardson, and C.F. Nordin, Bedload equation for ripples and dunes, *USGS Professional Paper*, *462-H*, 1-9, 1965.

Sirovich, L., and S. Karlsson, Turbulent drag reduction by passive mechanisms, *Nature*, *388*, 753-755, 1997.

Smith, J.D., Stability of a sand bed subjected to a shear flow of low Froude Number, *Journal of Geophysical Research*, *75*, 5928-5940, 1970.

Smith, J.D., and S.R. McLean, Spatially averaged flow over a wavy surface, *Journal of Geophysical Research*, *82*, 1735-1746, 1977.

Sontek, *ADV Operation Manual, Software Version 4.0*, Sontek, San Diego, 1997.

Southard, J.B., *Interpreting Primary Physical Bedding Structures: A Short Course given at the University of Southern California*, University of Southern California, Los Angeles, 1992.

Southard, J.B., and L.A. Boguchwal, Bed configurations in steady unidirectional water flow part 2. Synthesis of flume data, *Journal of Sedimentary Petrology*, *60*, 658-679, 1990.

Southard, J.B., and J.R. Dingler, Flume study of ripple propagation behind mounds on flat sand beds, *Sedimentology*, *16*, 251-263, 1971.

Sterling, S.M., and M. Church, Sediment trapping characteristics of a pit trap and the Helley-Smith sampler in a gravel bed river, *Water Resources Research*, *38*, 1029(1-11), 2002.

Stringham, D.B., D.B. Simons, and H.P. Guy, The behaviour of large particles in quiescent liquids, *USGS Professional Paper*, *562-C*, 1-36, 1969.

Sukhodolov, A., M. Thiele, and H. Bungartz, Turbulence structure in a river reach with sand bed, *Water Resources Research*, *34*, 1317-1334, 1998.

Taylor, G.I., Statistical theory of turbulence: Parts 1-4, *Proceedings of the Royal Society of London, Series A*, *151*, 421-511, 1935.

ten Brinke, W.B.M., A.W.E. Wilbers, and C. Wesseling, Dune growth, decay and migration rates during a large-magnitude flood at a sand and mixed-gravel bed in the Dutch Rhine river system, in *Fluvial Sedimentology VI*, edited by N.D. Smith, and J. Rogers, pp. 15-32, International Association of Sedimentologists, 1999.

Tennekes, H., and J.L. Lumley, *A First Course in Turbulence*, MIT Press, Cambridge, Massachusetts, 1972.

van den Berg, J.H., Bedform migration and bedload transport in some rivers and tidal environments, *Sedimentology*, *34*, 681-698, 1987.

van Rijn, *Principles of Sediment Transport in Rivers, Estuaries and Coastal Seas*, Aqua, Amsterdam, 1993.

van Rijn, L.C., Sediment transport II: Suspended load transport, *Journal of Hydraulic Engineering*, *110*, 1613-1641, 1984a.

van Rijn, L.C., Sediment transport III: Bed forms and alluvial roughness, *Journal of Hydraulic Engineering*, *110*, 1733-1754, 1984b.

Venditti, J.G., and B.O. Bauer, Turbulent flow over a dune: Green River, Colorado, *Earth Surface Processes and Landforms*, in review.

Venditti, J.G., and S.J. Bennett, Spectral analysis of turbulent flow and suspended sediment transport over fixed dunes, *Journal of Geophysical Research*, *105*, 22035-22047, 2000.

Villard, P.V., and M. Church, Dunes and associated sand transport in a tidally influenced sand-bed channel: Fraser River, British Columbia, *Canadian Journal of Earth Sciences*, *40*, 115-130, 2003.

Voulgaris, G., and J.H. Trowbridge, Evaluation of the acoustic Doppler velocimter (ADV) for tutrbulence measurements, *Journal of Atmospheric and Oceanic Technology*, *15*, 272-289, 1998.

Whiting, P.J., W.E. Dietrich, L.B. Leopold, T.G. Drake, and R.L. Shreve, Bedload sheets in heterogeneous sediment, *Geology*, *16*, 105-108, 1988.

Wiberg, P.L., and J.M. Nelson, Unidirectional flow over a assymetric and symmetric ripples, *Journal of Geophysical Research*, *97*, 12745-12761, 1992.

Wiberg, P.L., and J.D. Smith, A theoretical model for saltating grains in water, *Journal of Geophysical Research*, *90*, 7341-7354, 1985.

Wilcock, P.R., Experimental investigation of the effect mixture properties on transport dynamics, in *Dynamics of Gravel-Bed Rivers*, edited by P. Billi, R.D. Hey, C.R. Thorne, and P. Tacconi, pp. 109-131, Wiley, Chichester, 1992.

Williams, G.P., Flume width and water depth effects in sediment transport experiments, *USGS Professional Paper*, *37*, 562-H, 1970.

Williams, P.B., and P.H. Kemp, Initiation of ripples on flat sediment beds, *Journal of the Hydraulic Division of American Society of Civil Engineers*, *97*, 505-522, 1971.

Willis, J.C., and J.F. Kennedy, *Sediment Discharge of Alluvial Streams Calculated from Bed-Form Statistics*, 200 pp., Iowa Institute of Hydraulic Research, University of Iowa, Iowa City, Iowa, 1977.

Yalin, M.S., *River Mechanics*, Pergamon Press, New York, 1992.

Appendix A

Time series of dune crest and trough heights that reveal pulses in sediment observable when multiple consecutive crests or troughs are higher than neighbouring crests.

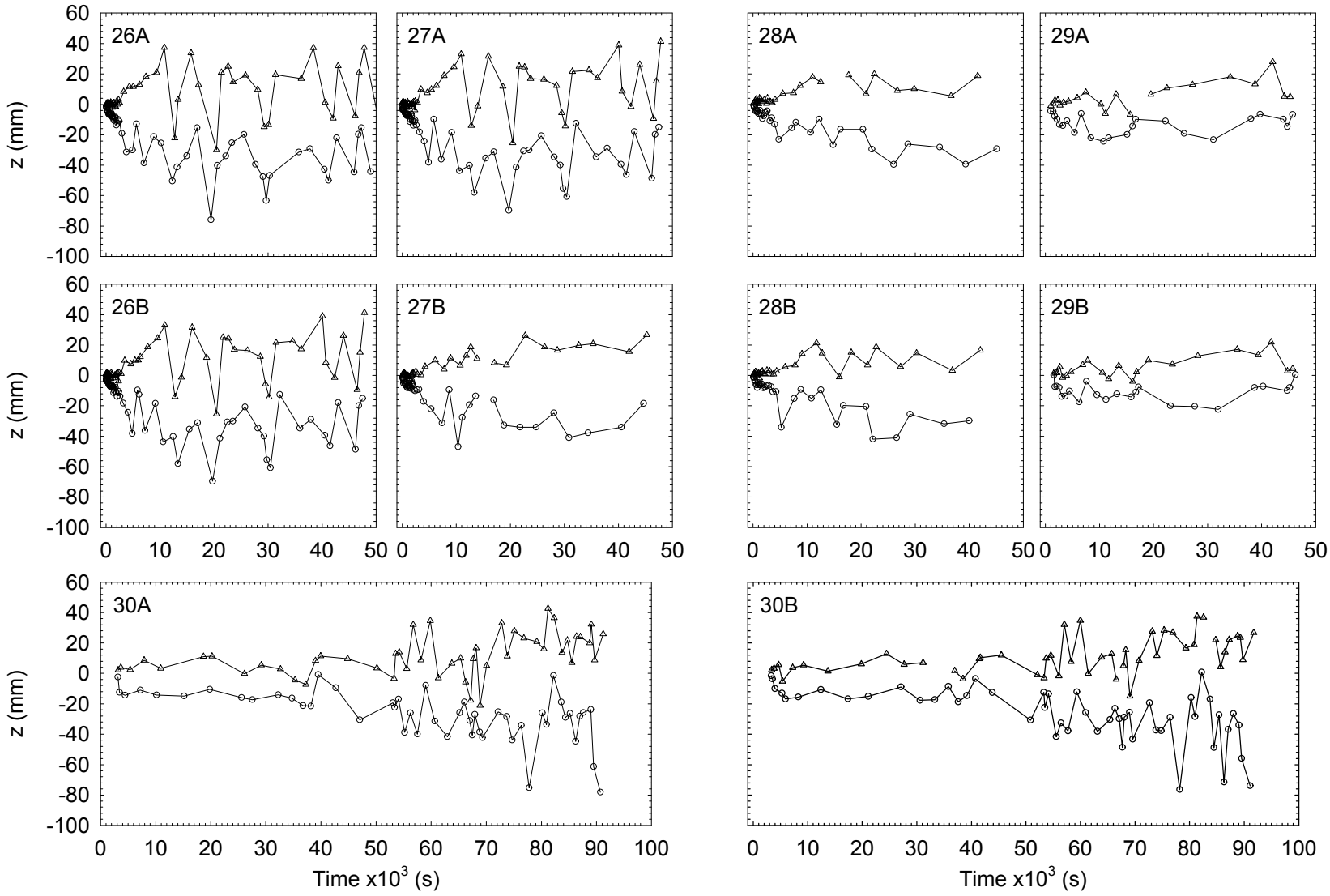

Figure A1: Time series of dune crest and trough heights that reveal pulses in sediment observable when multiple consecutive crests (triangles) or troughs (circles) are higher than neighbouring crests. Numbers in top left corner indicates run number (26 - 30) and the echo-sounder (A or B) (see Figure 2.3). *z* is height above the flat bed.

Appendix B (on attached CD)

Time-lapsed image sequence animations of bedform development and the transition between 2D and 3D bedforms. Animations are in Graphic Interchange Format (GIF) and can be viewed by opening the file in most non-Microsoft image viewers (e.g. ACDSee) or web browsers (e.g. Netscape).

Video clips:

1) Flow A - Instantaneous Bedform Development (Run 53).

2) Flow B - Instantaneous Bedform Development (Run 54).

3) Flow C - Instantaneous Bedform Development (Run 57).

4) Flow D - Bedform Development from a Negative Defect (Run 55).

5) Flow D - Bedform Development from a Positive Defect (Run 56).

6) Flow E - Bedform Development from a Negative Defect (Run 59).

7) Flow E - Bedform Development from a Positive Defect (Run 58).

8) Flow A - 2D-3D Bedform Transition (Run 53).

9) Flow B - 2D-3D Bedform Transition (Run 54).

10) Flow C - 2D-3D Bedform Transition (Run 57).

CD Envelope

Appendix C

Miscellaneous data extracted from the video image sequences in Arcview.

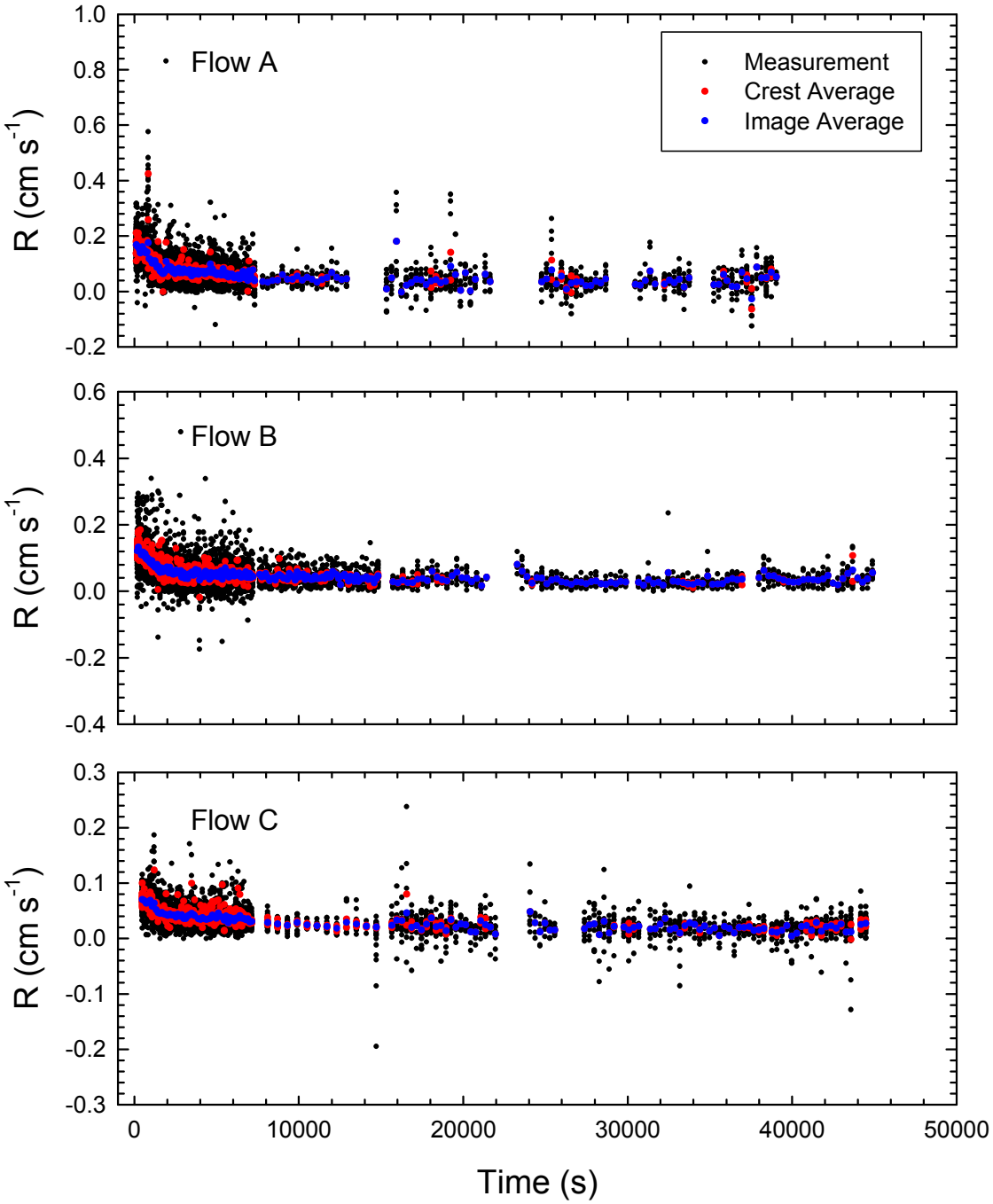

Figure C1: Migration rates, *R*, calculated as the distance the bedform crestline migrated between two video images. See section 4.2.3 for definitions of the time interval between analysed images. This distance was measured at 10 cm intervals across the flume using the crestlines digitised in Arcview. Black points are all observations, red points are crest averages and blue points are image averages.

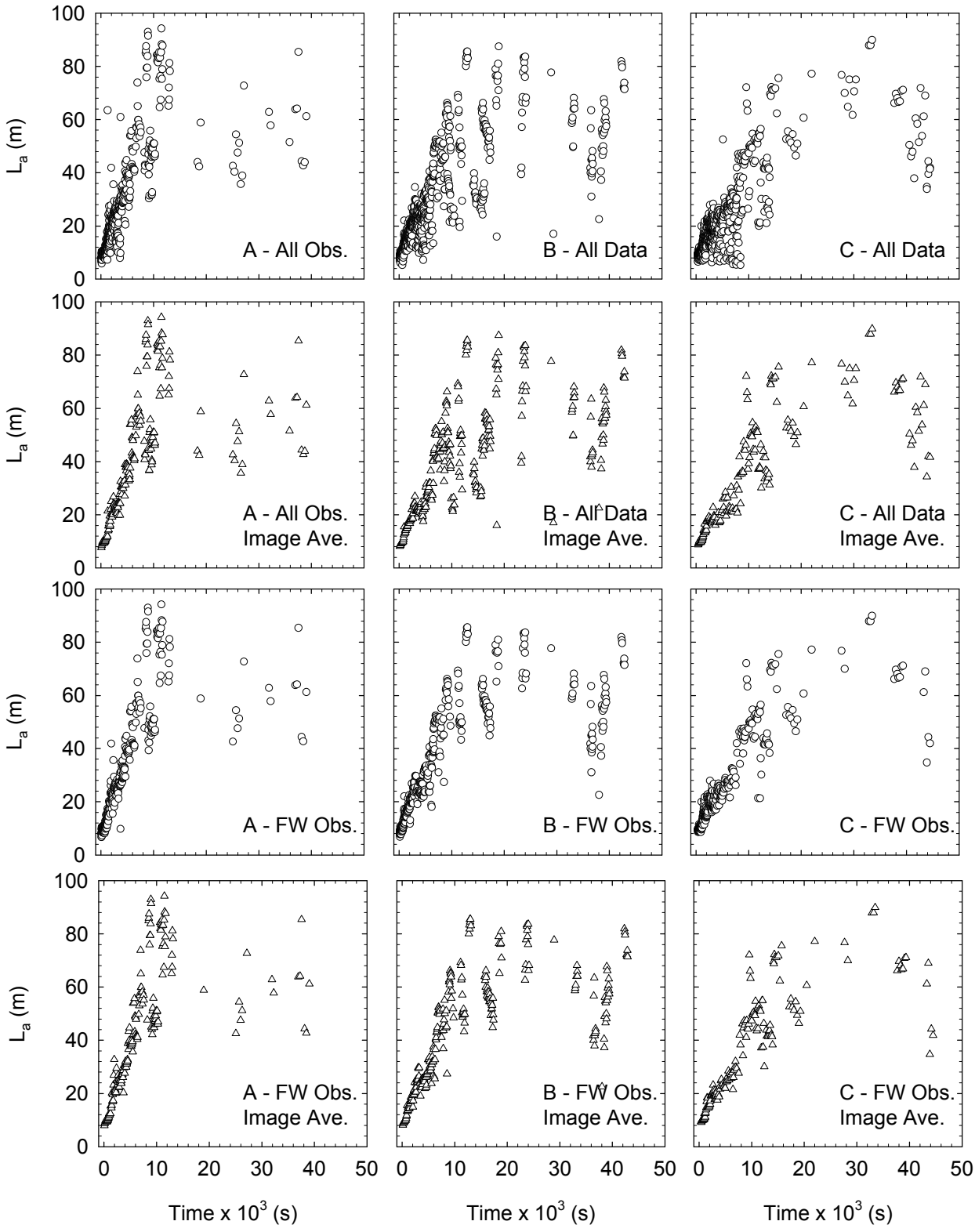

Figure C2: Areally averaged bedform lengths, L_a.

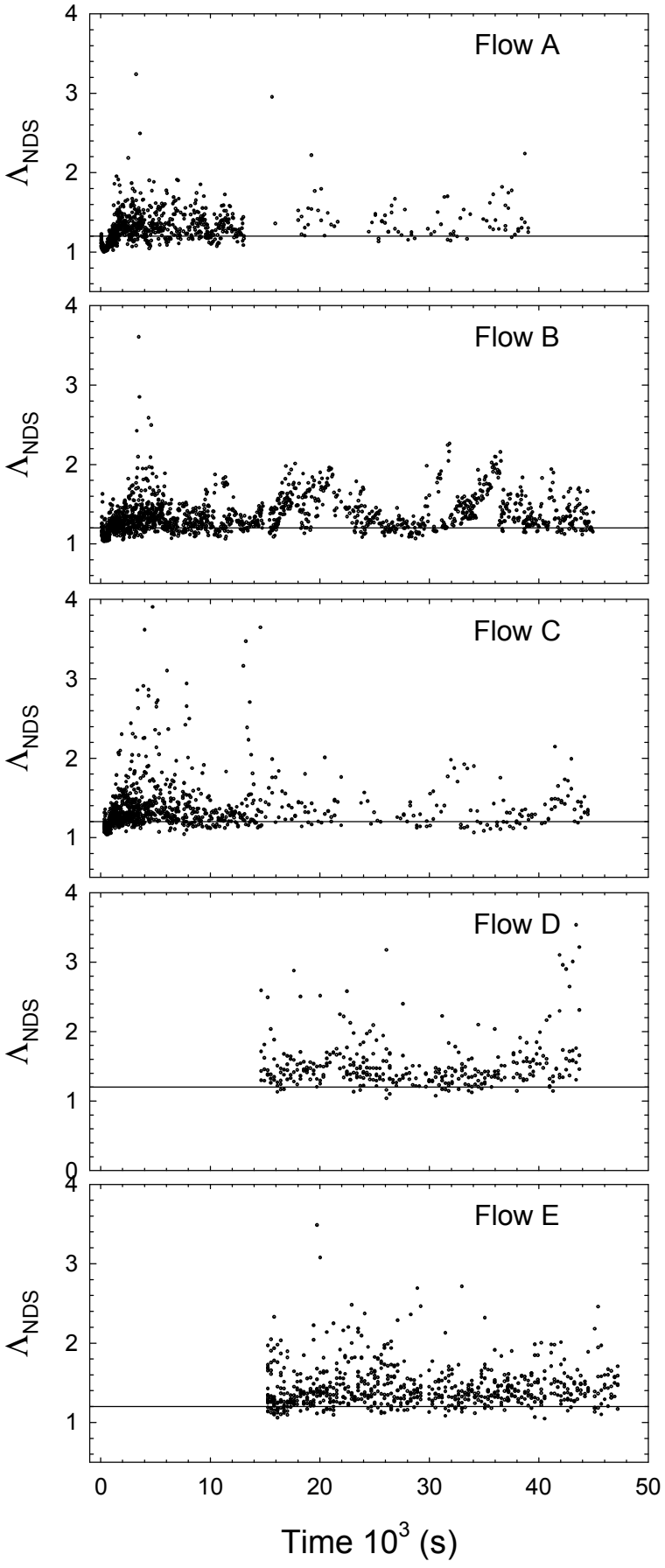

Figure C3: All observations of non-dimensional span, Λ_{NDS}.

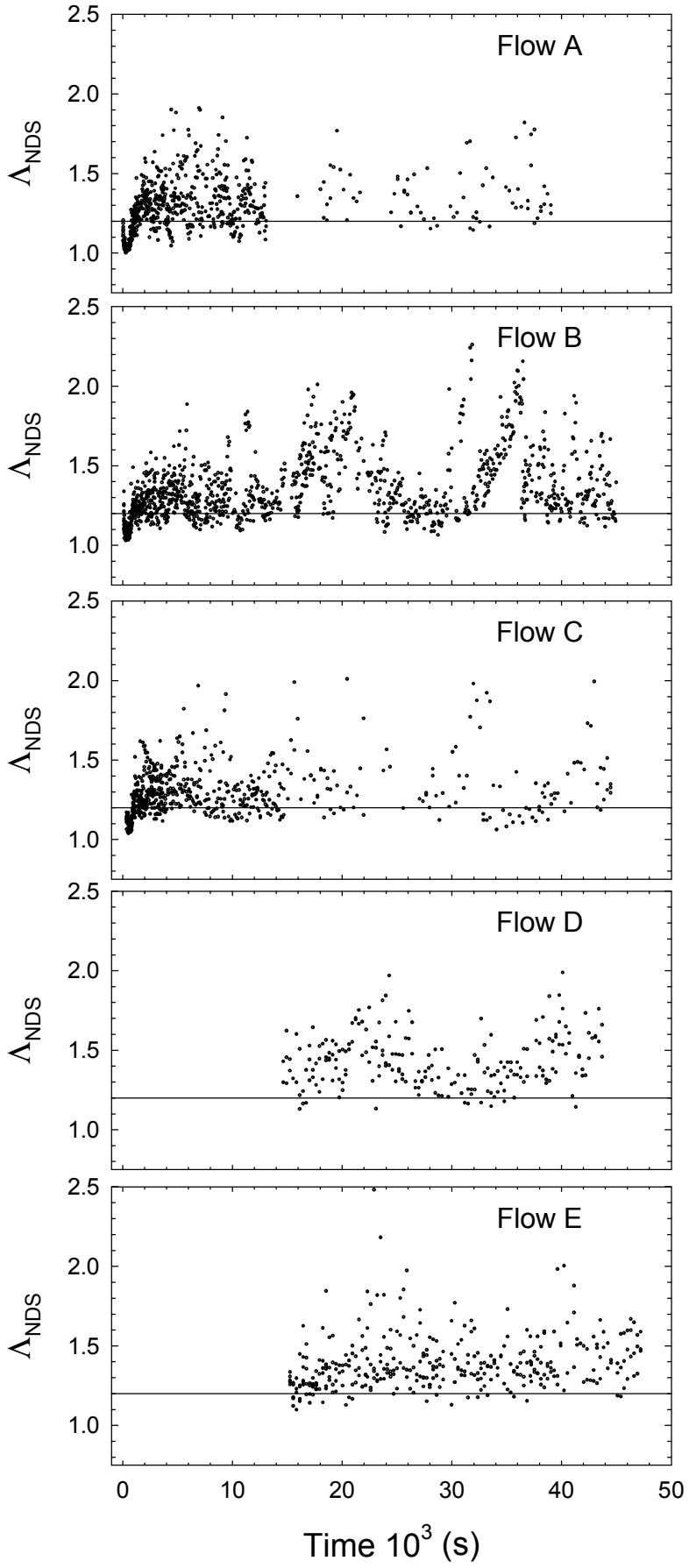

Figure C4: All observations of non-dimensional span, Λ_{NDS} where the cross-stream extent of the crestline exceeded 70 cm.

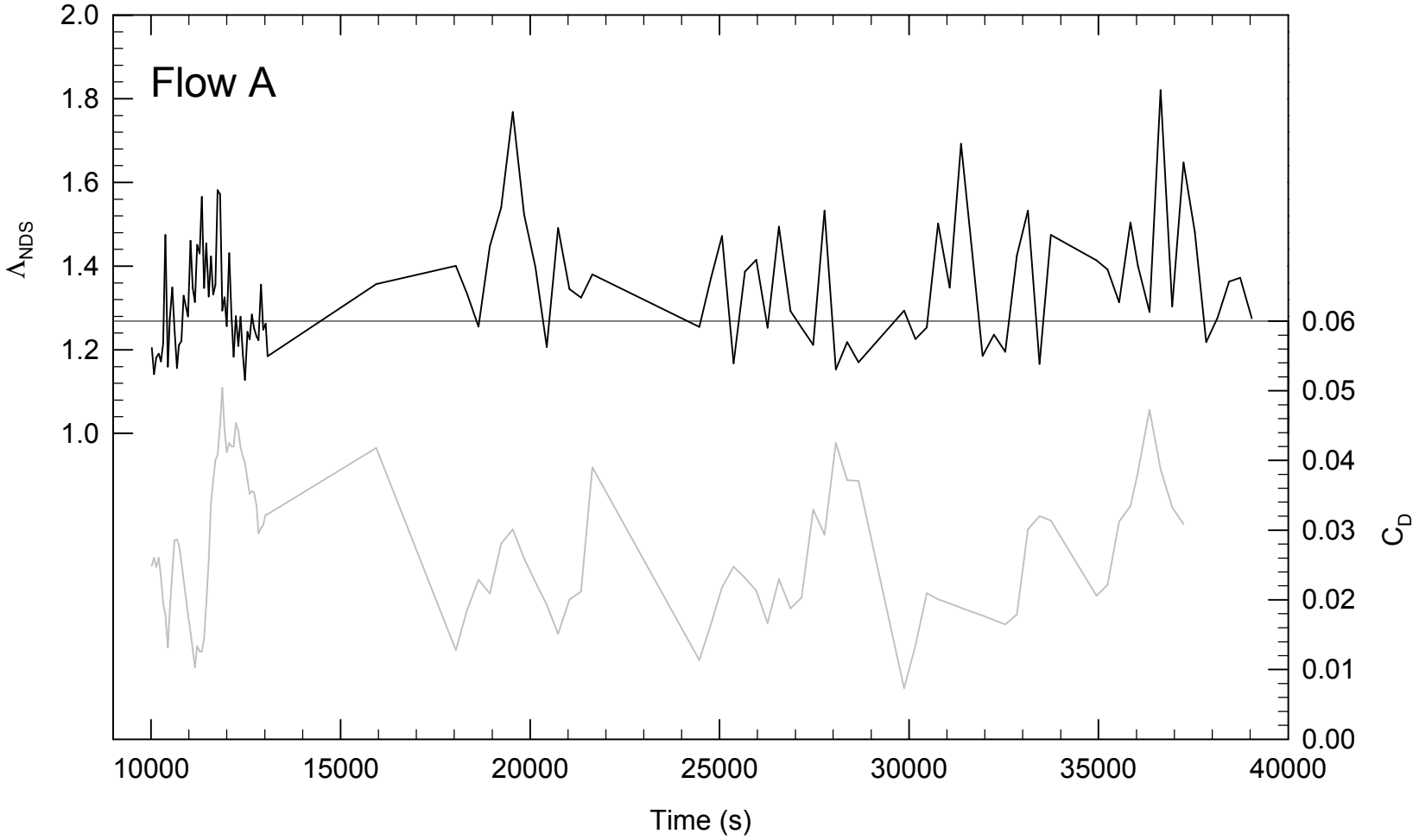

Figure C5: Non-dimensional span, Λ_{NDS}, and drag coefficients that represent the total drag, C_D, plotted as a function of time for Flow A.

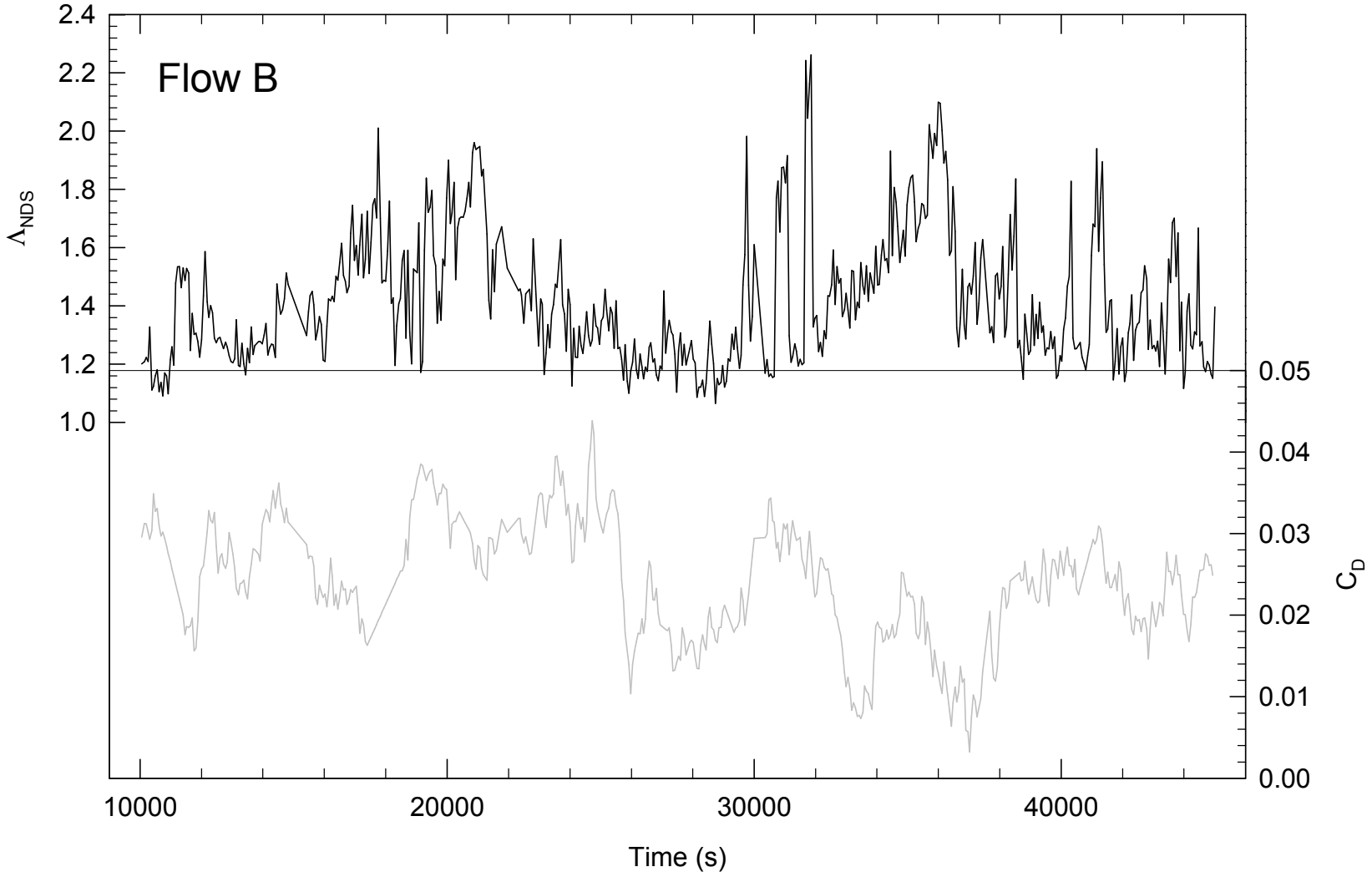

Figure C6: Non-dimensional span, Λ_{NDS}, and drag coefficients that represent the total drag, C_D, plotted as a function of time for Flow B.

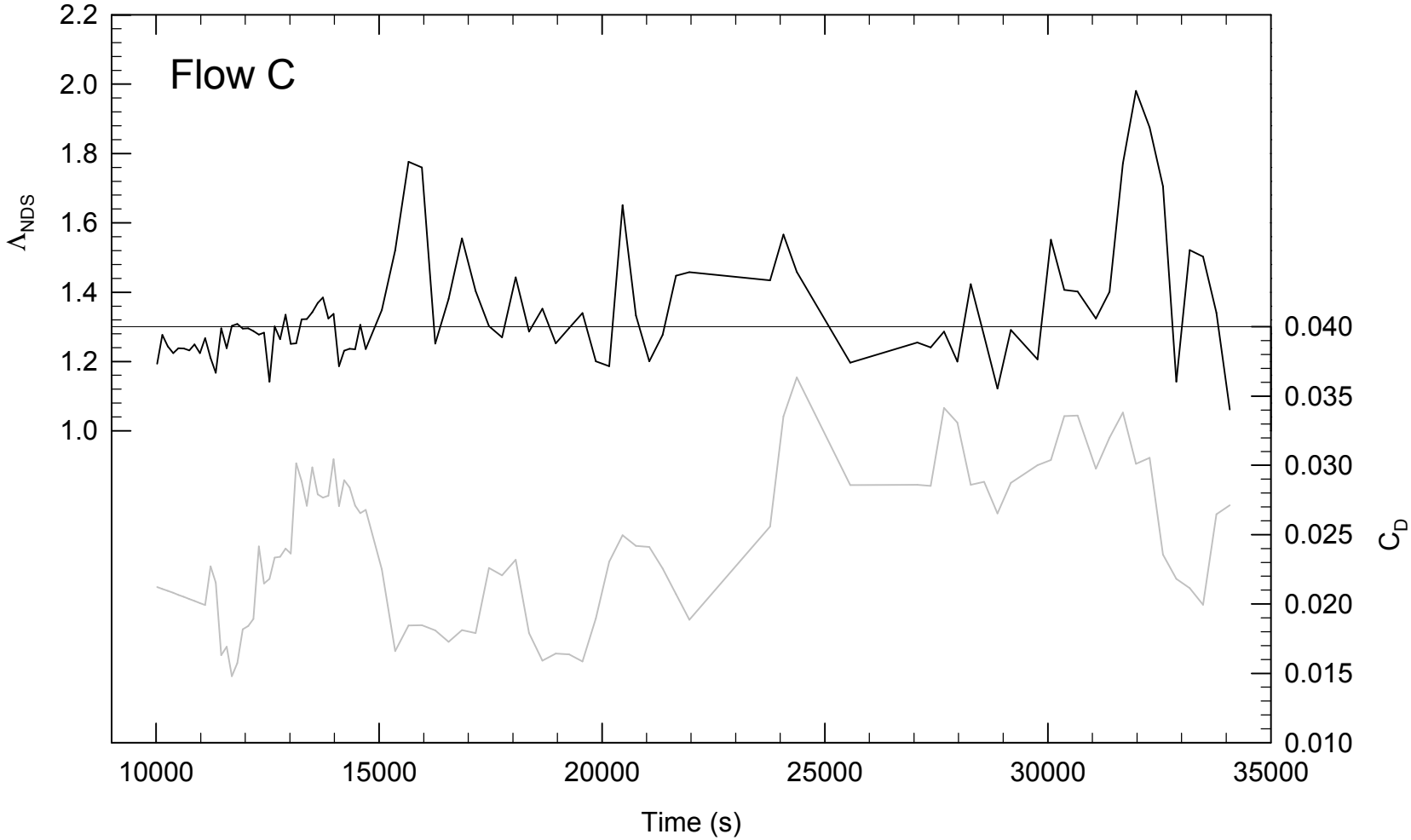

Figure C7: Non-dimensional span, Λ_{NDS}, and drag coefficients that represent the total drag, C_D, plotted as a function of time for Flow C.

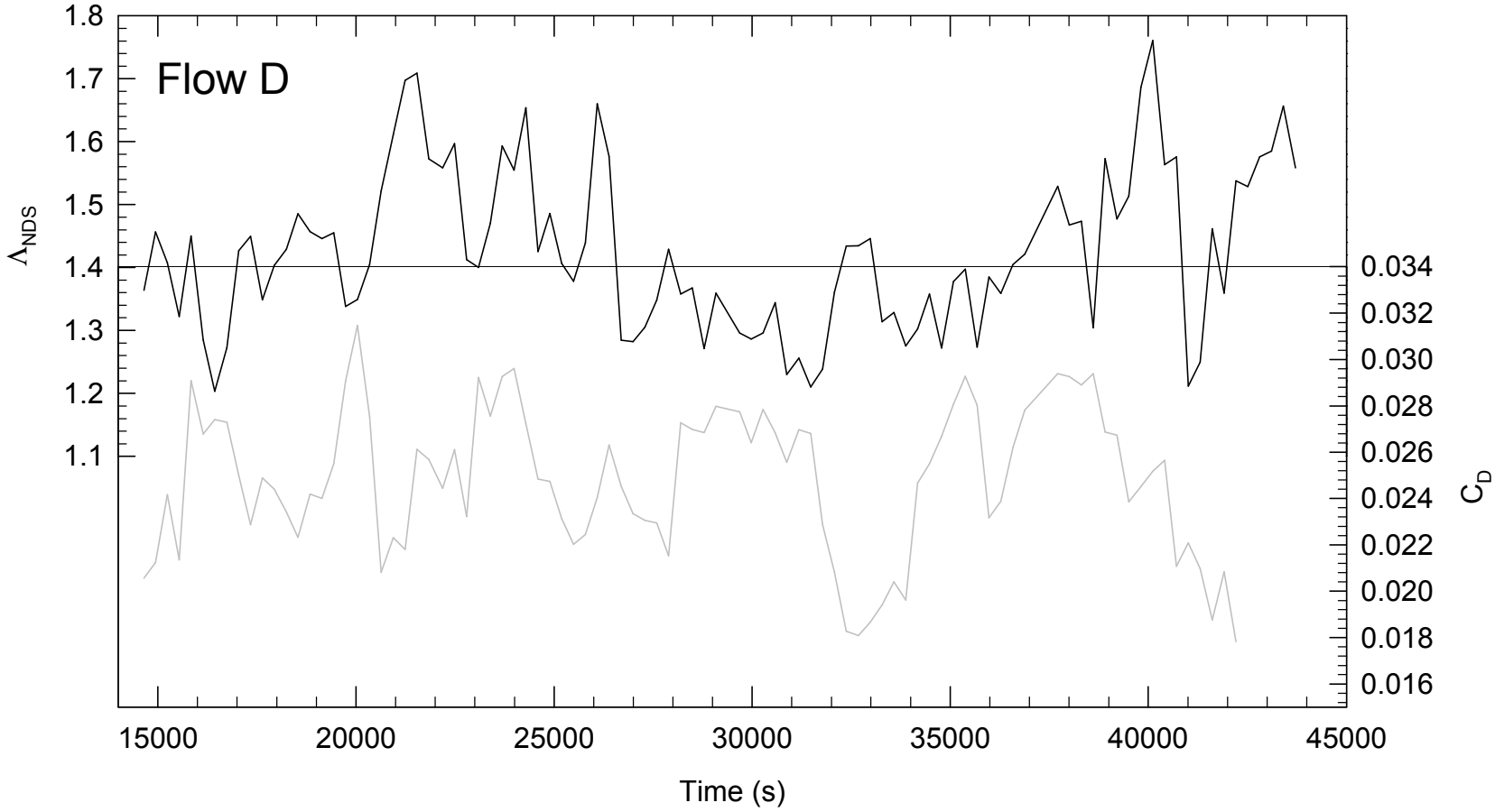

Figure C8: Non-dimensional span, Λ_{NDS}, and drag coefficients that represent the total drag, C_D, plotted as a function of time for Flow D.

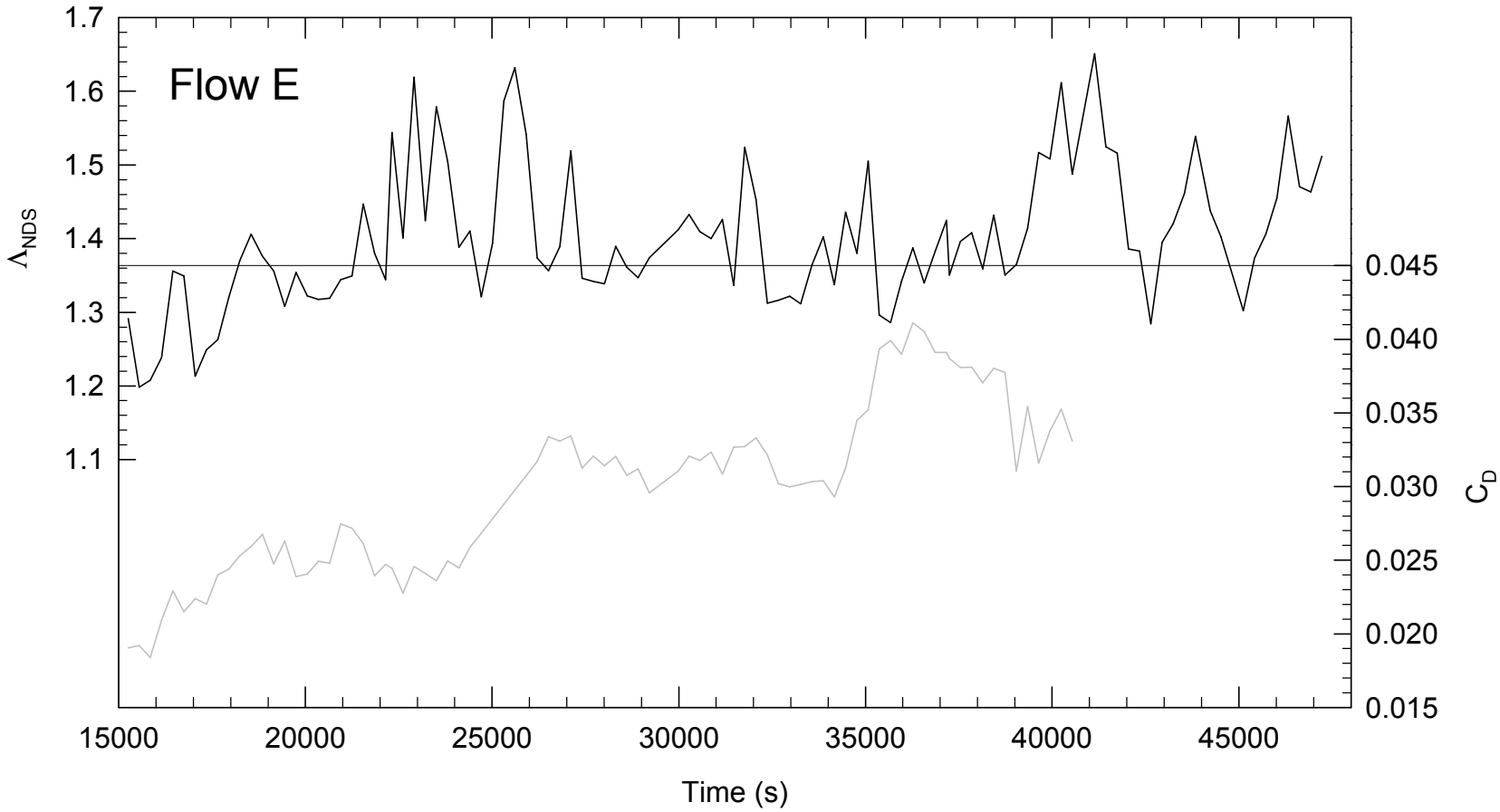

Figure C9: Non-dimensional span, Λ_{NDS}, and drag coefficients that represent the total drag, C_D, plotted as a function of time for Flow E.

Appendix D

Bed and water surface profiles over dunes and corresponding flow depths for each dune profile. Profile and at-a-point velocity measurement locations are also displayed in each figure. In the lower panel of each diagram, circles indicate where the probe was mounted in the 0^o position. Down oriented triangles indicate that the probe was in the 45^o position. Squares indicate that the probe was in the 90^o position. Up oriented triangles indicate that the probe was in the 0^o position but that the lower threshold for data retained after filtering was > 40% as opposed to the > 70% retention threshold used for the rest of the data.

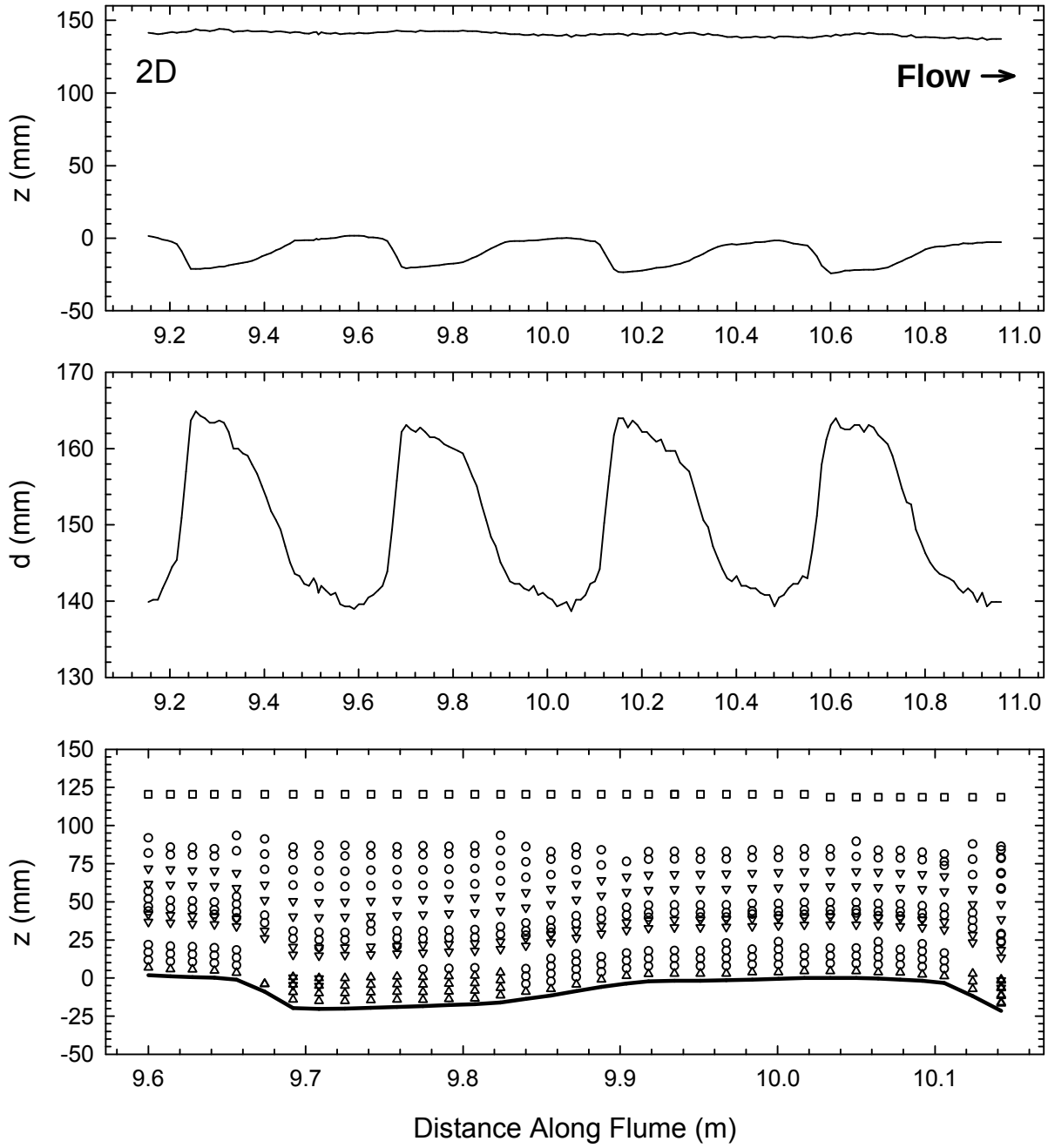

Figure D1: Bed and water surface, z, profiles over bedforms 5-9 (top) and corresponding flow depths, d, (middle) for the 2D dune configuration. Profiles were taken over the 8th downstream dune at the locations noted in the bottom panel.

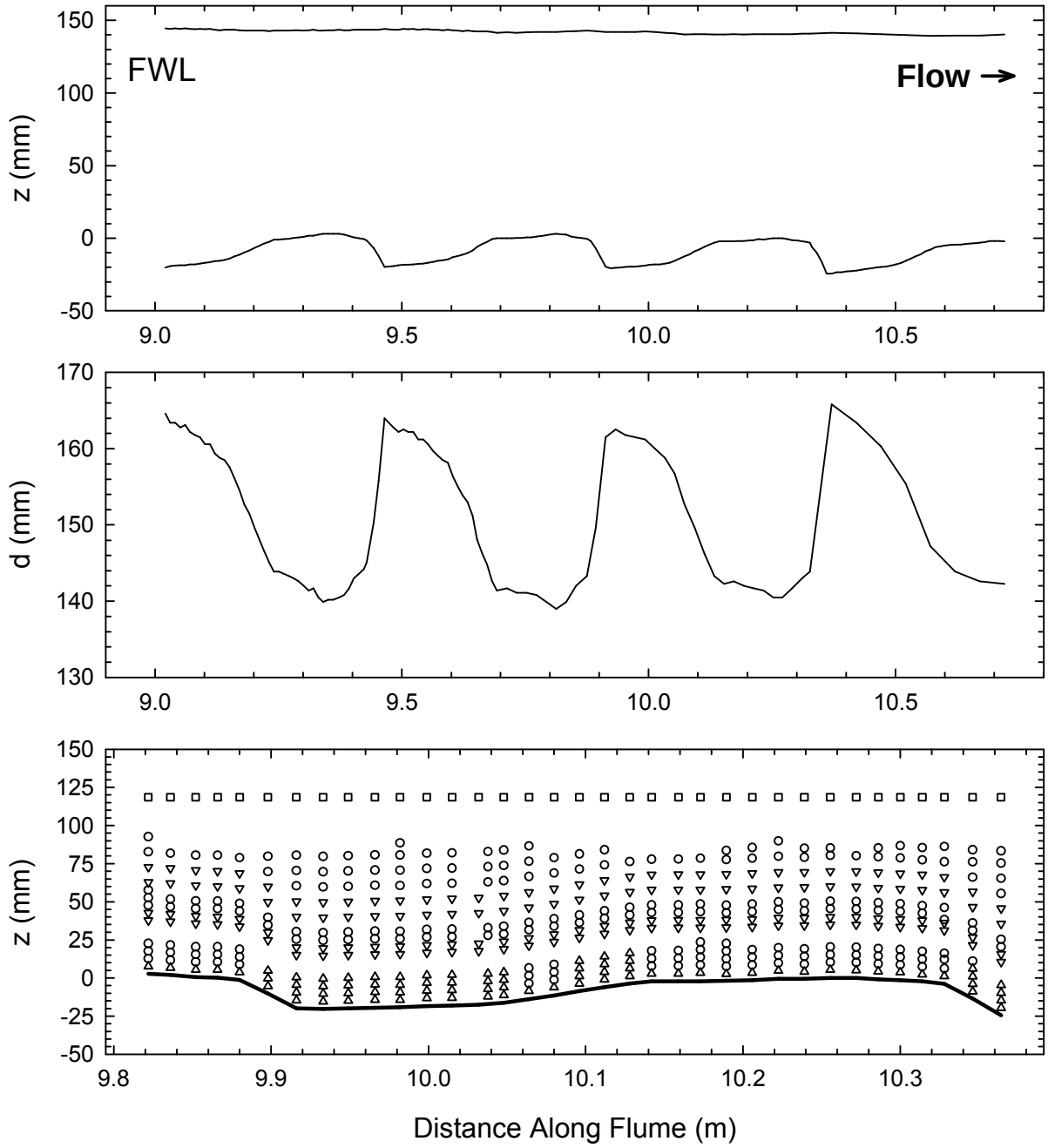

Figure D2: Bed and water surface, z, profiles over bedforms 6-9 (top) and corresponding flow depths, d, (middle) for the full-width lobe (FWL) dune configuration. Profiles were taken over the 8th downstream dune at the locations noted in the bottom panel.

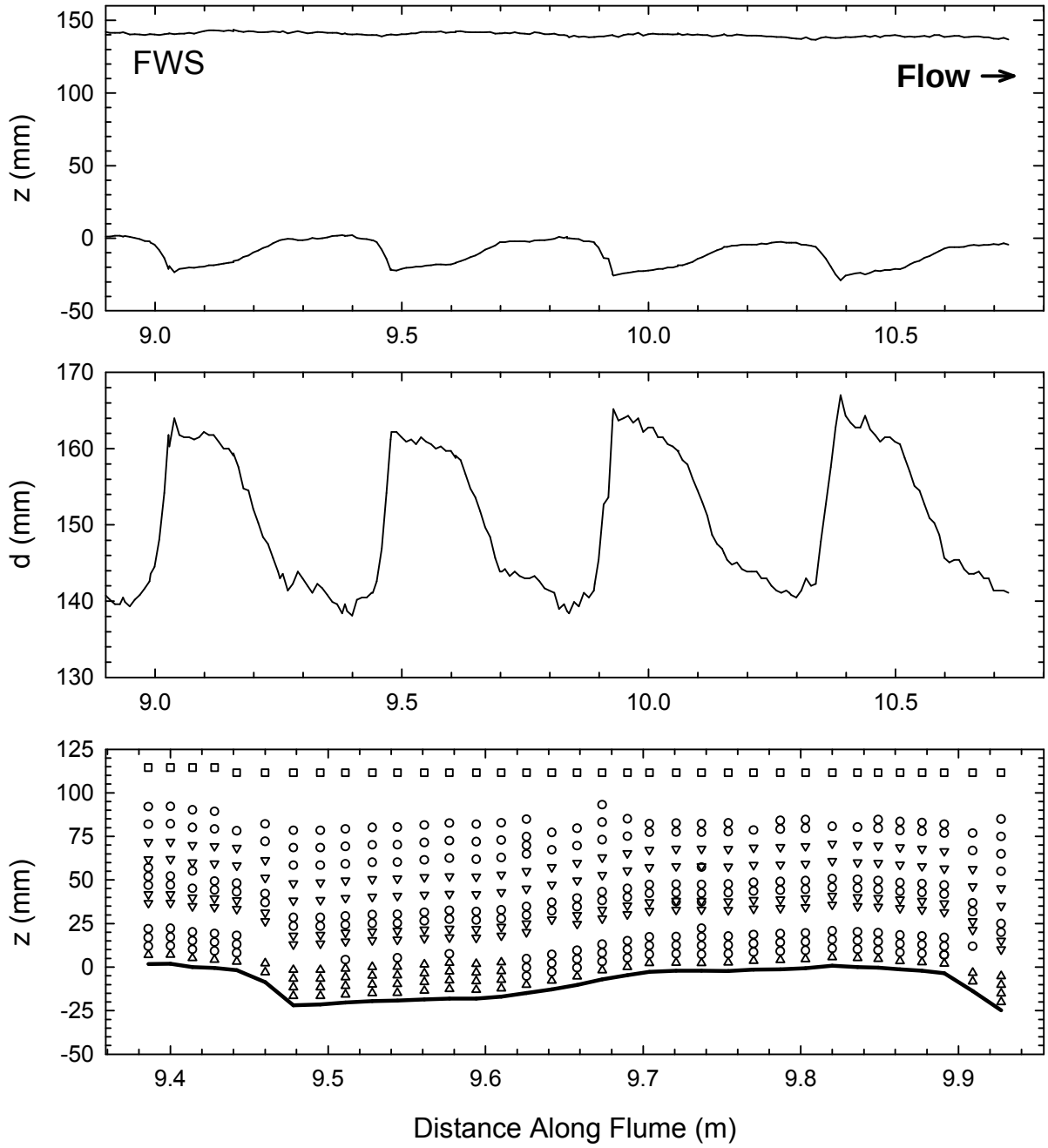

Figure D3: Bed and water surface, z, profiles over bedforms 5-9 (top) and corresponding flow depths, d, (middle) for the full-width saddle (FWS) dune configuration. Profiles were taken over the 8th downstream dune at the locations noted in the bottom panel.

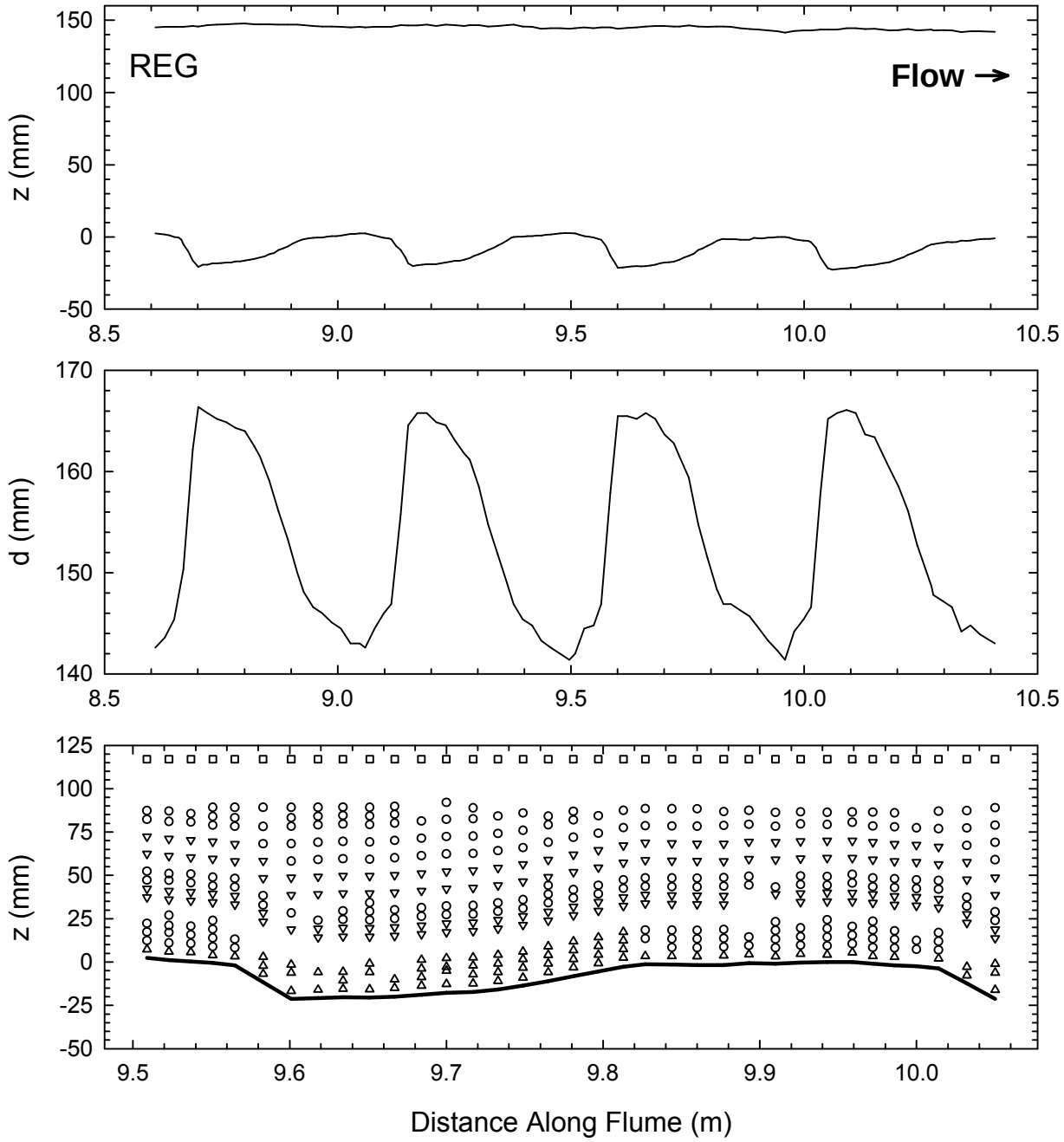

Figure D4: Bed and water surface, z, profiles over bedforms 5-9 (top) and corresponding flow depths, d, (middle) for the regular (REG) dune configuration. Profiles were taken over the 8th downstream dune at the locations noted in the bottom panel.

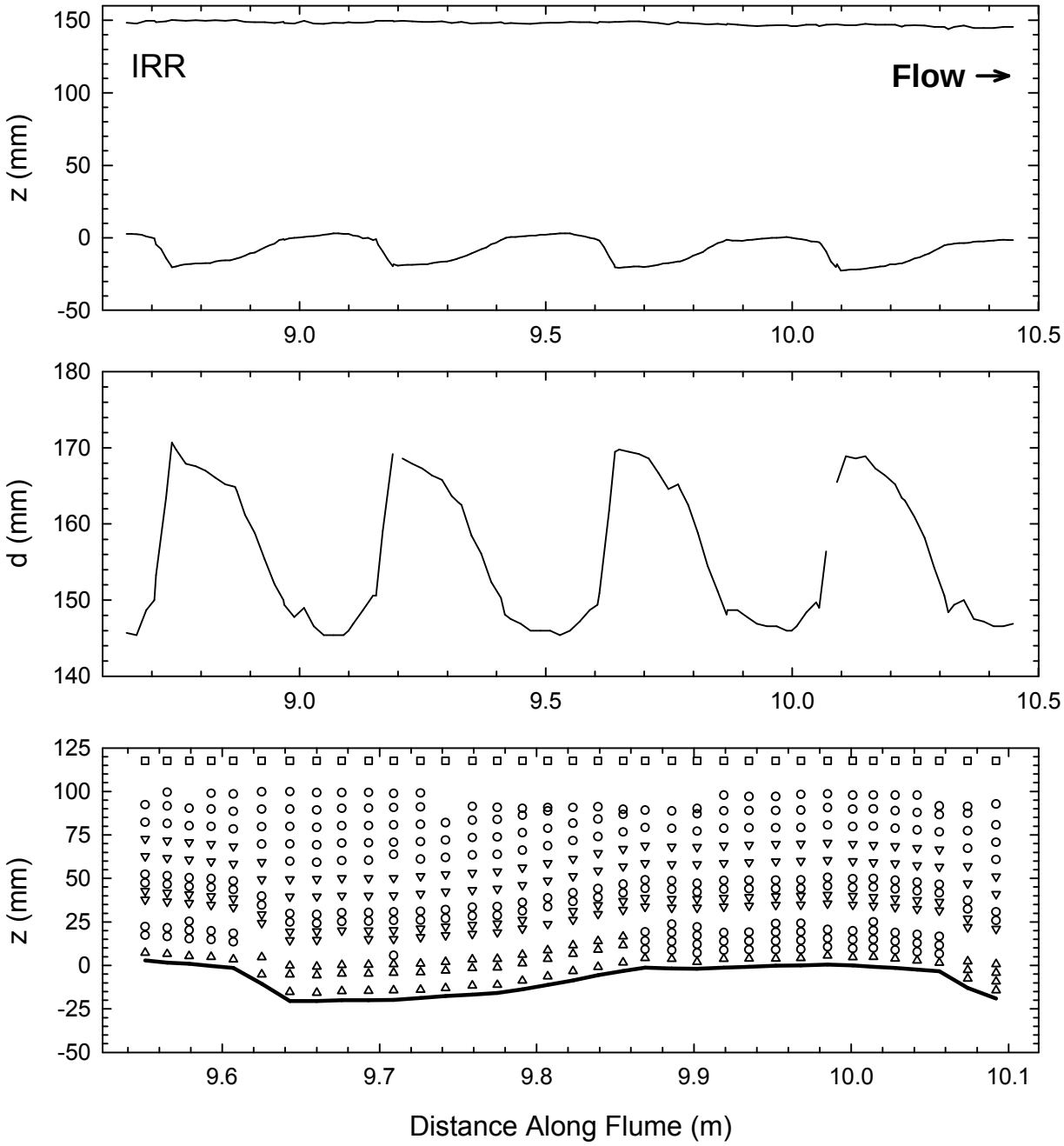

Figure D5: Bed and water surface, z, profiles over bedforms 5-9 (top) and corresponding flow depths, d, (middle) for the irregular (IRR) dune configuration. Profiles were taken over the 8th downstream dune at the locations noted in the bottom panel.

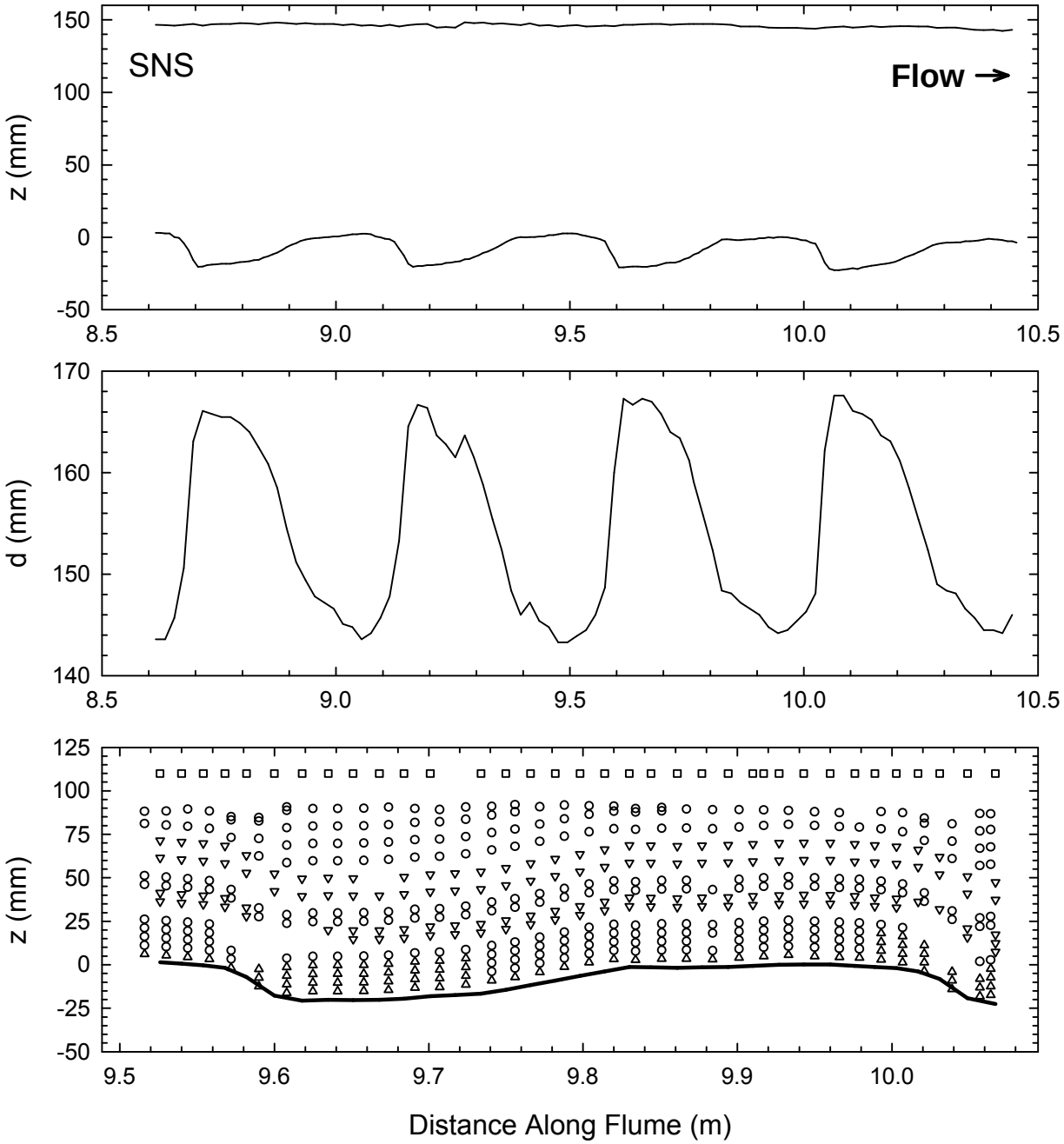

Figure D6: Bed and water surface, z, profiles over bedforms 5-9 (top) and corresponding flow depths, d, (middle) for the sinuous saddle (SNS) dune configuration. Profiles were taken over the 8th downstream dune at the locations noted in the bottom panel.

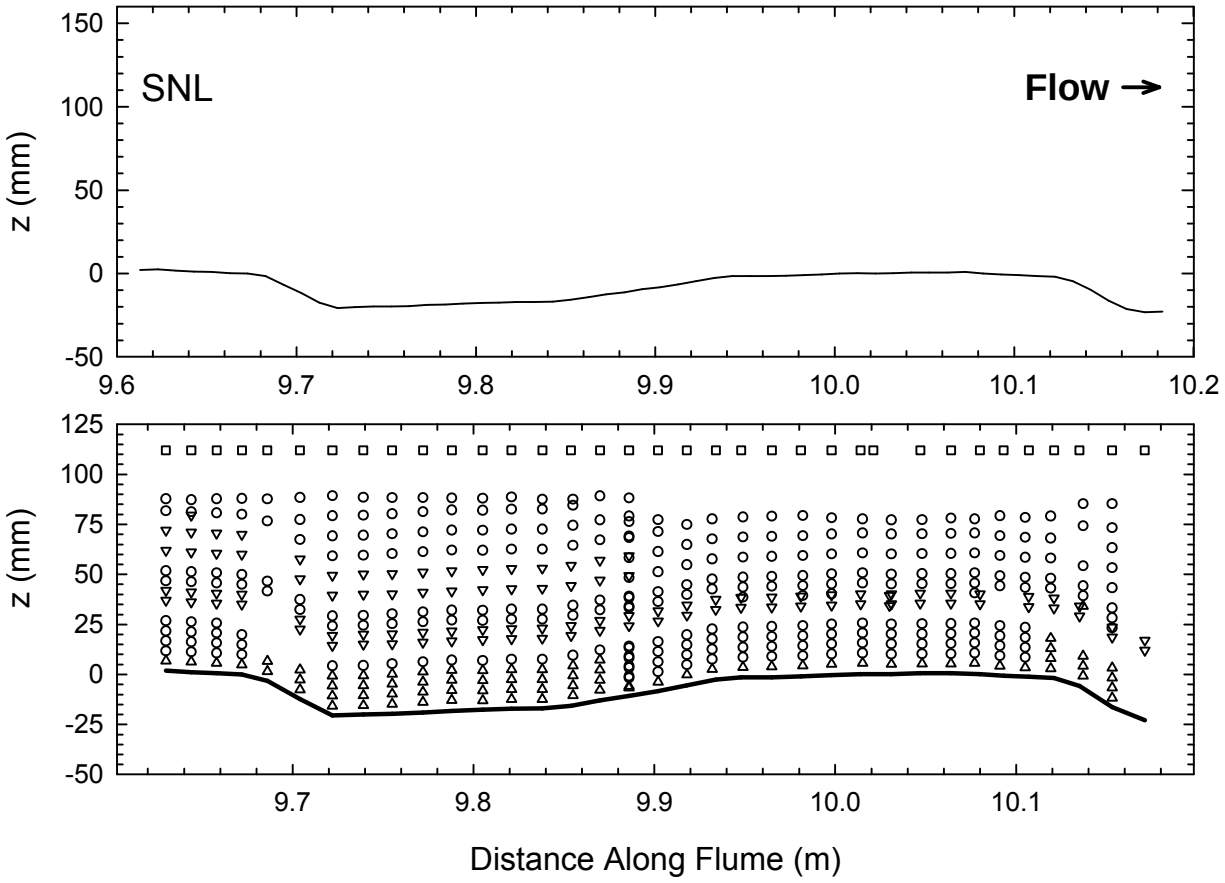

Figure D7: Bed and water surface, z, profiles over the 8th bedform (top) for the sinuous lobe (SNL) dune configuration. No water surface profile was taken over the sinuous lobe.

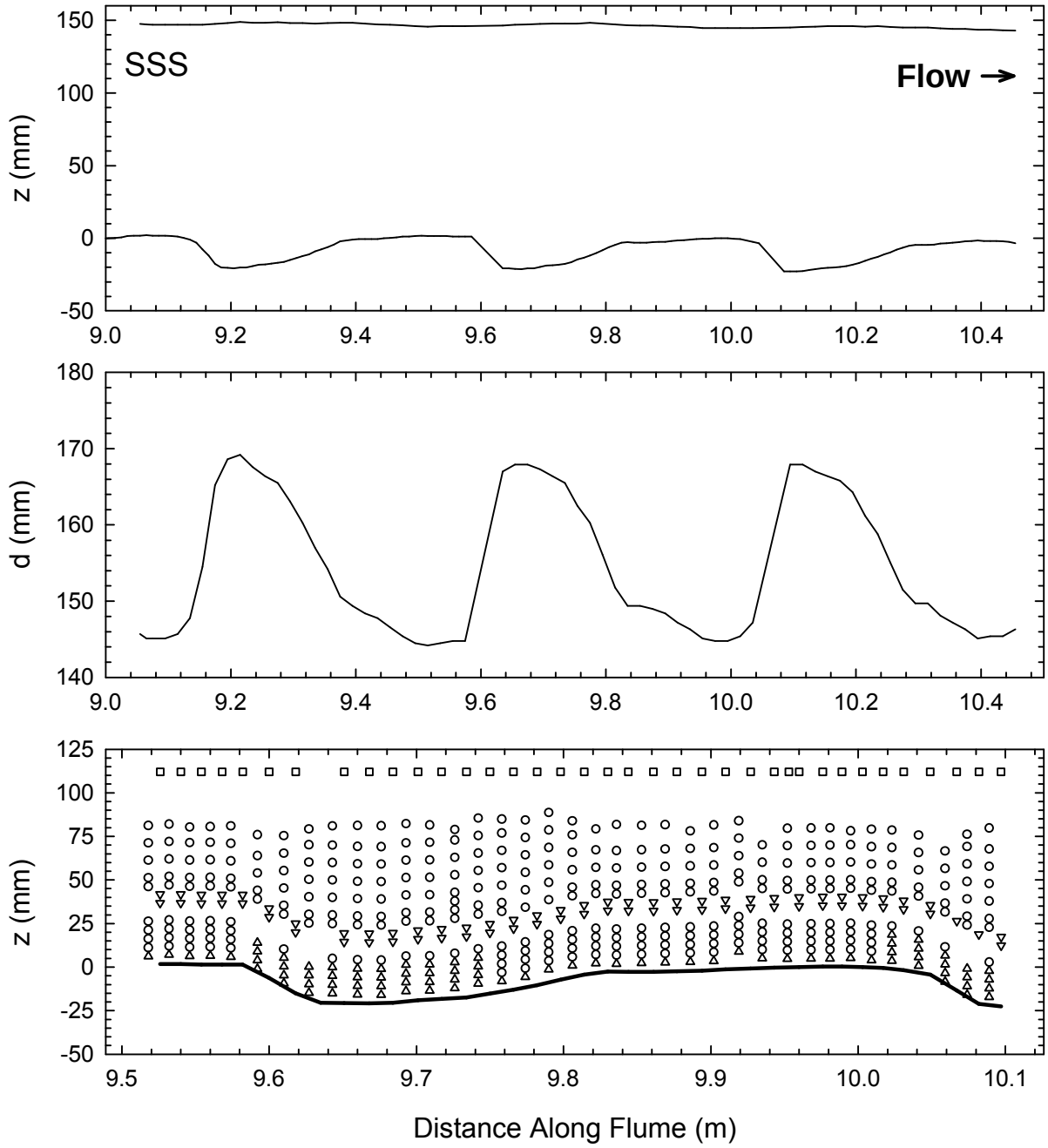

Figure D8: Bed and water surface, z, profiles over bedforms 6-9 (top) and corresponding flow depths, d, (middle) for the sinuous saddle dune configuration with the smoothed crestline (SSS). Profiles were taken over the 8th downstream dune at the locations noted in the bottom panel.

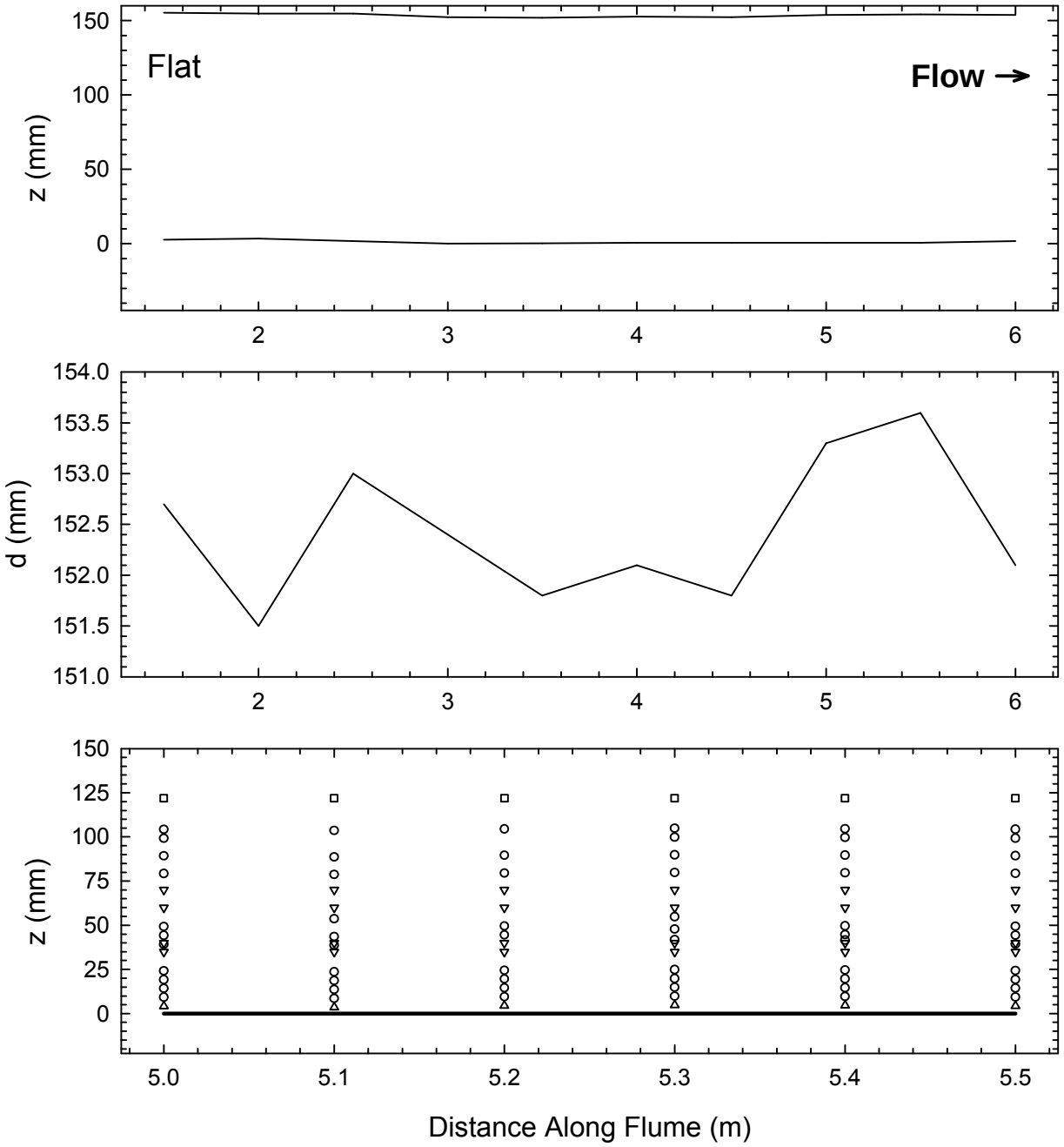

Figure D9: Bed and water surface, z, profiles over the flat bed and corresponding flow depths, d, (middle). Profiles were taken at the locations noted in the bottom panel.

Appendix E

Conventions for plotting spatially averaged profiles of mean streamwise velocity, U, and Reynolds shear stress, t_{uw} differ amongst sources. Thus, it is useful to compare the different ways the profiles may be constructed. Spatial averages can be calculated using either all the data between two successive crestlines or only data collected over the stoss slope of the dunes. Spatial averages may also be constructed at equal heights above a datum, z, such as the dune crest, or at lines equidistant from the boundary, z_{bed}.

Figure E1 plots averages based on all data between two successive crestlines relative to z and z_{bed}. Velocity measurements in the separation zone are included when profiles are calculated relative to z_{bed} and reduce the averages in the lower portion of the profile. This does not occur if the profiles are calculated relative to z. The upper portions of the profiles are similar.

Figure E2 plots averages of data collected on the stoss slope of the dunes only, relative to z and z_{bed}. Data from the separation zone is not included in the averages. The vertical rise over the stoss slope is only 3 mm, so the same data points are used to form averages and the profiles are identical.

Figures E3 and E4 both plot averages based on all data between two successive crestlines and averages of only these data collected over the stoss slope of the dunes. In Figure E3, both sets of averages are plotted relative to z. The profiles are nearly identical. In Figure E4, both sets of averages are plotted relative to z_{bed}. The lower portions of the profiles include data from the separation zone and average velocity is reduced. The upper portions of the profiles are nearly identical.

These plots indicate that the inner (lower) profile is affected by the plotting convention while the outer profile is not. This is particularly true if averages are plotted relative to z_{bed}. *Nelson et al.* [1993] and *McLean et al.* [1999] indicate that including data from the separation zone in spatial averages will produce biased inner profiles and that averages should include only data over the dune

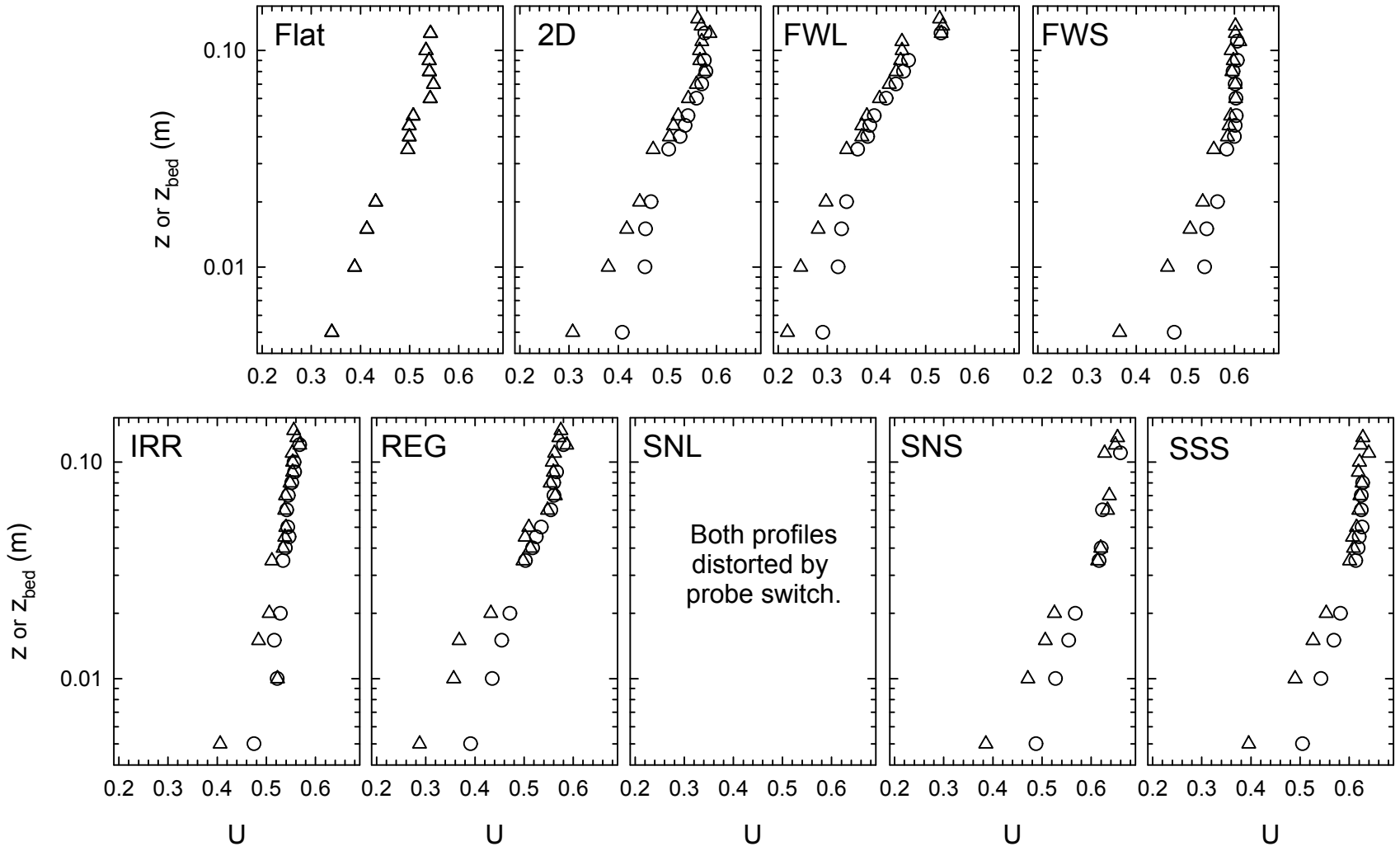

Figure E1: Spatially averaged streamwise velocity, U , profiles. Averages based on all data between successive crestlines (profiles 1-28 in Figure 5.3). Circles are averages calculated at constant heights above the dune crest and triangles are averages calculated at lines equidistant to the boundary. z is height above the crest and z_{bed} is height above the boundary. Profiles using data from profiles 1-28 in the averages over the sinuous lobe (SNL) were distorted because of the probe change and are not plotted.

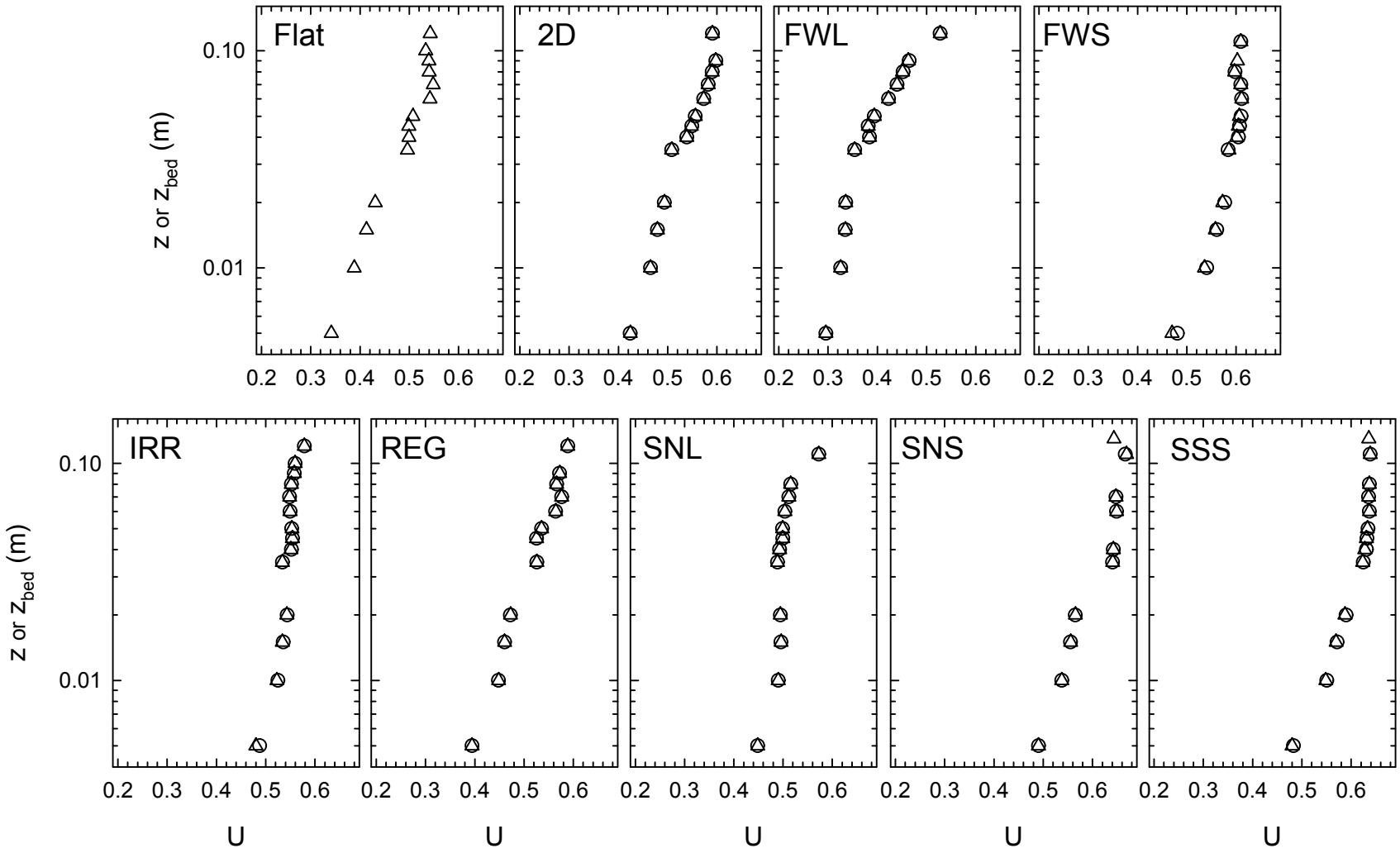

Figure E2: Spatially averaged streamwise velocity, U , profiles. Averages are based on data between *B1* and the dune crest (profiles 18-28 in Figure 5.3). Circles are averages calculated at constant heights above the dune crest and triangles are averages calculated at lines equidistant to the boundary. z is height above the crest and z_{bed} is height above the boundary.

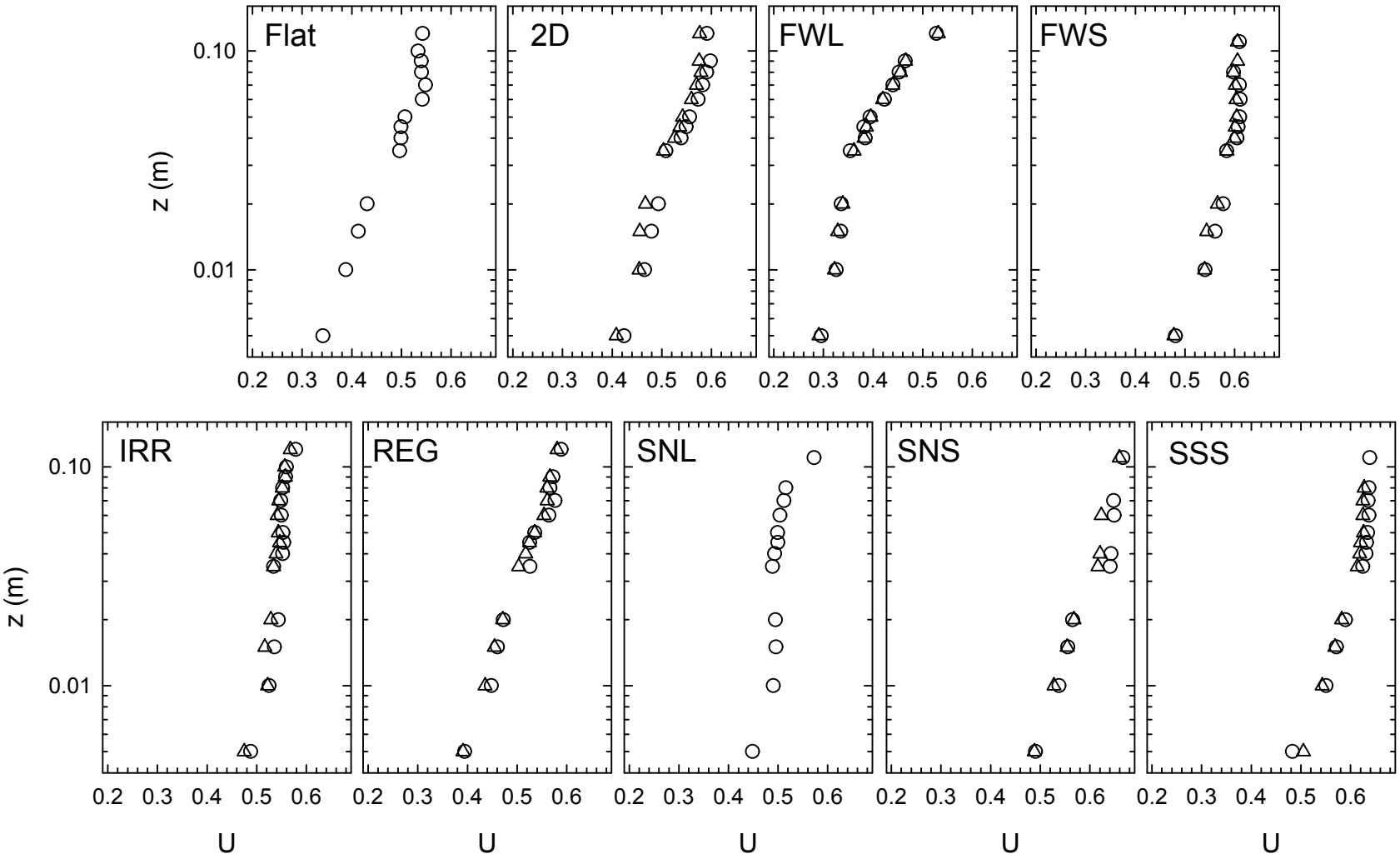

Figure E3: Spatially averaged streamwise velocity, U , profiles. Averages are calculated at constant heights above the dune crest. Circles are averages of data between *B1* and the crest (profiles 18-28 in Figure 5.3) and triangles are averages of all data between successive crestlines (profiles 1-28 in Figure 5.3). z is height above a datum that was the crest over the dunes and the bed over the flat bed. Profiles using data from profiles 1-28 in the averages over the sinuous lobe (SNL) were distorted because of the probe change and are not plotted.

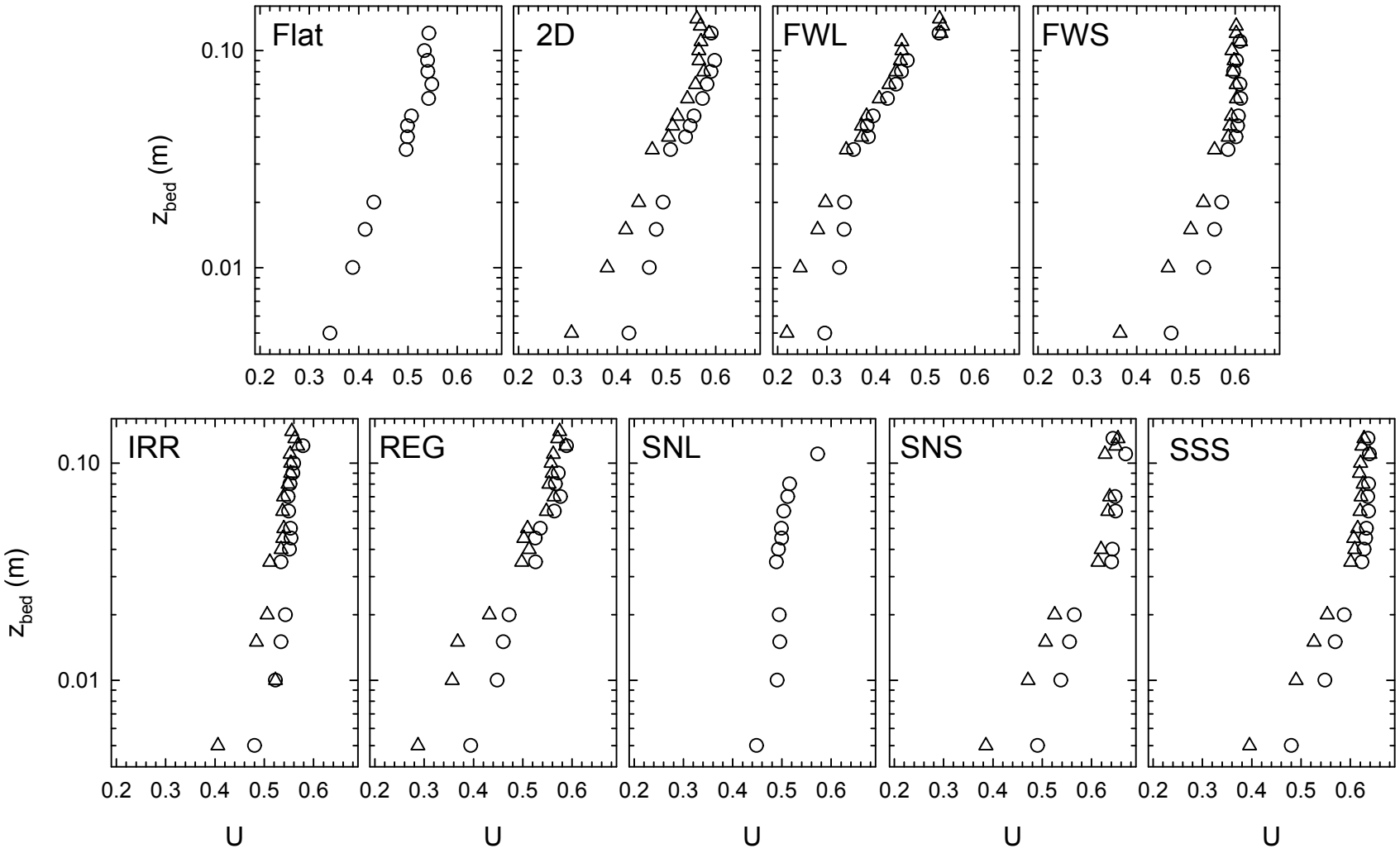

Figure E4: Spatially averaged streamwise velocity, U , profiles. Averages are calculated at lines equidistant to the boundary. Circles are averages of data between *B1* and the crest (profiles 18-28 in Figure 5.3) and triangles are averages of all data between successive crestlines (profiles 1-28 in Figure 5.3). z_{bed} is height above the boundary. Profiles using data from profiles 1-28 in the averages over the sinuous lobe (SNL) were distorted because of the probe change and are not plotted.

stoss slope. The outer profile is thought to represent the total shear stress over a dune so, logically, averaged profiles in the outer region should include all data between two successive crestlines. However, since the outer profile is not affected by the plotting convention, it is acceptable to calculate total shear stress from the outer profile over the stoss slope.

Spatially averaged t_{uw} profiles are meant to represent the total shear stress. Averages over the stoss slope will not represent the total stress and are excluded from consideration here. Figure E5 plots averages based on all data between two successive crestlines relative to z and z_{bed}. Profiles have similar shapes but the difference in the datum shifts the profiles down, which will affect the estimated spatially averaged boundary shear stress. The spatially averaged t_{uw} profile should be linear only well above the bedform, where values are not directly affected by flow separation. Thus, the more meaningful profile is from averages at constant heights above the dune crest [see *Nelson et al.*, 1993 and *McLean et al.*, 1999].

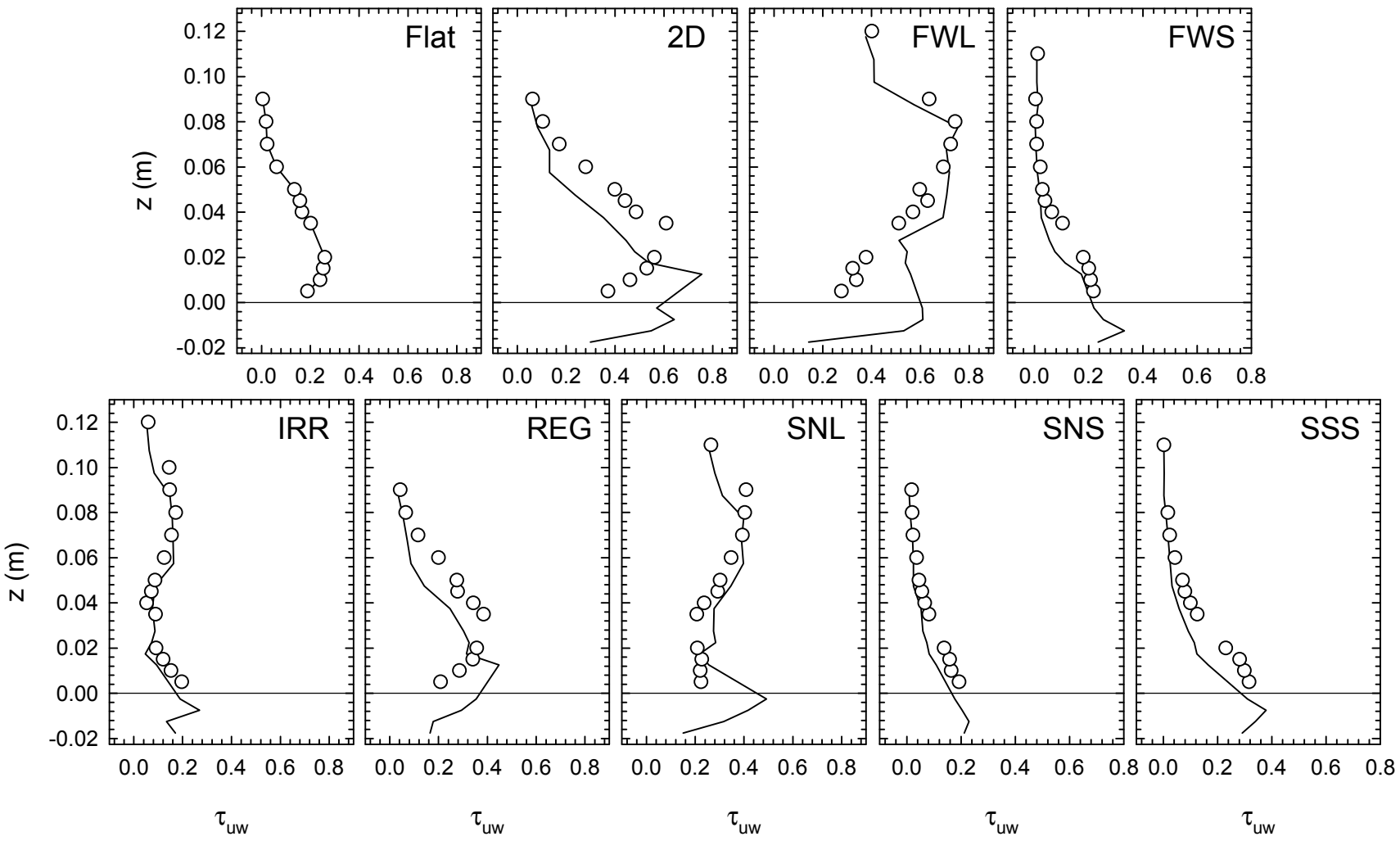

Figure E5: Spatially averaged Reynolds stress (τ_{uw}) profiles. Averages include all positive τ_{uw} values observed between two successive crestlines. Circles are averages along constant heights above a datum that was the crest over the dunes and the bed over the flat bed. Lines are averages calculated at lines equidistant to the boundary. All profiles are plotted with respect to height above the datum.